

Sunspot Group Evolution and the Global Magnetic Field of the Sun



Paul A. Higgins, BA (UC Berkeley)

School of Physics

University of Dublin, Trinity College

A thesis submitted for the degree of

Philosophiae Doctor (PhD)

October 1, 2012

Declaration

I, Paul A. Higgins, hereby certify that I am the sole author of this thesis and that all the work presented in it, unless otherwise referenced, is entirely my own. I also declare that this work has not been submitted, in whole or in part, to any other university or college for any degree or other qualification.

Name: Paul A. Higgins

Signature: **Date:**

The thesis work was conducted from October 2, 2008 to September 30, 2012 under the supervision of Dr. Peter T. Gallagher at Trinity College, University of Dublin.

In submitting this thesis to the University of Dublin I agree that the University Library may lend or copy the thesis upon request.

Name: Paul A. Higgins

Signature: **Date:**

Summary

Sunspots are regions of decreased brightness in the photosphere, or surface layer of the Sun, associated with strong magnetic fields. They are thought to be manifestations of an interior magnetic dynamo and are associated with activity in the atmosphere such as flaring and coronal mass ejections. Sunspots often emerge in groups with life-times on the order of days to weeks and their global emergence rate is characterized by an 11-year cycle. Additionally, they play an integral role in the 22-year magnetic cycle, and can be used as a tracer to study the internal magnetic dynamo.

To study sunspot groups over an entire solar cycle, we have developed the SolarMonitor Active Region Tracker (SMART) that applies a series of simple image processing techniques to photospheric magnetograms to detect, characterise, and track features manifested in the photospheric field.

This thesis addresses three questions:

- *What are the conditions in sunspot groups that result in solar flares?* A statistical study of the relationship between the properties of detected sunspot groups and the magnitude of their associated flares has allowed us to determine minimum values of properties allowing for the production of different flare magnitudes. Physical properties related to strong gradients between oppositely oriented magnetic fields are shown to be good indicators for a sunspot group's potential for flaring.
- *What mechanisms determine the configuration of the global magnetic field and how does this relate to the solar dynamo?* The properties of detected sunspot groups are compared between solar cycle phases to the global magnetic field configuration. This study shows that the plateau phase of the cycle exhibits an excess of features with large flux and that the global magnetic field configuration is strongly determined by the distribution of magnetic features in the photosphere.
- *What mechanisms govern the evolution and decay of sunspot groups?* The decay of sunspot groups is investigated by simulating solar surface flows. By comparing simulations of flux dispersal with observations diffuse magnetic flux, the diffusion coefficient characterising the flows is constrained.

Our results exemplify the benefit of using automated systems for solar feature analysis. For the first time, a time-dependent comparison between the

properties of magnetic features and flaring over the solar cycle is presented. Also novel is the comparison between feature properties and the global configuration of the Sun. Finally, the first direct comparison between the poleward propagation of dispersing sunspot flux and a data-driven simulation is presented. This work is a study of the emergence, evolution, and decay of the solar surface magnetic field.

For Grandpa Smith (the physics) and Grandpa Higgins (the mathematics).

Acknowledgements

This work could not have been completed without the support of many people, including my coworkers, friends, and family. The massive enthusiasm and commitment to good science of my supervisor, Dr. Peter T. Gallagher, has driven me complete this thesis. His knowledge and experience has consistently led me in the right direction. But his style of supervision gave me the freedom to collaborate and explore many fascinating avenues of this research. He also taught me how to schmooze, network, and advertise (what is the point of doing research if no one hears about it?). This has been paramount to my development as a researcher.

For the first half of my time at the College of the Holy and Undivided Trinity of Queen Elizabeth near Dublin, I resided on the 4th floor of the Sami Nasr Institute of Advanced Materials and had some of the best times of my life with the Astrophysics Research Group (ARG!) PhD students. I am thankful that most of the photos have been destroyed. In addition to running amok on the mean streets of Dublin (and beyond), we found time to do some exciting science. The work of the ARG members who have come before and after have always impressed me— and driven me to do my best. And my appreciation goes to my incredibly smart class mates, Sophie Murray and Peter Byrne (keep on rockin!).

During the second half of my PhD I switched offices to the 3rd floor of the Fitzgerald building. I begin everyday by passing the steely gazes of Hamilton and Schrodinger. I think this, in addition to sharing the office with two hard working postdocs has kept me motivated. Shaun Bloomfield has been instrumental in my understanding of many solar physics topics, and the insight he has provided for each of my projects has improved them immensely. I will never forget drinking tea by the fire in the staff common room on those rainy afternoons, ranting about the government like 75-year-olds. David Perez-Suarez has also been incredibly helpful, especially with regards to making me a better programmer— and his positivity and absurdist humour has gotten me through many a gray Dublin working day.

I would like to acknowledge the generous tax payers of the ESA member states (Prodex/Proba2, Framework 7/Helio) who have paid for the majority of this PhD, and the TCD school of physics who have paid for the rest. Thanks also go to my external collaborators (especially Tufan, Fraser, and

Cis, who accompanied me on those epic “steam trains” through Switzerland).

To Mr. Brian Cooney, for printing the very thesis draft that you are holding in your hand– I would not have gotten this thing submitted on time without your help! And to Pietro Zucca for printing the last 30 pages at the last minute, when I finally finished making changes to my last chapter (in the words of Aidan O’Flannagain, ”Balls to the wall, huh?”)...

To my irish family, thanks for making me feel like I belong in Ireland. Most importantly, my eternal gratitude goes to my immediate family, Mom, Dad, and Shannon, for their unending love and support, and to my grandmas for always being proud of me.

Lastly, to the real reason I was able to stay in Ireland these past years (despite the weather), Ms. Caitlin Cooney. Shine on, you crazy Diamond...

Refereed Publications

- [1] O. W. Ahmed, R. Qahwaji, T. Colak, **P. A. Higgins**, P. T. Gallagher, and D. S. Bloomfield. Solar Flare Prediction Using Advanced Feature Extraction, Machine Learning, and Feature Selection. *Solar Phys.*, page 404, November 2011.
- [2] **P. A. Higgins**, D. S. Bloomfield, and P. T. Gallagher. Active Regions and the Global Magnetic Field of the Sun. *Astronomy & Astrophysics*, May 2012. in prep. 187
- [3] **P. A. Higgins**, D. S. Bloomfield, and P. T. Gallagher. Quantifying Diffusion: Tracking Magnetic Flux Transport on the Sun. *Solar Physics*, May 2012. in prep. 215
- [4] **P. A. Higgins**, P. T. Gallagher, R. T. J. McAteer, and D. S. Bloomfield. Solar magnetic feature detection and tracking for space weather monitoring. *Advances in Space Research*, 47:2105–2117, June 2011.
- [5] D. S. Bloomfield, **P. A. Higgins**, R. T. J. McAteer, and P. T. Gallagher. Toward Reliable Benchmarking of Solar Flare Forecasting Methods. *Astrophys. J. Lett.*, 747:L41, March 2012.
- [6] D. S. Bloomfield, E. Carley, P. T. Gallagher, **P. A. Higgins**, D. M. Long, S. A. Maloney, S. A. Murray, A. O’Flannagain, D. Pérez-Suárez, D. Ryan, and P. Zucca. A Comprehensive Overview of the 2011 June 7 Solar Storm. *Astronomy & Astrophysics*, May 2012. in prep.
- [7] D. Pérez-Suárez, **P. A. Higgins**, D. S. Bloomfield, R. T. J. McAteer, L. D. Krista, J. P. Byrne, and P. T. Gallagher. *Automated Solar Feature Detection for Space Weather Applications*, pages 207–225. IGI Global, March 2011.
- [8] D. Perez-Suarez, S. A. Maloney, **P. A. Higgins**, D. S. Bloomfield, and 17 co-authors. Studying Sun-planet connections using the Heliophysics Integrated Observatory (HELIOS). *Solar Physics*, pages 1–19, August 2012. 10.1007/s11207-012-0110-x.
- [9] C. Verbeeck, **P. A. Higgins**, T. Colak, F. T. Watson, V. Delouille, B. Mampaey, and R. Qahwaji. A Multi-wavelength Analysis of Active Regions and Sunspots by

REFEREED PUBLICATIONS

- Comparison of Automatic Detection Algorithms. *Solar Phys.*, page 369, October 2011.
- [10] J. Zender, D. Berghmans, D. S. Bloomfield, C. Cabanas Parada, I. Dammasch, A. De Groof, E. D'Huys, M. Dominique, P. Gallagher, B. Giordanengo, **P. A. Higgins**, and 10 co-authors. The Projects for Onboard Autonomy (PROBA2) Science Centre: Sun Watcher Using APS Detectors and Image Processing (SWAP) and Large-Yield Radiometer (LYRA) Science Operations and Data Products. *Solar Phys.*, page 142, July 2012.

Contents

Refereed Publications	vii
List of Figures	xv
List of Tables	xix
1 Introduction	1
1.1 The Sun as a Star	2
1.2 The Core	8
1.3 The Radiative Zone	9
1.4 The Convection Zone	12
1.5 Large-scale Flows	14
1.6 The Solar Atmosphere	17
1.6.1 The Photosphere	21
1.6.2 The Chromosphere	24
1.6.3 The Corona	26
1.6.4 The Solar Wind	29
1.7 Sunspot Groups	32
1.7.1 Sunspot Emergence	32
1.7.2 Sunspot Structure	35
1.7.3 Sunspot Group Evolution	39
1.8 The Solar Activity Cycle	41
1.8.1 The Sunspot Cycle	41
1.8.2 Global Field Reversal	46
1.8.3 Active Sunspot Groups	48
1.9 Solar Eruptions	52
1.10 Thesis Aims	56
2 Theory of Magnetic Fields in a Plasma	59
2.1 Plasma Physics	59
2.2 Fluid Dynamics	63
2.3 Magnetohydrodynamics	65
2.4 Dynamo Theory	73

CONTENTS

2.5	Magnetic Fields in the Corona	76
2.6	Magnetic Reconnection	82
2.7	Quantifying Magnetic Fields at the Solar Surface	87
3	Instrumentation and Observations	95
3.1	Solar Magnetic Field Observations	96
3.1.1	Zeeman Effect	96
3.1.2	Early Observations	104
3.1.3	The Michelson Doppler Imager	106
3.1.4	The Helioseismic and Magnetic Imager	109
3.2	Feature and Event Lists	112
4	Detecting and Tracking Solar Active Regions	115
4.1	Introduction	116
4.2	Feature Extraction	119
4.2.1	Segmentation	120
4.2.2	Characterization	125
4.2.3	Secondary Characterisation Modules	130
4.2.4	Classification	132
4.3	Tracking	134
4.3.1	Consecutive Images	134
4.3.2	Far-side Passage	135
4.3.3	Cataloging	135
4.4	Results and Discussion	136
4.4.1	Magnetic Filling Factor	137
4.4.2	SMART Method Uncertainties	140
4.4.2.1	SMART-NOAA Comparison	140
4.4.2.2	Data Uncertainties	142
4.4.2.3	Tracking NOAA 10488	142
4.4.2.4	Tracking Behaviour Deviating from NOAA	145
4.4.3	Simulating Feature Tracking	147
4.4.3.1	Area Detection of a Circular Feature	147
4.4.3.2	Magnetic Properties of a Bipolar Feature	150
4.5	Conclusions	154
4.5.1	The SolarMonitor Active Region Tracker	155
4.5.2	Observational Uncertainties	155
4.5.3	Method Uncertainties	156
5	The Flare Productivity of Sunspot Groups	159
5.1	Introduction	160
5.2	Case Studies	161
5.2.1	NOAA 10365 (10386)	162
5.2.2	NOAA 11226	166
5.3	Properties of Flaring Sunspot Groups	171

CONTENTS

5.4	Solar Cycle Dependence of Flaring Sunspot Groups	175
5.5	Conclusions	182
5.5.1	Case Studies	183
5.5.2	Active Region Flaring Potential	184
5.5.3	Solar Cycle Dependence	185
6	Sunspot Groups and the Global Magnetic Field of the Sun	187
6.1	Introduction	188
6.2	Methods	190
6.2.1	Magnetic Butterfly Maps	191
6.2.2	Spherical Harmonic Decomposition	192
6.3	Results and Discussion	193
6.3.1	The Magnetic Active Region Cycle	193
6.3.2	The Global Magnetic Field	202
6.4	Conclusions and Future Work	212
7	Magnetic Flux Transport	215
7.1	Introduction	216
7.1.1	Modeling Supergranular Diffusion	216
7.1.2	Observational Studies	218
7.1.3	Simulation Studies	219
7.1.4	Constraining D	220
7.2	Observations	222
7.3	Methods	224
7.3.1	Latitude-time Mapping	225
7.3.2	Large-scale Flow Simulation	226
7.4	Results and Discussion	229
7.4.1	Diffusion Tracking	231
7.4.2	Simulations	232
7.4.2.1	Random-walk Simulation	233
7.4.2.2	Laplacian Continuous Simulation	236
7.4.2.3	Data-driven	239
7.5	Conclusions	239
7.5.1	Comparison to Previous Work	241
8	Conclusions and Future Work	243
8.1	Conclusions	243
8.2	Future Work	246
8.3	Detecting and Tracking Solar Active Regions	247
8.4	The Flare Productivity of Sunspot Groups	248
8.5	Sunspot Groups and the Global Magnetic Field of the Sun	251
8.6	Characterising the Transport of Diffuse Magnetic Flux	254
8.7	Outreach Activities	255

CONTENTS

References	257
Glossary	277
Reference Tables	281

List of Figures

1.1	A comparison between the theoretical and observed solar flux.	3
1.2	The BP2004 numerical model of the solar interior.	5
1.3	The layers of the Sun.	7
1.4	A Hertzsprung-Russel color-magnitude diagram.	8
1.5	A schematic diagram of the macroscopic motions on the solar surface. .	14
1.6	The solar differential rotation.	15
1.7	The progression of our understanding of the solar and stellar atmospheres.	18
1.8	The temperature and density dependence of the Solar atmosphere. . . .	19
1.9	A view of the Sun from SDO and SOHO/LASCO.	20
1.10	Rolling convection at the photosphere.	21
1.11	Magnetic elements at supergranule boundaries.	22
1.12	Oscillation modes within the Sun.	23
1.13	An image of the Sun at the H α absorption line.	25
1.14	A static model of the quiet Sun.	26
1.15	A image in EUV with the magnetic polarities indicated.	27
1.16	The height dependence of the plasma β parameter in the solar atmosphere.	28
1.17	A schematic of the Parker solar wind spiral in 3D.	30
1.18	A 1D map of the heliosphere.	31
1.19	A model of a toroidal flux rope rising in the convection zone.	33
1.20	A diagram of a sunspot above and below the photosphere.	37
1.21	The structure of a facular bright point.	38
1.22	A three dimensional model of an emerging sunspot.	39
1.23	The sunspot cycle over \sim 150 years.	45
1.24	The McIntosh sunspot group classification system.	49
1.25	The progression of a typical solar flare.	53
1.26	The frequency distribution of flare magnitudes measured in various studies.	55
2.1	A schematic of magnetic fields generated by the solar dynamo.	72
2.2	Coronal loops in an active region.	77
2.3	A schematic of a coronal loop.	78
2.4	An example of a potential field source surface extrapolation.	80
2.5	The change in magnetic field configuration over the course of a flare. .	83
2.6	A schematic of magnetic reconnection.	84

LIST OF FIGURES

2.7	A schematic of helicity within a sunspot.	89
2.8	An image of evolving magnetic features.	92
3.1	A schematic of Zeeman energy level splitting.	96
3.2	A comparison of the line splitting and polarisation due to the Zeeman effect.	101
3.3	A comparison of Stokes parameters for different magnetic fields.	103
3.4	A schematic of Hale's magnetometer.	104
3.5	A schematic of Babcock's Zeeman effect measurement.	105
3.6	A schematic diagram of MDI.	106
3.7	The instrument response of MDI.	107
3.8	A comparison between MDI and HMI.	109
3.9	A schematic of HMI.	110
3.10	A plot of the HMI filtergram bandpasses.	111
3.11	An example of Zeeman splitting of the Fe I line.	111
4.1	The SMART method.	118
4.2	The SMART segmentation method.	119
4.3	Example SMART image processing steps.	120
4.4	Maximum QS magnetic field over the solar cycle.	121
4.5	AR magnetic field distribution.	122
4.6	The SMART characterisation method.	125
4.7	SMART characterisation method for PSLs.	127
4.8	The SMART classification method.	128
4.9	Example PSL and Ising energy determination.	129
4.10	An example set of classified SMART detections.	132
4.11	A flux-tube observation schematic.	137
4.12	A schematic comparison between actual and observed flux-tubes.	139
4.13	NOAA and SMART detections over cycle 23.	141
4.14	Tracking of 20031026.MG.11.	143
4.15	SMART detection and tracking divergent from NOAA.	146
4.16	A simulation of a feature crossing the Sun.	147
4.17	The pixel area LOS correction factor.	148
4.18	Longitude dependence of area uncertainty.	149
4.19	A bipole feature disk-crossing simulation.	150
4.20	Plots of corrected area and flux.	152
4.21	Longitudinal dependence of magnetic gradient.	153
4.22	The longitude dependence of the BCL and PSL orientation.	153
5.1	NOAA 10365 detection contours.	163
5.2	NOAA 10365 property evolution.	165
5.3	NOAA 10365 photosphere and coronal evolution.	166
5.4	NOAA 10365 complexity evolution.	167
5.5	Long-term NOAA 11226 magnetic evolution.	168
5.6	Short-term evolution of NOAA 11226	170

LIST OF FIGURES

5.7	Flaring AR area distributions.	173
5.8	Flaring AR flux distributions.	174
5.9	Flaring AR R-value distributions.	175
5.10	AR R-value versus flux.	176
5.11	AR R-value versus WL_{SG}	177
5.12	AR butterfly diagram showing PSL strength.	178
5.13	Sun-averaged AR property time series.	179
5.14	Correlation between AR property time series and flaring.	181
6.1	The magnetic flux and sunspot number over cycle 23.	194
6.2	A butterfly map indicating magnetic flux emergence.	195
6.3	A plot of the amount of time flux emerges at each latitude.	198
6.4	The distribution of AR area and flux over the solar cycle.	200
6.5	Magnetic butterfly diagram of mean signed field.	202
6.6	The Φ_{net} measured in each hemisphere.	204
6.7	Comparison between PFSS extrapolations and white-light images.	208
6.8	Spherical harmonic visualisations.	210
6.9	Global magnetic field spherical harmonic strengths over time.	211
7.1	Schematics of the evolution of continuous and discrete random-walk diffusion.	217
7.2	Previous supergranular diffusion study results.	221
7.3	NOAA 8068 over 6 solar rotations.	223
7.4	The processing steps used to generate a butterfly map.	225
7.5	Assumed surface velocity profiles for the diffusion simulations.	227
7.6	An example of applying the Laplacian operator to simulate diffusion.	228
7.7	A magnetic butterfly diagram showing $\langle B_{\text{sign}} \rangle$	230
7.8	A zoom-in of Figure 7.7.	231
7.9	A random walk simulation.	233
7.10	The results of a random walk simulation.	234
7.11	Continuous diffusion simulation.	237
7.12	Continuous diffusion and flow simulation.	238
7.13	Data-driven diffusion simulations.	240
8.1	The 7 June 2011 eruption.	248
8.2	A block diagram of a flare prediction system.	249
8.3	A schematic of detected loops overlaid on a magnetogram.	250
8.4	A butterfly map of residual differential rotation.	252
8.5	An example star map.	256

LIST OF FIGURES

List of Tables

1.1	Physical properties of the Sun.	6
1.2	Characteristic property values for the solar surface and atmosphere.	17
1.3	The possible sunspot group classifications using the Hale scheme.	50
1.4	The GOES flare classification scheme.	56
4.1	List of magnetic properties.	124
4.2	A list of PSL-related physical properties.	126
5.1	Minimum AR property values for flaring.	172
6.1	Linear fits to AR emergence space-time extent.	196
6.2	Power-law fits to distributions of AR area and Φ_{tot}	201
7.1	The elements of the discrete Laplacian operator kernel.	228
7.2	A summary of random-walk simulation runs.	235
8.1	A list of physical constants.	282
8.2	A list of unit conversions.	283

LIST OF TABLES

1

Introduction

An overview of the properties of sunspot groups, solar activity, and the global magnetic field of the Sun is given in this chapter. The structure of the Sun is described, from the core to the outer atmosphere. The birth, evolution, and decay of sunspot groups and their connection to the large-scale magnetic field over the solar cycle is explained. Then, the properties of active sunspot groups and the eruptions they produce are discussed. Finally, the aims of this thesis are summarised.

Carl Sagan maintains, “the Sun is an ordinary, even a mediocre star” (162). While this statement makes our nearest star sound both mundane and uninteresting, the Sun provides a unique perspective on the physics of the average star. Unlike other stars that are effectively point sources, the Sun can be studied with unparalleled spatial resolution with a telescope. This permits us to spatially resolve features covering a small fraction of the solar disk, such as sunspots, magnetic loops, and coronal holes. The internal mechanics of the Sun may be inferred from studies of these features. For example, the solar activity cycle was discovered due to long-term observations of sunspots. Long-

1. INTRODUCTION

term photometric observations show that certain distant stars exhibit a cyclic variability (131); studies of the Sun indicate the phenomenon is tied to a magnetic dynamo (144). The physics of distant, spatially unresolved solar-type stars can thus be understood from detailed studies of our closest stellar neighbor.

The following sections provide a general discussion of the Sun as a star as well as our observational and theoretical knowledge of its long- and short-term dynamics. The current state of knowledge regarding the phenomena studied in this work is discussed. This includes the 22-year magnetic cycle, the 11-year activity cycle, the evolution of sunspot groups, and the large-scale transport of magnetic fields dispersing from decaying sunspot groups.

1.1 The Sun as a Star

The Sun is the nearest star to the Earth. Its existence is the result of the collapse of a cloud of interstellar gas and dust which initially reached an equilibrium between the inward force of gravitation and outward pressure forces, including that due to the subsequent energy release from nuclear fusion. The Sun is a Population I star, indicating that it may have emerged from the remains of two preceding generations of stars (Populations II and III). The ejected gas due to the energetic deaths of giant stars (supernovae) from early stellar populations contains heavy elements, fused from lighter elements during the explosions. The Sun later accreted this gas as it formed in the interstellar medium. The Sun has a mainly cosmic composition: 73.46% hydrogen, 24.85% helium, and 1.69% heavier elements, by mass.

In the standard stellar model, hydrostatic equilibrium is assumed throughout the solar interior. The force of gravity compresses material radially inward, resulting in an opposing force due to the resulting gradient in gas pressure,

$$\frac{dP}{dr} = -G \frac{M_r \rho}{r^2}, \quad (1.1)$$

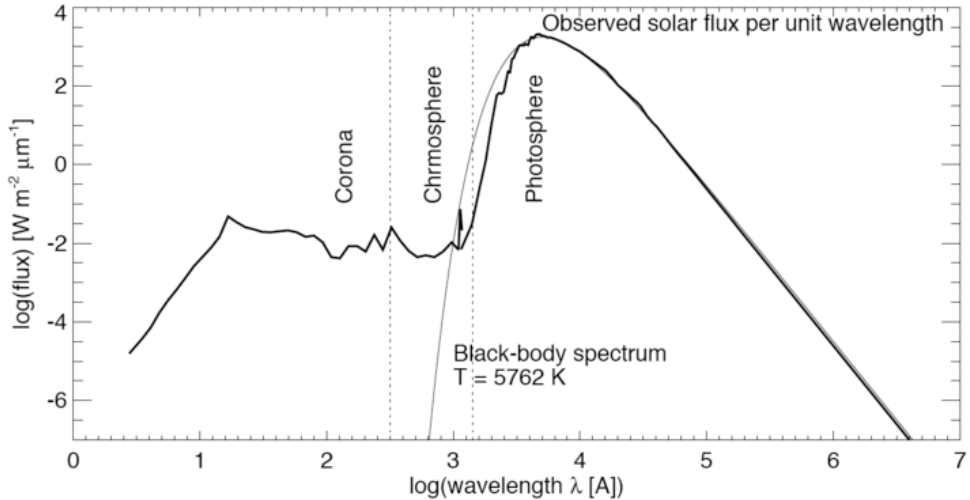


Figure 1.1: A comparison between the theoretical and observed solar flux over wavelength. The thick line shows the observed solar spectrum with emission and absorption lines at short and long wavelengths, respectively. A 5762 K black body spectrum is indicated by the thin line (from 7).

where M_r is the mass contained within a given radius and G is the gravitational constant. The pressure (P), density (ρ), and temperature (T) decrease monotonically with radius (r) from the centre to the solar surface. The majority of stars undergoing fusion are governed by the same force balance between gas pressure and gravity¹. The gas pressure is helped by radiation originating from fusion in the core, contributing to internal heating as well as a radiative pressure force.

It is also assumed that local thermodynamic equilibrium (LTE) is reached, implying that stellar material is thermalised and that both the material and radiation field are in equilibrium. The material is assumed to radiate as a black-body (perfect efficiency of absorption and emission). In LTE the distance particles travel between collisions is much smaller than the length-scale over which temperature varies, the temperature scale height, $T/(dT/dr)$. The Planck function gives the distribution of energy emitted

¹radiation pressure is negligible in the Sun, but plays a dominant role in the largest stars. Also, electron and neutron degeneracy pressures support white dwarf and neutron star interiors, respectively

1. INTRODUCTION

as a function of temperature and wavelength,

$$B_\lambda(T) = \frac{2hc^2/\lambda^5}{e^{hc/\lambda k_B T} - 1}, \quad (1.2)$$

which has units of $\text{erg s}^{-1} \text{cm}^{-2}$. Here, h is Planck's constant, c is the speed of light, λ is wavelength, and k_B is the Boltzmann constant. This equation solved the “ultraviolet catastrophe”, whereby a classical mechanics treatment of the blackbody gives an infinite radiant energy. This equation was derived by Planck on the assumption that radiation is quantised into energy packets, or photons. The Sun is not a perfect blackbody, as shown by the comparison between theory and data (Figure 1.1). This is mostly due to spectral emission and absorption lines that are formed in the solar atmosphere, as described in Section 1.6.

The peak in emission wavelength, λ_{\max} , of a blackbody spectrum is inversely related to temperature,

$$\lambda_{\max}T = 0.290 \text{ [cm K]}, \quad (1.3)$$

where λ_{\max} is given in cm. This is known as Wien's displacement law. Solar emission peaks in the green region of the visible spectrum with a temperature of 5 770 K and λ_{\max} of 5 030 Å, but averaged over the whole visible spectrum, essentially appears white¹.

To determine the total energy emitted by a star, we first integrate the black-body equation over all wavelengths leading to the Stephan-Boltzmann law,

$$j_{\text{bb}} = \sigma_{\text{sb}}T^4, \quad (1.4)$$

which indicates the power radiated through a surface element of a black body. Here, σ_{sb} is the Stephan-Boltzmann constant and has a value of $5.67 \times 10^{-8} \text{ J s}^{-1} \text{ m}^{-2} \text{ K}^{-4}$. Equation 1.4 is then integrated over a spherical surface yielding a monochromatic luminosity,

¹The Earth's atmosphere scatters much of the Sun's blue light, causing it to appear yellow from the ground.

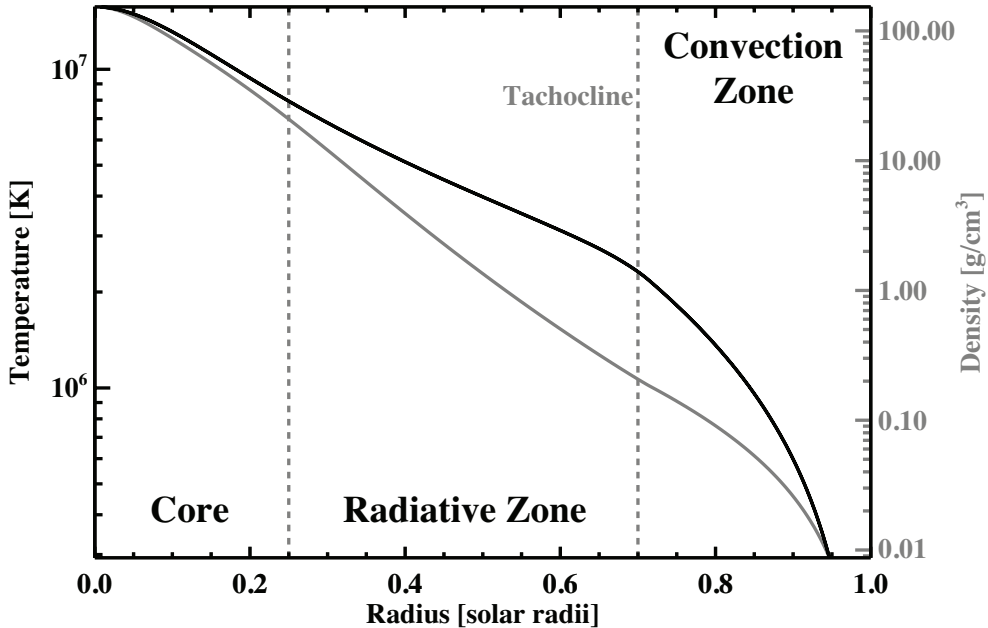


Figure 1.2: The BP2004 numerical model (15) of the solar interior. The approximate positions where nuclear fusion ceases and where the efficiency of convective energy transport overtakes radiative energy transport are indicated by the dashed lines.

independent of λ ,

$$L_{\text{bb}} = 4\pi R_{\odot}^2 \sigma_{\text{sb}} T^4, \quad (1.5)$$

which has units of erg s^{-1} and where R_{\odot} is the solar radius. In this case, T is “effective temperature”, essentially the temperature required to produce the observed luminosity, assuming a blackbody spectrum.

The following equations describe stellar energy release from fusion in the core and transport throughout the interior. Including Equation 1.1, the equations form a closed system: the stellar equations of structure,

$$\text{Equation of State: } P = \frac{\rho k_B T}{\mu m_H}, \quad (1.6)$$

$$\text{Mass Continuity: } \frac{dM_r}{dr} = 4\pi r^2 \rho, \quad (1.7)$$

$$\text{Energy Source: } \frac{dL_r}{dr} = 4\pi r^2 \rho \epsilon, \quad (1.8)$$

1. INTRODUCTION

Table 1.1: Physical properties of the Sun (5).

In the core:	
Density	160 g cm^{-3}
Temperature	$15 \times 10^6 \text{ K}$
In the photosphere:	
Total Mass	$1.989 \times 10^{33} \text{ g}$
Radius	696 Mm
Acceleration of Gravity	274 m s^{-2}
Escape Velocity	617.7 km s^{-1}
Effective Temperature	5770 K
Luminosity	$3.827 \times 10^{33} \text{ erg s}^{-1}$
Visual Magnitude	$+4.83$

$$\text{Radiative Transport: } \frac{dT}{dr} = -\frac{3}{4a_r c} \frac{\bar{\kappa} \rho}{T^3} \frac{L_r}{4\pi r^2}, \quad (1.9)$$

$$\text{Convective Transport: } \frac{dT}{dr} = -\left(1 - \frac{1}{\gamma}\right) \frac{\mu m_H}{k_B} \frac{GM_r}{r^2}, \quad (1.10)$$

where μ is the mean molecular weight, m_H is the mass of hydrogen, M_r is the integrated mass from the centre to a given radius, ϵ is the total energy emitted by nuclear reactions and gravitational heating (contraction) or cooling (expansion) per gram per second, a_r is the radiation constant ($a_r = 4\sigma_{SB}/c$), $\bar{\kappa}$ is the mean opacity (averaged over wavelength), L_r is the integrated luminosity to a given radius, and γ is the ratio of specific heat at constant pressure (C_P) to that at constant volume (C_V).

These equations have not been solved analytically, but using numerical methods they provide a first-order prediction of the temperature, pressure, and density profiles within the solar interior. This standard model neglects many higher order phenomena known to be present on the Sun such as rotation, magnetic fields, and density stratification due to the distribution of heavier elements. The model is limited in describing dynamic situations. Figure 1.2 shows a highly detailed numerical solution that takes into account many of these effects (15).

Stars undergoing fusion in their cores are governed by a mass-luminosity scaling law.

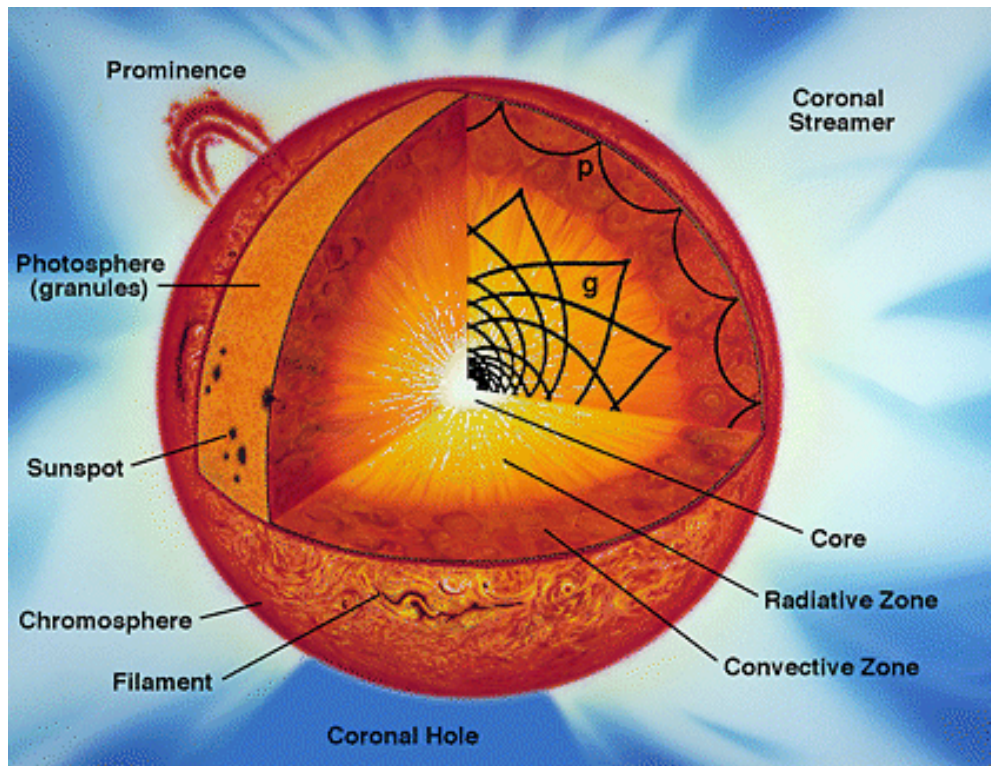


Figure 1.3: The layers of the Sun, from the core to the corona (courtesy of NASA). Various features and phenomena associated with the Sun are represented.

The Sun falls on this stellar “main-sequence” (as shown in Figure 1.4) while undergoing fusion, which lasts for the order of 10^{10} years. Stars in non-fusion phases of evolution fall to the upper-right (red giants) and lower-left (white-dwarfs) of the main sequence. Stars on the main sequence can be classified by their spectra, which are related to their surface temperatures. The Sun is a G2 (yellowish) star.

Stars may vary in their subsurface layers depending on mass and their stage of evolution. The standard model of stellar structure describes the interior of the Sun in three layers: the core, radiative zone, and convection zone (Figure 1.3). The Sun is powered by nuclear reactions in its core, extending from the centre out to $\sim 1/4 R_\odot$. The radiative zone is described by where fusion ends and energy is merely transported, mostly through radiation. The convection zone extends from $\sim 2/3$ to $\sim 1 R_\odot$ and is

1. INTRODUCTION

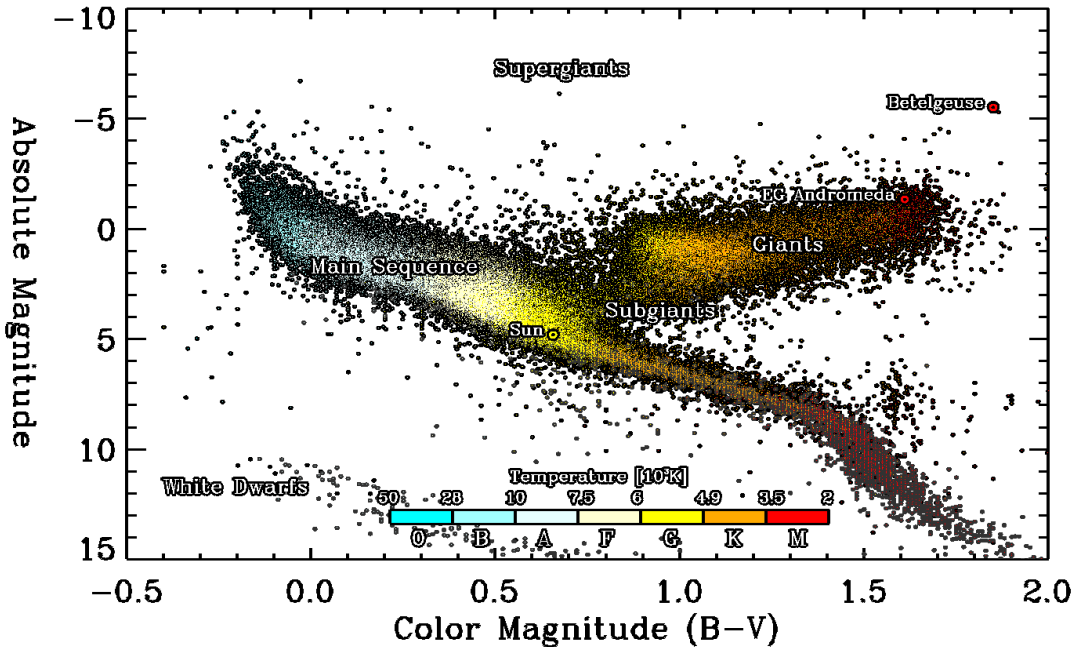


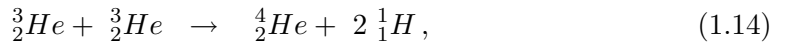
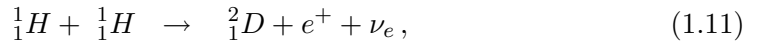
Figure 1.4: A Hertzsprung-Russel color-magnitude diagram. The color bar indicates the spectral class and temperature range. The HIPPARCOS (black dots) and “Gliese 1991” (dark gray dots) catalogues have been used, excluding binary systems. The main stars studied in the Astrophysics Research Group at Trinity College Dublin are highlighted.

dominated by convective heat transport.

1.2 The Core

The Sun has a dense core with a temperature of ~ 15 MK. The immense temperatures and pressures in the core provide enough free energy to ignite nuclear fusion in hydrogen. The Coulomb repulsion of hydrogen nuclei is barely overcome, but quantum tunneling through this potential barrier allows fusion to occur often enough to power a total solar luminosity of 3.8×10^{33} erg s $^{-1}$. As hydrogen burns in the core, helium builds up and may diffuse outward, forming a shell as fusion continues. A chain of particle interactions occurs that begins with hydrogen nuclei and ends with hydrogen nuclei. This is called the proton-proton (PP) chain. There are four possible paths to

achieving this process, with the most probable occurring $\sim 86\%$ of the time¹, the PP I branch, summarised here: (1) two hydrogen nuclei (H) fuse to form a deuterium (D) nucleus, a positron (e^+), and an electron neutrino (ν_e); (2) the positron immediately annihilates with a nearby electron, producing two gamma rays (γ); (3) the deuterium fuses with another hydrogen nucleus resulting in a helium (He) isotope with one neutron and another gamma ray is released; (4) finally, two helium isotopes fuse, resulting in a helium nucleus with two neutrons and two protons. This process is represented by the following equations,



The total energy released by these reactions is included as ϵ in Equation 1.8. The neutrinos generated by this process predominantly leave the core unhindered. The photons emitted scatter repeatedly, resulting in a random-walk that takes the energy hundreds of thousands of years to reach the solar surface.

1.3 The Radiative Zone

Outside of its core, energy transport within the Sun is dominated by radiation until the gradient in temperature becomes too steep and the opacity too great, at around $0.7 R_\odot$. Radiative energy transport for a given wavelength is given by the radiative

¹In the Sun, the PP II branch occurs $\sim 14\%$ of the time and dominates at temperatures between 14 MK and 23 MK. The PP III branch occurs $\sim 0.11\%$ of the time and dominates at temperatures above 23 MK. A PP IV branch is theoretically possible but is extremely rare.

1. INTRODUCTION

transfer equation,

$$-\frac{1}{\kappa_\lambda \rho} \frac{dI_\lambda}{ds} = I_\lambda - S_\lambda, \quad (1.15)$$

where, S_λ is the source function, I_λ is specific intensity, and κ_λ is opacity. For a given layer in the solar interior, this indicates how much radiation passes through the layer, and how much is emitted by the layer. In LTE, the source function is composed of blackbody radiation and is obtained from the Planck function. Equation 1.9 can then be obtained from 1.15, giving the radiative temperature gradient.

Specific intensity is the amount of radiation at a given wavelength passing through a unit surface area (dA) into a unit solid angle ($d\Omega$) over a unit time interval (dt),

$$I_\lambda = \frac{E_\lambda d\lambda}{d\lambda dt dA \cos \theta d\Omega}, \quad (1.16)$$

where E_λ is photon energy and θ is the angle of the propagation direction to the surface normal. The specific intensity averaged over θ is $\langle I_\lambda \rangle$. For blackbody radiation, which is isotropic, $B_\lambda = \langle I_\lambda \rangle$. The final intensity of monochromatic radiation passing through a depth of material (s) is,

$$I_\lambda = I_{\lambda,0} \exp \left(- \int_0^s \kappa_\lambda \rho ds \right), \quad (1.17)$$

where $I_{\lambda,0}$ is the initial intensity of the radiation.

The transport of energy by radiation is dependent on the density of material encountered as it propagates. The mean-free-path is the statistical distance a photon can travel without being scattered or absorbed,

$$l = \frac{1}{n\sigma_{\text{cs}}} = \frac{1}{\kappa_\lambda \rho}, \quad (1.18)$$

where n is the number density, σ_{cs} is the collisional cross-section, and κ_λ is opacity. Opacity is the absorption cross-section for a given amount of material. Integrating

1.3 The Radiative Zone

opacity over a thickness of material, s , we get the optical depth,

$$\tau_\lambda = - \int_0^s \kappa_\lambda \rho \, ds \quad (1.19)$$

An average continuum photon released into space by the Sun is emitted from an optical depth of 1. Equation 1.17 can then be rewritten,

$$I_\lambda = I_{\lambda,0} e^\tau \quad (1.20)$$

The total opacity is the sum of contributions from electron scattering and bound-bound, bound-free, and free-free electron transitions. Electron scattering is dominant in hot stellar atmospheres and cores. Scattering can occur when an electron is completely free (Thompson), loosely bound with the photon wavelength being much smaller than the atom (Compton) or with the wavelength being much larger than the atom (Rayleigh). Bound-bound transitions occur when a bound electron absorbs a photon, transitioning to a less bound state, and are responsible for the spectral absorption lines in stellar spectra. Bound-free absorption occurs when the energy of the absorbed photon is large enough to free the electron, ionizing the atom. Free-free absorption occurs when an unbound electron near an ion absorbs a photon, resulting in an increase in the electron's kinetic energy. In general stellar interiors electron scattering dominates the low density, high temperature regime. In the high density, low temperature regime free-free and bound-free absorption dominates the opacity. At temperatures less than 10^4 K H^- absorption dominates. For the solar interior, free-free and bound-free absorption dominates. Kramers' law states that when the opacity is dominated by bound-free and free-free absorption, $\kappa \propto \rho T^{-7/2}$. Thus κ is indicative of the amount of absorption and increases rapidly with decreasing temperature, reducing the rate of radiative transport and further steepening the temperature gradient.

1. INTRODUCTION

1.4 The Convection Zone

As the gradient in temperature increases at larger radii, material becomes convectively unstable. This occurs when the magnitude of the adiabatic temperature gradient is overtaken by the radiative temperature gradient,

$$\left| \left(\frac{dT}{dr} \right)_{\text{radiative}} \right| > \left| \left(\frac{dT}{dr} \right)_{\text{adiabatic}} \right| \quad (1.21)$$

Equation 1.21 is known as the Schwarzschild criterion. In the simplest model, the adiabatic temperature describes that of a convecting cell, while the radiative temperature is that exterior to the cell. It is assumed the cell cools adiabatically as it rises (if buoyant) and so $|(dT/dr)_{\text{adiabatic}}|$ is the derivative of the temperature of the cell with respect to height in the solar interior. The ambient temperature exterior to the cell is determined from radiative flux transport and $|(dT/dr)_{\text{radiative}}|$ is the static solar interior temperature gradient derived from this.

A cell of fluid in the convection zone must cool faster adiabatically than it does radiatively to remain buoyant and rise toward the surface. In this way it does not exchange much heat with its surroundings and maintains its original thermal energy. In the Sun, the adiabatic and radiative gradients are equal at $\sim 0.7 R_\odot$, forming a boundary called the tachocline.

Convective heat transport is dominant above the tachocline. Convection occurs on a range of scales. The largest takes the form of “giant cells” extending from deep in the convection zone to near the surface. “Banana cells” may exist, parallel to the axis of rotation. The cells would alternate in vorticity and upward and downward flow. Nearer to the surface are smaller scale convective cells resulting in granulation (on the scale of magameters) and supergranulation (on the scale of tens of megameters). Turbulent flows occur at the top of the convection zone, as described in Chapter 2.

The length scale at which convection occurs is determined by the local temperature

gradient. Mixing length theory can be used to determine the scale over which a parcel of fluid maintains its properties. The mixing length of a fluid parcel is analogous to the mean free path of a particle. The difference in temperature between a convective cell and its surroundings at a given time is given by,

$$\Delta T = \left(\left| \left(\frac{dT}{dr} \right)_{\text{radiative}} \right| - \left| \left(\frac{dT}{dr} \right)_{\text{adiabatic}} \right| \right) l \equiv \Delta \left(\frac{dT}{dr} \right) l, \quad (1.22)$$

where l is the mean free path. The mixing length at a given radius is often approximated as some multiple of the pressure scale height,

$$L_{\text{ML}} = \alpha_{\text{ML}} \frac{k_B T}{g m_H \mu}, \quad (1.23)$$

where α_{ML} is a proportionality constant and g is the local acceleration of gravity. Considering buoyancy and gravity, the average velocity of rising cells could be approximated, allowing a determination of the convective heat flux. The heat is deposited as cells mix with their surroundings over L_{ML} .

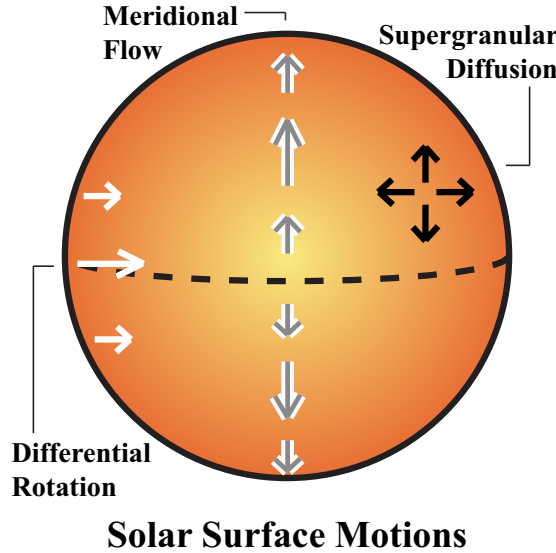
The radial rising motion of a cell is principally determined by the sum of gravitational (F_G) and buoyancy (F_B) forces,

$$F_G = -(V\rho_i)\mathbf{g}, \quad (1.24)$$

$$F_B = (V\rho_e)\mathbf{g}, \quad (1.25)$$

where V is the volume of the cell, ρ_i is the density inside, and ρ_e is the external density. The mass of the cell is given by $V\rho_i$, while the “displacement” mass is $V\rho_e$. When $\rho_i < \rho_e$ the cell is buoyant.

1. INTRODUCTION



Solar Surface Motions

Figure 1.5: A schematic diagram of the macroscopic motions on the solar surface affecting the evolution of diffuse magnetic features. The white and gray arrows qualitatively indicate the relative speeds of the meridional flow and solar rotation at different latitudes. The black arrows indicate the dispersive effect that supergranular motions have on diffuse magnetic flux.

1.5 Large-scale Flows

In the following section, several types of bulk plasma flows observed to occur near the solar surface are characterised. Together with rolling convection, a differential rotation along lines of latitude within the Sun's convection zone and a meridional flow acting along lines of longitude are both important for the evolution of magnetic flux on large scales. A schematic of the directionality of each flow is shown in Figure 1.5.

As discussed in Section 1.6.1, the surface of the quiet Sun is characterised by the turbulent motions of rolling convection by supergranular and granular flow patterns. These patterns are indicative of the convective flows throughout convection zone. While the flows of supergranules have a cellular structure (179), on large scales (~ 100 Mm), their motions average out. The flows cause weak magnetic flux elements to exhibit a random walk across the solar surface (211).

As mentioned in the previous section, supergranular flows are primarily parallel

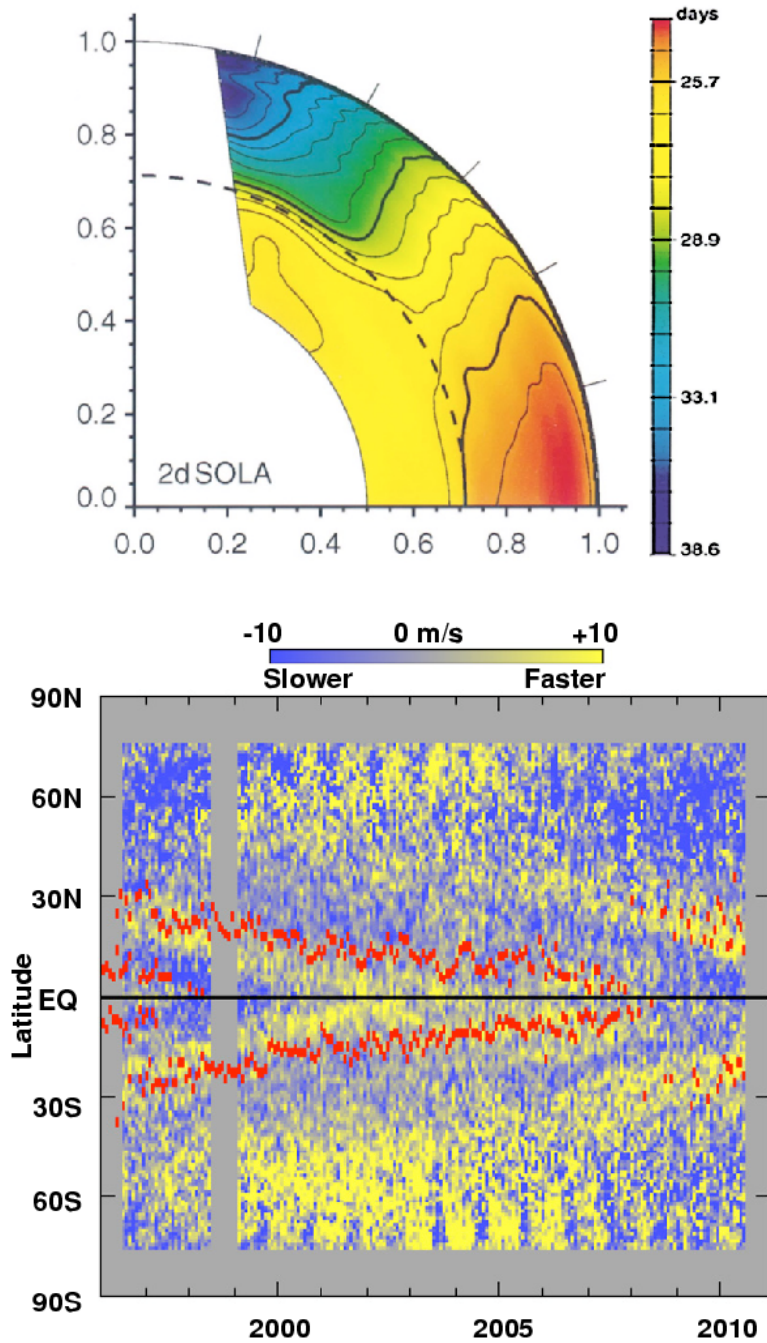


Figure 1.6: *Top:* The rotation period over latitude and radius determined using helioseismology (from 169). A higher period is observed near the equator. Below the convection zone boundary (the tachocline; dashed line), the Sun rotates as a rigid body. *Bottom:* The residual rotation after subtracting the time averaged profile from a latitude-time map of the solar rotation rate (from 91). The rotation profiles were derived using a cross-correlation technique on surface magnetic field observations.

1. INTRODUCTION

to the solar surface ($\sim 300 - 500 \text{ km s}^{-1}$), but the much smaller perpendicular component of the flows ($\sim 10 - 30 \text{ km s}^{-1}$) has been observed using Doppler measurements (53; 93). Internally, convective cells are thought to partially organize into large-scale latitudinally-oriented bands of up-welling (hot) and sinking (cool) plumes of material. This has been shown to occur in global convection simulations (29), but has not been conclusively observed, save for a high correlation of the supergranular pattern over time (133).

The sidereal solar rotation period varies over latitude, measured to be ~ 27 days at the equator and exceeding 30 days at high latitudes. This produces weak, slow shearing of large scale surface magnetic features, since flux near the poles rotates at a slower angular rate than flux near the equators. This differential rotation has been measured at the solar surface using sunspot tracking (140), correlation of large-scale magnetic fields (223), and spectroscopic measurements (100). Within the solar interior differential rotations is measured using helioseismology (169). The profile of rotation period with latitude and radius derived from helioseismology is shown in Figure 1.6. The Sun rotates rigidly below the tachocline at $0.7 R_\odot$, where the speed of rotation matches that of rotation in the convection zone between $\sim 30^\circ$ and $\sim 45^\circ$. This is coincident with the “active latitudes” at which sunspot groups emerge.

There is a higher-order moment of differential rotation called the torsional oscillation. This is manifested as two bands of latitude (one in each hemisphere) that progress from the poles toward the equator. The poleward edge of this band rotates slightly faster and the equator-ward edge rotates slightly slower than the time-averaged rotation speed of the Sun at a given latitude. The progression of this oscillation is correlated with the solar cycle.

The meridional flow occurs along lines of longitude and is much slower than differential rotation, having peak surface flow speeds of $10 - 20 \text{ m s}^{-1}$. It was first theorised as a mechanism to more rapidly transport magnetic flux to the poles in models of the

Table 1.2: Characteristic height, temperature, number density, magnetic field, and Plasma- β values ranging from the solar surface to the outer atmosphere (7; 71; 76). Plasma- β is the ratio of gas to magnetic pressure as defined in Chapter 2. Characteristic values for Earth’s atmosphere are provided for context.

Layer	Height	T [K]	n [cm $^{-3}$]	B [G]	Plasma- β
Photosphere	0–0.25 Mm	5×10^3	2×10^{17}	500	14
Chromosphere	0.25–2.5 Mm	10^4	10^9	300	0.001–1
Transition Region	2–3 Mm	10^4 – 10^6	10^9 – 10^{11}	300	0.001
Corona	2.5 – $1 R_\odot$	1 – 3×10^6	10^9	10	0.07–0.2
Outer Corona	$1 R_\odot$ –100 AU	10^6	1×10^7	0.1	7
Earth’s Atmosphere	Sea Level	10^2	2×10^{19}	0.5	$\gg 1$

magnetic solar cycle, than by diffusion alone (136; 186). Generally the meridional flow acts toward the poles, but equatorward flows have been observed at high latitudes, resulting in a bunching of magnetic elements due to the convergence of poleward and equatorward flows (206). High latitude equatorward flows are likely due to submerged cells of plasma (counter-cells) flowing opposite to the general direction of the meridional flow (78).

1.6 The Solar Atmosphere

The photosphere reaches from the $\tau = 1$ surface of the Sun, decreasing in temperature, until a minimum is reached. At this point the chromosphere begins and the temperature increases by several times. The temperature then begins to rapidly increase, as the chromosphere ends and the transition region begins, increasing by more than an order of magnitude. The transition region ends as the temperature levels off and the lower corona begins. A characteristic height, temperature, number density, magnetic field, and the dominance of magnetic pressure over gas pressure (plasma- β) for the quiet Sun is given in Table 1.2. In the photosphere, features such as sunspot groups are formed by the balance of gas and magnetic pressure, which is what results in their complex dynamics, while in the upper atmosphere the magnetic field dominates the dynamics,

1. INTRODUCTION

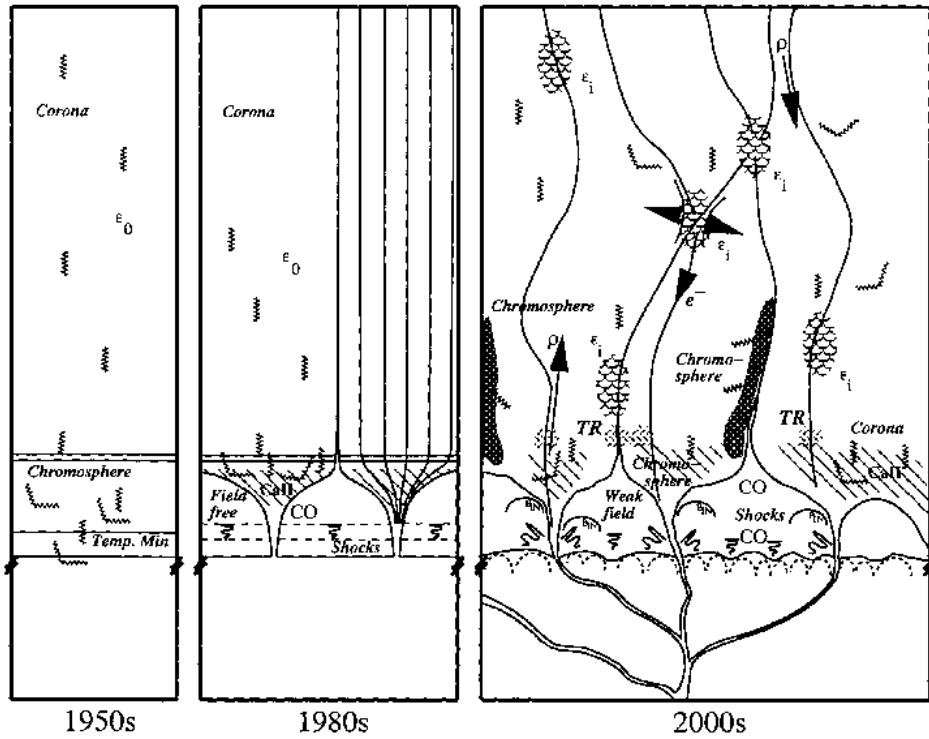


Figure 1.7: The progression of our understanding of the solar and stellar atmospheres (from 172). Early models prescribed a field-free atmosphere stratified in temperature (left). Magnetic fields were introduced at supergranular network boundaries, expanding with height to fill the magnetic canopy (middle). Later models exhibited a much less stratified structure and a range of heating mechanisms (right).

resulting in structures that follow the directionality of the magnetic field (like dropping iron filings around a bar magnet), such as coronal loops. The lower solar atmosphere (i.e., photosphere and chromosphere) has properties varying by orders of magnitude over the scale of a few Mm. The small scale height, due to the sharp drop-off in density is what gives the visible solar disk its sharp edge.

Features such as sunspot groups in the photosphere are connected to structures far from the solar surface. Figure 1.9 shows full-disk and zoomed images of the Sun on the day of the first X-class flare of solar cycle 24, on 14 February 2011. A large multipolar magnetic structure is visible in the zoomed magnetogram, while a sunspot group is observed in the continuum at visible wavelengths. A complex loop structure

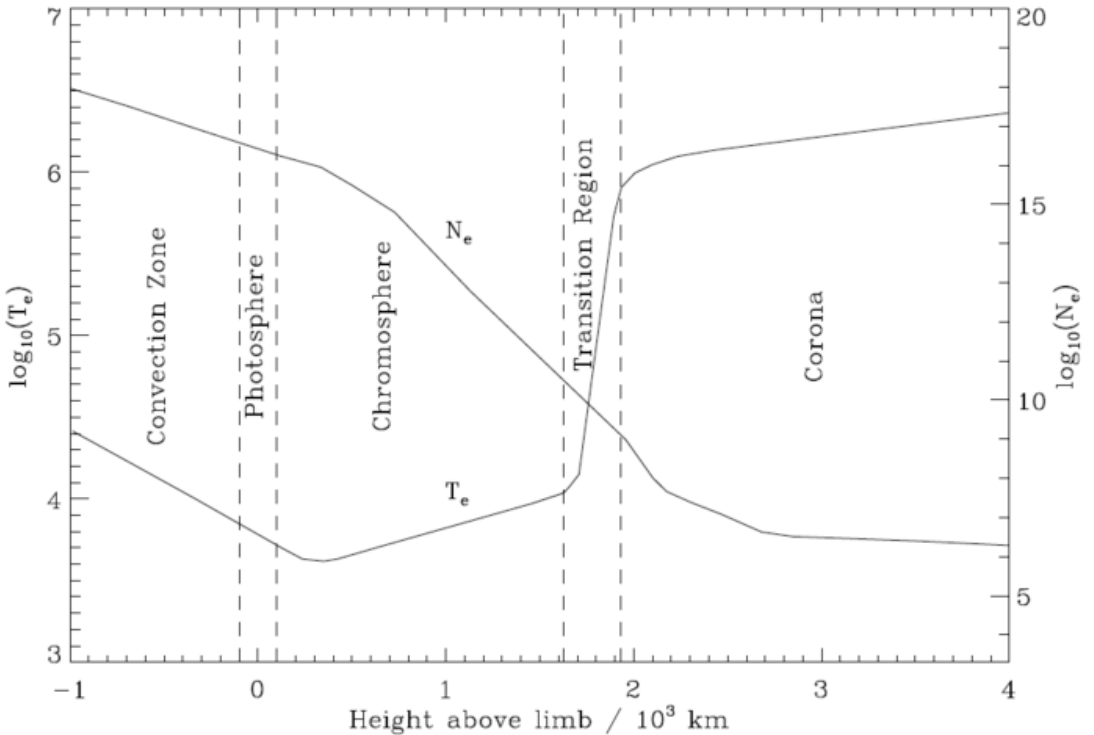


Figure 1.8: The temperature and density dependence of layers in the Solar atmosphere in the quiet Sun (from 68). The dashed lines define boundaries between the layers. The electron temperature (T_e) rises steeply in the transition region, while the electron number density (N_e) decreases more gradually through the chromosphere and transition region.

lying above the sunspot group and manifested by its magnetic footprint is imaged at extreme ultraviolet (EUV) wavelengths. The highest coronal loop structures are dragged outward by the solar wind pressure and are visible far from the Sun as coronal streamers in the coronagraph image.

Figure 1.7 illustrates the evolution of our understanding of the solar atmosphere over time. Decades ago, the atmosphere was considered to be featureless and static. Now our models must include complex magnetic field orientations and mass flows over a range of scales (172). The rough density and temperature dependencies for different layers in the atmosphere are shown in Figure 1.8.

1. INTRODUCTION

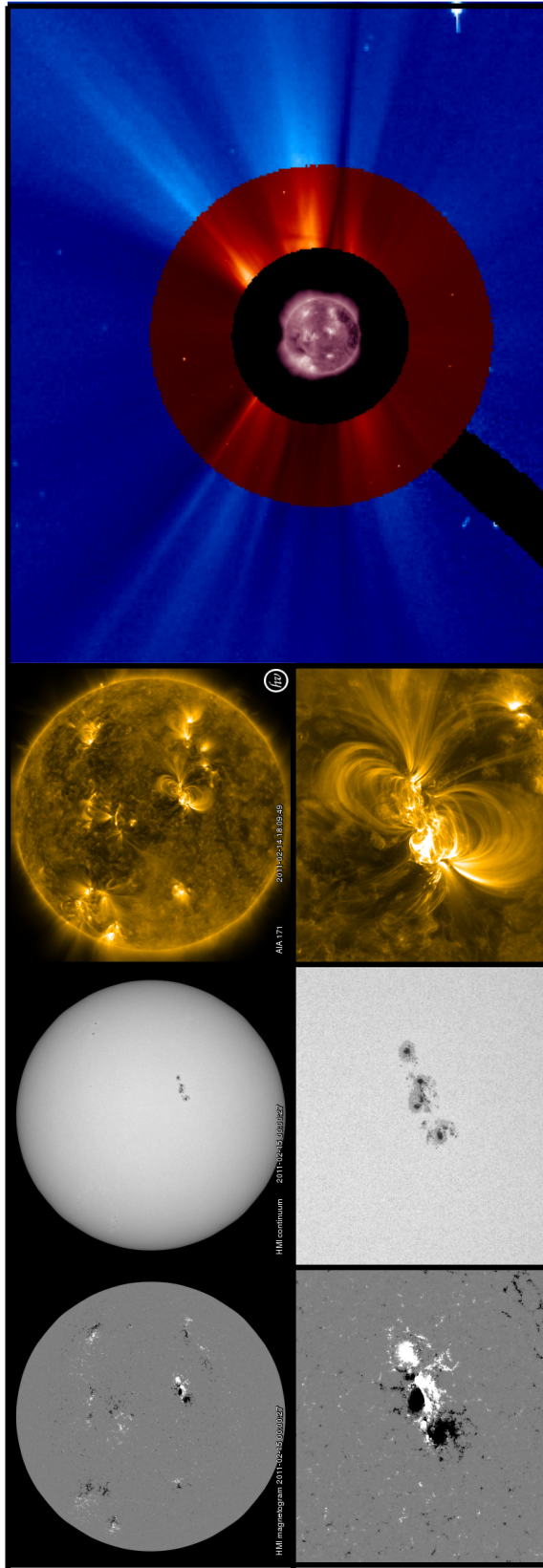


Figure 1.9: A multiscale, multilayered view of the Sun from SDO and SOHO/LASCO. *Left:* The surface magnetic field and a zoomed-in image of a multipolar magnetic feature. *Middle:* The photosphere in the visible continuum and an image of the magnetic feature reveals a sunspot group. *Right:* The corona in EUV and the loop structures lying in the atmosphere above the sunspot group. *Far-right:* Magnetic structures in the outer corona, observed by the LASCO coronagraph, that are mainly associated with magnetic features in the lower corona and thus to those observed in the photosphere.

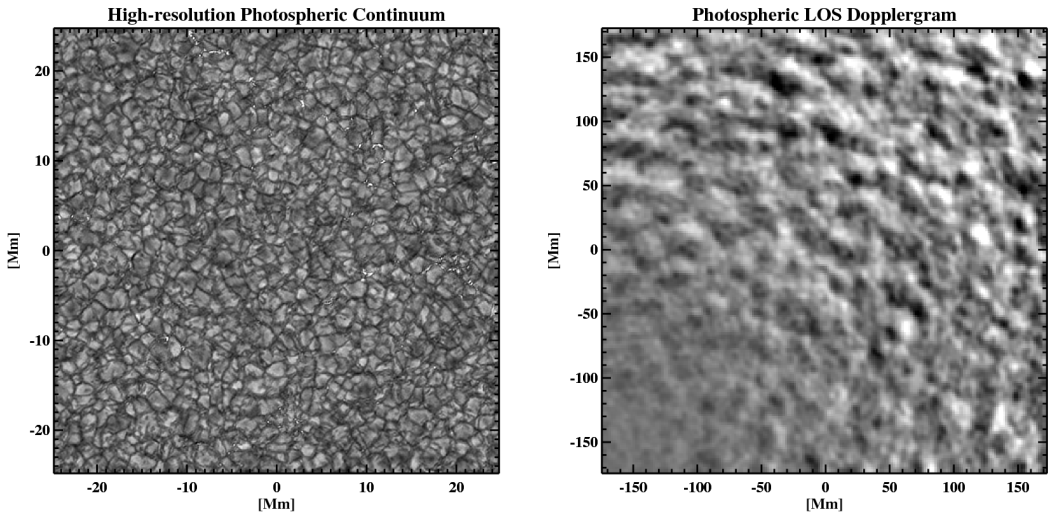


Figure 1.10: Rolling convection at the photosphere. *Left:* Granulation is visible in sub-arcsecond resolution white-light images from the Dutch Open Telescope. *Right:* Supergranulation is visible as the mottled pattern away from solar disk-centre (the lower-left corner of the image) in line-of-sight dopplergrams. This image is the average of 25 GONG dopplergrams with 1-minute cadence.

1.6.1 The Photosphere

Above the convection zone, the visible surface, or photosphere of the Sun, is defined as the physical layer where the optical depth, τ for $5\,000\text{ \AA}$ light is unity. This can be thought of as a surface of last scattering for solar optical photons. The temperature of the bottom of the photosphere is around $6\,500\text{ K}$, while the top of the photosphere 500 km above at the “temperature minimum” is around $4\,400\text{ K}$. The opacity in the photosphere is dominated by bound-free and free-free absorption, as well as (free) electron scattering. The solar surface appears sharp because the pressure scale height is small at this radius, so the density drops off quickly. Away from the centre of the solar disk the brightness appears to decrease. This phenomenon is called “limb-darkening” and occurs because radiation emitted near the limb that reaches an observer must leave the Sun at an angle. For this radiation $\tau = 1$ occurs at a slightly larger radius. Since temperature rapidly decreases with radius, the radiation is emitted by material at lower

1. INTRODUCTION

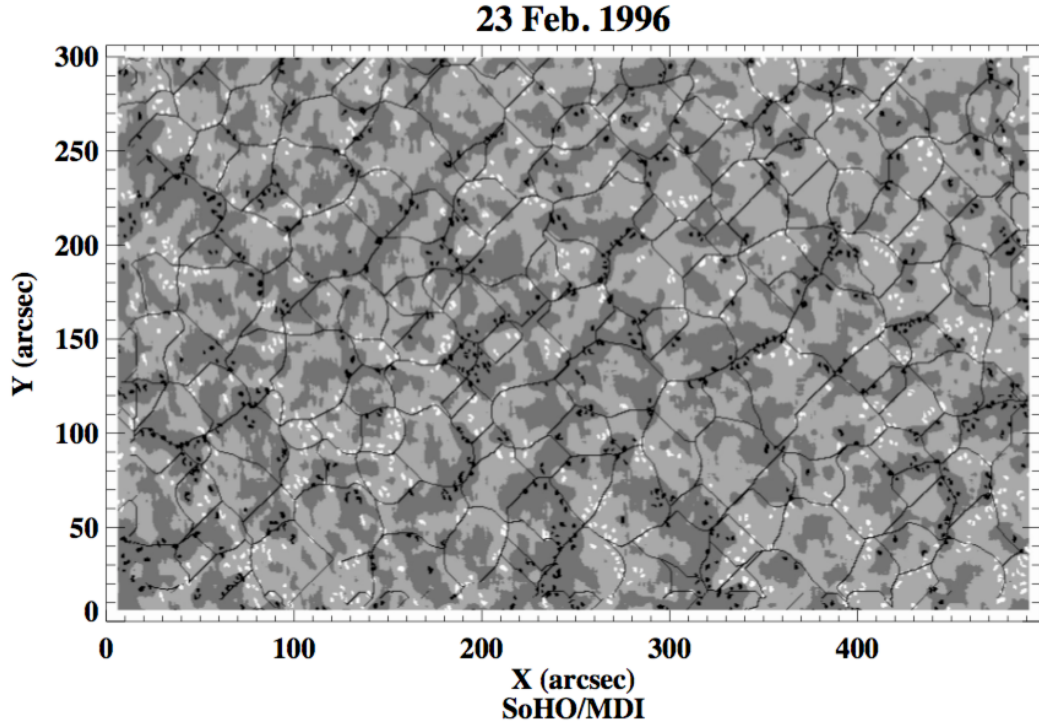


Figure 1.11: Magnetic elements at supergranule boundaries. Three hours of high resolution MDI magnetograms of the quiet Sun are averaged to produce this image. The supergranule boundaries are derived from local correlation tracking (LCT; from 180).

temperature than that near disk centre. The effect of limb darkening is seen in the top middle panel of Figure 1.9. Plane-parallel models of the stellar atmospheres set $\tau = 2/3$ because when the angular dependence of radiation resulting from a spherical surface is lost, but is approximated in models by allowing the radiation to be emitted from higher in the atmosphere. The effective temperature of the Sun at $\tau = 2/3$ is 5 770 K.

The surface of the quiet Sun is characterised by the turbulent motions of rolling convection. The effects of emerging cells on a range of scales are observed in the photosphere. The most well known patterns are the ~ 1 Mm diameter granulation pattern and the ~ 30 Mm diameter supergranulation pattern. The lifetime of a granule is tens of minutes while a supergranule lasts for tens of hours. Granule boundaries are observed in high-resolution continuum images, while supergranule motions are inferred

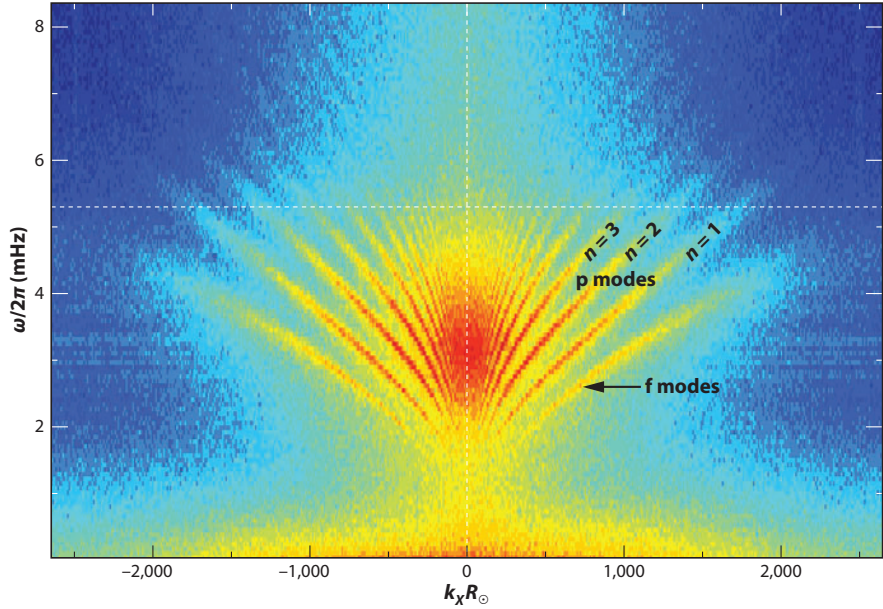


Figure 1.12: Oscillation modes within the Sun obtained from MDI dopplergrams. As a cut is taken through $k_y = 0$ only waves traveling equatorially are shown. The horizontal dashed line indicates the acoustic cutoff frequency, beyond which waves are damped. Waves below ~ 1.5 mHz are due to convection, supergranulation and granulation (from 74).

by the random walk of magnetic flux tubes frozen into near surface plasma and can be observed away from disk centre in line-of-sight (LOS) dopplergrams (Figure 1.10). The effects of supergranulation are observed as a mottled pattern in images of the chromosphere (e.g., ultraviolet). The motions of supergranules are difficult to track, much less to characterise, due to our inability to image them directly at disk-centre (see 159, and references therein). The motion of magnetic flux elements under the influence of supergranules can be tracked using magnetograms, as shown in Figure 1.11. The predominately horizontal supergranular motions cause translations of weak magnetic features. The sizes, velocities, and life-times inferred using this method is affected by the sampling rate and selection bias of magnetic features chosen for tracking. Granulation occurs over a range of scales but the probability distribution peaks at granulation and supergranulation scales (160).

On the scale of granulation, the smallest observable magnetic elements converge in

1. INTRODUCTION

inter-granular lanes. They appear as bright points in the highest resolution visible continuum images, as seen scattered throughout the image in the left panel of Figure 1.10. This is because they have a lower density than the surrounding plasma, due to a partial evacuation due to the addition of magnetic pressure. This decreased density results in a decreased opacity so the observed radiation is coming from deeper, hotter, layers of the Sun (194). The radiating material is heated by the surrounding convective plasma.

Larger magnetic features are swept into the convergent lanes between adjacent supergranules. They tend to collect in sinks, where multiple cells converge to a single point. In quiet Sun regions, these features are often small dipoles, called ephemeral regions that have life-times of hours (79). They are thought to form near the surface in the turbulent motions of the convecting plasma. The quiet-Sun distribution of magnetic elements is called the “magnetic carpet” (180), as seen in Figure 1.11.

The solar surface is also characterised by ubiquitous \sim 5-minute oscillations. There is also a \sim 3-minute periodicity, but this is mainly observed in the chromosphere (191). Observations of these trapped helioseismic waves give us a wealth of information about the structure of the solar interior. They begin at the surface and propagate inward, but are refracted back toward the surface as they transit layers of varying sound speed. They follow parabolic paths, being repeatedly reflected at the surface. Properties of the internal structure of the Sun are obtained from helioseismology, the study of surface oscillations. A wide distribution of spatial oscillation modes occur within the Sun and are studied with surface Doppler velocity data, as shown in Figure 1.12. The power of oscillations is shown as a 2D function of wave number ($k = 2\pi/\lambda$) in the longitudinal direction versus frequency ($\nu = \omega/2\pi$).

1.6.2 The Chromosphere

Just above the photosphere, the temperature of the atmosphere reaches a minimum. The layer cools due to radiative losses. Above this, the temperature increases again in

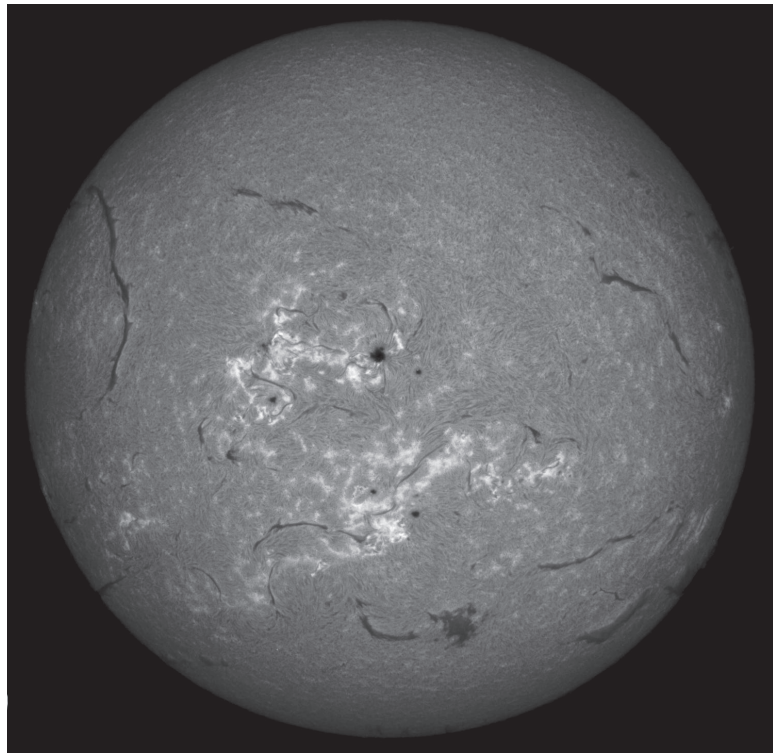


Figure 1.13: An image of the Sun at the H α (6563Å) emission line (courtesy of the Big Bear Solar Observatory). The mottled appearance of the surface is a chromospheric signature of supergranulation. The apparently dark filaments are composed of cooler material that is held above the solar surface in magnetic channels.

the layer called the chromosphere which extends from 500–2300 km above the $\tau = 1$ surface. The chromosphere is heated by acoustic waves (164). The \sim 3–5 minute oscillations resulting from granulation in the photosphere propagate into the chromosphere. Over a few acoustic wavelengths, the amplitude of the waves increase as they approach the acoustic cut-off and the waves shock. This converts the wave energy into thermal energy in the chromosphere (7).

In (67), a model is constructed in which the gas pressure scales with height assuming hydrostatic equilibrium. Also, magnetic flux tubes are confined to intergranular lanes and rapidly expand with height as the ambient gas pressure decreases (Figure 1.14). The isothermal contours in the modeled chromosphere rise and fall with the supergranular structure. This explains why the supergranular structure is observed above

1. INTRODUCTION

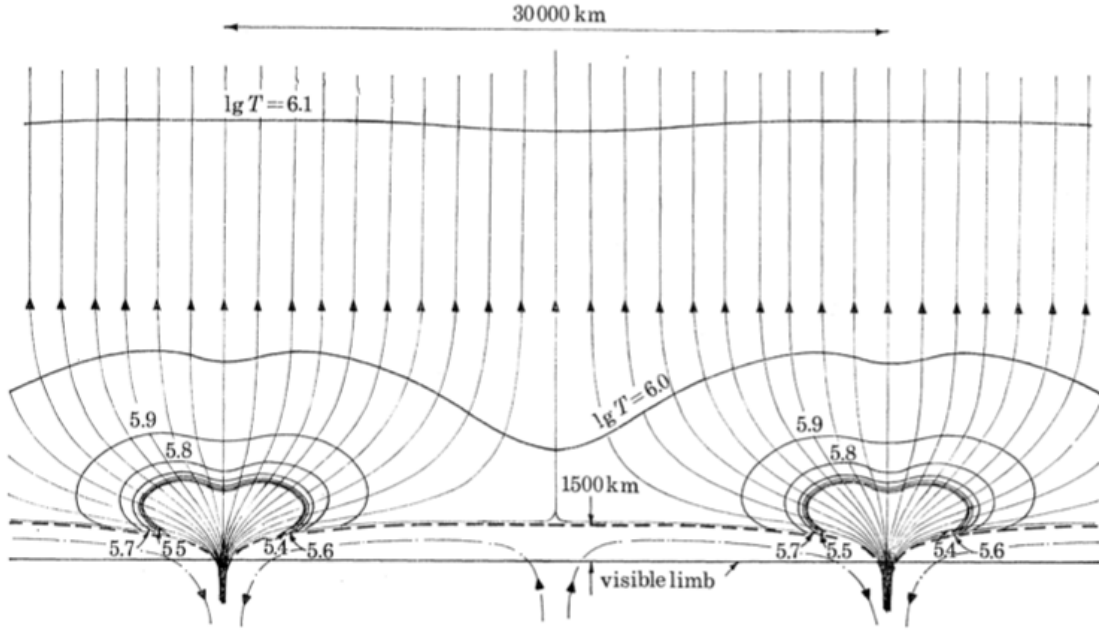


Figure 1.14: A static model of the quiet Sun (from Gabriel (67)). This model is alluded to in Figure 1.7 and introduces a simple magnetic field configuration, where vertical flux tubes are confined to supergranule boundaries. The fields expand with height and decreasing gas pressure.

the photosphere in chromospheric images, such as image of the Sun in H α , shown in Figure 1.13. The legs of the flux-tubes appear as filamentary structures called spicules. These tubes turn over and connect to each other, forming the “magnetic canopy”. The model was tested and supported in (69).

1.6.3 The Corona

Above the chromosphere lies the transition region where the temperature increases abruptly by more than an order of magnitude to ~ 1 MK over ~ 300 km. Above this region is the corona, extending outward from the top of the transition region at ~ 2600 km above the $\tau = 1$ surface. Here the atmosphere is optically thin, and it is far from static. Among other missions, the Solar Dynamics Observatory (SDO; 151) has shown us that the solar corona is highly dynamic at the small scale, where bright-points (150; 209)

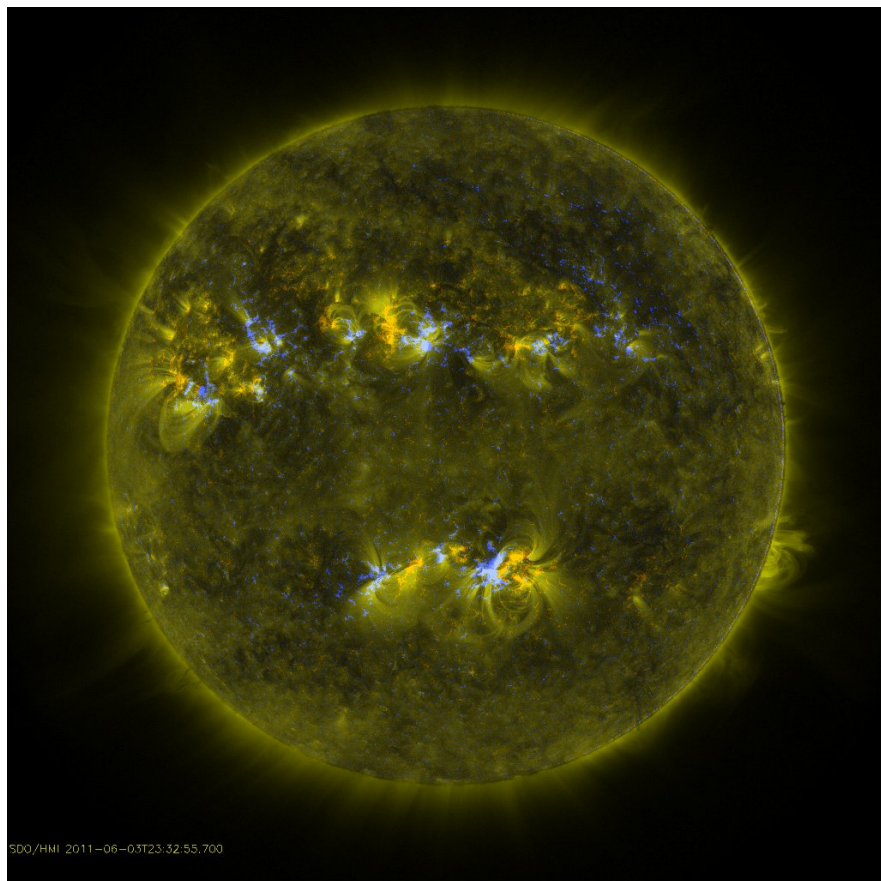


Figure 1.15: An image at the 171 Å emission line from AIA (yellow) with the LOS magnetic field polarity indicated (red points toward the observer and blue points away) from HMI onboard SDO (courtesy of LMSAL). The foot points of 3D magnetic field structures seen in the EUV are rooted in regions of strong localised surface magnetic field.

and coronal jets (104) are observed, to the global scale, where waves are observed to propagate across the Sun in the corona (121). Figure 1.15 shows a composite image comparing structures in the corona with their magnetic foot points in the photosphere. Bipolar magnetic field configurations (two regions of oppositely oriented magnetic field in close proximity) result in loops extending into the atmosphere. In the lower corona, the magnetic pressure dominates, but higher up the gas pressure dominates as the magnetic field dies off, as shown in Figure 1.16 (71). The “coronal approximation” is often invoked: it is assumed to be fully ionised; it is assumed that the rate of collisional

1. INTRODUCTION

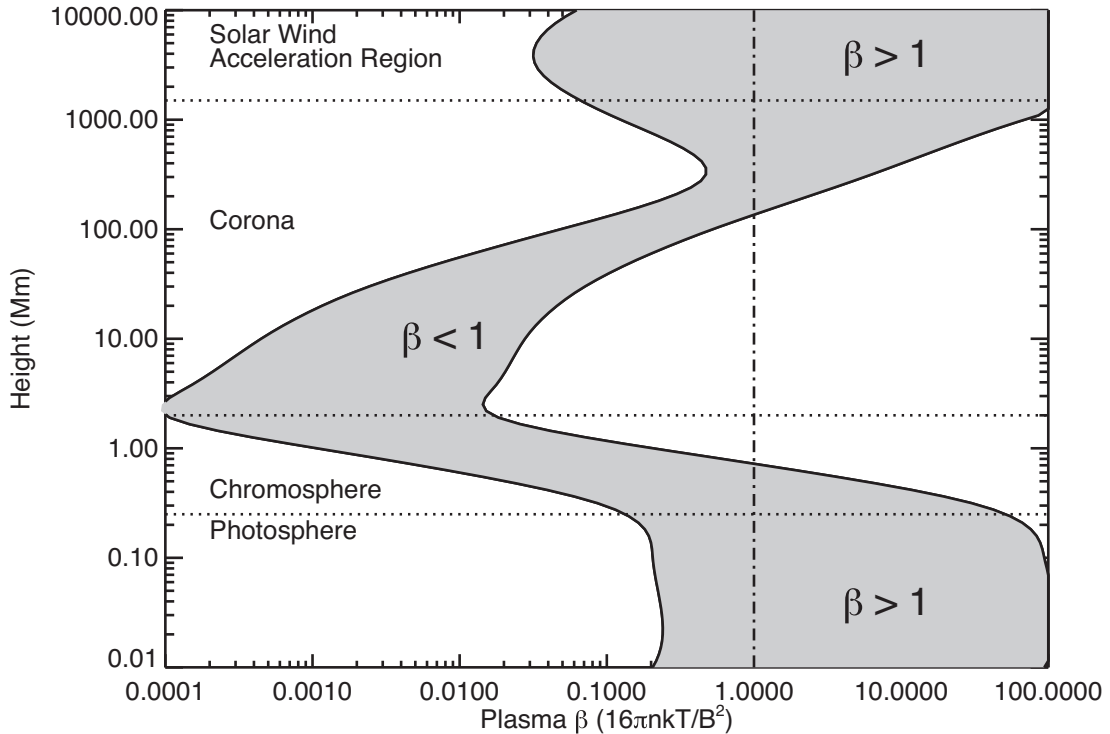


Figure 1.16: The height dependence of the plasma β parameter in the solar atmosphere (from 71). In the lower corona, the magnetic field strongly dominates over gas pressure. In the photosphere, chromosphere, and solar wind, the dominance varies, based on the magnetic field structures present.

excitation is balanced by the rate of radiative decay. The latter assumption, for a given ion population and electron transition between the ground (g) and an excited state (j), is governed by,

$$n_g n_e C_{gj} = n_j A_{gj}, \quad (1.26)$$

where n_g , n_e , and n_j are the number densities of ions in the ground state, of electrons, and of ions in the excited state, respectively. C_{gj} is the collisional excitation rate for the given transition and A_{gj} is the sum of transition probabilities from the excited state to the ground state.

Observations of the corona rely on spectral emission lines of mostly heavy elements. Although the metallicity of the Sun is higher than many stars (Population II and

III), the fraction of heavy elements in the Sun is tiny compared to the amount of hydrogen. However, a much larger fraction of certain heavy elements is observed in the chromosphere, compared to the photosphere (~ 3 -fold for Na, Mg, Al, Si, Ca, Ni; ~ 10 -fold for Fe). This due to a combination of the abundance of the elements and that their first ionisation potential (FIP) is significantly lower than elements with very high abundance (e.g., hydrogen and helium). Once elements with low FIP are ionised they are readily accelerated by electric fields and transported into the chromosphere. As a result, there are strong chromospheric spectral lines associated with these elements of low-FIP that would not otherwise be visible.

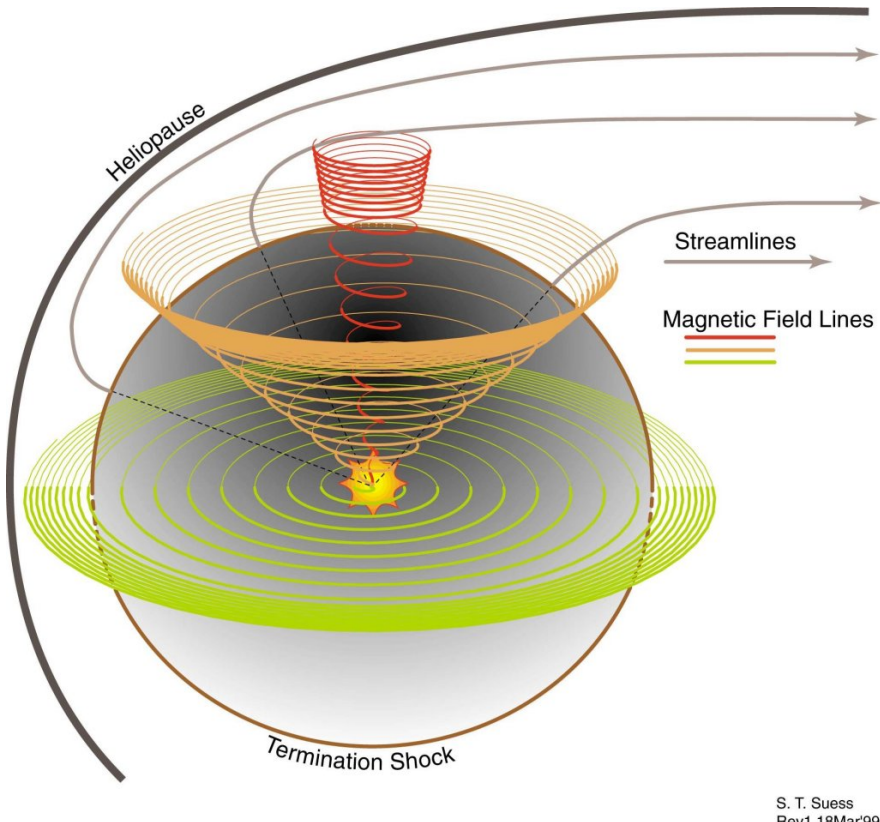
1.6.4 The Solar Wind

In addition to the observed reconfiguration of magnetic structures in the atmosphere, it has been known since the 1960s that a pervasive wind flows from the Sun with speeds of $300 - 800 \text{ km s}^{-1}$. The slower speed wind emanates from lower latitudes, while the faster speeds are associated with outflow from coronal holes. These appear as dark regions in EUV images and have lower densities than the surrounding corona due to their fast outflow along predominantly open magnetic field lines. The out-flowing material has been shown to originate in the chromospheric boundaries between supergranular cells (88), or the “network” (69). The regions associated with different wind components can be determined by comparing atomic abundances.

Chapman & Zirin (34) explored a static model of the solar corona, including both hydrostatic equilibrium and and a heat conduction term that resulted in a slower decrease in pressure with radius. This lead to the conclusion that the corona should not end near the Sun. In fact, at infinity the model predicted an asymptotic value of pressure that was much larger than that expected of the interstellar medium. This is an unphysical solution and showed that the atmosphere cannot be static.

The solar wind was predicted in (148). The wind could not be thermal in origin,

1. INTRODUCTION



S. T. Suess
Rev1,18Mar'99

Figure 1.17: A schematic of the Parker solar wind spiral in 3D (courtesy of Steve Suess, NASA/MSFC). Red, orange, and yellow lines denote magnetic field lines rooted at high, medium, and low latitudes on the Sun. The quiet solar wind flows radially, but exhibits a structure following that of the magnetic field lines.

since the escape velocity of hydrogen between $1 - 2 R_{\odot}$ is greater than its thermal speed assuming a temperature of $1 - 2$ MK. So, the assumption of hydrostatic equilibrium was disregarded and the additional energy needed to drive the wind was obtained from the vertical pressure gradient. Since the outflow speed at the Sun begins at rest and the speed measured at Earth is supersonic, the wind solution must be transonic. The Parker solution is derived assuming the wind is isothermal, constant, and spherically isotropic.

At a few tens of solar radii, the wind stops accelerating and essentially propagates freely. Streams from different regions on the surface accelerate the wind to different

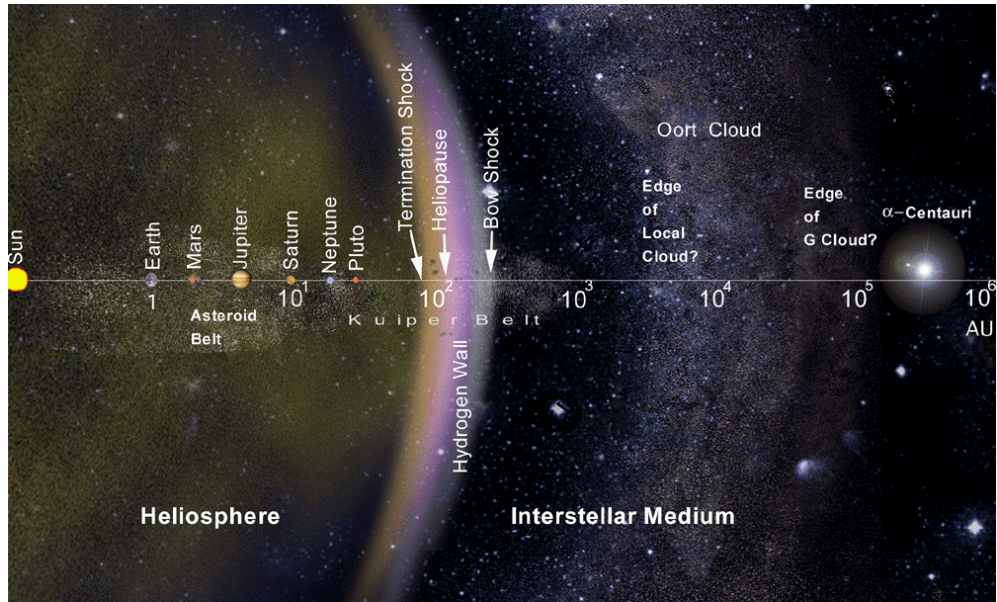


Figure 1.18: A 1D map of the heliosphere (courtesy of NASA). The Sun’s influence extends to the edge of the heliosphere and most magnetic fields permeating the region connect back to the solar surface. At the bow shock, the solar wind comes into contact with the interstellar medium, including the winds from other stars.

speeds. As the Sun rotates, the streams form a spiral pattern, the “Parker Spiral” shown in Figure 1.17. The shape of the spiral is Archimedean and a given stream with constant velocity is given by,

$$r - r_0 = -\frac{v}{\omega_{\odot}}(\theta - \theta_0), \quad (1.27)$$

where r_0 can be taken at the solar surface (R_{\odot}), v is the radial wind speed, θ is a longitude angle, and ω_{\odot} is the angular rotation speed of the Sun. The shape of a high-speed wind stream from a coronal hole can also be described by this, but is associated with a shock at its leading edge, called a co-rotating interaction region, and a trailing rarefaction region.

The isothermal Parker wind model can explain the slow solar wind, but it does not explain how the fast solar wind is accelerated in coronal holes. Currently the most likely driver is the Alfvén wave that oscillates along magnetic field lines and can deposit

1. INTRODUCTION

momentum into the out-flowing material. Models relying on Alfvén waves achieve wind speeds sufficient to account for the observations (142).

The solar wind dominates the dynamics of the outer corona. Here the magnetic field is too weak and the wind drags out the magnetic loop structures in to helmet shaped streamers as shown in the far right panel of Figure 1.9. The corona and solar wind end at the edge of the heliosphere, the heliopause. Here, the outermost corona impacts the interstellar medium and forms the termination shock (Figure 1.18). Our protective plasma bubble extends out for 100 AU, as noted in Table 1.2.

1.7 Sunspot Groups

Sunspot groups are the photospheric interface of buoyant magnetic flux ropes that are thought to rise through the solar convection zone and into the atmosphere. Most of the community agrees that the large scale magnetic structure of sunspots is formed at the base of the convection zone (193). However, there is an alternative theory that small-scale turbulent magnetic fields in the near-surface shear layer can coalesce to form a large-scale magnetic structure that may emerge to form sunspot groups (24). Henceforth, sunspots will be discussed in the context of the former model.

Sunspots are visible for days to weeks and have a characteristic pattern of emergence, evolution, and decay. They are also associated with solar eruptions. The detailed three dimensional structure of sunspots is very complicated, owing to the balance of gas and magnetic pressures. The interplay between hydrodynamic and magnetic forces allows for interesting dynamics.

1.7.1 Sunspot Emergence

Sunspot groups are thought to be an element of a large-scale toroidal magnetic field within the solar convection zone. This field is organised into a structure called a flux

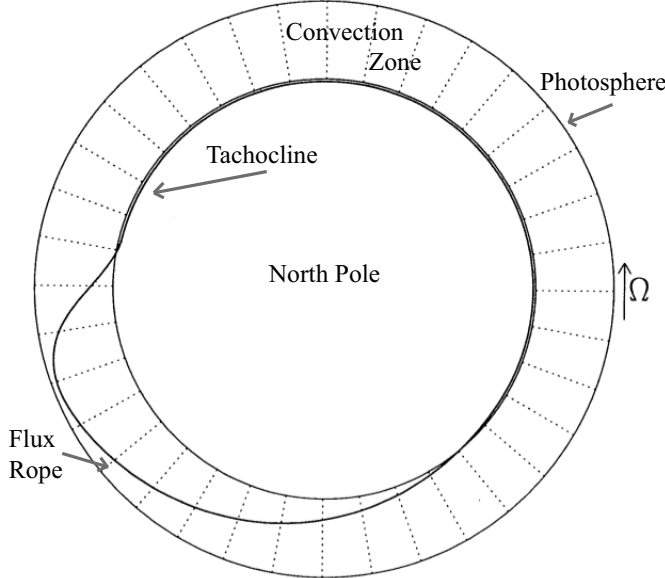


Figure 1.19: A model of a toroidal flux rope rising in the convection zone. The view is looking down on the north pole of the Sun. The rope is rising asymmetrically, with the leading portion of the rope being less perpendicular to the surface than the following portion (from: 30).

rope, which is a twisted collection of flux-tubes. Observations of the switching dipole and long-term sunspot observations led to the formulation of the $\alpha\text{-}\Omega$ dynamo (147). The magnetic dynamo is described further in Chapter 2. The Ω -effect describes a rising toroidal (longitudinally oriented) flux rope, affected by magnetic buoyancy. The flux rope rises since the density in the flux rope is lower than the ambient density. The flux rope has both gas and magnetic pressure internally, while externally gas pressure dominates (145).

Considering the flux rope as a monolithic structure, the internal pressure is the sum of the gas pressure ($P_{G,f}$) and the magnetic pressure ($P_{B,f}$); this is balanced by the external gas pressure ($P_{G,e}$), while the magnetic field outside of a flux rope is assumed to be negligible. The pressure balance is given by,

$$P_{B,f} + P_{G,f} = P_{G,e}, \quad (1.28)$$

1. INTRODUCTION

$$\frac{\mathbf{B}^2}{2\mu_0} + \rho_f \frac{k_B T_f}{\mu} = \rho_e \frac{k_B T_e}{\mu}, \quad (1.29)$$

where ρ_f and T_f are the density and temperature inside the flux ropes and ρ_e and T_e are the external density and temperature, respectively; k_B is Boltzmann's constant μ_0 is the magnetic permeability and μ is the mean molecular weight. From the above, we know $P_{f,G} < P_{e,G}$, so $\rho_f T_f < \rho_e T_e$. If the external temperature is equal to the internal, then the internal density will certainly be lower than the external. The internal temperature of the flux rope is generally higher than the external because the flux rope originates from a deeper hotter place than it ends up (i.e., at larger solar radii where the temperature is lower). Also the strong magnetic field inhibits cross-field conduction, allowing the flux rope to maintain its higher temperature.

The magnetic tension force will resist the rising motion of flux ropes which bend as they drift toward the surface. However, it has been shown that as long as the buoyant portion is at least twice the length of the local pressure scale height, tension will be overcome (145). A simulated rising flux rope is shown in Figure 1.19. Also, during the rise, mass flows along the rope, increasing the buoyancy; once the rise has begun it is unlikely to stop. Although, convective motions could break the rising structure apart. Simulations have shown that a minimum twist in the rope is necessary to maintain its stability (59, and references therein).

The α -effect describes a supposed twisted geometry of the rising flux rope. There are two mechanisms which could produce this effect. At the base of the convection zone, twist in a longitudinally oriented flux tube may result in a kink instability, which could produce an α -shaped loop. Also, the Coriolis force may cause a rising flux tube to rotate. The direction of rotation will be opposite in the northern and southern hemispheres. At the surface, an inclination between the equator and the line connecting the positive and negative polarities as well as rotation of sunspot groups is observed (this is known as "Joy's Law"; discussed further in Section 1.8.1).

In addition to the buoyancy force, the rising flux rope also undergoes expansion as the external pressure decreases. Updrafts and downdrafts due to convection currents will also affect the rising rate of the flux rope. The Coriolis force causes the flux tube to be deflected equator-ward (37).

As a flux tube crosses the photosphere the relative magnitude of magnetic to gas pressure of fields reaching into the atmosphere above results in a low value of β , causing the magnetic fields to fan apart. At the photospheric interface, the structure appears as a magnetic dipole with part of the flux tube coming out of the surface and the other part entering again. The magnetic structure in and above the photosphere up to a few ~ 100 Mm into the atmosphere is called an active region. Active regions are observed to have varying complexity. Complexity classification is discussed in Section 1.7.2.

1.7.2 Sunspot Structure

A sunspot group is thought to be the photospheric interface of the emergence of the flux rope described in the previous section, exhibiting \sim kG magnetic fields. Sunspots are a magnetic phenomenon observed in the photospheric continuum, generally occurring in groups, called active regions when including their coronal structure¹. They usually emerge as compact magnetically bipolar features, but range in size by orders of magnitude (149). Their global pattern of emergence follows a roughly 11-year cycle. It is not well understood how the average properties of active regions change over a solar cycle (87). Also, patterns in the flux imbalance of active regions have been observed, but not understood (230).

Sunspots appear within active regions when the local magnetic field is sufficiently large to suppress convective flows. When observed in white-light continuum images, sunspots are composed of a dark umbral core of \sim 4 000 K surrounded by a less dark penumbra of about \sim 5 000 K. Fields are primarily vertical in umbral cores and turn

¹Active regions can be spotless, but any spotted region would be denoted an active region.

1. INTRODUCTION

over at the boundaries, becoming horizontal in penumbrae.

Sunspots are dark because they are cooler than the surrounding photosphere. Sunspot cooling is not completely understood, but one explanation is that the strong subsurface magnetic fields inhibit convective cells from replenishing the region with hot plasma from deeper in the convection zone. This allows the sunspot to cool radiatively. The Evershed flow (56) advects heat away from sunspots through the penumbra (167). Up-welling plasma is constrained to flow radially outward, along magnetic fields in the penumbra (192). While the Evershed outflow is observed in and around penumbrae, a down-flow is observed within umbrae, below the surface (52).

Outside of penumbral boundaries further “moat” outflow is observed and creates a small ring where very little LOS magnetic field is observed (25). This flow advects heat from convective cells away from sunspots (66). Convective up-flows encounter penumbral fields and are forced outward. As the outflow cools and becomes a down flow, material is pulled inward toward the sunspot to maintain pressure balance (98). These flows are shown in Figure 1.20. The moving magnetic features associated with the moat flow maybe due to undulating penumbral fields, rising above and falling below the photosphere (217).

Umbrae are observed to be depressed compared to the surrounding photosphere; this is known as the Wilson depression. The depression is due to the optical depth reaching unity in the umbra further along the observer’s LOS than in the surrounding regions. The cooler surface temperature of sunspot umbrae decreases the rate of H⁻ absorption, thus decreasing the local opacity. H atoms are polar and may become anions when a free electron becomes weakly bound to them. They may then absorb a photon, freeing the extra electron. This phenomenon is strongly dependent on temperature. The cooler temperatures in sunspots decrease the ionization fraction and the number of H⁻ anions, which are more common with more free electrons. In addition to this, sunspots have a magnetic field pressure in addition to gas pressure. Since they are essentially static

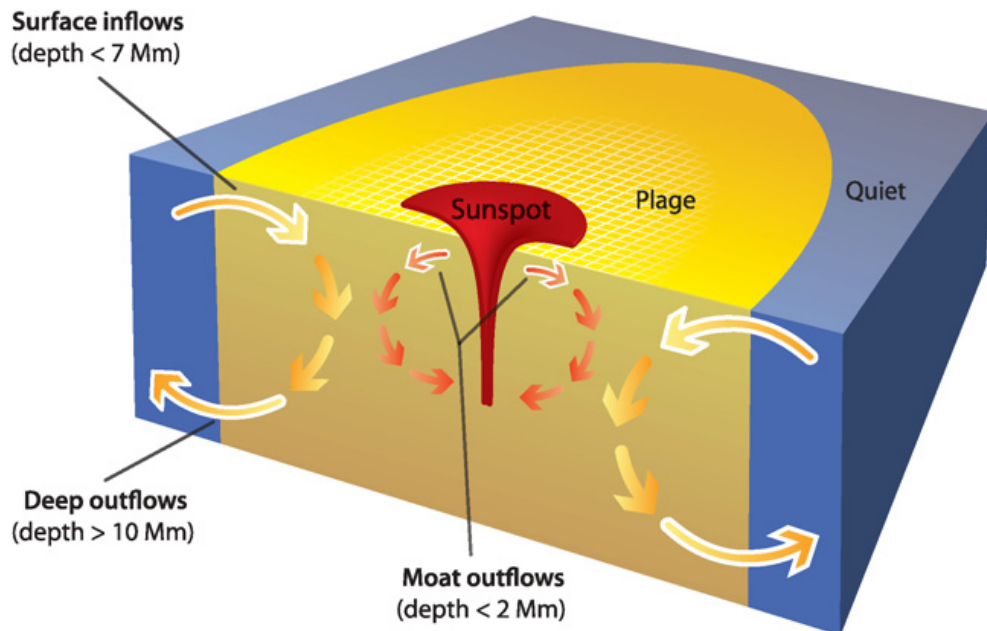


Figure 1.20: A diagram of a sunspot above and below the photosphere (from 98). Convection is disturbed by sunspot magnetic fields. This generates toroidal flows that are observed in the photosphere both toward and away from the sunspot.

structures, hydrostatic equilibrium is maintained with their surroundings and sunspots must have a lower mass density, which also decreases their opacity. Gravity allows the compression of gas along the umbral column due to the lower density.

In addition to sunspots, there are also diffuse magnetic structures observed in images of active regions called “plage faculaire”¹, often called simply faculae (usually when referring to white-light images) or plage (usually when referring to chromospheric images). These features generally occur in the trailing portions of active regions. The reason for trailing structures being more diffuse than leading ones is not well understood. Fan *et al.* (60) presents simulations illustrating that the magnetic field in the leading portion of an active region is around half of that in the following portion due to the action of Coriolis effects during emergence. Plasma is evacuated out of the leading portion, causing a compression and enhancement of the magnetic field. The following

¹From the french, literally meaning “beach of little torches”.

1. INTRODUCTION

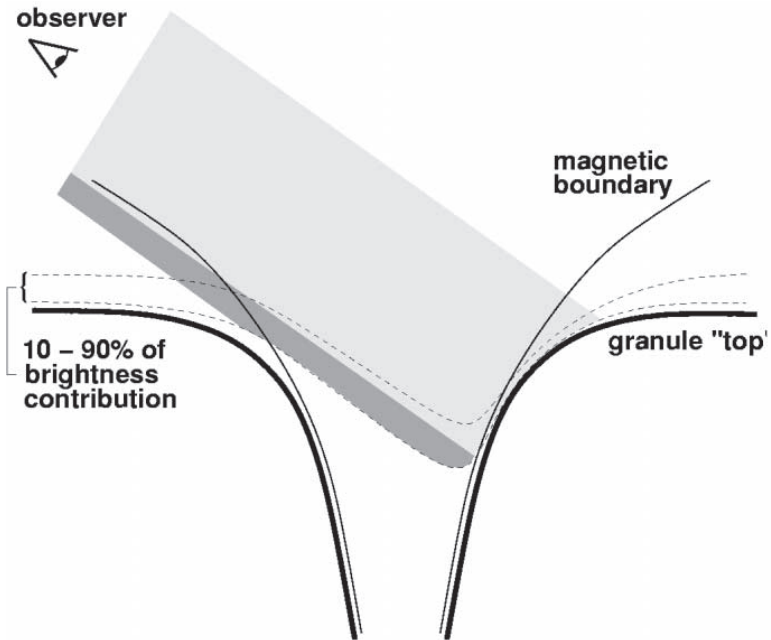


Figure 1.21: The structure of a facular bright point away from disk centre (from 106). The observer's sight lines are represented by the shaded rectangles, with color representing the observed brightness of the photosphere.

portion is more susceptible to turbulent decay due to its weaker magnetic field. In white-light images, faculae appear brighter than the quiet Sun and are most visible near the solar limb. This is explained by the “hot wall” model (194). The sides of magnetic flux-tubes forming faculae, which are oriented roughly radially and are more visible near the limb, are hotter than the centres (106). This phenomenon is illustrated in Figure 1.21

The structure of active regions (ARs) and sunspots in the corona has been studied using EUV observations (10). Three-dimensional loop structures are observed in the corona above ARs as shown in Figure 1.22. The magnetic foot points of these loops are observed in magnetograms connecting to the subsurface structure, known through local helioseismology methods. The structure of ARs near the surface (above and below) is well understood, but the deep structure of ARs and mechanisms of AR emergence remain poorly explained. A combined subsurface-atmospheric model of an emerging

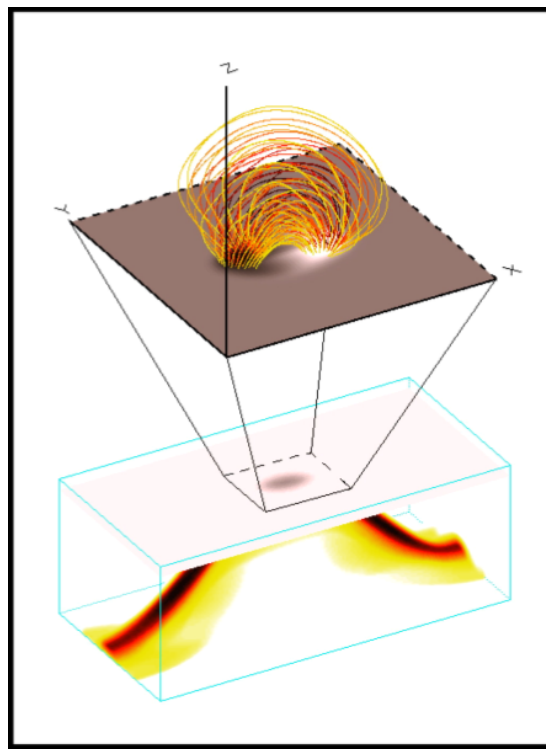


Figure 1.22: A three dimensional model of an emerging sunspot (from 1). The sunspot is the top of a buoyant flux rope and loop structures are visible in the atmosphere above.

sunspot group is shown in Figure 1.22.

1.7.3 Sunspot Group Evolution

Once they have emerged, sunspot groups evolve by several mechanisms. Further flux may emerge within their boundaries, increasing their magnetic strengths. Turbulent flows due to granulation and supergranulation act to disperse their fields. Finally, adjacent magnetic field structures interact—structures of the same orientation merge and those of opposite orientation cancel.

Complex active region configurations can result from shear and helicity injection which can be partially attributed to flows in the photosphere. Shear often occurs when two opposite polarity flux elements move past each other in opposite directions along their polarity separation line. On a small scale this may result from a vortex

1. INTRODUCTION

at the junction of several supergranules or a sunspot undergoing rotation (11). On larger scales this may occur during flux emergence as the cross-section of a helical flux rope passes through the photosphere. Disorganised flows due to turbulence can also contribute to the complexity of an active region (96). The development of a strong polarity separation line may result from both shear and helicity injection, and is an important indicator for flaring (see Section 1.8.3). The configurations described above contribute to the amount of non-potential magnetic energy within an active region. Non-potential fields are described in Chapter 2.

Having emerged, active regions evolve due to the turbulent motions and large-scale flows of solar plasma. The differential axial-rotation of the Sun stretches features longitudinally, increasing their hemispheric coverage. Supergranular motions disperse magnetic flux, while the meridional flow carries weak flux elements poleward (136). Since we can only observe magnetic field evolution near the solar surface, we are most concerned with surface flows. Sunspot group decay is predominantly caused by local dynamics: supergranule motions; magnetic flux cancellation; magnetic flux submergence (180). This process can be modeled as turbulent diffusion (195) and acts to spread magnetic elements over the solar surface. As the leading sunspot in a group is generally the strongest and most compact, the following spot tends to fragment much more rapidly. The dispersion of strong-field features is known to be slower than that of weak-field features (178). This is because magnetic forces begin to compete with the fluid advection.

At the surface, small concentrations of opposite polarity flux come into contact are observed to disappear. In theory, the magnetic fields of each concentration reconnect—this forms a new flux loop very close to the photospheric surface, which may be submerged due to the convective downdrafts in supergranule lanes (180). Magnetic reconnection is described further in Chapter 2. With regards to large magnetic structures, a subsurface “sea serpent” process may occur in which a toroidal flux-tube becomes

buoyant at multiple locations along its length, forming a number of inverted “u” structures (195). After emerging, the structures could reconnect with overlying poloidal fields, forming flux rings that are not rooted within the convection zone. These rings could conceivably leave the surface of the Sun. This allows the removal of flux without the need for surface flows.

1.8 The Solar Activity Cycle

The global evolution of the solar magnetic field is characterised by a 22-year magnetic cycle. The Solar dipole field undergoes a polarity reversal and return to its initial configuration. The cause of this can be described through the large-scale circulation of magnetic flux (13; 112). The fields begin as buoyant flux tubes formed from the shearing of toroidal fields at the base of the convection zone. The flux tubes later emerge as sunspot groups that later fragment. One polarity of the field is preferentially transported to the nearest pole, decreasing and eventually reversing its magnetic field, while the rest submerges or cancels with opposite polarity field. The most extensively studied part of the system is the sunspot group, who’s life-cycle fuels the 22-year cycle. During every half magnetic cycle, an 11-year sunspot cycle occurs.

1.8.1 The Sunspot Cycle

The 11-year solar cycle is characterised by an increased emergence rate of sunspot groups progressing from high to low latitudes, leaving a “zone of avoidance” at the equator; this is known as Spörer’s law (124). The start of the following cycle begins as new high latitude flux begins to emerge near the end of the preceding cycle. At the beginning of the cycle, the leading polarity of sunspot groups is the same as that of the nearest global polar field and opposite to that of the following polarity; this is known as Hale’s law (83). The line connecting the centroids of the two polarities is

1. INTRODUCTION

inclined toward the equator (“Joy’s Law”; 83) by $\sim 4^\circ$, and the inclination decreases with emergence latitude (101). An overview of these phenomena is given in Hathaway (89). The buoyant flux tubes are affected by the α -effect (as a result of the Coriolis effect; 59, and references therein) on their way to emerging at the photosphere as active regions. This results in a pattern of active region equatorward tilts, decreasing with latitude (101). The more fragmented trailing portion of active regions relative to the leading portion allows a preferential dispersion of the trailing polarity by supergranular motions. This phenomenological model is qualitatively the most successful for reproducing the observed solar activity cycle (138).

Since systematic observations of the Sun began with Galileo’s astronomical application of the telescope in the 17th century, various observers have kept a record of the number of sunspots appearing on the Sun’s disk each day. It was first reported in 1776 that the emergence of sunspots is periodic, and in (184) a period of about 10 years is determined. The average sunspot cycle is about ~ 11 years, but may vary by several years. The numbers of emerging active regions rise and fall with the cycle as shown in the plot of observed sunspots over time (Figure 1.23). The solar cycle also relates to eruptive phenomena, as the frequency of flares and coronal mass ejections show similar trends to that of sunspot group emergence. These events are clearly related to sunspot groups (see Section 1.8.3).

A ~ 22 year cycle is observed which includes two sunspot cycles. When this cycle begins at “solar minimum”, characterized by a minimum in the rate of sunspot emergence, the global magnetic field is bipolar with magnetic north matching the spin-axis north pole. The bipolar field lines are then displaced longitudinally and stretched into a toroidal configuration due to differential rotation, in which the rotational angular velocity of the Sun decreases with latitudinal distance from the equator. As the global bipolar field becomes toroidal, the polar magnetic field strengths decrease and a sharp increase in the number of emerging sunspots is observed. For several years

during sunspot maximum, the global dipole switches polarity and the spin-axis north pole becomes magnetic south. Over the course of the next \sim 6 years, the rate of sunspot emergence decreases to a new minimum and the second half of the 22 year cycle follows, similar to the first, but with a flipped global dipole.

It is commonly understood that during the solar cycle the polar fields are reversed by the accumulation of weak magnetic flux elements at high latitudes, carried from lower latitudes (13; 112). It is thought that the combination of Joy's Law, the poleward meridional flow, and supergranular diffusion allow this process to occur (136). Small flux concentrations are carried to the poles more swiftly (than would be due to their diffusive random walk alone) by the meridional flow. The meridional flow itself has been indirectly measured using both surface tracking methods and helioseismology techniques (78; 90; 228). Since following (leading) flux concentrations in dipoles tend to be weaker (stronger), they are more affected by flows (178). Thus slightly more (less) of the flux of the following (leading) polarity will random-walk to the nearest hemispheric pole before completely decaying. The process has been studied extensively by directly observing large scale quiet-Sun magnetic fields (85; 176; 206) and by using surface flux transport models (112; 175; 214). These models are able to qualitatively reproduce the evolution of the distribution of photospheric magnetic fields on the Sun.

Ulrich *et al.* (207) shows that the global dipole field reversal is driven by the bursty emergence and poleward migration of ARs over a short period of time, rather than a continuous flux emergence process. The meridional flow latitude profile has been measured using Doppler data (206), surface feature tracking methods (90), and helioseismology techniques (78; 228). Each study presents observations of a reverse of direction in the meridional flow at high latitudes at different phases in the solar cycle. Schrijver & Liu (176) use measurements of the dipole strength and surface flux transport modeling to conclude that this dynamic meridional flow is responsible for cycle to cycle differences in the polar field strengths.

1. INTRODUCTION

Magnetic flux imbalance is an observational effect resulting from summing the signed magnetic flux within a limited surface area on the Sun. It is important in the analysis of the large-scale magnetic field. Hemispheric flux imbalance, the magnetic polarity imbalance between the North and South hemispheres, affects the structure of the global magnetic field. For instance, a purely dipole field results from having a single opposing polarity in each hemisphere. In reality, the Sun's field is multipolar. Large scale measurements of the imbalance between outward (positive) and inward (negative) directed magnetic flux from 1975-2000 have been studied by Choudhary *et al.* (36) and it is seen that hemispheric flux imbalance is a function of the solar cycle and furthermore switches sign between cycles. A clear signal is found in the northern hemisphere, but is much less clear in the southern. Upon measuring flux imbalance in individual ARs, a larger percentage imbalance is found than that determined hemispherically. It is reasoned that this indicates ARs must be balanced by long-range connections to oppositely imbalanced ARs at similar latitudes and the hemispheric imbalance is resolved by trans-equatorial connections. If ARs were balanced using trans-equatorial connections then the hemispheric imbalance could be much larger.

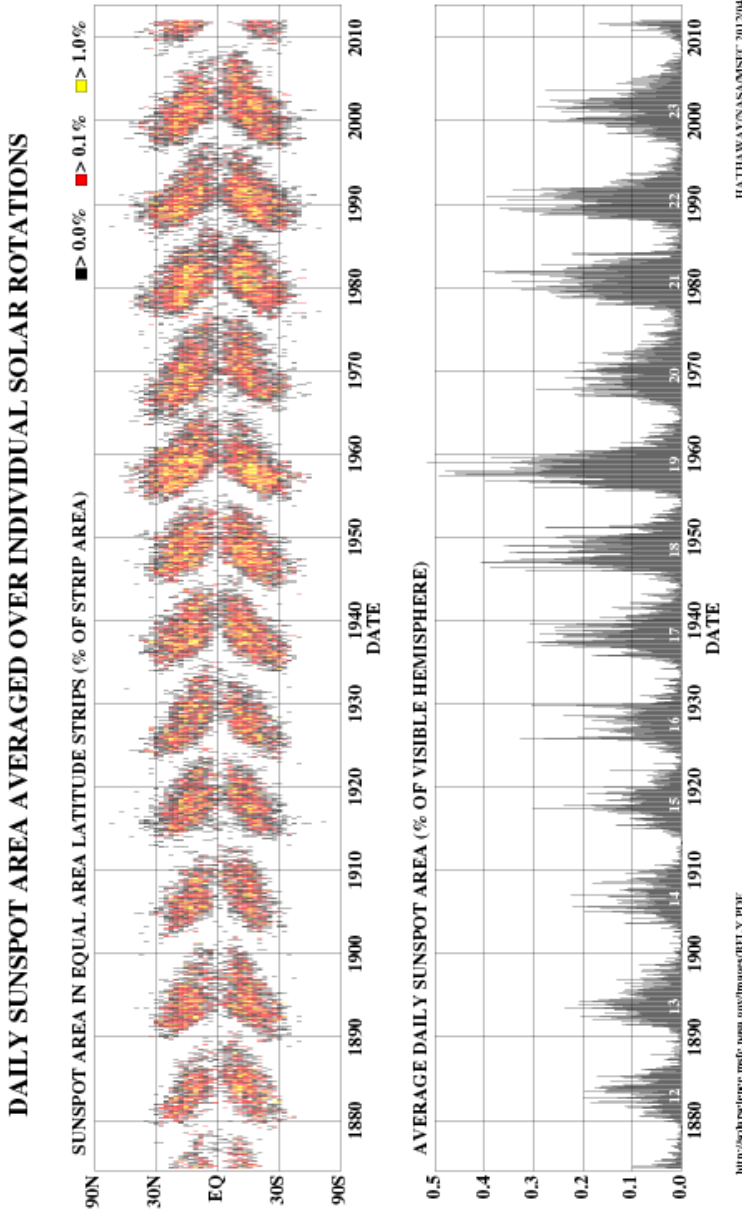


Figure 1.23: The sunspot cycle over ~ 150 years (from 89). *Top:* the number of sunspots at each latitude over time. This plot exhibits the characteristic butterfly shape. *Bottom:* the total number of sunspots over time. The 11-year cycle is seen to occur with a varying peak sunspot number.

1. INTRODUCTION

1.8.2 Global Field Reversal

The large-scale configuration of the magnetic field within the convection zone is thought to transition between being poloidal and toroidal, every 11 years (144). The process which facilitates this reorganisation is the magnetic dynamo. Longitudinal flows drag poloidal fields into a toroidal configuration and meridional flows then help to reverse the process. The poloidal field is measured at the North and South poles of the Sun during solar minimum (86). The large-scale toroidal field has also been directly measured by taking advantage of line-of-sight magnetic field measurements at the solar limb (206). Toroidal fields at the tachocline are stretched into thin flux tubes by shearing at the interface of the rigidly rotating radiative zone and regions where the differentially rotating convection zone is moving at a different speed. Turbulent perturbations introduce instability into the flux-tubes and magnetic buoyancy becomes important and causes them to rise toward the surface, as described in Section 1.7.

The combination of these phenomena causes a reversal of the polar magnetic fields (13; 112). The Babcock-Leighton process can be seen in large-scale magnetogram observations (85) and successfully reproduced using surface flux transport models (175; 214). These models imply a buildup of net magnetic flux (an imbalance of + and – magnetic polarities) should occur at mid to low latitudes of the same polarity as the pole in that hemisphere. At higher latitudes, flux of one polarity builds up as magnetic elements are swept poleward. Low latitude flux from opposite hemispheres eventually diffuses toward the equator and cancels or submerges. Since net flux must sum to zero globally, one should measure the same magnitude, but opposite sign, of net flux at high and low latitudes in each hemisphere. For the first time we present a quantitative comparison of the amount of imbalanced flux in the AR bands and at high latitudes (Section 6.3.2). Regardless of the vehicle for flux decay and redistribution, the total observed flux decreases but physically the net flux must be conserved due to the solenoidal constraint (Gauss' Law), as there are no magnetic monopoles ($\nabla \cdot \mathbf{B} = 0$). Locally on the

1.8 The Solar Activity Cycle

Solar surface, non-zero positive (negative) net flux may exist as it may be connected to distant negative (positive) flux concentrations, or may be quasi-open (connected to the solar wind) and balanced by other quasi-open negative (positive) flux concentrations on the solar surface.

Latitudinal observations of net flux over time show that while the active region belt progresses from high to low latitudes, net unipolar flux is observed to be transported poleward, as observed in magnetic butterfly diagrams (85). Choudhary *et al.* (36) investigate large-scale flux imbalances finding that the signed flux imbalance between the North and South hemispheres is a function of the solar cycle and furthermore switches sign between cycles. Zharkov & Zharkova (230) study flux imbalance in individual sunspot groups statistically for a portion of solar cycle 23. Opposite imbalances in each hemisphere are found that reverse at the solar minimum. Zharkov *et al.* (229) state that a phase relation exists between active region flux imbalances and the background high-latitude magnetic field. These results support the Babcock-Leighton model.

The properties of detected ARs, such as flux imbalance, affect the solar magnetic structure locally, while on a global scale, hemispheric flux imbalance affects the structure of the solar magnetic field. For instance, a purely dipole configuration results from having a single opposing polarity in each hemisphere. Mordvinov (134) determines a relationship between the IMF and global field harmonic modes—especially the $[l = 2, m = 0]$ (quadrupole) mode. Generally, the global field is multipolar and we can describe its structure extending into the solar atmosphere using the superposition of spherical harmonics, with a potential field source surface (PFSS) model.

Some studies focus on periodicities in the harmonic coefficients over multiple solar cycles finding separate frequencies in axisymmetric and non-axisymmetric modes (107; 196; 197). It has been determined that to accurately predict the magnetic field at Earth, the properties of low latitude magnetic features on the Sun must be taken into account (175; 183; 213). The distribution of open flux and the global field configuration

1. INTRODUCTION

determine the shape of the heliospheric field and thus can affect the space weather environment at Earth. Taking these findings into account, we seek to better understand the evolution of the global solar magnetic field in the context of a full 11 year activity cycle (half of a magnetic cycle) by characterizing spatio-temporal distributions of magnetic feature properties.

1.8.3 Active Sunspot Groups

Sunspots are formed beneath the solar surface and emerge through the photosphere and into the corona. Turbulent photospheric and sub-photospheric motions jostle around the flux tubes forming sunspots, possibly resulting in destabilisation that leads to a flare (42). Other phenomena, such as shearing and helicity injection, may build up stress in an AR leading to strong electric currents that correlate with flaring (173; 181). Currently the exact conditions that are necessary for or lead to flaring are not known. This is partly due to limitations in our observational capabilities. Only the magnetic fields at the foot points of sunspot groups can be imaged, while flares actually occur some distance above the sunspot in the solar atmosphere. Flaring sunspot groups tend to be big and ugly (and thus bad). The largest eruptions and flares are released by large but compact sunspot groups with complicated magnetic configurations. In this section we will refer to active magnetic structures, including sunspot groups, as “active regions” to include the entire system (surrounding magnetic flux elements and loop structures in the corona) connected to a flare.

Several classifications of active regions were designed to describe alternatively white-light and magnetogram observations of sunspot groups. The most common, McIntosh classification (Figure 1.24), is an expansion of the Zurich system. It describes the number and development of sunspots within a group, including properties of umbrae and penumbrae. (128) finds that the scheme is adept at indicating the relative flare productivity of a given class.

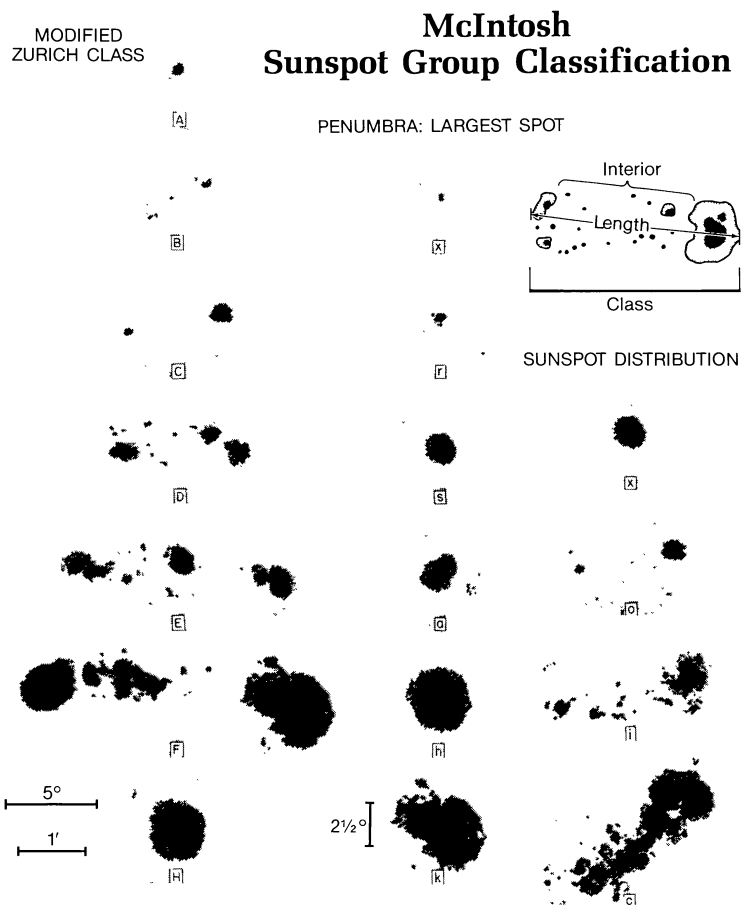


Figure 1.24: The McIntosh sunspot group classification system (from 128) The left column depends on the presence of spot penumbrae and group length. The middle column indicates features of the largest spot's penumbra. The right column is determined by the amount of spot coverage between the leading and trailing edges of the group.

The Hale classification system classifies the distribution of polarities in the active region, as described by Table 1.3. This system has been expanded to include the δ -class, which is given when two polarities are present within a single sunspot penumbra (109). The α indicates only one polarity of spot is visible, with p (f) meaning that any spots

1. INTRODUCTION

Table 1.3: The possible sunspot group classifications using the Hale scheme (83) with the appended δ -class (109). The “p” (“f”) denote whether the strongest spot is preceding (following).

Unipolar	Multipolar	Mixed
α	β	$\beta\delta$
αp	βp	$\beta\gamma\delta$
αf	βf	
	$\beta\gamma$	

precede (follow) the magnetic field distribution. The β indicates both spot polarities of spot are visible with p and f indicating which spot is larger. The γ indicates spots of one polarity are on both sides of one or more spots of opposite polarity. Sunspot groups denoted as δ -class are shown to produce the most significant flares (163). These classification schemes are well correlated to quantitative descriptions of active region complexity (105).

Classification has been shown to be useful for grouping active regions by their expected flare productivity. The quantification of active region properties allows a physical comparison and deeper understanding of the actual causes flaring. Complexity, often quantified by fractal index (41; 42; 125) and scale-power distributions (2; 96) is shown to be correlated with flare productivity. However, recent work has shown that fractal dimension is not a good flare predictor (72). The presence of shear and helicity injection are shown to initiate flaring within active regions (182). Strong polarity separation lines with large gradients and large field magnitudes on either side are known to be one of the best indicators of flaring (173).

Generally active regions emerge up to a certain size while their non-potential characteristics (such as polarity separation line strength) continue to evolve. Upon reaching a state of maximum complexity, active regions are observed to produce the most significant flares. The relationship between flux and the sum of magnetic gradients along a polarity separation line (WL_{SG}) is shown to be a power law (58).

Various statistical methods have been used in conjunction with an assortment of

1.8 The Solar Activity Cycle

physical properties to forecast flares. Current forecasting systems are limited (130) and often generate incorrect predictions. The inaccuracy of forecasting systems may be very costly. Depending on the application, false alarm forecasts may result in lost revenue during satellite shut-downs, diverting trans-polar flights, delayed spacecraft launches. On the other hand, missed flares could result in damage to sensitive space-born instruments, such as those on communications, scientific, or military satellites, or the endangerment of pilots on transpolar flights and astronauts on space-walk (143). In 1989 a solar storm caused disruptions to power grids in Quebec, the northeastern United States, and areas of Sweden causing blackouts for hours. Recently, communications with the civilian Galaxy 15 satellite were compromised in April 2010, and the spacecraft was unable to respond to commands from the ground for months. As our society and military become increasingly technologically advanced, we become more directly affected by solar activity.

Past work on predicting the occurrence of flares in sunspot groups has focused on determining a set of sunspot group properties important for flaring (70). This requires a large set of characterized sunspot group detections, which is used to train a prediction system. Automated detection and characterization systems, such as the SolarMonitor Active Region Tracker (SMART; 97) developed by our team, are useful for this task and often focus on characterizing magnetic field properties. Using these detection methods, modules may be applied to determine various properties: size; magnetic flux; polarity separation line length; magnetic energy; magnetic connectivity. The sunspot group detections are then associated with a flare catalog and correlations are determined for specific properties and various prediction time windows and latencies.

There have been many studies attempting to find the most significant sunspot group properties for predicting flares. (114; 115; 116) and (16) test a large number of vector magnetic properties (e.g., moments of the vector magnetic field, magnetic shear, and current helicity) in various combinations and find that characterizing a sunspot group at

1. INTRODUCTION

one point in time has limited bearing on whether it will flare in the future. More recent work, such as (39) and (4) use machine learning prediction systems to forecast flares, and achieve much more accurate prediction results, while investigating much fewer properties.(39) rely on automatic sunspot classification to make predictions, while (4) use the line-of-sight magnetic properties defined in (97). Using a completely different approach, (221) achieves good results predicting flares on the assumption that if a flare has occurred, more will occur. This shows that the history of activity of a sunspot group is a significant predictor. For the purposes of reliable operational forecasting, all existing systems are still limited, as their use results in substantial numbers of false alarms and missed flares.

Most studies use point-in-time detections of sunspot groups to predict flares. (123) are an exception, and show promise in predicting flares using previous changes in magnetic properties. The concept of relating sunspot group dynamics and evolution has not been extensively explored.

1.9 Solar Eruptions

Solar eruptive activity is associated with large complex sunspot groups. The solar activity cycle is mainly observed by monitoring the number of sunspots on disk (sunspot number). On \sim year timescales the number of eruptive events observed is well correlated with the sunspot number. Each eruption is different and there are a wide variety of phenomena that are generally associated with them. To present a common scenario: often, as a sunspot group evolves, material can cool and collect in a “channel”, suspended above by the magnetic loop structure along a sheared polarity separation line (PSL). This material is called a filament or prominence depending whether it is observed from above or side-on. The shear and twist in the system introduces magnetic stresses. At some point an instability occurs and the fields are thought to rapidly re-

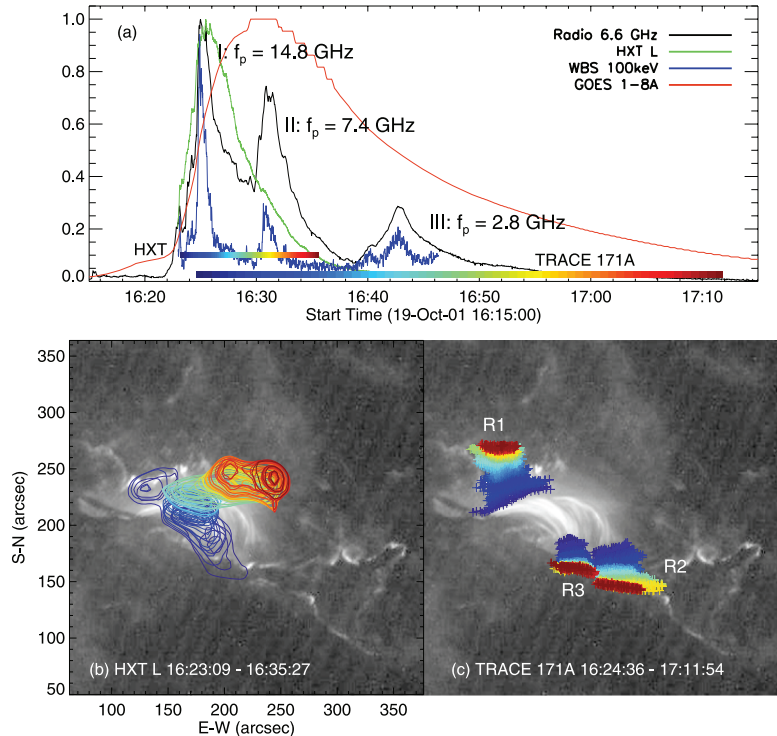


Figure 1.25: The progression of a typical solar flare (from 156). *Top*: the impulsive phase is characterised by a rapid burst of hard X-rays (HXT), followed by the gradual decay of soft X-rays (GOES). *Bottom left*: The contours indicate the location of HXR emission. *Bottom right*: During the course of the flare, the foot points move apart, as indicated by the colored marks.

organise to a lower energy state. Theoretically, this reorganisation releases part of the stored magnetic energy as radiation and non-thermal particle acceleration (64). This conversion and release of energy is called a flare. The converted magnetic energy is considered to be part of the “non-potential” portion of the magnetic energy in the system, as discussed in Chapter 2. Often this is accompanied by the release and acceleration of matter called a coronal mass ejection (CME) which carries another large portion of the energy. The kinetic CME energy has been shown to be greater, but of the same order of magnitude as the radiative flare energy (55). The accelerated matter generally includes filament material forming the “core” and an overarching twisted magnetic loop structure called a flux rope forming the “front” of the CME.

1. INTRODUCTION

Solar flares are among the most energetic events occurring in the solar system, influencing a panorama of physical systems: from the solar surface and atmosphere, through the heliosphere, and into geo-space. Flares, along with coronal mass ejections, are a major contributor to space weather: the interaction of magnetic fields and particles accelerated on or near the Sun with the Earth’s magnetosphere and upper atmosphere. Although significant progress has been made in understanding the fundamental physics of flares, their accurate forecasting remains impossible.

Flares occur in volumes of the atmospheric plasma above sunspot groups with increased emission at temperatures of 1 000 000 K or more. There are many flare cartoons which mainly rely on the release of magnetic energy through reconnection¹. It is thought that magnetic reconnection occurs at strong current sheets where magnetic fields are oppositely aligned, causing particle acceleration. Their occurrence tends to be along polarity separation lines (173). High-energy particles stream down the legs of the reconnecting structure, impacting the chromosphere, and producing EUV and X-ray radiation. High energy X-ray, or hard X-ray (HXR), emission is concentrated at the foot points and the apex of the structure near the reconnection region. Lower energy, or soft X-ray (SXR), emission is focused in different regions depending on the phase of the flare evolution, but is generally more widely distributed over the loop structure.

There are several stages in the evolution of a flare: the pre-flare, impulsive, and gradual phases (64). The behaviour of emission at different wavelengths and the motions of the flare foot points is shown in Figure 1.25. In the pre-flare phase, heating occurs that signals the oncoming flare. This often takes the form of a filament activation that is observed as a brightening of filament material in H- α observations. During the impulsive phase, rapid brightenings in HXRs and radio (type III bursts) are observed. The main brightening in SXR occurs more slowly and its peak divides the impulsive and gradual phases. During the initial SXR brightening and peak, the

¹See: <http://solarmuri.ssl.berkeley.edu/~hhudson/cartoons/>.

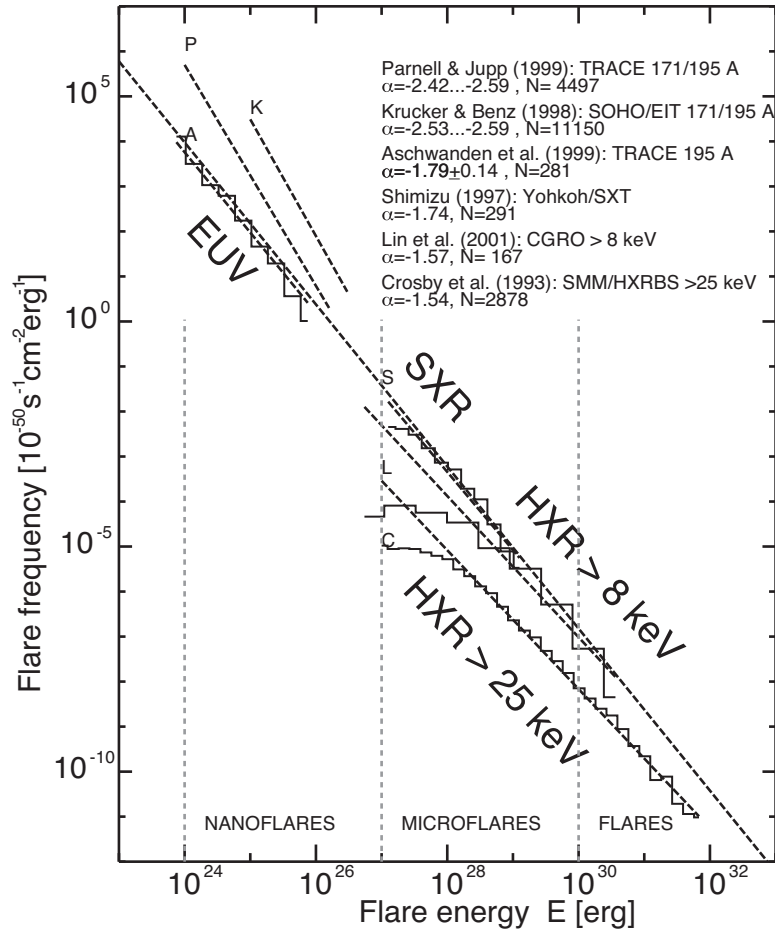


Figure 1.26: The frequency distribution of flare magnitudes measured in various studies (from 9).

shape of the time profile of HXR emission generally follows the time derivative of the SXR emission. This is called the Neupert effect and is thought to occur because the cooling timescale of coronal SXR emitting plasma is longer than that of the chromospheric heating mechanism. Electrons accelerated during the flare cause non-thermal HXR emission and chromospheric “evaporation” that heats the corona above, resulting in thermal SXR emission. This effect was first noted by (139) by comparing X-ray and microwave observations.

Large flares release around 10^{32} erg of energy through radiation. They are often

1. INTRODUCTION

Table 1.4: The GOES flare classification scheme, where peak fluxes are integrated over the 1-8 Å bandpass.

Class	Peak Flux [W m ⁻²]
X10	10^{-3}
X	10^{-4}
M	10^{-5}
C	10^{-6}
B	10^{-7}
A	10^{-8}

characterised by the magnitude of their peak emission in SXRs using a 1-8 Å bandwidth. This classification system is a base-ten magnitude system called the GOES Class after the instrument used to define it and is summarised by Table 1.4. Each higher class of flare exhibits peak SXR emission ten times greater than the last. Within a single class, flares are usually ordered by the first two significant digits of their flux. For example, a flare with a peak flux of $4.5 \times 10^{-5} \text{ W m}^{-2}$ would be given a classification of M4.5. The frequency flare occurrence with increasing magnitude follows a decreasing power law. A slope between -1.5 and -2.5 is measured in various studies (see Figure 1.25; 9). Also, the distribution of waiting times between flares over long time-scales has been shown to be a power law over time-scales greater than a few hours, pointing to an avalanche model (122), but is exponential when considering the statistics over multiple solar cycles, indicating flaring is a random Poisson process (219). Individual active regions exhibit an exponential distribution of flaring rates (220) and it is well known that the best predictor for a flare to occur in the future is that a flare has occurred in the past (221).

1.10 Thesis Aims

Very few sunspot-related phenomena are well understood. It is only superficially known how the large-scale plasma circulation and the decay and dispersion of sunspot magnetic

fields are connected to the reversal of the global magnetic field. Above the photosphere, the magnetic field strength and structure can only be roughly estimated, and below the photophere neither is known to any certainty. Additionally, predicting the strength of the next solar cycle, sunspot emergence, and the occurrence of flares with the accuracy required by the operational community is not possible.

The aim of this thesis is to better understand the evolution of individual sunspot groups and the global magnetic field. The study aims to address three questions in a series of studies:

- *What are the conditions in sunspot groups that result in solar flares?* The relationship between flaring and sunspot group property dynamics is investigated. Property distributions associated with different flare magnitudes are compared. The properties of sunspot groups over the solar cycle are compared to global flare productivity.
- *What mechanisms determine the configuration of the global magnetic field and how does this relate to the solar dynamo?* The distribution of magnetic features affects the global magnetic field of the Sun. A comparison between the properties of sunspot groups and the global field configuration over solar cycle 23 is presented.
- *What mechanisms govern the evolution and decay of sunspot groups?* A mechanism for the decay of sunspot groups is investigated by comparing a large-scale observation of magnetic field dispersion to a simulation.

To allow a large-scale study of the solar magnetic field, a combination of image processing techniques is used to automatically detect, characterise, and track sunspot groups over time.

The remainder of this thesis is organised as follows. The theory describing magnetic fields in a plasma is presented in Chapter 2. The magnetic field observations and other data used in the investigations are described (see Chapter 3). The methods for

1. INTRODUCTION

automatically detecting and characterising sunspot groups are described in 4. Three scientific studies of the solar magnetic field follow in Chapters 5, 6, and 7. Finally, the main results and conclusions of the studies, including prospects for future work, are summarised in Chapter 8.

2

Theory of Magnetic Fields in a Plasma

In this chapter, theories explaining the dynamics and energetics of magnetised plasmas are discussed. Electrodynamic, fluid, and plasma equations leading to magnetohydrodynamics are described. Also, magnetic fields in the solar atmosphere, the magnetic energy release in flares, and the quantification of surface fields are explained. This chapter summarises the background theory of ideas presented throughout this thesis.

2.1 Plasma Physics

The material composing the Sun can be described as a plasma, which is defined as a gas in which a significant fraction of atoms are ionised. This ionisation is due to the enormous temperatures and pressures in the Sun. The fraction of ionisation varies with

2. THEORY OF MAGNETIC FIELDS IN A PLASMA

location and is described by the Saha equation,

$$\frac{n_{i+1}}{n_i} = \frac{2Z_{i+1}}{n_e Z_i} \frac{(2\pi m_e k_B T)^{3/2}}{h^3} e^{(-\chi_i/k_B T)}, \quad (2.1)$$

where, n_i and n_{i+1} are the number of ions in the ionisation state i and $i+1$, respectively. The partition function of each state is given by Z ($Z_i \approx 2$ and $Z_{i+1} \approx 1$), and χ_i is the ionisation energy for a given state. For hydrogen this reduces to,

$$\frac{(n^+/n)^2}{1 - (n^+/n)} = \frac{4 \times 10^{-9}}{\rho} T^{3/2} e^{(-1.6 \times 10^5 / T)}, \quad (2.2)$$

where n^+ is the number density of ions and n is the summed number density of neutrals and ions, assuming macroscopic charge neutrality. This can also be written in terms of pressure,

$$\frac{(n^+/n)^2}{1 - (n^+/n)} = \frac{4 \times 10^{-9}}{\rho^{5/2}} \frac{P \mu m_H}{k_B}^{3/2} e^{(-1.6 \times 10^5 \rho k_B / \mu m_H P)}, \quad (2.3)$$

Hydrogen transitions from nearly neutral to almost completely ionised over a narrow transition region in temperature centered at $\sim 10\,000$ K. This temperature occurs at outer layers of the solar convection zone. The Saha equation can not be applied in most of the solar atmosphere where local thermodynamic equilibrium does not hold. Also, in the core of the Sun, the pressure is so immense and the density so large that adjacent hydrogen atoms are close enough to effect each other's ionisation energies. Thus, in the core, the ionisation fraction approaches unity due to the added effect of "pressure ionisation".

The average random kinetic (thermal) energy for a plasma is given by,

$$\langle E \rangle = (3/2)k_B T. \quad (2.4)$$

The charged particles of a plasma are in constant motion, striving to cancel charge imbalance locally. The electron plasma oscillation frequency due to this motion is

given by,

$$\omega = \sqrt{\frac{ne^2}{m_e \epsilon_0}}, \quad (2.5)$$

where e is the charge of an electron, m_e is the mass of an electron, and ϵ_0 is the permittivity of free space. In cgs this can be written,

$$f_p = \frac{\omega_p}{2\pi} = 9\,000\sqrt{n_e}, \quad (2.6)$$

where the result is in Hz.

The Debye length is given by,

$$\lambda_D = \sqrt{\frac{\epsilon_0 k_B T_e}{e^2 n_e}} \quad (2.7)$$

This is the distance over which an electron's charge is “felt” by other charged particles. An electron's electric potential falls off exponentially outside of its Debye sphere. The plasma parameter is,

$$\Lambda = 4\pi n \lambda_D^3, \quad (2.8)$$

and indicates the number of particles within a Debye sphere. If $\Lambda \gg 1$, the plasma is strongly coupled (regarding collective effects), or weakly coupled if $\Lambda \ll 1$. Generally, strongly coupled plasmas are “cold” and dense (as in white dwarf and neutron star atmospheres), while weakly coupled plasmas are diffuse and hot (as in solar and space plasmas). In a “collisional plasma”¹, the mean free path of particles within the plasma is small compared to the observational length scale² and is given by,

$$\lambda_{mfp} = 1/\sigma_{cs} n, \quad (2.9)$$

where σ_{cs} is the the collisional cross-section. For charged particles σ_{cs} is much larger

¹Collisional plasmas include those in collisional equilibrium, such as the solar corona.

²The observational length-scale determines the scale on which plasma phenomena are observed.

2. THEORY OF MAGNETIC FIELDS IN A PLASMA

than for neutrals due to the Coulomb force,

$$F = \frac{1}{4\pi\epsilon_0} \frac{q_1 q_2}{r^2}, \quad (2.10)$$

where q_1 and q_2 are the charges of each particle, and r is the distance between the particles. The collision frequency is,

$$\nu \approx \frac{\sqrt{2}\omega_p^4}{64\pi n_e} \left(\frac{k_B T}{m_e} \right)^{-3/2} \ln \Lambda, \quad (2.11)$$

where n_e is the electron number density. In the absence of magnetic fields, disturbances in the plasma travel at the sound speed,

$$v_s = \sqrt{\frac{\gamma p}{\rho}}, \quad (2.12)$$

where γ is the ratio of specific heat at constant pressure (C_P) to that at constant volume (C_V).

Magnetic and electric fields are ubiquitous on the Sun. In general, these fields are governed by Maxwell's equations, the equations of electrodynamics,

$$\nabla \cdot \mathbf{E} = \frac{1}{\epsilon_0} \rho_e \quad (\text{Gauss's law}), \quad (2.13)$$

$$\nabla \cdot \mathbf{B} = 0 \quad (\text{solenoidal constraint}), \quad (2.14)$$

$$\nabla \times \mathbf{E} = -\frac{\partial \mathbf{B}}{\partial t} \quad (\text{Faraday's law}), \quad (2.15)$$

$$\nabla \times \mathbf{B} = \mu_0 \mathbf{j} + \mu_0 \epsilon_0 \frac{\partial \mathbf{E}}{\partial t} \quad (\text{Ampére's law}), \quad (2.16)$$

where \mathbf{E} is the electric field, \mathbf{B} is the magnetic field, \mathbf{J} is the current, ρ_e is the charge density, ϵ_0 is the permittivity of free space, and μ_0 is the permeability of free space. The equation of motion for a charged particle traveling through electric and magnetic

fields is,

$$m_e \frac{\partial^2 \mathbf{x}}{\partial t^2} = \mathbf{F} = \underbrace{q\mathbf{E}}_{\text{Coulomb}} + \underbrace{q\mathbf{v} \times \mathbf{B}}_{\text{Lorentz}}, \quad (2.17)$$

where q is charge of the particle and \mathbf{v} is the velocity of the particle moving through the field. In Section 2.3 dynamics will be described in terms of a magnetised fluid, rather than of a single particle.

The force on a charged particle due to a vertical magnetic field results in the particle revolving around the field in the horizontal plane. Considering an electron, the frequency at which this occurs is the electron gyrofrequency,

$$\omega_g = -\frac{eB}{m_e} \quad (2.18)$$

The gyroradius is then,

$$r_g = \frac{v_\perp}{\omega_g} \quad (2.19)$$

This motion results in gyro-synchrotron emission which is often observed in regions of strong magnetic field on the Sun at microwave wavelengths (77).

2.2 Fluid Dynamics

In general, the Sun can be treated as a fluid. The fluid approximation allows one to model solar material as a continuous spatial distribution of fluid parcels, rather than a collection of particles. The principle fluid equations are,

$$\frac{\partial \rho}{\partial t} + \nabla \cdot (\rho \mathbf{v}) = 0 \quad (\text{mass continuity}), \quad (2.20)$$

$$\rho \frac{D\mathbf{v}}{Dt} = -\nabla P + \mathbf{F} \quad (\text{equation of motion}), \quad (2.21)$$

$$\frac{D}{Dt} \left(\frac{P}{\rho^\gamma} \right) = -\mathcal{L} \quad (\text{energy equation}), \quad (2.22)$$

$$P = \frac{\rho k_B T}{m_p \bar{\mu}} = n k_B T \quad (\text{ideal gas law}), \quad (2.23)$$

2. THEORY OF MAGNETIC FIELDS IN A PLASMA

where \mathbf{F} denotes external forces on the fluid, \mathcal{L} is the total energy loss rate, γ is the ratio of specific heats (of constant pressure to constant volume), m_p is the mass of a proton, $\bar{\mu}$ is the mean molecular weight, and

$$\frac{D}{Dt} = \frac{\partial}{\partial t} + \mathbf{v} \cdot \nabla \quad (2.24)$$

is the convective time derivative. The mean molecular weight is ~ 0.6 for ionised solar plasma, but for small ionisation fractions μ is \sim unity.

The Reynolds number indicates whether the inertial or viscous forces in a fluid dominate. The Reynolds number is given by,

$$R_e = \frac{VL}{\nu_{visc}} = \frac{\rho VL}{\mu_{visc}}, \quad (2.25)$$

where, V is a characteristic velocity in the fluid, L is a characteristic length scale of the system, ρ is the fluid density, $\nu_{visc} = \mu_{visc}/\rho$ is the kinematic viscosity, and μ_{visc} is the dynamic viscosity, a measure of how much the fluid resists an applied shearing force. Turbulence becomes an important form of energy transport for fluids of Reynolds number (R_e) greater than ~ 5000 . In the convection zone and lower photosphere R_e is many orders of magnitude larger than this; in the granulation layer it is estimated to be $\approx 10^9$ (44). Turbulent flows are highly disorganised and exhibit a cascade of energy to smaller scales. At the smallest scales the kinetic energy of the flows is dissipated as heat through molecular diffusion and viscosity. The turbulent heat flux is

$$H_k = v\rho C_P T, \quad (2.26)$$

where v is the speed of a turbulent fluctuation, C_P is the specific heat at constant pressure, and T is the temperature of the fluctuation. The turbulent length scale

2.3 Magnetohydrodynamics

where energy is dissipated as heat (the Kolmogorov scale) is given by,

$$\eta_k = \frac{\nu^3}{\epsilon_k}, \quad (2.27)$$

where ϵ_k is the rate of energy dissipation.

The distribution of energy with scale can be obtained by Fourier decomposing a given flow field and considering Equation 2.27 and the scales of turbulence, $\eta_k \ll \ell_k \ll L$, where ℓ_k denotes the medium turbulent scales and L , the largest scales in the system. The scale of ℓ_k is defined somewhat arbitrarily, limited by the molecular scale η_k and the observational length scale. The distribution of energy is then,

$$E(r) = C \epsilon_k^{2/3} k^{-5/3}, \quad (2.28)$$

where C is a universal scaling constant and the wavenumber, $k = 2\pi/\ell_k$. Kolmogorov thus derived a universal scaling law of $-5/3$ for the turbulent energy cascade over spatial scale. Many studies have tried to determine the scale dependence of features on the Sun (96; 149), relating their properties to turbulent phenomena.

2.3 Magnetohydrodynamics

To describe the dynamics of solar plasma, an electrically charged fluid, we utilize magnetohydrodynamics (MHD). This framework differs from electrodynamics in its fluid mechanics component. Maxwell's equations are altered using several assumptions. It is assumed that the plasma is in collisional equilibrium, which is true in the solar interior and lower atmosphere. It is also assumed that the plasma flow velocities are much less than the speed of light. We may then neglect the displacement current in Ampère's law, which becomes,

$$\nabla \times \mathbf{B} = \mu_0 \mathbf{j}, \quad (2.29)$$

2. THEORY OF MAGNETIC FIELDS IN A PLASMA

where \mathbf{B} , μ_0 , and j are the magnetic field vector, magnetic permeability, and current density vector, respectively. Charge neutrality is also assumed, which implies that an electric field can only be induced by a changing \mathbf{B} field and $\nabla \cdot \mathbf{E} = 0$, since excesses of charge are not allowed to accumulate. Faraday's law governs this induced electric field,

$$\frac{\partial \mathbf{B}}{\partial t} = -\nabla \times \mathbf{E} \quad (2.30)$$

Currents are generated in the plasma by a non-zero \mathbf{E} or a changing \mathbf{B} and are determined using the generalized Ohm's law,

$$\mathbf{j} = \sigma(\mathbf{E} + \mathbf{v} \times \mathbf{B}), \quad (2.31)$$

where σ and \mathbf{v} are the electrical conductivity and plasma velocity, respectively. We can then solve for \mathbf{E} in Equation 2.31 and substitute it into Equation 2.30,

$$\frac{\partial \mathbf{B}}{\partial t} = -\nabla \times \left(\frac{\mathbf{j}}{\sigma} - \mathbf{v} \times \mathbf{B} \right) \quad (2.32)$$

Thus, currents can be defined in terms of \mathbf{B} alone. Equation 2.29 is then rearranged and substituted for \mathbf{j} ,

$$\frac{\partial \mathbf{B}}{\partial t} = \nabla \times (\mathbf{v} \times \mathbf{B}) - \nabla \times \left(\frac{\nabla \times \mathbf{B}}{\mu_0 \sigma} \right) \quad (2.33)$$

A vector identity,

$$\nabla \times \nabla \times \mathbf{A} = \nabla(\nabla \cdot \mathbf{A}) - \nabla^2 \mathbf{A}, \quad (2.34)$$

is then applied to the second term,

$$\frac{\partial \mathbf{B}}{\partial t} = \nabla \times (\mathbf{v} \times \mathbf{B}) + \nabla^2 \left(\frac{\mathbf{B}}{\mu_0 \sigma} \right) - \nabla \times \left(\nabla \left(\nabla \cdot \frac{\mathbf{B}}{\mu_0 \sigma} \right) \right), \quad (2.35)$$

2.3 Magnetohydrodynamics

where the third term is cancelled using the solenoidal constraint ($\nabla \cdot \mathbf{B} = 0$). Simplification is performed by assuming σ is constant and defining magnetic diffusivity, $\eta \equiv 1/\mu_0\sigma$,

$$\frac{\partial \mathbf{B}}{\partial t} = \nabla \times (\mathbf{v} \times \mathbf{B}) + \eta \nabla^2 \mathbf{B} \quad (2.36)$$

This is known as the “induction equation”, and is fundamental in explaining the creation and destruction of magnetic fields in plasmas.

The first term on the right-hand side is the advective term which describes magnetic field dynamics due to plasma flows, and the second is the diffusive term which describes diffusion of the field due to gradients in the magnetic field itself. The advective timescale (Equation 2.37) is often much shorter than the diffusive (Equation 2.38), so flows tend to dominate the magnetic field dynamics. By dimensional analysis of Equation 2.36, characteristic timescales may be derived,

$$\frac{\Delta \mathbf{B}}{\Delta t} = \frac{\mathbf{v} \mathbf{B}}{\Delta l} \Rightarrow \tau_{adv} = \frac{\Delta l \Delta \mathbf{B}}{\mathbf{v} \mathbf{B}}, \quad (2.37)$$

$$\frac{\Delta \mathbf{B}}{\Delta t} = \eta \frac{\mathbf{B}}{\Delta l^2} \Rightarrow \tau_{diff} = \frac{\Delta l^2 \Delta \mathbf{B}}{\eta \mathbf{B}}, \quad (2.38)$$

where Δl is a characteristic length scale and $\Delta \mathbf{B}$ is the difference in magnetic field between the start and end of the time-scale which is roughly equivalent to the characteristic field, \mathbf{B} .

When applied to a medium-sized sunspot at the photosphere, Δl is of order 10 Mm, v is of order 10^{-4} Mm s $^{-1}$, and η is of order 10^{-9} Mm 2 s $^{-1}$. A τ_{diff} of ~ 3000 years and a τ_{adv} of ~ 1 day is determined. Sunspots are observed for days (the longest-lived last for months), not years; the advective term is clearly the more important for photospheric magnetic feature dynamics. Sunspot decay is thus due to convective (plasma flow) dispersion as discussed in (171). Assuming the conductivity (σ) to be infinite results

2. THEORY OF MAGNETIC FIELDS IN A PLASMA

in ideal MHD. In ideal MHD, Equation 2.36 becomes,

$$\frac{\partial \mathbf{B}}{\partial t} = \nabla \times (\mathbf{v} \times \mathbf{B}) \quad (2.39)$$

The ratio of the diffusive and advective terms in the induction equation yield the magnetic Reynold's number,

$$R_m = \frac{VL}{\eta}, \quad (2.40)$$

where V is a characteristic fluid speed and L is a characteristic length scale. This number indicates the relative importance of fluid motions to magnetic diffusion in the evolution of the magnetic field. In most cases for the Sun $R_m \gg 1$, so the magnetic diffusion term in Equation 2.36 can be neglected. There are a few cases where this is far from true, such as in flares. In Ideal MHD the frozen-in condition applies and magnetic field lines are permanently embedded in the plasma they inhabit. Thus the field is advected with plasma motions or plasma is constrained to flow along field lines.

To complete the set of MHD equations, we rewrite the fluid equations, coupling some of them to the electrodynamic ones. Using the vector identity,

$$\nabla \cdot (a\mathbf{A}) = (\nabla a) \cdot \mathbf{A} + a(\nabla \cdot \mathbf{A}), \quad (2.41)$$

we can rewrite Equation 2.20,

$$\frac{\partial \rho}{\partial t} + (\mathbf{v} \cdot \nabla)\rho + \rho \nabla \cdot \mathbf{v} = 0 \quad (2.42)$$

For an incompressible plasma, this becomes $\nabla \cdot \mathbf{v} = 0$. Equation 2.17 is substituted into Equation 2.21 for \mathbf{F} , coupling the fluid and electrodynamic forces,

$$\rho \frac{D\mathbf{v}}{Dt} = -\nabla P + \mathbf{J} \times \mathbf{B} + \rho \mathbf{g} \quad (2.43)$$

2.3 Magnetohydrodynamics

Assuming the fluid evolves adiabatically, no heat flows between fluid parcels and $\mathcal{L} = 0$. Thus Equation 2.22 and 2.20 are combined to become,

$$\frac{\partial P}{\partial t} + \mathbf{v} \cdot \nabla P = -\gamma P \nabla \cdot \mathbf{v} \quad (2.44)$$

The energy density of a magnetic field is given by,

$$u_B = \frac{B^2}{2\mu_0} \quad (2.45)$$

The total magnetic energy in a region of space is given by integrating over volume,

$$U_B = \int_V \frac{B^2}{2\mu_0} dV \quad (2.46)$$

Considering the time evolution of the total energy and using a dot-product identity,

$$\frac{dU_B}{dt} = \frac{1}{2\mu_0} \int_V \frac{d}{dt}(\mathbf{B} \cdot \mathbf{B}) dV \quad (2.47)$$

Using the product rule,

$$\frac{dU_B}{dt} = \frac{1}{2\mu_0} \int_V \mathbf{B} \cdot \frac{d\mathbf{B}}{dt} + \frac{d\mathbf{B}}{dt} \cdot \mathbf{B} dV = \frac{1}{\mu_0} \int_V \mathbf{B} \cdot \frac{d\mathbf{B}}{dt} dV \quad (2.48)$$

Equation 2.33 is then substituted for $d\mathbf{B}/dt$,

$$\frac{dU_B}{dt} = \frac{1}{\mu_0} \int_V \mathbf{B} \cdot (\nabla \times (\mathbf{v} \times \mathbf{B}) - \nabla \times (\eta \nabla \times \mathbf{B})) dV \quad (2.49)$$

The following equation can be derived from this by using a vector identity and substituting for current,

$$\frac{dU_B}{dt} = - \int \frac{j^2}{\sigma} dV - \int \mathbf{v} \cdot (\mathbf{j} \times \mathbf{B}) dV \quad (2.50)$$

2. THEORY OF MAGNETIC FIELDS IN A PLASMA

The left term represents energy lost through the dissipation of currents. This is also known as ohmic or Joule heating. The right term represents energy lost through work done on the plasma by the Lorentz force.

In addition to separating magnetic energy losses into components, the same can be done with magnetic forces. Combining Equation 2.29 and the Lorentz force in Equation 2.43 we can write,

$$F_L = \frac{(\nabla \times \mathbf{B}) \times \mathbf{B}}{\mu_0} \quad (2.51)$$

Using a vector identity ($(\mathbf{C} \times \mathbf{B}) \times \mathbf{A} = \mathbf{A} \times (\mathbf{B} \times \mathbf{C})$) this can be rewritten,

$$F_L = \frac{\mathbf{B} \times (\mathbf{B} \times \nabla)}{\mu_0} \quad (2.52)$$

The force can then be split into two components using Equation 2.34,

$$F_L = \underbrace{-\nabla \frac{B^2}{2\mu_0}}_{\text{pressure}} + \underbrace{\frac{1}{\mu_0}(\mathbf{B} \cdot \nabla)\mathbf{B}}_{\text{tension}} \quad (2.53)$$

Thus, the Lorentz force has a component acting perpendicular to the field, magnetic pressure¹, and a component acting along the field, magnetic tension. These forces can conveniently be attributed to many dynamic phenomena independently. Magnetic pressure is attributed to the apparent expansion of coronal loops as they reach higher into the atmosphere, while tension explains the restoring force that allows a coronal loop to spring back into place after it is disturbed by an external force.

The dominance of fluid forces over electrodynamic forces can be determined from the ratio of gas pressure to magnetic pressure,

$$\beta = \frac{P_G}{P_B} = \frac{nk_B T}{B^2/2\mu_0} \quad (2.54)$$

¹The magnetic pressure, $B^2/2\mu_0$ is numerically equivalent to the magnetic energy density.

2.3 Magnetohydrodynamics

In the solar interior $\beta \gg 1$ and magnetic fields dynamics are dominated by plasma motions, while in the corona $\beta \ll 1$ and magnetic fields determine plasma motion. In sunspots $\beta \sim 1$, and the dynamics become very complicated.

Magnetic tension and pressure are restoring forces that allow oscillations to take place along magnetic field lines. There are several types of waves that may occur. Alfvén waves are incompressible transverse waves and only involve magnetic tension. The plasma motion due to the waves occurs perpendicularly to the wave vector and the magnetic field. The “group” speed at which Alfvén wave energy travels along field lines is the Alfvén speed,

$$v_A = \frac{B}{\sqrt{\mu_0 \rho}} \quad (2.55)$$

When the ratio of gas to magnetic pressure, $\beta \ll 1$, then $v_A \gg v_s$. The phase speed of the wave pattern is given by,

$$\frac{\omega}{k} = \pm v_A \cos \theta, \quad (2.56)$$

where ω is the angular frequency of the wave, k is the wave vector, and θ is the angle between B and k . Alfvén waves allow for energy to be transported into the corona, as they are not affected by the acoustic cut-off frequency. They are thought to be partially responsible for the fast solar wind.

Magnetoacoustic waves come in two forms: “fast” and “slow”. Fast waves propagate isotropically and are governed by magnetic pressure in media where $\beta \ll 1$ or by gas pressure when $\beta \gg 1$. The phase speed is given by,

$$v_{p,f} = \frac{\omega}{k} = \left(\frac{1}{2}(v_A^2 + v_s^2) + \frac{1}{2}\sqrt{(v_A^2 + v_s^2)^2 - 4v_A^2 v_s^2 \cos^2 \theta} \right)^{1/2}, \quad (2.57)$$

where v_s is the speed of sound in the plasma. For waves propagating parallel to \mathbf{B} , $v_{p,f} = v_A$ or perpendicular to \mathbf{B} , $v_{p,f} = \sqrt{v_A^2 + v_s^2}$. Slow waves mostly propagate along \mathbf{B} and are governed by gas pressure when $\beta \ll 1$ or magnetic tension when $\beta \gg 1$.

2. THEORY OF MAGNETIC FIELDS IN A PLASMA

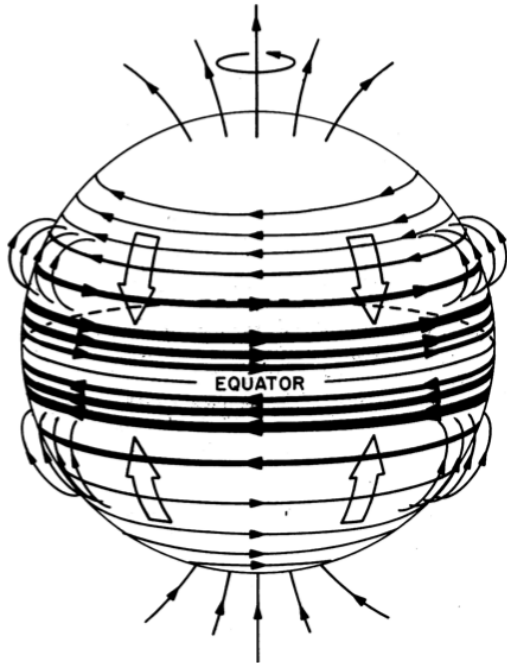


Figure 2.1: A schematic of the large-scale magnetic fields generated by the solar hydromagnetic dynamo. The thick lines represent bands of migrating toroidal flux in the convection zone. Thinner lines represent the ambient toroidal and poloidal field (from 147).

Their phase speed is given by,

$$v_{p,s} = \frac{\omega}{k} = \left(\frac{1}{2}(v_A^2 + v_s^2) - \frac{1}{2}\sqrt{(v_A^2 + v_s^2)^2 - 4v_A^2 v_s^2 \cos^2 \theta} \right)^{1/2} \quad (2.58)$$

For waves propagating parallel to \mathbf{B} , $v_{p,s} = v_s$. They do not propagate perpendicular to \mathbf{B} .

2.4 Dynamo Theory

An important question in solar physics is how the large-scale magnetic field is generated. It is observed to change configuration over the solar cycle, so it must be time dependent. Also, sunspots are thought to be a manifestation of the large-scale field. The underlying process, responsible for the dynamic solar magnetic field and driven by internal flows,

2.4 Dynamo Theory

is called the dynamo.

In general, the main goal of a dynamo theory is to solve the induction equation (Equation 2.36) for a given velocity and magnetic field. Assuming a velocity field within the Sun due to large-scale flows,

$$v(r, \theta) = \underbrace{\mathbf{u}_p(r, \theta)}_{\text{meridional}} + \underbrace{\bar{\omega}\Omega(r, \theta)\hat{e}_\phi}_{\text{rotational}}, \quad (2.59)$$

where \mathbf{u}_p is the meridional (poloidal) flow, $\bar{\omega} = r \sin \theta$, and Ω is the solar rotation, a differential toroidal flow that varies with depth and latitude. The magnetic field can be broken into a poloidal and toroidal component,

$$\mathbf{B}(r, \theta, t) = \underbrace{\nabla \times (A(r, \theta, t)\hat{e}_\phi)}_{\text{poloidal}} + \underbrace{B(r, \theta, t)\hat{e}_\phi}_{\text{toroidal}}, \quad (2.60)$$

where A and B are scalar functions that determine the field components. While the magnetic field varies with time, the large-scale flows are assumed to be static. Combining Equation 2.36, 2.59, and 2.60 we have a differential equation for the poloidal and toroidal components of the magnetic field,

$$\frac{\partial A}{\partial t} = \eta \left(\nabla^2 - \frac{1}{\bar{\omega}^2} \right) A - \frac{\mathbf{u}_p}{\bar{\omega}} \cdot \nabla(\bar{\omega}A), \quad (2.61)$$

and,

$$\frac{\partial B}{\partial t} = \eta \left(\nabla^2 - \frac{1}{\bar{\omega}^2} \right) B + \frac{1}{\bar{\omega}} \frac{\partial \bar{\omega}}{\partial r} \frac{\partial \eta}{\partial r} - \bar{\omega} \nabla \cdot \left(\frac{B}{\bar{\omega}} \mathbf{u}_p \right) + \underbrace{\bar{\omega} (\nabla \times (A \hat{e}_\phi)) \cdot \nabla \Omega}_{\text{shear term}} \quad (2.62)$$

where η is the magnetic diffusivity. The shear term generates the toroidal field with a strength $\propto \nabla \Omega$.

Crowling's theorem says that an axisymmetric flow cannot generate an axisymmetric magnetic field. Also, a field with an electric current limited to a finite volume cannot

2. THEORY OF MAGNETIC FIELDS IN A PLASMA

be maintained by a flow with finite amplitude. The fields decay because of the finite conductivity (magnetic diffusivity term). Because of this, most dynamo models use an extraneous source term to initialise the field.

(144) finds oscillatory solutions to Equations 2.103 and 2.62 in rectilinear coordinates that result in equatorward propagating dynamo waves. The waves take the form of bands of toroidal flux and are thought to explain the equatorward progression of sunspot group emergence over the solar cycle. A schematic of the process is shown in Figure 2.1. This result led to the formulation of many other dynamo models (35).

In the “mean-field” model, small scale turbulence leads to macroscopic fields. This leads to another term in Equation 2.36 that is related to the curl of an electromotive force generated by the combination of the Coriolis force (large scale) and turbulent diffusion (small scale). The electromotive force is given by,

$$\varepsilon = \alpha \mathbf{B} + \beta \nabla \times \mathbf{B}, \quad (2.63)$$

where α is proportional to (negative) kinetic helicity and β is related to turbulent diffusion. Here, α is a coefficient of the source term that results in the “ α -effect” where,

$$\alpha = -\frac{1}{3}\tau_c \langle \mathbf{v}' \cdot (\nabla \times \mathbf{v}) \rangle, \quad (2.64)$$

in units of m s^{-1} , where \mathbf{v}' represents turbulent flows, \mathbf{v} represents large-scale flows, and τ_c is the correlation time scale for the diffusion. The coefficient governing the turbulent source term is given by,

$$\beta = \frac{1}{3}\tau_c \langle \mathbf{v}'^2 \rangle, \quad (2.65)$$

in units of $\text{m}^2 \text{ s}^{-1}$. The time scale governing turbulent diffusion is,

$$\tau_{diff} = \frac{R_\odot^2}{\eta_e}, \quad (2.66)$$

where η_e is the diffusivity, dominated by turbulence, rather than microscopic magnetic diffusion. Assuming a η_e of $10^8 \text{ m}^2 \text{s}^{-1}$ and a length scale of 10^8 m , the turbulent decay time scale for the Sun is ~ 3 years, which is of the same order of magnitude as the solar cycle length. Equation 2.64 and 2.65 can be used to determine new equations for $\partial A/\partial t$ and $\partial B/\partial t$, with terms relating to magnetic induction due to the α -effect and the “ Ω -effect” (determined by the rotation of the convective zone), and magnetic diffusivity.

A simplified model, the “linear α - Ω dynamo” neglects the meridional flow. Linear equations for B and A can be obtained leading to a dynamo wave equation. The direction of the waves is determined by,

$$\mathbf{s} = \alpha \nabla \Omega \times \hat{\mathbf{e}}_\phi, \quad (2.67)$$

where Ω is the differential rotation profile and α is a coefficient determining the strength of the α -effect, as before. At the high-latitude regions of the tachocline, $\nabla \Omega$ points radially inward. With a positive α this results in an equatorward dynamo wave propagation.

There are also phenomenological models that reproduce the Babcock-Leighton dynamo, as discussed in Section 1.8. (112) first explored this numerically and more complete models followed (138). Here, the toroidal bands of magnetic flux erupt as localised dipoles. These dipoles are an artificial source term introduced to Equation 2.103. This usually takes the form of a function with a prescribed operating range of toroidal magnetic field strengths. This means that once the critical field strength is reached, dipoles rise toward the surface through magnetic buoyancy. Also, the α -effect causes a rotation in the dipoles due to the Coriolis force, in which kinetic helicity is acquired ($H_k = \omega \cdot \mathbf{v}$).

2. THEORY OF MAGNETIC FIELDS IN A PLASMA

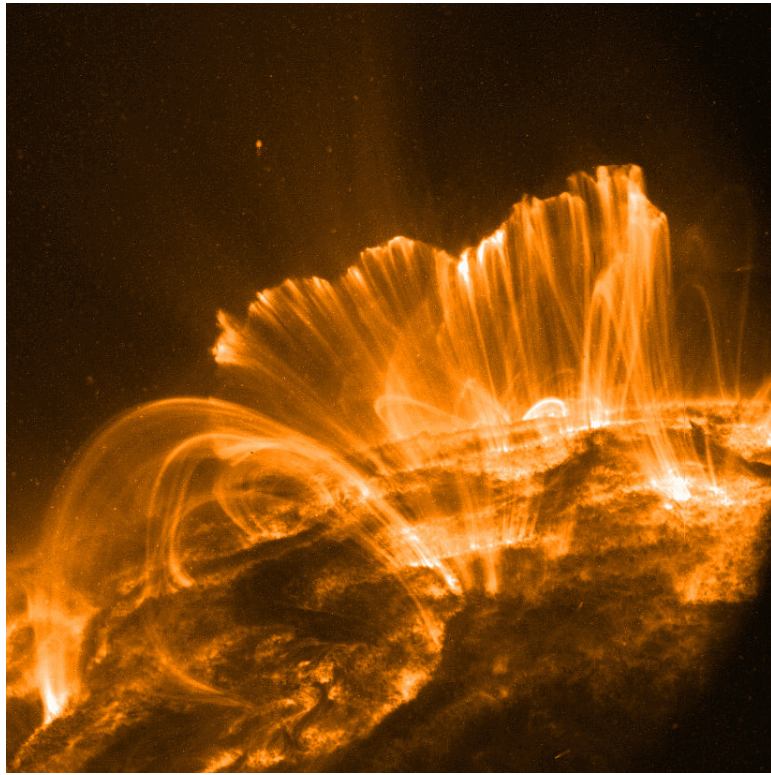


Figure 2.2: An EUV image of coronal loops in an active region (from 157).

This rotation is the underlying reason for Joy's Law of sunspot tilt. After emerging at the surface, the dipoles begin to decay as their fields are dispersed by supergranulation. Net (signed) flux is dragged poleward from dipoles by the meridional flow. This process rearranges toroidal fields (dipoles) into poloidal fields and is described in more detail in Section 1.8.1. The development of these models still has a long way to go, as the necessity for artificial sources implies. Furthermore, it is still not possible to predict the strength of the next solar cycle. For instance, the extended minimum of cycle 23–24 was quite unexpected.

2.5 Magnetic Fields in the Corona

A magnetic field line is a curve tangent to the magnetic field at each point and is described by,

$$\frac{d\mathbf{r}}{d\ell} = \frac{\mathbf{B}(\mathbf{r}(\ell))}{|\mathbf{B}(\mathbf{r}(\ell))|}, \quad (2.68)$$

where \mathbf{r} is a vector pointing from the origin to a point along the line and ℓ is the arc length along the line. A given line can be determined by integrating the equation from a given starting point. While field lines are not an actual physical entity, they are useful in describing the magnetic field topology of a given system. The density of field lines indicates the magnetic field magnitude in a given region.

A coronal loop is often modeled as a thin magnetic flux-tube, composed of a bundle of individual filaments. Since magnetic pressure should cause the loop to expand, the loop is thought to be twisted, causing magnetic tension to resist the expansion. Coronal loops are rooted in the photosphere at either end, forming a closed field geometry. An extreme ultraviolet (EUV) image of coronal loops within an active region is shown in Figure 2.2. In the photosphere, a flux-tube is in magnetohydrostatic equilibrium, where the internal magnetic and gas pressure balances the external gas pressure. In the photosphere, flux tubes are constantly swept into down-draft regions between supergranules (188). Within flux tubes, flows are confined to the direction of the field and this leads to an evacuation of the flux-tube. These flows are shown to be $>250 \text{ m s}^{-1}$ (190). Since magnetic flux is frozen-in and total flux through a surface is conserved, any increase in external gas pressure leads to a compression of the flux-tube and results in an increase in the internal magnetic field. This process is called convective collapse (161). A schematic of this situation is shown in Figure 2.3.

In active regions with simple configurations, coronal loops are often observed to be stable structures on the scale of τ_{adv} (Equation 2.37). Above the photosphere, flux-tubes expand, as the ambient gas pressure drops off with height. This occurs rapidly

2. THEORY OF MAGNETIC FIELDS IN A PLASMA

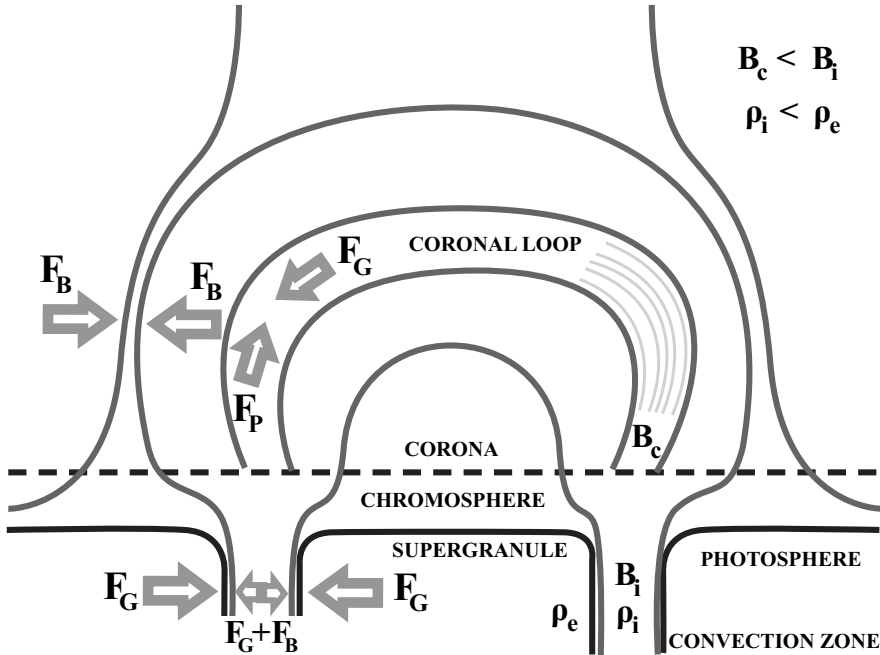


Figure 2.3: A schematic of a coronal loop, with its foot points located at down-flow regions between supergranules. The combination of gas and magnetic pressure within flux-tubes at the photosphere are balanced by exterior gas pressure. In the corona, the gas pressure drops off, leaving the magnetic pressure and tension forces to define structures. Hydrostatic equilibrium is achieved along the curve of a coronal loop.

within the chromosphere and more slowly in the corona as the pressure gradient levels off until the magnetic forces are in equilibrium. In the corona, $\beta \ll 1$ so plasma is confined to flow parallel to the field lines. A given coronal loop exhibits hydrostatic equilibrium along its curvature. Coronal loops are bright because they are hot and heating may be due to small flares (DC) or waves (AC) along the loop (157).

The magnetic properties of coronal loops can be determined by extrapolating the magnetic field from magnetogram observations and comparing the result to loop observations. To obtain a static solution, the sum of forces included in Equation 2.43 cancel out,

$$\sum F = -\nabla P + \mathbf{j} \times \mathbf{B} + \rho \mathbf{g} = 0 \quad (2.69)$$

Additionally, the “force-free” approximation is used, where each force is assumed to be

2.5 Magnetic Fields in the Corona

negligible. Dimensional analysis shows the gravitational force is small compared to the pressure force. The pressure gradient is not important if scales are considered that are much less than the pressure scale height ($H = k_B T / \bar{\mu} m_H g$), the distance over which the pressure drops by $1/e$. Since $\beta \ll 1$, the Lorentz force dominates over the other forces,

$$0 = -\nabla P + \mathbf{j} \times \mathbf{B} + \rho \mathbf{g}, \quad (2.70)$$

$$0 = \mathbf{j} \times \mathbf{B} \quad (2.71)$$

Two solutions to this are $\mathbf{j} = 0$ or that $\mathbf{j} \parallel \mathbf{B}$. In the former case, from Equation 2.29 this leads to,

$$\nabla \times \mathbf{B} = 0, \quad (2.72)$$

which is the current-free solution and results in “potential fields” that are curl and divergence free. For the latter case, the currents are field-aligned and Equation 2.29 can be written,

$$\nabla \times \mathbf{B} = \mu_0 j \hat{\mathbf{B}} = \alpha B \hat{\mathbf{B}}, \quad (2.73)$$

$$\nabla \times \mathbf{B} = \alpha \mathbf{B}, \quad (2.74)$$

where α is a scalar derived from Equation 2.73,

$$\alpha = \frac{j \mu_0}{B} \quad (2.75)$$

These fields can be “non-potential” and result in a twist in the field.

For the potential case, α is set to 0,

$$\nabla \times \mathbf{B} = 0, \quad (2.76)$$

2. THEORY OF MAGNETIC FIELDS IN A PLASMA

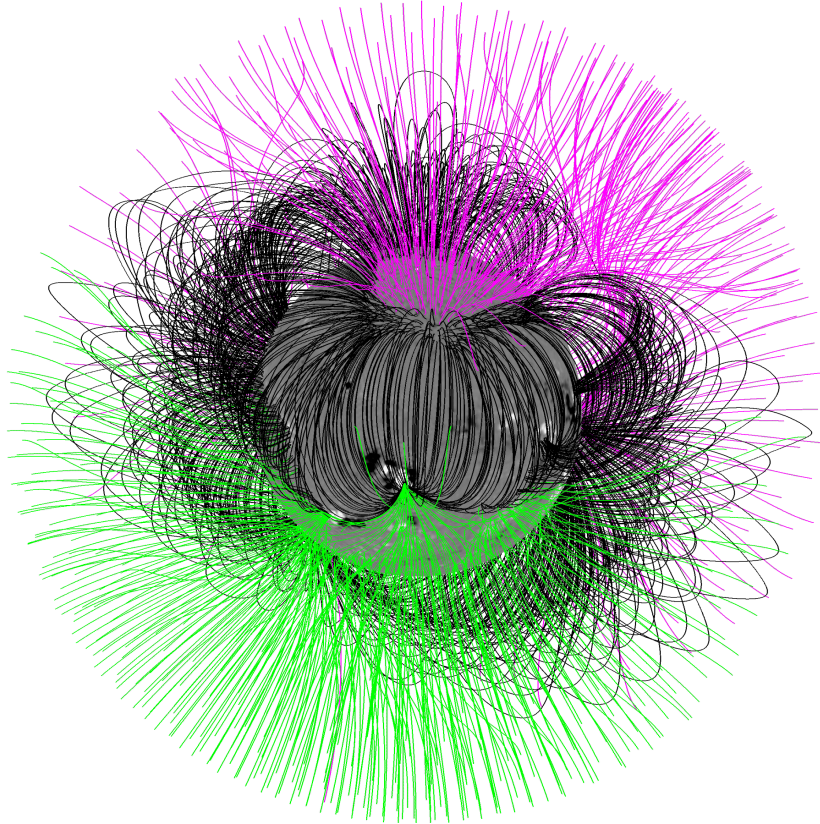


Figure 2.4: An example of a spherical potential field source surface extrapolation using MDI line-of-sight magnetograms as input (courtesy of Marc DeRosa). Field lines are traced separately for closed (black), positive open (out of the Sun; green), negative open (into the Sun; magenta).

so \mathbf{B} can be written as the gradient of some scalar potential field,

$$\mathbf{B} = \nabla \Psi \quad (2.77)$$

It can be seen that Ψ satisfies Laplace's equation by taking the divergence of both sides of Equation 2.77,

$$\nabla \cdot \mathbf{B} = \nabla \cdot \nabla \Psi, \quad (2.78)$$

$$\nabla \cdot \mathbf{B} = 0, \quad (2.79)$$

$$\therefore \nabla^2 \Psi = 0 \quad (2.80)$$

2.5 Magnetic Fields in the Corona

A solution to Equation 2.80 in spherical coordinates is the superposition of a series of spherical harmonics,

$$\Psi(r, \theta, \phi) = \sum_{\ell, m} \left(A_\ell^m r^\ell + B_\ell^m r^{-(\ell+1)} \right) Y_\ell^m(\theta, \phi), \quad (2.81)$$

where r is the radius from solar centre, A_ℓ^m and B_ℓ^m are coefficients determining the importance of each harmonic, and $Y_\ell^m(\theta, \phi)$ are the pure harmonic modes. The subscripts m and ℓ define the number of sectors in the longitudinal ($n_\phi = m + 1$) and latitudinal ($n_\theta = \ell + 1$) directions, respectively. The spherical harmonics are given by,

$$Y_\ell^m(\theta, \phi) = C_m^\ell P_m^\ell(\cos \theta) e^{im\phi}, \quad (2.82)$$

where $P_m^\ell(\cos \theta)$ are the Legendre polynomials and,

$$C_m^\ell = (-1)^m \left[\frac{2\ell + 1}{4\pi} \frac{(\ell - m)!}{(\ell + m)!} \right]^{1/2} \quad (2.83)$$

The boundary conditions are chosen so that at $r = R_\odot$, the magnetic field is determined by line-of-sight (LOS) magnetic field observations and an upper boundary is determined by an arbitrary “source surface” where the field becomes radial. Conventionally, this is usually $2.5 R_\odot$. These conditions stipulate a unique solution for the field. The coefficients can be solved by substituting Equation 2.81 into Equation 2.77 and applying the boundary conditions. An example spherical extrapolation¹ using potential field assumptions is shown in Figure 2.4; this is called a potential field source surface (PFSS) extrapolation.

If $\alpha \neq 0$ in Equation , then field aligned currents may exist. Taking the divergence of Equation ,

$$\nabla \cdot (\nabla \times \mathbf{B}) = \nabla \cdot (\alpha \mathbf{B}) = 0, \quad (2.84)$$

¹From <http://www.lmsal.com/~derosa/pfsspack/#usersguide>.

2. THEORY OF MAGNETIC FIELDS IN A PLASMA

due to the solenoidal constraint. So, the gradient of α along \mathbf{B} can not vary. Thus, a property of α is that it must be constant along a given field line, but can vary between field lines. Making the assumption that α is constant over all space,

$$\nabla^2 \mathbf{B} = -\alpha^2 \mathbf{B}, \quad (2.85)$$

can be derived. This relation defines a “linear force-free” field. If α is not assumed constant over all space,

$$\nabla^2 \mathbf{B} + \alpha^2 \mathbf{B} = \mathbf{B} \times \nabla \alpha, \quad (2.86)$$

and

$$\mathbf{B} \cdot \nabla \alpha = 0, \quad (2.87)$$

define the field. A field defined by these relations is termed “non-linear force-free”.

2.6 Magnetic Reconnection

Solar flares result in a rapid change in the 3D magnetic field topology of an active region. Over the course of a large flare there is often an observable transition from a stressed to a simpler and more relaxed field configuration. A schematic of this transition is shown in Figure 2.5. A common situation involves filament material suspended above sheared fields becoming unstable and lifting off or erupting.

There are a number of possible instabilities that could result within coronal magnetic structures and trigger a flare. The tearing mode instability results when the magnetic gradient within a small region becomes sufficiently large. The magnetic energy within strongly sheared magnetic fields is converted by ohmic heating due to currents. A kink instability results when a long flux tube’s azimuthal magnetic field becomes large enough, compared to the magnetic field along its length. Depending on the type of magnetic field (i.e., linear force-free, non-linear force-free, etc.) the kink instability

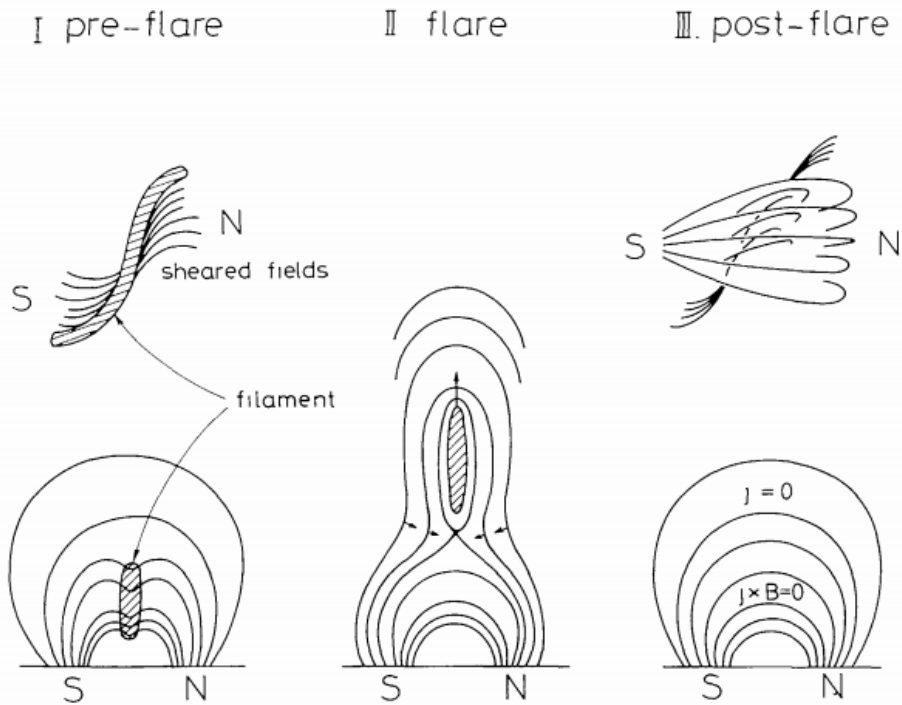


Figure 2.5: A cartoon illustrating the change in magnetic field configuration over the course of a flare (from 201).

can occur after $1.65 - 3$ turns. A pressure difference between the inner and outer parts of the kink enhances the instability.

A common cartoon used to explain how flares are driven assumes that at the heart of the eruption is a region where fields of opposite orientation are compressed and form an “X-point” and a strong current sheet, denoted by the thick line at the centre of the X, as shown in panel A of Figure 2.6. At some point this current sheet becomes unstable due to an instability (i.e., tearing mode) that causes the plasma resistivity to increase. Currents in the localised region are sufficiently large that the region surrounding the X-point is rapidly heated. The breakage of field lines within the “diffusion region” of the current sheet allows the change in magnetic topology. In the end, magnetic energy is released in the resistive dissipation of the current sheet and the acceleration of electrons out of the diffusion region.

2. THEORY OF MAGNETIC FIELDS IN A PLASMA

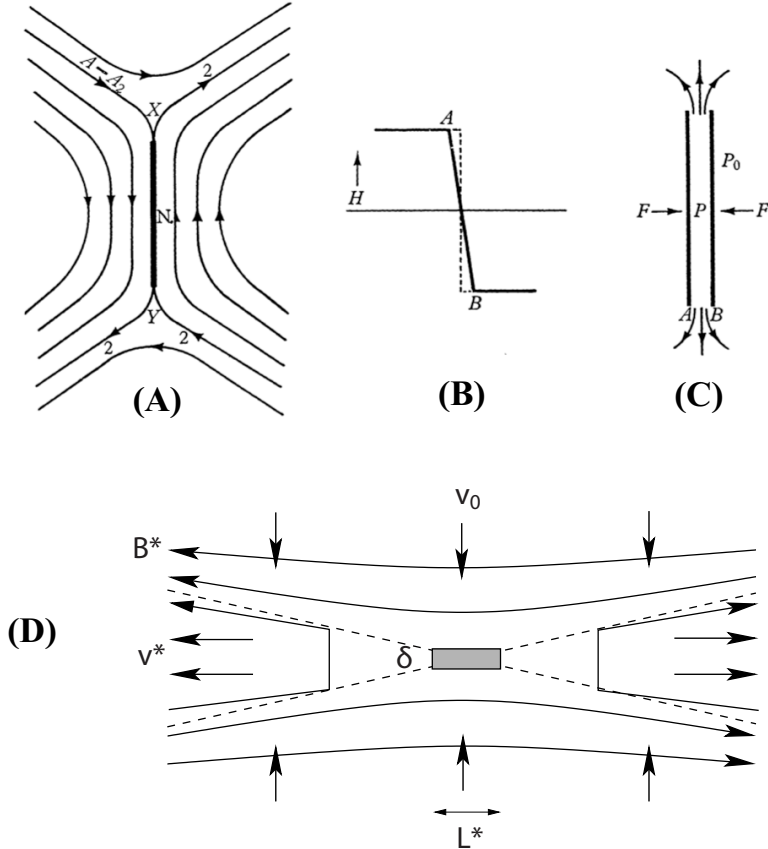


Figure 2.6: A schematic of magnetic reconnection. Panels *A*–*C* show the 2D “x-point” magnetic field configuration, a cross-section of the field across the current sheet, and the fluid flow directions for Sweet-Parker reconnection (from 200). Panel *D* shows the contracted current sheet in the centre and the shocks at the left and right outflow regions of the “x-point” in Petzschel reconnection (from 63).

In 2D Sweet-Parker reconnection (146; 200), plasma flows perpendicularly into the diffusion region along the x-axis and flows out parallel to it along the y-axis, as shown in panel *C* of Figure 2.6. The outflow length-scale is much smaller than the inflow length-scale. The z-axis is oriented out of the page. The magnetic field orientation and strength across the current sheet is shown in panels *B* and *C*.

The inflow speed of the plasma is approximated by $\mathbf{E} \times \mathbf{B}$ drift,

$$v_{in} \sim \frac{E_z}{B_y}, \quad (2.88)$$

2.6 Magnetic Reconnection

where the electric field is perpendicular to the diffusion region (into the page) and the magnetic field is parallel to it. The electric field can be approximated from Ohm's law,

$$E_z \sim \frac{\eta B_y}{\mu_0 \delta}, \quad (2.89)$$

where δ is the width of the outflow region and η is the magnetic diffusivity. Assuming the flows are incompressible, the flow speeds and length scales can be related using the mass continuity equation,

$$Lv_{in} \sim \delta v_{out}, \quad (2.90)$$

where L is the length-scale of the inflow region, v_{out} is the outflow speed. Assuming that the magnetic pressure in the outflow region is balanced by the gas pressure, the fluid equation of motion can be used to obtain:

$$\rho v_{out}^2 \sim \frac{B^2}{2\mu_0} \quad (2.91)$$

The outflow speed can then be approximated by the Alfvén speed ($v_{out} \sim v_A$), leading to a Mach number for the inflow speed,

$$M_{in} = \frac{v_{in}}{v_A} \quad (2.92)$$

The Lundquist number is roughly equivalent to the magnetic Reynolds number (as defined in Equation 2.25) and indicates the ratio of the strength of advection to diffusion of the magnetic field,

$$L_u = \frac{\mu_0 L v_A}{\eta}, \quad (2.93)$$

where v_A is the Alfvén speed. This can be written in terms of the Alfvén Mach number,

$$L_u = M_{in}^{-2} \quad (2.94)$$

2. THEORY OF MAGNETIC FIELDS IN A PLASMA

In solar flares L_u is estimated to be $\sim 10^8$, L is ~ 10 Mm, and v_A is ~ 100 km s $^{-1}$. This leads to time scales of tens of days, which is much greater than actual flare time scales of minutes to hours. Sweet-Parker reconnection is too slow to account for flares due to the size of the Lundquist number in the corona.

(152) was able to increase the reconnection rate by finding a way to decrease the current sheet length and allowing a shock at each end of the x-point, where outflow occurs. This field and flow configuration is shown in panel *D* of Figure 2.6. Processes within the current sheet are the same as in the Sweet-Parker model. While the width and speed of the outflow region is the same as Sweet-Parker, the length of the diffusion region is now determined from mass continuity, assuming an incompressible flow,

$$L_P = \frac{\delta}{M_{in}} \quad (2.95)$$

A maximum rate of reconnection can be derived, above which no Petschek solutions exist,

$$M_{in,max} = \frac{\pi}{8 \ln(L_u)}, \quad (2.96)$$

and is generally orders of magnitude greater than the Sweet-Parker rate. While this solves the time-scale problem of Sweet-Parker, the model has never been successfully proven using self-consistent numerical simulations. On the other hand, Sweet-Parker reconnection has been successfully simulated and has also been observed in lab plasmas.

These models are both 2D and steady-state, which is obviously limiting since flares are very much time dependent and occur in 3D. Time-dependent 2D models have been considered, such as those relying on the tearing-mode instability within current sheets (65). More realistic models have also been explored by running numerical simulations in 3D (225). The precise mechanism for the release of magnetic energy during flares is still a major problem in solar physics.

2.7 Quantifying Magnetic Fields at the Solar Surface

The work described throughout this thesis is concerned with investigating the nature of magnetic features observed at the solar surface. To study them, we must physically characterise them. In this section we summarise some physical properties that can be used to characterise the fields of solar features at the solar surface.

Magnetic flux quantifies the amount of magnetic field normal to an open surface,

$$\Phi = \int_S \mathbf{B} \cdot d\mathbf{A} \quad (2.97)$$

The magnetic area is defined by determining a boundary around strong magnetic field regions. This boundary is determined using image processing methods outlined in Chapter 4.

In this work we assume the magnetic field direction to be perpendicular at the solar surface. Since we are using LOS magnetic field observations, the inclination of the true field vector to the magnetic surface is not known. In weak-field plage regions and sunspot umbrae the field vector is mostly perpendicular at the surface, while in penumbrae, it is significantly inclined. Considering the schematic shown in Figure 2.3, plage flux tubes are compressed between vertical supergranule downdrafts; above the surface the fields expand parallel to the surface, in all directions. However, this happens above the $\tau = 1$ surface where the fields are measured, as shown in Figure 1.14. This assumption is not completely accurate; during a flare the inclination of plage fields has been shown to change by $\sim 10^\circ$ (137). The fields also expand outward above the surface of sunspots, so that umbrae are held vertical by a combination of magnetic pressure and tension. But around the periphery, the lack of magnetic pressure allows penumbrae to turn over. The larger penumbral field strengths, as compared plage, cause this to happen below the $\tau = 1$ surface. The perpendicular field assumption leads to a significant underestimate of flux in penumbral regions near disk center. Near

2. THEORY OF MAGNETIC FIELDS IN A PLASMA

the limb, the disk-ward portion of a sunspot's penumbra will point generally along the LOS and the limb-ward portion will point generally away from it. This results in two opposing effects which act to cancel each other. This often results in a false North-South polarity separation line to be observed within the sunspot.

While the total flux observed at the photosphere may change with time, the net flux must be conserved due to the solenoidal constraint: there are no macroscopic magnetic monopoles¹,

$$\nabla \cdot \mathbf{B} = 0 \quad (2.98)$$

Net flux is defined as the sum of positive and negative flux,

$$\Phi_{\text{net}} = \Phi_+ + \Phi_- = \int \mathbf{B}_+ \cdot d\mathbf{A} + \int \mathbf{B}_- \cdot d\mathbf{A}, \quad (2.99)$$

where \mathbf{B}_+ is positive magnetic field and \mathbf{B}_- is negative magnetic field. Locally on the Solar surface, non-zero positive (negative) net flux may exist as they may be connected to far-away negative (positive) flux concentrations, or may be quasi-open and balanced by non-local quasi-open negative (positive) flux concentrations.

Since net flux is conserved, the polarity-preferential transport of flux to high latitudes necessarily results in a local Φ_{net} at lower latitudes. A fractional measure of Φ_{net} , flux imbalance, is given by,

$$\Phi_{\text{imb}} = \frac{\Phi_{\text{net}}}{\Phi_{\text{tot}}} \quad (2.100)$$

A Φ_{imb} of zero is a region of equal parts Φ_+ and Φ_- , while Φ_{imb} of unity is a region of completely unipolar flux.

While flux imbalances have implications for the global magnetic field configuration, helicity has implications for flare potential energy. It can indicate the amount

¹See: Mengotti *et al.* (129) for evidence of nano-scale magnetic monopoles.

2.7 Quantifying Magnetic Fields at the Solar Surface

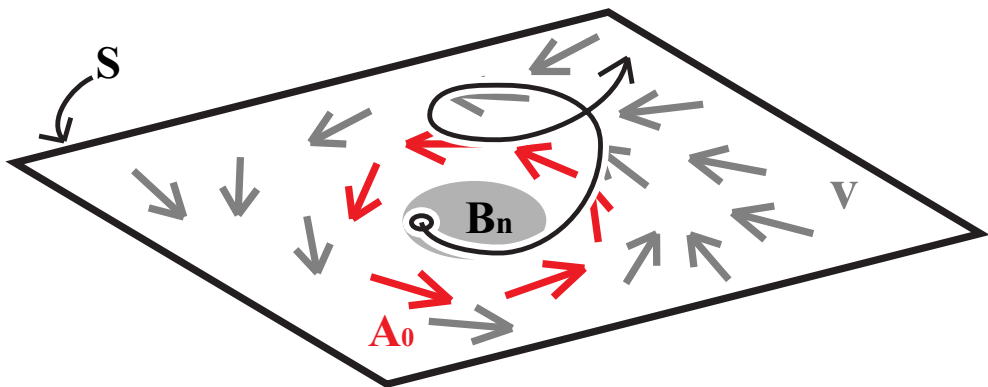


Figure 2.7: A schematic of a sunspot exhibiting helical magnetic fields (large curved black arrow) extending through the photosphere and into the corona. The gray circle represents the vertical sunspot magnetic field, while the red arrows show its vector potential field at the boundary of the sunspot. The gray arrows indicate the surface flow field.

of rotation in the magnetic field of a particular feature; a large twist indicates that a feature is highly non-potential, as discussed in Section 2.5. Non-potential fields can carry currents, which are important for flaring, as discussed in Section 2.6.

Active regions are often composed of a flux rope with constituent sunspots indicating the interface between the flux rope and the photosphere. As such, sunspots are often observed to have twisted magnetic fields and a rapid rotation (up to 200° in 3–5 days; 26). It is not known whether the apparent rotation is due to the 3D flux rope rigidly passing through the solar surface as it emerges or remaining vertically stationary but exhibiting a change in twist due to magnetic or fluid forces.

Helicity is used to quantify the amount of twist the magnetic field contains. Total helicity is defined as,

$$\mathcal{H} = \int_V \mathbf{A} \cdot \mathbf{B} dV, \quad (2.101)$$

where \mathbf{A} is the vector potential of the magnetic field and is defined by,

$$\mathbf{B} = \nabla \times \mathbf{A} \quad (2.102)$$

The vector field \mathbf{A} has the property that the gradient of an arbitrary scalar field can be

2. THEORY OF MAGNETIC FIELDS IN A PLASMA

added to it and the resulting \mathbf{B} will not be altered. This is called a gauge transformation and can simplify certain problems. Provided that the magnetic field normal to the surface of the integrated volume vanishes, \mathcal{H} is unaffected by the transformation. For ideal MHD, plasma motions can be related to \mathbf{A} by,

$$\frac{\partial \mathbf{A}}{\partial t} = \mathbf{v} \times \mathbf{B} \quad (2.103)$$

Figure 2.7 shows a schematic of a sunspot with twisted magnetic fields in the presence of a helical flow field. Total helicity increases with the amount of magnetic field aligned with the vector potential field (shown by the red arrows).

Helicity can also be written as the sum of the “writhe” and “twist” in the field, weighted by flux,

$$\mathcal{H} = \Phi^2(T_{\mathcal{H}} + W_{\mathcal{H}}),. \quad (2.104)$$

Topographically, twist can be thought of as the number of turns in a helical field in a given volume and writhe can be explained by the number times a field line crosses over itself when viewed from a particular direction.

It can then be shown that the time derivative of \mathcal{H} is 0 by substituting Equation 2.39 and 2.103 into 2.101,

$$\frac{\partial \mathcal{H}}{\partial t} = \int_V \frac{\partial}{\partial t} \mathbf{A} \cdot \mathbf{B} dV, \quad (2.105)$$

$$= \int_V \mathbf{B} \cdot \frac{\partial \mathbf{A}}{\partial t} + \mathbf{A} \cdot \frac{\partial \mathbf{B}}{\partial t} dV, \quad (2.106)$$

$$= \int_V \cancel{\mathbf{B} \cdot (\mathbf{v} \times \mathbf{B})} + \mathbf{A} \cdot (\nabla \times \mathbf{v} \times \mathbf{B}) dV, \quad (2.107)$$

$$= \int_V \cancel{\mathbf{A} \cdot (\nabla \times \frac{\partial \mathbf{A}}{\partial t})} dV = 0 \quad (2.108)$$

Thus, the total magnetic helicity in a closed volume is conserved, provided that the

2.7 Quantifying Magnetic Fields at the Solar Surface

field is only subjected to plasma flows and infinite conductivity is assumed. Regardless, \mathcal{H} cannot be measured in reality because the magnetic field throughout a volume of plasma on the Sun is not known. Additionally, there is no observable magnetic field structure on the Sun that has no normal component to a given closed volume.

To work around this problem, a “relative helicity” is defined, whereby the magnetic field can be normal to the boundaries of the volume,

$$\mathcal{H}_R = \int_V \mathbf{A} \cdot \mathbf{B} dV - \int_V \mathbf{A}_0 \cdot \mathbf{B}_0 dV \quad (2.109)$$

This can be rewritten as,

$$\mathcal{H}_R = \int_V (\mathbf{B} - \mathbf{B}_0) \cdot (\mathbf{A} + \mathbf{A}_0) dV \quad (2.110)$$

The vector fields are related by,

$$(\mathbf{B} - \mathbf{B}_0) \cdot \hat{\mathbf{n}} = 0, \quad (2.111)$$

and

$$(\mathbf{A} - \mathbf{A}_0) \times \hat{\mathbf{n}} = 0 \quad (2.112)$$

A gauge transformation is chosen to determine \mathbf{A}_0 and satisfy this equation.

Both plasma surface motions and the emergence of new flux can inject helicity (\mathcal{H}) into magnetic surface features. While the relative helicity itself cannot be measured, its time-rate of change, or helicity injection, can be determined by,

$$\frac{d\mathcal{H}_R}{dt} = 2 \int_S (\mathbf{v} \cdot \mathbf{A}_0) B_n da - 2 \int_S (\mathbf{B} \cdot \mathbf{A}_0) v_n da, \quad (2.113)$$

where the integrals are performed over a surface. The field B_n and v_n are the magnetic

2. THEORY OF MAGNETIC FIELDS IN A PLASMA

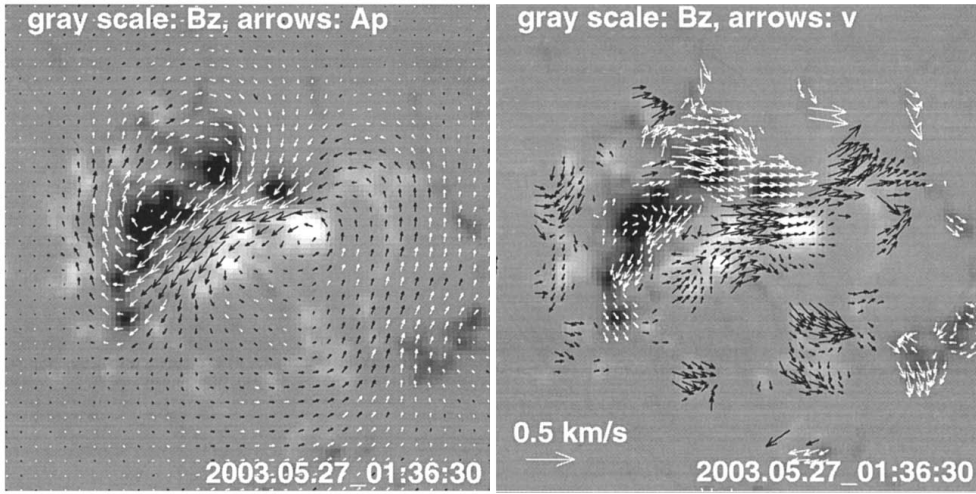


Figure 2.8: An image of evolving magnetic features with the superposed arrows indicating (left) the derived vector potential field and (right) the resulting surface flow field (from 33). The surface flow field vectors are only shown for regions above some magnetic strength (the author does not specify the value).

and velocity field components normal to the surface. Considering helicity injection into the corona from the photosphere, the equation can be rewritten in terms of discrete magnetic flux tubes,

$$\frac{d\mathcal{H}_R}{dt} = - \underbrace{\frac{1}{2\pi} \sum_i \phi_i^2 \omega_i}_{\text{spinning}} - \underbrace{\frac{1}{2\pi} \sum_i \sum_{j \neq i} \phi_i \phi_j \omega_{ij}}_{\text{braiding}}, \quad (2.114)$$

where ϕ_i and ϕ_j are a pair of flux tubes, ω_i is the angular rotation speed of the i th flux tube, and ω_{ij} is the angular rotation speed of the connecting line between the pair of flux tubes. The first term is called the spinning contribution, and results from the rigid rotation of individual magnetic flux elements. The second term is called the braiding helicity flux and results from pairs of flux elements circling around each other. Integrating over t then yields the total accumulated relative helicity, \mathcal{H}_R . Figure 2.8 shows a magnetogram with the vector potential and surface flow fields indicated by arrows.

2.7 Quantifying Magnetic Fields at the Solar Surface

The observed rotation of a sunspot group's polarity separation line (PSL) with respect to the line connecting the two main spots has been used as a proxy for helicity (135). Although it is much faster to calculate, this proxy is much less stable than the local correlation tracking (LCT) helicity injection calculation (32; 210). This is because far fewer points in an image are used. However, both bipole rotation and \mathcal{H}_R have both been shown to be important indicators of flare activity (33; 135).

2. THEORY OF MAGNETIC FIELDS IN A PLASMA

3

Instrumentation and Observations

In this chapter, the background theory and instrumentation used to obtain magnetic observations of solar surface features and the large scale solar magnetic field are explained. The Zeeman effect and the instruments that take advantage of it to image the LOS field are discussed. Also, the event lists used in Chapter 5 and a catalog of detected active regions used in Chapter 4 are described.

The investigations described throughout this thesis mainly rely on the analysis of data from two instruments designed to record images of the line-of-sight (LOS) strength in the solar photosphere and the feature and event lists. Section 3.1 includes a description of the theory behind the interaction between magnetic fields and light (Section 3.1.1), previous methods used to determine the LOS field (Section 3.1.2), the Michelson Doppler Imager (MDI) instrument (Section 3.1.3), and the Helioseismic Magnetic Imager (HMI) instrument (Section 3.1.3). Lastly, in Section 3.2, the X-ray

3. INSTRUMENTATION AND OBSERVATIONS

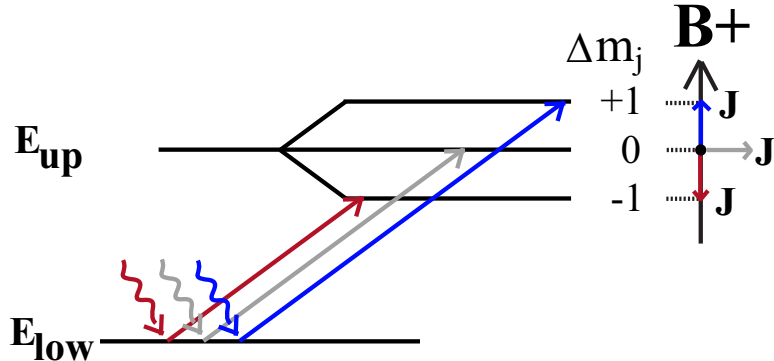


Figure 3.1: A schematic of the electron energy level splitting due to the Zeeman effect. Absorption lines are red shifted when \mathbf{J} is oriented opposite to \mathbf{B} , blue shifted when the \mathbf{J} and \mathbf{B} are aligned, and not shifted at all when the \mathbf{J} and \mathbf{B} are perpendicular to each other.

flare catalogs used to determine the activity of tracked sunspot groups and the NOAA active region catalog are described.

3.1 Solar Magnetic Field Observations

In this section the method by which magnetic fields are determined, and the instruments used to do so are described. The phenomena that allows one to determine the magnetic field of radiating material remotely, the Zeeman splitting of a spectral line, is put into theoretical context (Section 3.1.1). The basic experimental set-up used to measure Zeeman splitting on the Sun is described using historical examples (Section 3.1.2). Finally, the modern instruments used to magnetically image the photosphere of the Sun are described (Sections 3.1.3 and 3.1.4).

3.1.1 Zeeman Effect

In this section, we determine the effect that an external magnetic field has on radiating material. The presence of a magnetic field alters the energy of a particular atomic

3.1 Solar Magnetic Field Observations

energy state as given by,

$$H = H_0 + V_M , \quad (3.1)$$

where H_0 is the unperturbed Hamiltonian of the system and V_M is the perturbation due to an external magnetic field. The perturbation is given by,

$$V_M = -\mu \cdot \mathbf{B} , \quad (3.2)$$

where \mathbf{B} is the external magnetic field vector and μ , the magnetic moment, is given by,

$$\mu = -\mu_B g \mathbf{J} / \hbar , \quad (3.3)$$

where μ_B is the Bohr magneton (9.3×10^{-21} erg G $^{-1}$), g is the “g-factor”, \mathbf{J} is the sum of the orbital (\mathbf{L}) and spin (\mathbf{S}) angular momenta, and \hbar is Planck’s constant divided by 2π . The g-factor is a dimensionless term relating the magnetic moment of a particle to its angular momentum number, and the Bohr magneton.

We can substitute for \mathbf{J} obtaining,

$$\mu = -\mu_B (g_l \mathbf{L} + g_s \mathbf{S}) / \hbar , \quad (3.4)$$

where $g_l = 1$ and $g_s \approx 2^1$. For light atoms, the orbital and spin angular momentum of individual electrons (ℓ and s , respectively) may be summed,

$$\mathbf{L} = \sum_i^n \ell_i , \quad (3.5)$$

$$\mathbf{S} = \sum_i^n s_i \quad (3.6)$$

¹Using a classical derivation of angular momentum, $g = 1$. For orbital angular momentum, the classical assumption gives the correct result and so $g_l = 1$. However, the electron spin angular momentum must be derived in the framework of relativistic quantum mechanics. Fine structure splitting gives the deviation from 2, $g_s \approx 2.0023193\dots$

3. INSTRUMENTATION AND OBSERVATIONS

Also, L and S maybe summed to determine the total angular momentum, J ,

$$g\mathbf{J} = \langle g_l \mathbf{L} + g_s \mathbf{S} \rangle \quad (3.7)$$

where the averaging is done over a state with a particular value for \mathbf{J} . It is said that the orbital and spin angular momentum are coupled (\mathbf{L} - \mathbf{S} coupling). If the external magnetic field is small (such as on the Sun), the total angular momentum is conserved,

$$\mathbf{J} = \mathbf{L} + \mathbf{S} \quad (3.8)$$

The time-averaged orbital and spin angular momenta are given by,

$$\langle \mathbf{S} \rangle = \frac{(\mathbf{S} \cdot \mathbf{J})}{J^2} \mathbf{J}, \quad (3.9)$$

$$\langle \mathbf{L} \rangle = \frac{(\mathbf{L} \cdot \mathbf{J})}{J^2} \mathbf{J} \quad (3.10)$$

\mathbf{L} and \mathbf{S} precess around \mathbf{J} over time, so the average vectors are projected onto \mathbf{J} .

Rearranging Equation 3.8 gives,

$$\mathbf{S} = \mathbf{J} - \mathbf{L} \text{ and} \quad (3.11)$$

$$\mathbf{L} = \mathbf{J} - \mathbf{S} \quad (3.12)$$

Separately dotting \mathbf{J} with Equation 3.11 and squaring both sides of Equation 3.11 gives,

$$\mathbf{S} \cdot \mathbf{J} = J^2 - \mathbf{L} \cdot \mathbf{J} \text{ and} \quad (3.13)$$

$$\mathbf{L} \cdot \mathbf{J} = - \left(\frac{S^2 - J^2 + L^2}{2} \right) \quad (3.14)$$

3.1 Solar Magnetic Field Observations

Combining Equation 3.13 and 3.14 gives,

$$\mathbf{S} \cdot \mathbf{J} = \frac{1}{2}(\mathbf{S}^2 - \mathbf{L}^2 + \mathbf{J}^2) \quad (3.15)$$

Following the same procedure using Equation 3.12 gives,

$$\mathbf{L} \cdot \mathbf{J} = \frac{1}{2}(\mathbf{L}^2 - \mathbf{S}^2 + \mathbf{J}^2) \quad (3.16)$$

The time-averaged energy perturbation can be obtained by combining these equations with Equation 3.4 and 3.2,

$$\langle V_m \rangle = -\frac{\mu_B}{\hbar J^2}(g_l \mathbf{L} \cdot \mathbf{J} + g_s \mathbf{S} \cdot \mathbf{J}) \mathbf{J} \cdot \mathbf{B}, \quad (3.17)$$

and substituting with Equations 3.15 and 3.16,

$$\langle V_m \rangle = -\frac{\mu_B}{2\hbar J^2}(g_l(\mathbf{L}^2 - \mathbf{S}^2 + \mathbf{J}^2) + g_s(\mathbf{S}^2 - \mathbf{L}^2 + \mathbf{J}^2)) \mathbf{J} \cdot \mathbf{B}. \quad (3.18)$$

In terms of their quantum numbers the spin, orbital, and total angular momentum are,

$$\mathbf{S} = \hbar^2 s(s+1) \quad \text{where } s = 0, \frac{1}{2}, 1, \frac{3}{2} \dots \quad (3.19)$$

$$\mathbf{L} = \hbar^2 l(l+1) \quad \text{where } l = 0, 1, 2, 3 \dots \quad (3.20)$$

$$\mathbf{J} = \hbar^2 j(j+1) \quad \text{where } j = 0, \frac{1}{2}, 1, \frac{3}{2} \dots \quad (3.21)$$

Taking the component of \mathbf{J} along a vertical magnetic field, $J_z = \hbar m_j$, where m_j is the total angular momentum along z, the time-averaged energy perturbation can then be rewritten,

$$\langle V_m \rangle_z = \mu_B m_j B g_j, \quad (3.22)$$

3. INSTRUMENTATION AND OBSERVATIONS

where g_j is the Landé g -factor,

$$g_j = \frac{-g_l(\mathbf{L}^2 - \mathbf{S}^2 + \mathbf{J}^2) + g_s(\mathbf{S}^2 - \mathbf{L}^2 + \mathbf{J}^2)}{2J^2}. \quad (3.23)$$

The Landé g -factor indicates how sensitive a particular state is to an external magnetic field. Substituting with Equations 3.19 and 3.20 and evaluating $g_l = 1$,

$$g_j = \frac{(1 - g_s)l(l + 1) + (g_s - 1)s(s + 1)}{2j(j + 1)} + \frac{1 + g_s}{2}. \quad (3.24)$$

The main result of the Zeeman effect is that a given energy state in the presence of a magnetic field is split into three components with $\Delta m_j = -1, 0, +1$, depending on the orientation of the total angular momentum vector to the magnetic field, as shown in Figure 3.1. When a particular energy state transition to the split state occurs, the change in m_j between the two states must be $+1$, 0 , or -1 , regardless of which transition is involved. The wavelength shift between the perturbed states and the unshifted ($\Delta m_j = 0$) state is given by,

$$\Delta\lambda = \pm 46.67g_j\lambda_0^2B, \quad (3.25)$$

where $\Delta\lambda$ is the difference between the shifted wavelength and λ_0 and λ_0 is the wavelength of the unperturbed π component. This holds for the “normal” Zeeman effect when the g_j of the initial and final states is the same. The “anomalous” Zeeman effect occurs when this is not the case and more than three energy components are possible. In this case the g -factor of the initial and final states must be taken into account,

$$\Delta\lambda = 46.67(g_{j,i}m_{j,i} - g_{j,f}m_{j,f})\lambda_0^2B, \quad (3.26)$$

where i denotes an initial state and f denotes a final state.

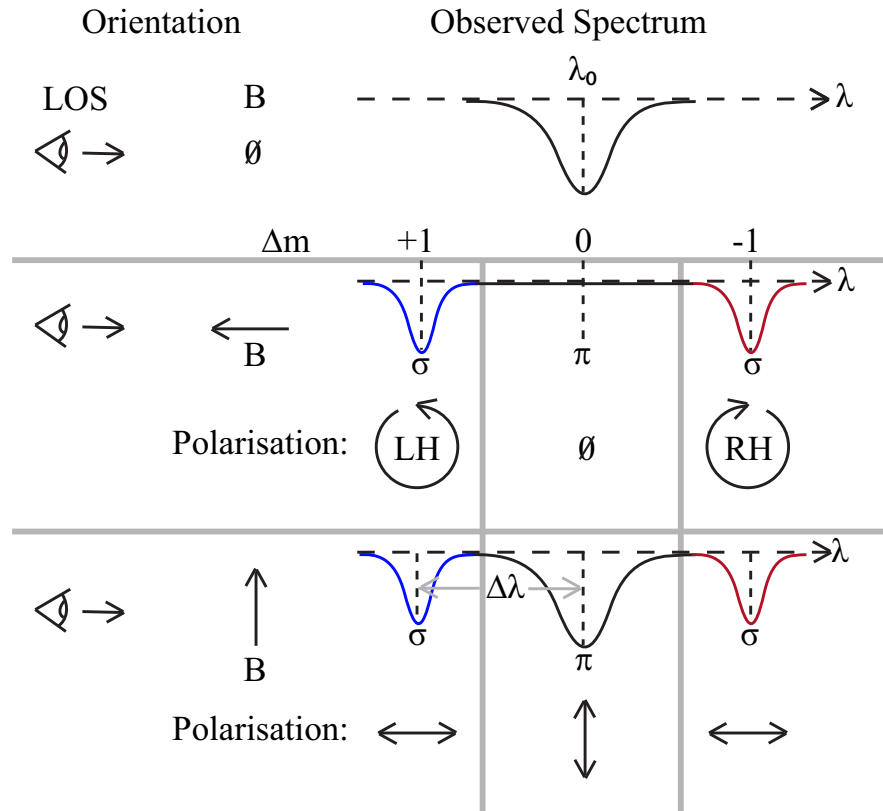


Figure 3.2: A comparison of the observed line splitting and polarised components for no magnetic field (top), a LOS field (middle), and a transverse field (bottom). Circularly or linearly polarised split components are observed, depending on whether the magnetic field is along the LOS or transverse to it, respectively.

When considering the shift in a single component of a Zeeman-split spectral line as compared to its rest wavelength, the Doppler effect must be accounted for in determining the shift due to magnetic effects. When the LOS velocity of radiating matter is much less than the speed of light ($v_{LOS} \ll c$) the Doppler shift in wavelength is given by,

$$\frac{\Delta\lambda}{\lambda_0} = \frac{v_{LOS}}{c}, \quad (3.27)$$

where $\Delta\lambda$ is the same as in Equation 3.25.

For absorption, the allowed polarisation of an incoming resonant photon is dependent on the orientation of the magnetic field to the observer and hence the orientation

3. INSTRUMENTATION AND OBSERVATIONS

of the electron's magnetic dipole moment that aligns with it. Combinations of the observed polarised light components are used to determine the vector components of the magnetic field. The Stokes parameters (198) define the polarisation of the spectral line profile. They are directly observable and provide a convenient way to determine the magnetic field vector. The four parameters are,

$$I = \odot + \circlearrowleft \text{ or } \uparrow + \leftrightarrow \text{ etc.,} \quad (3.28)$$

$$Q = \leftrightarrow - \uparrow , \quad (3.29)$$

$$U = \nearrow - \nwarrow , \quad (3.30)$$

$$V = \odot - \circlearrowleft . \quad (3.31)$$

where \odot and \circlearrowleft represent right and left circularly polarised light, \uparrow and \leftrightarrow represent linearly polarised light in the 90° and 0° directions, and \nearrow and \nwarrow represent polarisation in the 45° and 135° directions.

The comparison of modelled and measured I, Q, U, and V profiles can be used to determine the magnetic field vector at the source of the spectral line. Observers fit modeled versions to actual measurements of the Stokes parameters to determine the magnetic field strength and direction. The formation of a spectral line occurs over a range of heights in the solar atmosphere so a model of the atmosphere must be used. The process of fitting I, Q, U, and V may involve 10 parameters, even when making severe assumptions about the atmosphere, such as using the Milne-Eddington limit, whereby the atmosphere is assumed to be plane-parallel and only absorption effects are considered.

In this work, we only consider LOS magnetic fields. Figure 3.3 compares the observed spectra and polarised components for a LOS field toward and away from the observer. To determine the strength and direction of this field, only the Stokes V need be considered since the LOS component of the magnetic field is manifested only in the

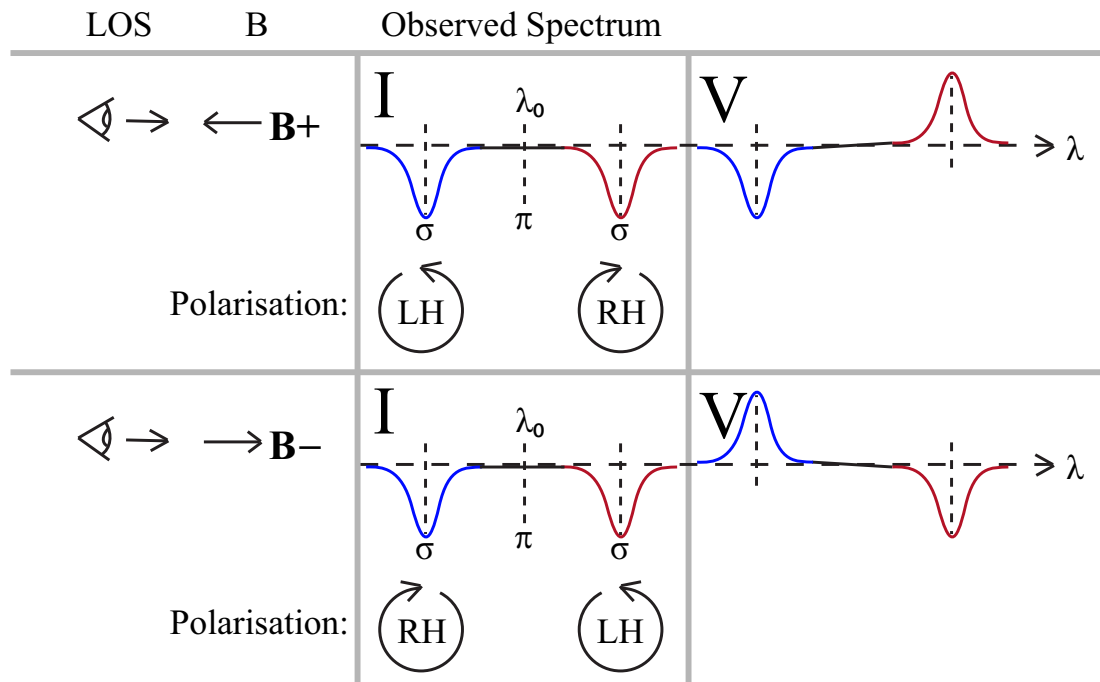


Figure 3.3: A comparison of Stokes parameters for magnetic field directed toward and away from the LOS. The polarisation of the two split components switches depending on the orientation, as indicated by the sign \mathbf{V} .

circularly polarised light.

The better resolved the observed spectral line is, the better the magnetic field measurement accuracy will be. Unfortunately, there is a trade-off between spatial resolution and spectral resolution due to the bandwidth and memory limitations of instruments. Also, to avoid mixing space and time in the measurements, the time to make an observation must be less than the dynamic time-scale of the observed phenomena at the given spatial resolution. Instruments used to image the solar magnetic field must strike a balance between spatial resolution, spectral resolution, acquisition time, and memory usage.

3. INSTRUMENTATION AND OBSERVATIONS

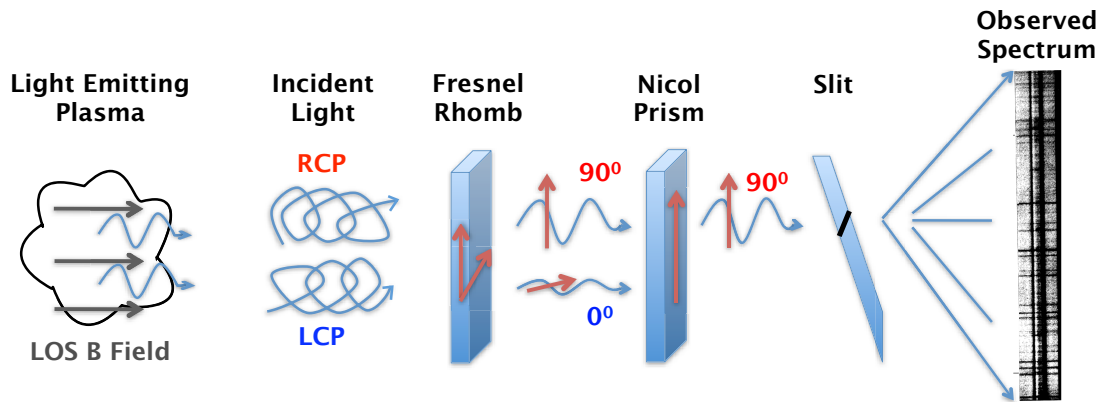


Figure 3.4: A schematic diagram of the magnetometer used by Hale to measure the LOS magnetic field at a single point on the solar surface. Light emitted at the solar surface is split into right and left circularly polarised components using the combination of a Fresnel rhomb and Nicol prism. The spectrum is then dispersed by a slit for analysis.

3.1.2 Early Observations

Although he interpreted his results as inconclusive, (82) is credited with the first direct measurement of the magnetic field within a sunspot. Using the Mount Wilson telescope, he constructed an apparatus to measure the Zeeman splitting in the 6 000–6 200Å wavelength range. The light from the projected image of the Sun from the telescope was passed through a plane-polarising Fresnel rhomb¹ to convert the circular polarisation to plane-polarised light, differing by 90° in phase. A Nicol prism² then allowed each polarisation to be isolated. Finally, a slit at the focal point of the optics dispersed the spectrum. The slit was partially covered to narrow the spatial extent of the observation. The slit opening could then be centred on a sunspot umbra, for instance. A schematic of this instrument is shown in Figure 3.4.

¹Fresnel rhombs are generally prisms with a parallelogram-shaped cross-section. Incident light undergoes two internal reflections before exiting the prism. Each reflection produces a 45° phase delay between the two linearly polarised components of the light. This results in the conversion of a linear to circular, or in the case of a magnetometer, a circular to linear polarisation.

²Nicol prisms are traditionally made from Icelandic feldspar, a type of calcite. Light of different polarisations incident on this material experiences different refractive indices. The prism face is cut at an angle of 68° to the crystal structure and is also cut diagonally and glued back together to create an internal interface. Light of one linear polarisation will experience total internal reflection at this interface, while light of the other polarisation will pass through the prism.

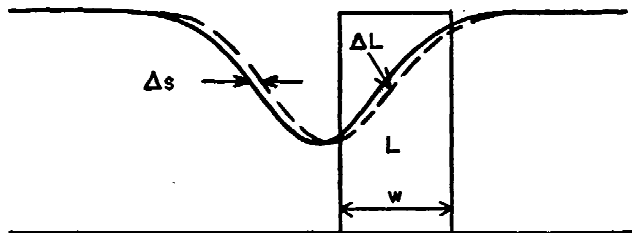


Figure 3.5: A schematic diagram of the Zeeman effect observed at one point on the focal plane using a Babcock magnetometer (from 12). The shifts are measured in the wing of a spectral line, allowing smaller magnetic fields to be observed than in Hale's case.

Much later (12) presented the Babcock magnetograph. This operated under the same principle as the apparatus used by Hale to measure the Zeeman effect by alternatively comparing the right-hand-circularly-polarised (RCP) and left-hand-circularly-polarised (LCP) light from a particular location on the Sun. The advance here is that two spectral slits are used to determine line shifts by amplifying the difference in the intensity at the wings of an absorption line, as shown in Figure 3.5. Phototubes are used to electronically measure the signals of each slit and their difference is amplified by a narrowband amplifier. This method of measuring the spectral shift results in the instrument having a sensitivity down to 1 G, since the splitting of the line does not have to be resolved as in the case of Hale's instrument. The biggest leap forward was the addition of a scanning device to allow an automatic measurement of the magnetic field over the entire solar disk. Previously, the magnetic field of a single spot on the Sun could be analysed, but now a global analysis of the surface magnetic field of the Sun was possible.

This work paved the way for modern magnetographs that use tuneable Michelson-Morley interferometers in place of slits to simultaneously allow the spectral analysis of every point on the Sun. The instrument, called the Fourier Tachometer, employs narrowband filters to allow wavelength positions to be sampled across a given spectral line (51). The advantage of this is that a grid of points in the 2D plane-of-sky can be sampled simultaneously, but the disadvantage is that the filters introduce substantial

3. INSTRUMENTATION AND OBSERVATIONS

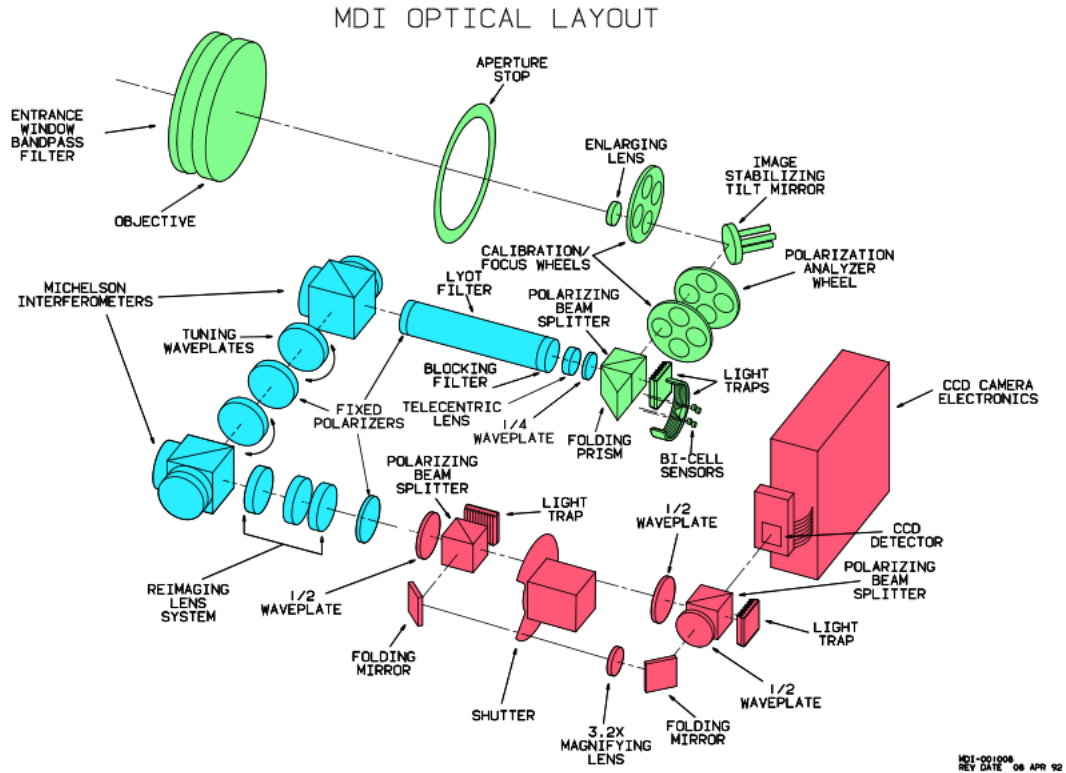


Figure 3.6: A schematic diagram of the MDI instrument (from 165). The same basic method is used as in the Hale magnetometer to split up the polarised components. Here, Michelson-Morley interferometers allow a determination of the solar magnetic field in 2D.

noise (27). Thus there is a tradeoff between noise, spatial resolution, and temporal resolution. The work presented in this thesis is concerned with the large spatial- and temporal-scale evolution of the Sun, for which Fourier Tachometer-type instruments are used.

3.1.3 The Michelson Doppler Imager

The methods described in this work involve the image processing of full-disk LOS magnetograms taken by the Solar and Heliospheric Observatory (SOHO)/Michelson Doppler Imager (MDI; 165). This instrument is a magnetograph which uses a complex array of optical equipment to take advantage of the Zeeman effect in order to deter-

3.1 Solar Magnetic Field Observations

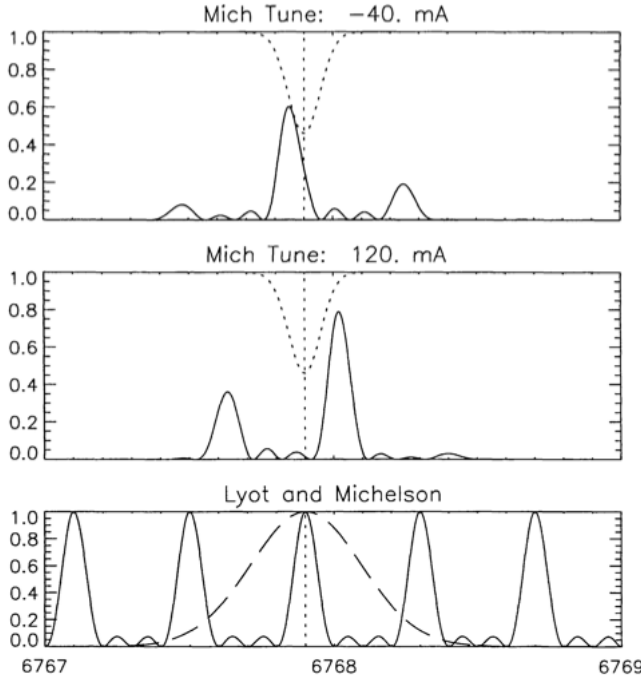


Figure 3.7: Bottom to Top: the response function of the Ni I line-centered filters (dotted line) and the Michelson interferometers (solid line); the resulting response of the filter and interferometers tuned to two different wavelengths (solid line) and the Ni I line profile (dotted line; from 165).

mine the LOS magnetic fields in the photosphere, as discussed in Section 3.1.1. As well as being sensitive to the strong magnetic fields in sunspots, MDI is also sensitive to weak fields in quiet-Sun regions since it uses the same principles as the Babcock magnetometer (see Section 3.1.2).

Figure 3.6 shows a diagram of the MDI optical path and Figure 3.7 shows the response functions of the main optical components. Incoming light passes through a series of narrowing filters which center on the Ni I 6768 Å absorption line. The observed splitting of this line is used to measure the solar magnetic field. The light then passes through one Michelson interferometer, a series of tuning wave plates, a second Michelson interferometer, and re-imaging lenses. These components allow the tuning of the narrow instrument bandpass around the Ni I line. A linear polarizer and half-wave plate alternatively allow the passage of right and left circularly polarised light

3. INSTRUMENTATION AND OBSERVATIONS

depending on the half-wave plate orientation. Finally, the resulting image is collected at a 1024^2 pixel charge-coupled device (CCD) camera.

A series of images are taken at several tuned wavelengths and combined to determine values which are proportional to actual magnetic fields. MDI takes filtergrams at 5 tuned wavelengths equally separated by $75\text{ m}\text{\AA}$: F_0 in the continuum, F_1 and F_4 in the wings of the line, and F_2 and F_3 in the core of the line. A unit-less measure of the line shift (α) is determined for both left-hand (α_{LHC}) and right-hand (α_{RHC}) circularly polarized light independently, where,

$$\alpha = (F_1 + F_2 - F_3 - F_4)/(F_1 - F_3), \text{ if numerator} > 0 \quad (3.32)$$

$$= (F_1 + F_2 - F_3 - F_4)/(F_4 - F_2), \text{ if numerator} \leq 0. \quad (3.33)$$

The line depth is estimated by,

$$I_{depth} = \sqrt{2((F_1 - F_3)^2 + (F_2 - F_4)^2)}, \quad (3.34)$$

using a discrete Fourier transform (DFT) of the line profile ($I_{cont} - I_{depth} \cos(2\pi(\lambda - \lambda_0))$) and assuming the filtergrams are evenly spaced over one period. The continuum intensity is given by,

$$I_c = 2F_0 + I_{depth}/2 + \langle F_{1-4} \rangle, \quad (3.35)$$

where $\langle F_{1-4} \rangle$ is the average of the filtergrams in the absorption line.

If unpolarised light was used, it would be impossible to tell whether the line shift, α , was caused by the Zeeman effect or a Doppler shift. The shift due to the Zeeman effect alone is then,

$$\alpha_{Zeeman} = \alpha_{RHC} - \alpha_{LHC}. \quad (3.36)$$

These values are calibrated to physical units using a look-up table, which is generated by a static solar atmosphere model.

3.1 Solar Magnetic Field Observations

Property	MDI	HMI
Target line	Ni I 6768 Å	Fe I 6173 Å
Aperture	12.5 cm	14.0 cm
Optical resolution (λ/D)	1.17 arcsec	0.91 arcsec
Pixel size	1.98 arcsec (FD) 0.61 arcsec (HR)	0.505 arcsec
CCD	One 1024×1024 $21\text{ }\mu\text{m}$	Two 4096×4096 $12\text{ }\mu\text{m}$
Front window FWHM	50 Å	50 Å
Blocking filter FWHM	8 Å	8 Å
Lyot design	1:1:2:2:4:8	1:2:4:8:16
Untuned FWHM	465 mÅ	612 mÅ
Tunable element FWHMs	94 mÅ Michelson 189 mÅ Michelson	86 mÅ Michelson 172 mÅ Michelson 344 mÅ Lyot
Final filter FWHM	85 mÅ	76 mÅ
Spectral resolution ($\lambda/\text{FWHM}/1000$)	80	81
Polarization	$I \pm Q$ and $I \pm V$	All
Filtergram cadence	3 seconds	3.75 seconds per camera 1.875 overall
Filtergram positions	5 at 75 mÅ spacing	6 at 69 mÅ spacing
Nominal observables cadence	60 seconds	45 seconds
Data rate	160 kbit s^{-1} (FD and HR) 5 kbit s^{-1} (Structure)	55 Mbit s^{-1}

Figure 3.8: A comparison of the specifications of HMI to MDI (from 170). In the table FD stands for full-disk images, and HR stands for high-resolution images. Most importantly for HMI, the pixel size of is $\sim 1/4$ that of MDI, all of the Stokes components can be obtained, the data rate is ~ 300 times that of MDI.

3.1.4 The Helioseismic and Magnetic Imager

The Helioseismic and Magnetic Imager (HMI; 166) on board the *Solar Dynamics Observatory (SDO)* is a magnetograph with essentially the same design to MDI, as shown in Figure 3.9. One difference is that HMI uses the Fe I 6173 Å absorption line to measure the Zeeman effect. This line has a g_J of ~ 2.5 giving it a better sensitivity to magnetic fields than the Ni line used for MDI with a g_J of ~ 1.4 . The most important difference between the two instruments is the four-fold increase in resolution of HMI and its

3. INSTRUMENTATION AND OBSERVATIONS

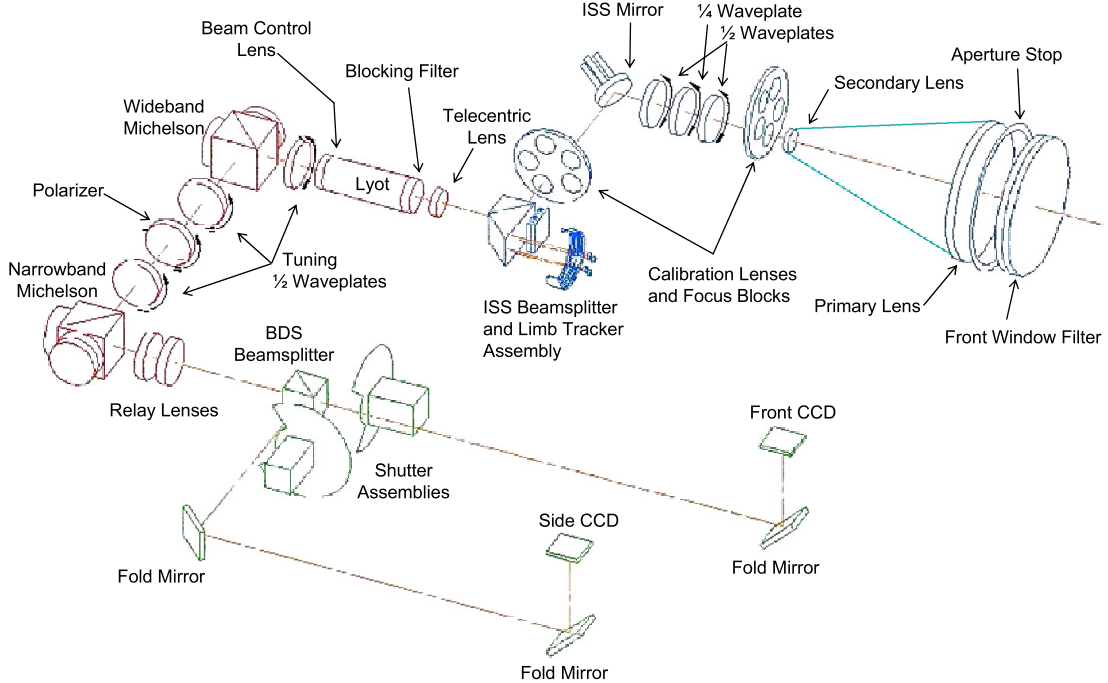


Figure 3.9: A schematic diagram of the HMI instrument (from 170). The overall setup is the same as that of MDI.

ability to generate vector magnetic fields. Norton *et al.* (141) argue that HMI should produce reliable measurements for magnetic fields within umbrae and penumbrae. In this work, only the LOS magnetic field data are used. The method of calibrating the LOS magnetic field is very similar to the algorithm used by MDI.

HMI uses six filtergrams with bandpasses centered at different wavelengths along the Fe I absorption line as shown in Figure 3.10. An example of the possible line profile resulting from the magnetic field in a sunspot penumbra is shown in Figure 3.11. Considering a single spatial position in the filtergrams, six discrete points along the actual line profile at a given location on the Sun are sampled. These points are used to determine the first two sets of Fourier coefficients ($i = [1, 2]$) of the Fe I line intensity profile (43),

$$a_i \approx \frac{2}{T} \int_{-\frac{T}{2}}^{+\frac{T}{2}} \cos\left(i2\pi\frac{\lambda}{T}\right) d\lambda, \quad (3.37)$$

3.1 Solar Magnetic Field Observations

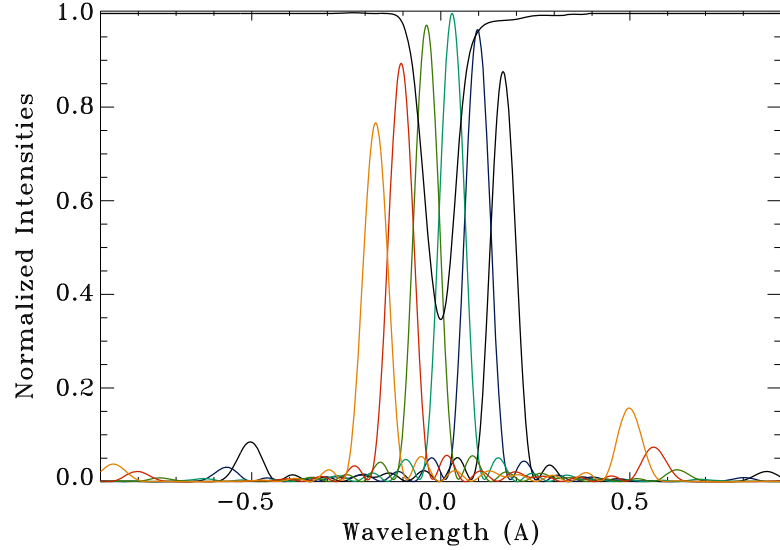


Figure 3.10: An example of the filtergram bandpasses used to produce an HMI magnetogram relative to the Fe I absorption line (from 170). Each color represents a different tuning of the filters; each part of the Fe I line is sampled.

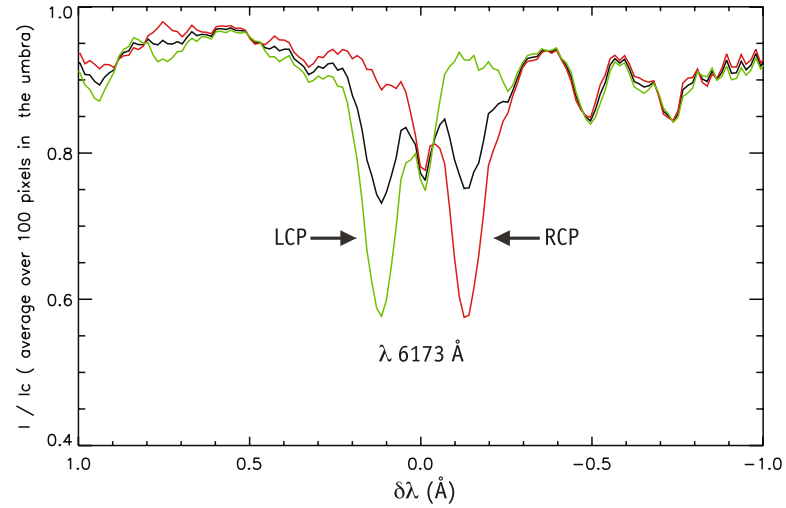


Figure 3.11: An example of Zeeman splitting in the Fe I absorption line measured by the IBIS ground-based spectropolarimeter instrument in a sunspot penumbra (from 141).

$$b_i \approx \frac{2}{T} \int_{-\frac{T}{2}}^{+\frac{T}{2}} \sin \left(i2\pi \frac{\lambda}{T} \right) d\lambda, \quad (3.38)$$

where i is the order of the coefficient in the Fourier series decomposing the line profile, T is the “period” of the wavelength range covered by the six filters ($T = 412.8 \text{ m}\text{\AA}$),

3. INSTRUMENTATION AND OBSERVATIONS

and λ is wavelength. In practice DFT versions of Equation 3.37 are used,

$$a_1 \approx \frac{2}{6} \sum_{j=0}^5 = I_j \cos \left(2\pi \frac{2.5 - j}{6} \right), \quad (3.39)$$

where j denotes each filtergram sampling point. These are determined separately for RCP and LCP light. A line shift in terms of velocity is determined from each polarisation,

$$v = \frac{T}{2\pi} \frac{dv}{d\lambda} \tan^{-1} \left(\frac{b_1}{a_1} \right), \quad (3.40)$$

The filter bandpasses are not delta functions, so the Fourier coefficient determinations are not used directly. A theoretical Fe I line profile is convolved with each of the filter bandpasses for a range of velocities. The resulting sampled simulated intensities are used to construct a look-up table of Fourier coefficients. This is used to determine corrected shifts in terms of velocity (V_{LCP} and V_{RCP}) from the Fourier coefficients determined from the measured line profile. Finally, these velocities are used to determine the LOS magnetic field strength,

$$B = (V_{\text{LCP}} - V_{\text{RCP}})K_m, \quad (3.41)$$

where K_m is a calibration constant determined from Equation 3.25,

$$K_m = 2.0 \times 4.67 \times 10^{-5} \lambda_0 g_j c = 0.231 \text{ G m}^{-1} \text{ s}, \quad (3.42)$$

where λ_0 is the central Fe I line wavelength and c is the speed of light.

3.2 Feature and Event Lists

The results of a number of investigations presented in this work are compared to a number of feature and event catalogues. For this work these catalogs are a useful

for providing context to an event or to provide a ground truth which an automated algorithm can be tested against. In this work, a sunspot group catalog and two flare catalogs are used in this way.

The catalogue of National Oceanic and Atmospheric Association (NOAA) sunspot group numbers and locations cataloged by the NOAA Space Weather Prediction Center is used to benchmark the detections made by the SolarMonitor Active Region Tracker (SMART; see Chapter 4) in magnetogram data. Sunspot groups are detected manually using ground-based white-light data. Thus, since magnetic fields are not used in the detection, the measured properties of NOAA and SMART detections cannot be inter-compared. For instance, the sunspot area of a NOAA cataloged region can not be compared with the area of the same region detected by SMART because different physical structures are observed in white-light than magnetogram images. However, the observed numbers of NOAA and SMART detections can be compared.

To indicate the activity of sunspot groups, we use two flare lists. A list of flares observed by the Geostationary Operational Environmental Satellites (GOES; 84) distributed by the National Geophysical Data Center (NGDC) is used to statistically determine the characteristics of sunspot groups that produce flares. In case studies presented in Chapter 5, we associate observations of NOAA 10365 and 10377 with flares observed and characterised by the Reuven Ramaty High Energy Solar Spectroscopic Imager (RHESSI; 118) team and distributed in the RHESSI flare list¹.

¹see [http://sprg.ssl.berkeley.edu/\\$simm/hessi/hsi_flare_list.html](http://sprg.ssl.berkeley.edu/$simm/hessi/hsi_flare_list.html)

3. INSTRUMENTATION AND OBSERVATIONS

4

Detecting and Tracking Solar Active Regions

*The majority of this chapter is based on research published in Higgins et al., *Advances in Space Research* (2011) and several techniques were first defined in Verbeeck & Higgins et al., *Solar Physics* (2011). All of the work presented is my own, except where otherwise specified. In this chapter we describe and test a system for detecting, characterising, and tracking strong magnetic features in the photosphere. The methods used are benchmarked by comparing a sample of detections to the NOAA active region catalog. The uncertainties involved in characterising features using line-of-sight magnetic field observations are discussed. A good agreement is found between our system and NOAA, but we find the behaviour of each tracking method differs since the NOAA tracking is performed by eye on continuum data and the SMART system is automatically run on magnetic field observations. Finally, to determine the reliability of our property determinations, a simulation of a feature crossing the solar disk is run and illustrates that properties incorporating the magnetic gradient incur large errors away from disk center.*

4. DETECTING AND TRACKING SOLAR ACTIVE REGIONS

4.1 Introduction

The automatic identification and characterization of solar features is of great importance to both solar activity monitoring and space weather operations. This has become a particular issue due to the high spatial and temporal resolution solar imagers, such as those flown on the *Project for On-Board Autonomy 2 (PROBA2)* and *Solar Dynamics Observatory (SDO)*, which will force data providers to distribute subsets of their science products instead of the full image data set. Traditionally, solar feature catalogs were created by hand, using visual recognition to record the position, size, and other properties of features (e.g., 31). An early attempt to overcome this was Solar-Monitor¹(70), which labels active regions (ARs) in solar images using National Oceanic and Atmospheric Association (NOAA) numbers and locations cataloged by the Space Weather Prediction Center. More recently, researchers have begun to catalog features using automated methods. The European Grid of Solar Observations² (EGSO; 18), for example, catalogs solar features using H α and Ca II K images and a neural network algorithm (231; 232).

One of the first applications of automated image processing techniques to AR identification is the Automated Region Selection Extraction algorithm (126). This algorithm creates a binary mask of features using a static noise threshold applied to a line-of-sight (LOS) magnetogram. A sub-image is extracted, centered on the pixel with the highest value. Closed contours enclosing an area centered on the seed are grouped as a region. The detected region is saved and removed from the magnetogram. The pixel of the next highest value is selected and the process repeated. Some saved regions are associated

¹See: <http://www.SolarMonitor.org>

²See: <http://www.egso.org>

4.1 Introduction

with NOAA cataloged regions which may be tracked across the disk. More recently, LaBonte *et al.* (110) extracted ARs using full-disk magnetograms that are smoothed by roughly one supergranule diameter. Region candidates are tested for bipolar flux and east-west orientation. A dynamic noise threshold is calculated using the median of average magnetic field values for a series of annuli centered on the AR candidate. The AR boundary is chosen by comparing the average magnetic field values of smaller annuli with the calculated noise threshold. Using annuli to test for region boundaries allows one to isolate ARs from large AR complexes since the dynamic noise threshold will be set relative to the surrounding regions.

An alternative to identifying ARs solely using their magnetic signatures was discussed in a series of papers by Qahwaji & Colak (155) and Colak & Qahwaji (38, 39). In their hybrid extraction algorithm, sunspots detected in white-light images are grouped using feature boundaries extracted from magnetograms. Both forms of data are segmented using dynamic thresholding. White-light candidates coinciding with magnetogram candidates are grouped using growing circles, while a neural network is used to determine which candidates to retain and how to group them. This system has the advantage that it compares well the NOAA AR identification scheme, but it does not give any insight into AR properties thought to be related to flaring (e.g., horizontal B-field gradients, total flux, fractal dimension, etc.).

It is known that complicated magnetic field configurations tend to produce more M- and X-class flares than simpler ones (109; 128). A number of algorithms have been developed to measure AR magnetic characteristics postulated to be related to flaring: Gallagher *et al.* (70) measure gradients in the magnetic field of ARs; McAteer *et al.* (125) establish an AR fractal dimension lower limit of 1.2 for M- and X-class flares to occur; Georgoulis & Rust (73) calculate the magnetic connectivity between fragments of an AR; Conlon *et al.* (41, 42) measure the multifractal nature of AR flux; Hewett *et al.* (96) determine the multiscale power-law index; and Falconer *et al.* (57) establish

4. DETECTING AND TRACKING SOLAR ACTIVE REGIONS

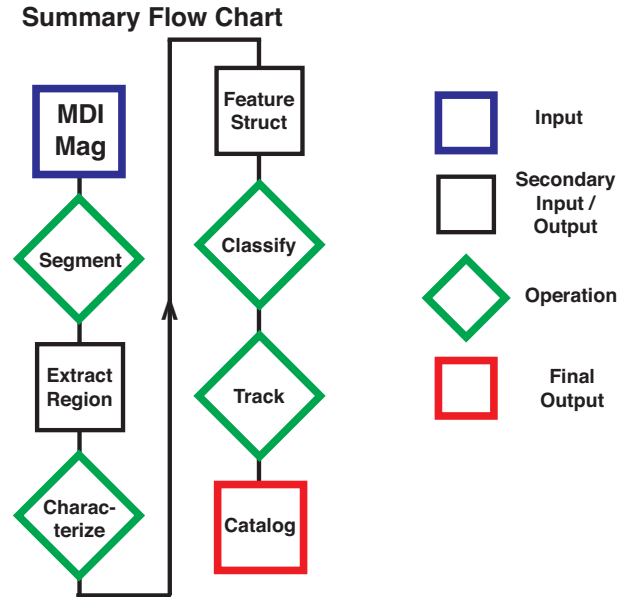


Figure 4.1: Flow chart summarizing the SMART algorithm processing method.

a gauge of AR non-potentiality. The overall aim of these algorithms is to extract a physically-motivated measure of the characteristics of a region, subsequently using this information to better understand the fundamental physics of ARs, and to relate the properties of AR magnetic fields to their flaring potential. This is essential to building an automated AR monitoring and flare forecasting system as discussed in McAteer *et al.* (127).

In this chapter we present a new algorithm, the SolarMonitor Active Region Tracker (SMART). SMART combines extraction techniques with AR magnetic property determinations (Section 4.2), region tracking, and cataloging (Section 4.3). A cross comparison of SMART and NOAA detections as well as a discussion of errors in property measurements and feature tracking test cases are presented in Section 4.4. Our conclusions are presented in Section 4.5.

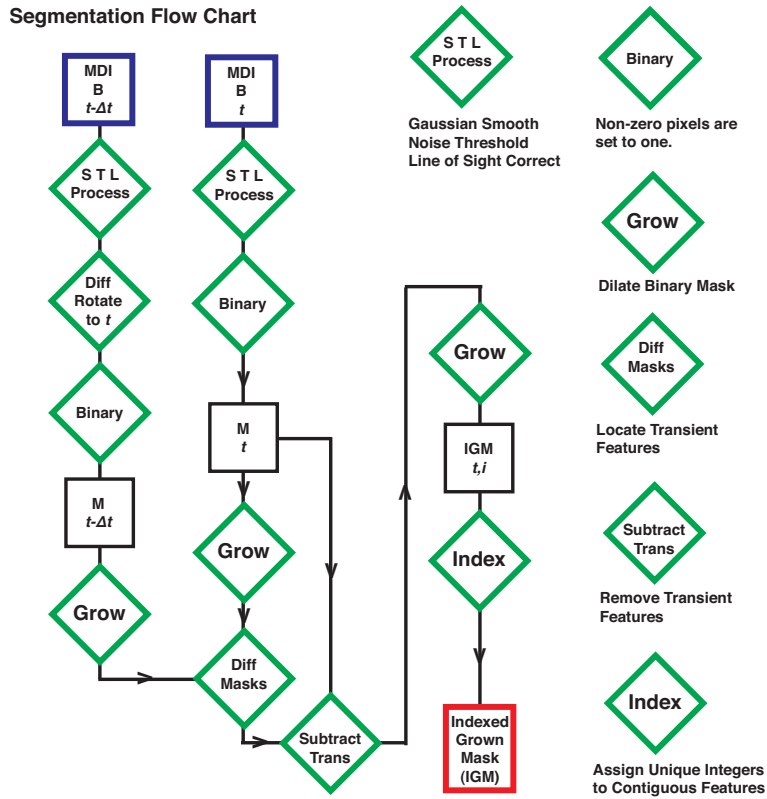


Figure 4.2: Flow chart summarizing the magnetogram segmentation method.

4.2 Feature Extraction

The SMART method of operation is summarized in Figure 4.1. Initially, magnetograms are segmented into individual feature masks (Section 4.2.1). A characterization algorithm is then run on each extracted region to determine feature properties (Section 4.2.2). These region properties are subsequently used to classify the form of solar features (Section 4.2.4). The final output is a set of data structures for each magnetogram, including each feature present. The following sub-sections provide details on the operations outlined above.

4. DETECTING AND TRACKING SOLAR ACTIVE REGIONS

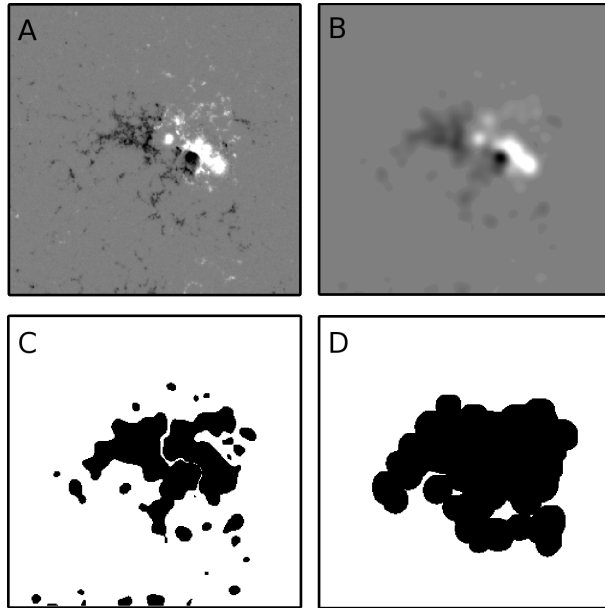


Figure 4.3: Processing steps for an example feature extraction on 25 November 2003. A) Calibrated magnetogram B_t clipped to $\pm 1\,000$ G and cropped around NOAA 10507. B) B_t with Gaussian smoothing and noise thresholding. C) Mask ($M_{f,t}$) with transient filtering and area threshold of 50 pixels. D) Final indexed grown feature mask, $IGM_{t,i}$.

4.2.1 Segmentation

The segmentation process depicted in Figure 4.2 begins with two consecutive Michelson Doppler Imager (MDI) full-disk, LOS, level 1.8 magnetograms¹. Nominally these are 96 minutes apart, but there are sporadic gaps in the MDI data set (only rarely is there an entire day with no data). We use two magnetograms recorded close in time to remove short-lived features, such as ephemeral flux regions and small bipoles, and to extract time-dependent properties. The magnetogram of interest (Figure 4.3 A) is denoted as B_t and the previous magnetogram as $B_{t-\Delta t}$. If Δt is greater than one day, the detections are discarded.

Magnetograms are first checked for problems using properties extracted from the Flexible Image Transport System (FITS) data file headers, such as the spacecraft roll angle and the number of missing pixel values. Magnetograms are rotated as necessary,

¹See <http://soi.stanford.edu/magnetic/Lev1.8/>

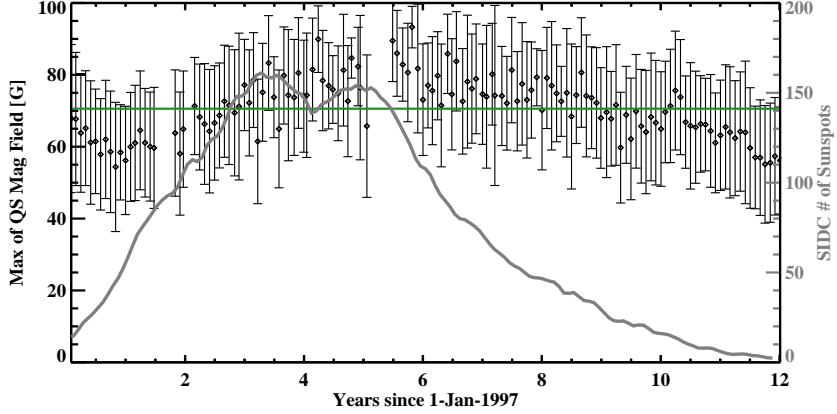


Figure 4.4: The maximum of quiet-Sun magnetic field values over solar cycle 23. Each point is the mean maximum value for a month of magnetograms (nominally two per day are used, but less for particularly active periods). The vertical bars indicate the spread of values using the standard deviations of each month’s set of values. The green line indicates the mean of the monthly mean values. The continuous gray line is the smoothed, monthly sunspot number from Solar Influences Data Analysis Center (SIDC; <http://sidc.oma.be>).

so that solar north points up, using nearest neighbor sampling interpolation, while those with missing values are discarded. A solar energetic particle (SEP) event that occurs during a magnetogram exposure results in many bright pixels randomly scattered about the image,. This does not interfere with the AR detection, as the bright pixels are smoothed out and not detected as an AR, but can affect magnetic property determinations.

We first apply smoothing, a noise threshold, and a magnetic field LOS correction, respectively, to the data (Figure 4.3 B). This set of operations is represented by *STL Process* in Figure 4.2. The smoothing operation is necessary to remove ephemeral regions that have size scales on the order of 10 Mm (79), which corresponds to 7 MDI pixels at disk center. To this end, $B_{t-\Delta t}$ and B_t are convolved with a 10×10 pixel² kernel containing a 2D gaussian with a full-width at half-maximum (FWHM) of 5 pixels, which is sufficient to avoid detecting them. A 2D boxcar smoothing was also attempted, but resulted in linear artifacts in the final detections.

We use a static threshold of ± 70 G to remove the background. Figure 4.4 shows

4. DETECTING AND TRACKING SOLAR ACTIVE REGIONS

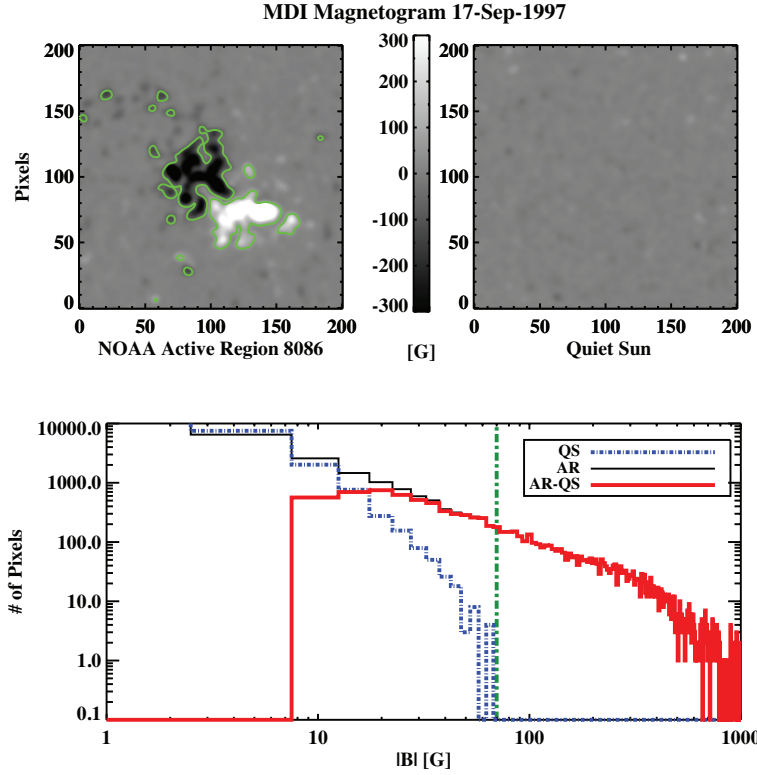


Figure 4.5: A comparison of magnetic field value distributions for a quiet-Sun and solar feature region. *Top left:* Magnetogram of NOAA 8086, gaussian smoothed using a FWHM of 5 pixels. *Top right:* A nearby region of quiet Sun in the same full-disk image. *Bottom:* The feature and quiet-Sun unsigned magnetic field distributions. The thick red line is the difference between the quiet-Sun and AR distributions and the vertical dash-dotted line denotes 70 G.

the variation in the monthly averages of maximum values of quiet-Sun (QS) magnetic field recorded throughout cycle 23. The maximum value varies by roughly 5 G over the cycle which is less than the monthly standard deviation of these maxima. The mean of the maximum unsigned quiet-Sun magnetic field values is ~ 70 G.

Degradation in the MDI instrument may contribute to a portion of the variability seen in these mean values over the solar cycle. (119) find a random offset in MDI magnetogram values that varies between ± 2 G due to noise resulting from the camera shutter. The maximum magnitude of the offset appears to increase from ~ 1 to ~ 1.5 between the period 1997 to 2001. In (168) a measure of charge leakage in the CCD is

determined for the period of 1996–2004. This increases by $\sim 25\%$ during 1996–2002 and then levels off and decreases slightly in 2003–2004. It is not indicated how charge leakage affects measured field values. The quiet-Sun magnetic field values peak at solar maximum and show minima at solar minimum. Without considering these instrumental errors, this is explained by the greater amount of emerging and decaying flux observed on disk that contributes to the background quiet-Sun. Using a static threshold results in more or less background flux being included in a given detection, depending on the phase of the solar cycle.

Figure 4.5 shows a smoothed AR and nearby quiet-Sun region contoured at ± 70 G. The histogram shows the distributions of magnetic field values for the AR and quiet-Sun regions, including the difference between the two distributions. Thresholding at the ± 70 G level removes small features which have been smoothed out by the gaussian convolution but maintains extended strong-field features, such as bipolar and plage regions. Pixels in $B_{t-\Delta t}$ and B_t with absolute values less than 70 G are zeroed.

In the case where magnetic fields are primarily normal to the solar surface, the LOS component of the field is reduced toward the limb. This does not hold for sunspot penumbrae, as discussed in Section 2.7. As such, a feature with the same magnetic field strength and orientation with respect to the solar surface will appear lower in magnitude when located toward the solar limb than at disk center. This LOS effect is corrected at each MDI pixel using a cosine correction factor. This method results in detections that include sunspot penumbrae having lower total magnetic flux values, due to their non-normal fields. After this stage, $B_{t-\Delta t}$ data is differentially rotated to time t to correct for feature motions due to solar rotation using the latitudinal dependence derived in Howard *et al.* (102).

The corrected magnetograms are made binary by setting all pixels with magnetic field values above the ± 70 G threshold equal to one, yielding masks $M_{t-\Delta t}$ and M_t . This thresholding is the initial segmentation of the magnetogram into separate features.

4. DETECTING AND TRACKING SOLAR ACTIVE REGIONS

Data Type	Identifier	Explanation
Feature Array	$B_{t,i}$	extracted feature magnetogram
	$IGM_{t,i}$	extracted feature mask
	HG_t	heliographic position map
	$A_{cos,t,i}$	$\frac{IGM_{t,i}}{\cos(HG_t)} \times (1.4 \text{ Mm}^2/\text{pixel})^{-1}$
	$\Phi_{t,i}$	$B_t \times A_{cos,t,i}$
	$\frac{d\Phi}{dt} _{t,i}$	$\frac{(B_t - B_{t-\Delta t}) \times A_{cos,t,i}}{\Delta t}$
Property Value	$HG_{pos,t,i}$	$\frac{\sum_{pix}(B_{t,i} \times HG_t)}{\sum_{pix}(HG_t \times IGM_{t,i})}$
	$B_{max,t,i}$	maximum value of $B_{t,i}$
	$B_{min,t,i}$	minimum value of $B_{t,i}$
	$B_{tot,t,i}$	$\sum_{pix} B_{t,i}$
	$B_{tot\ uns,t,i}$	$\sum_{pix} B_{t,i} $
	$\mu, \sigma^2, \gamma, \kappa$	mean, variance, skewness, kurtosis
	$A_{tot,t,i}$	$\sum_{pix} A_{cos,t,i}$
	$\Phi_{+,t,i}$	$\sum_{pix} (\Phi_{t,i} > 0)$
	$\Phi_{-,t,i}$	$\sum_{pix} (\Phi_{t,i} < 0)$
	$\Phi_{uns,t,i}$	$\sum_{pix} \Phi_{t,i} $
	$\Phi_{imb,t,i}$	$\frac{ (\Phi_{+,t,i} - \Phi_{-,t,i}) }{\Phi_{uns,t,i}}$
	$\frac{d\Phi}{dt} _{net,t,i}$	$\sum_{pix} \frac{d\Phi}{dt} _{t,i}$

Table 4.1: Feature magnetic properties derived from characterization processing.

Features consisting of less than 50 pixels and those which are not present in both masks are removed by the following operations (Figure 4.3 C). Firstly, each mask is dilated by 10 pixels to allow for region expansion between consecutive images. This means that each detected boundary is expanded radially.

Secondly, the binary masks are subtracted such that non-zero pixels in the difference mask identify features only occurring in $M_{t-\Delta t}$ or M_t . These transient features are subsequently removed from the un-dilated version of M_t , which is then dilated by 10 pixels to form $M_{f,t}$ (Figure 4.3 D). Individual contiguous features in $M_{f,t}$ are indexed by assigning ascending integer values (beginning with one) in order of decreasing feature size. This indexing is indicated by the subscript i in array and property variables and means that the variable corresponds to a specific feature, rather than the entire solar disk. The segmentation output is an indexed grown mask (IGM_t), as shown by the

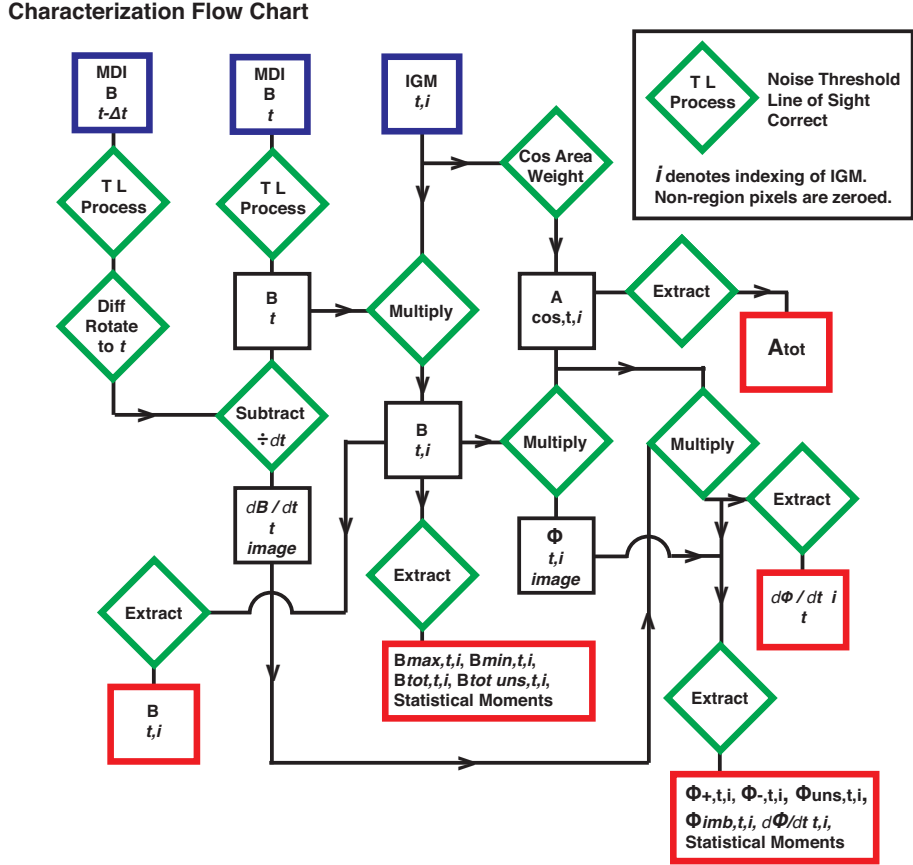


Figure 4.6: Flow chart summarizing the feature magnetic property characterization method.

thick red box in Figure 4.2. The IGM_t for a given feature is shown in Figure 4.3 D.

4.2.2 Characterization

The aim of SMART is to characterize ARs in a manner which does not make many theoretical assumptions (except for the assumption that magnetic fields are normal to the solar surface) or require many observations of the same feature. Our design is adaptable, so that the software may produce initial results in near-realtime for operational purposes, but allows the retrospective addition of complex property measurements (e.g., magnetic helicity). These requirements define criteria for the selection of initial property calculations. There are many AR properties that may be derived from

4. DETECTING AND TRACKING SOLAR ACTIVE REGIONS

Data Type	Identifier	Explanation
Feature Array	$M_{PSL,t,i}$	polarity separation line mask
	$M_{PSL,thin,t,i}$	thinned polarity separation line mask
Property Value	$L_{PSL,t,i}$	$\sum_{pix} M_{PSL,thin,t,i}$
	$L_{sg,t,i}$	$L_{PSL,t,i} > 50 \text{ G Mm}^{-1}$
	$R_{t,i}$	R -value: flux near a PSL
	$R_{t,i}^*$	$\sum_{pix} (M_{PSL,t,i} * \text{Gauss}_2D) \times B_{t,i}$
	$WL_{sg,t,i}$	non-potentiality gauge
	$WL_{sg,t,i}^*$	$\sum_{pix} M_{PSL,t,i} \times \nabla B_{t,i}$

Table 4.2: Feature magnetic properties derived from polarity separation line characterization.

magnetograms. A subset of these are derived from 96 minute LOS data and those output by SMART are included in Tables 4.1 and 4.2.

The SMART characterization process utilizes the feature mask (IGM_t) retrieved by the methods outlined in the previous section, following the procedure detailed in Figure 4.6. This mask contains all of the features visible on the solar disk at a given time. The property measurements are derived from the magnetogram taken at time, t which is processed in the manner detailed below. We subscript the mask containing all features by i to extract a single feature mask, $IGM_{t,i}$. A cosine-corrected pixel-area map, $A_{cos,t,i}$, is constructed that contains pixel areas corrected to solar surface area rather than plane-of-sky area, and is summed to yield total feature area, $A_{tot,t,i}$.

Full-disk magnetograms $B_{t-\Delta t}$ and B_t are processed as in Section 4.2.1 (thresholding, LOS correction, $B_{t-\Delta t}$ differentially rotated to time t), but without smoothing. Single features are extracted for magnetic property determination using the indexed grown mask,

$$B_{t,i} = IGM_{t,i} \times B_t , \quad (4.1)$$

yielding an array where all pixels but those in the feature are set to zero. The processed magnetograms are subtracted and divided by their time separation to yield a map of the temporal change in field strength, $dB/dt|_t$, leading up to time t . This is combined

4.2 Feature Extraction

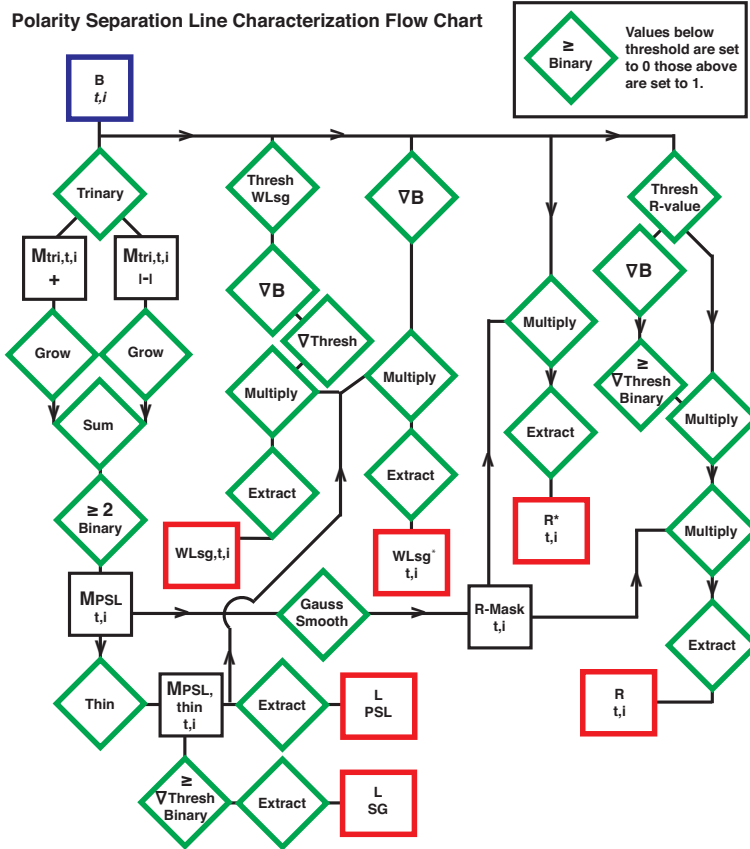


Figure 4.7: Flow chart summarizing the quantities derived from feature polarity separation lines.

with $A_{cos,t,i}$ to determine the flux emergence rate, $d\Phi/dt|_{t,i}$, of feature i .

The extracted $B_{t,i}$ is used to extract other properties from feature i (as detailed in Table 4.1) such as statistical moments of the magnetic field and the minimum and maximum magnetic field values ($B_{min,t,i}$ and $B_{max,t,i}$). $B_{t,i}$ is multiplied by $A_{cos,t,i}$ to derive the total positive, negative, and unsigned flux ($\Phi_{+,t,i}$, $\Phi_{-,t,i}$, and $\Phi_{uns,t,i}$), the relative flux imbalance ($\Phi_{imb,t,i}$), and the net flux emergence rate ($d\Phi/dt|_{net,t,i}$).

The extracted feature magnetogram, $B_{t,i}$, is also used to derive properties based on the polarity separation line (PSL). Figure 4.7 summarizes the extraction of feature properties related to PSLs and Table 4.2 lists the properties derived. Initially, the feature is segmented into its positive and negative components. These components are

4. DETECTING AND TRACKING SOLAR ACTIVE REGIONS

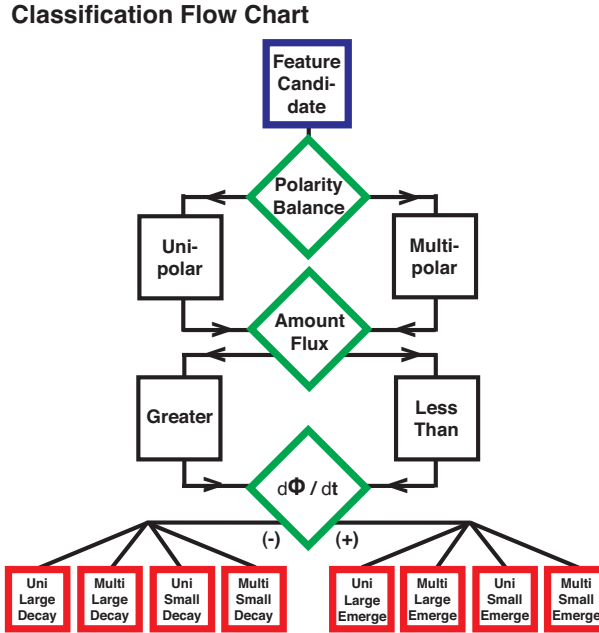


Figure 4.8: Flow chart summarizing the feature classification method.

used to create a positive and negative mask, each of which is dilated by 4 pixels. The two masks are summed and the region of mask overlap becomes the PSL binary mask, $M_{PSL,t,i}$. The algorithm then thins¹ $M_{PSL,t,i}$ to a single pixel width ($M_{PSL,thin,t,i}$) and sums the non-zero pixels to determine the PSL length ($L_{PSL,t,i}$). $L_{sg,t,i}$ is obtained by summing only those pixels which have $\nabla B_{t,i} > 50 \text{ G Mm}^{-1}$, where $\nabla B_{t,i}$ is calculated by numerical differentiation using 3-point Lagrangian interpolation.

We also calculate the R-value ($R_{t,i}$) as presented in Schrijver (173) and the WL_{SG} gauge ($WL_{sg,t,i}$) as presented in Falconer *et al.* (57). R-value is the amount of total flux near a PSL and WL_{SG} is the sum of the gradient along a PSL. Both of these use specific gradient and magnetic field thresholding when extracting the PSL. These measures are important for flaring, as shown by the investigation in Chapter 5. Using $M_{PSL,t,i}$ we calculate $R_{t,i}^*$ which is a more sensitive version of the R-value, since it

¹Thinning is done using a morphological algorithm including a sequence of erosions using specific kernels. The IDL M_THIN routine is used, as described on page 25 of http://www.cis.rit.edu/class/simg782/lectures/lecture_04/lec782_05_04.pdf

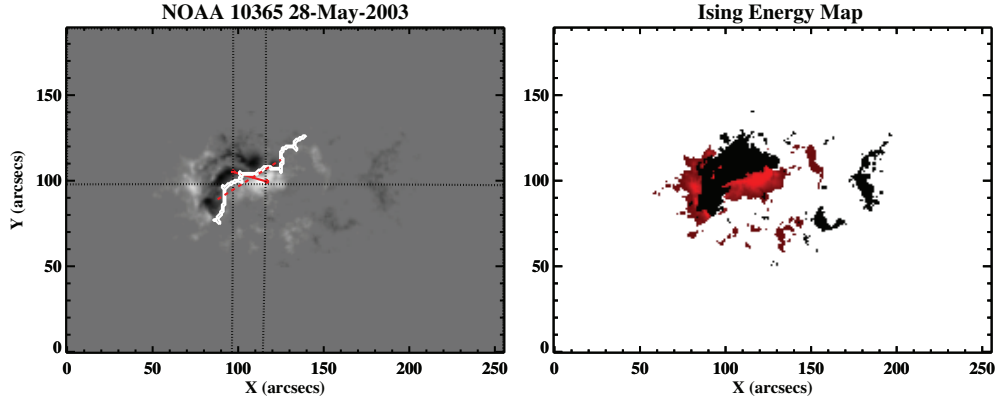


Figure 4.9: Left: NOAA 10365 highlighting the PSL (white contour), a linear fit to the locus of PSL positions (dotted red line), bipolar connection line (solid red line), and heliographic longitude and latitude reference lines (dotted black lines). Right: An Ising energy map of the same region. Red represents the magnitude of energy for each pixel from highest (light) to lowest (dark). Since the connection between pixels of opposite polarity is being represented, the energy map is only shown for one of the polarities.

contains no gradient thresholding and the magnetic field threshold of ± 70 G is much lower than the ± 150 G used in Schrijver (173). The algorithm convolves $M_{PSL,t,i}$ with a 20×20 pixel² kernel containing a 2D gaussian with a FWHM of 10 pixels, which is multiplied by $B_{t,i}$ and summed to achieve $R_{t,i}^*$. Similarly, an alternative of $WL_{sg,t,i}$, $WL_{sg,t,i}^*$ is calculated by applying the Falconer *et al.* (57) method, but using a magnetic field threshold of ± 70 G and no gradient threshold. The measures, $R_{t,i}^*$ and $WL_{sg,t,i}^*$ are useful for characterising small, weak, or emerging features that may not have developed strong PSLs and may have $R_{t,i}$ and $WL_{sg,t,i}$ values equal to zero.

A set of data structures is created for each magnetogram including the above mentioned properties of each extracted feature (used for classification; Section 4.2.4) and the feature’s heliographic location and time of measurement (used for feature tracking; Section 4.3).

4. DETECTING AND TRACKING SOLAR ACTIVE REGIONS

4.2.3 Secondary Characterisation Modules

Several auxiliary physical property modules have been designed, used in their original form, or adapted and run on SMART detections for the investigations presented in Chapter 5. The modules measure the orientation of the sunspot group magnetic polarities, a proxy for multi-scale energy distribution, and proxies for the magnetic interconnectivity of magnetic elements within a sunspot group. While these properties are not linearly independent as they are all related to polarity mixing, used in conjunction they give a more reliable picture of the evolution of sunspot group magnetic fields.

The tilt of a sunspot group is obtained by measuring the angle between the line connecting the centroids of the positive and negative blobs of largest flux (solid red line in left panel of Figure 4.9) and the heliographic latitude line passing through the centroid of the sunspot group. The length of this bipole connecting line (BCL) line is also determined and provides a measure of relative compactness when compared to the evolution of total area (left panel of Figure 4.9). Additionally, the angle (α) detected between the best-fit line to the locus of pixels forming the main PSL and the BCL is measured. The main PSL is defined as that separating the aforementioned largest flux-weighted positive and negative blobs. The temporal derivative of the angle α is shown to be a useful proxy for the occurrence of helicity injection (135), which may be an important flare predictor (110). The evolution of this angle is studied in Chapter 5.

These properties are less informative when studying sunspot group complexes or non-bipolar groups, since often no main axes can be discerned, making a description of the group's orientation impossible. Complexes are often highly flare-productive, so an assessment of separate regions within a single complex would be useful. This could be done by dividing up a complex into constituent regions using the more compact white-light signatures of sunspots.

Here, the complexity of sunspot groups is defined by the mixing of opposite polari-

ties. A dipole is considered less complex than a group with a quadrupolar configuration. Since magnetic connectivity is thought to depend on the distance between regions of opposite polarity, it is used to indicate complexity. The magnetic free-energy available for flaring is thought to be larger in more interconnected and complex sunspot groups(58; 73; 174). The properties used in this work as proxies for inter-connectivity and complexity in sunspot groups, “B-effective” (B_{eff} ; 73) and Ising energy (3), are known to be related to flare productivity. Large values of either one have been shown to indicate the flare productivity of a sunspot group. The calculation of each is explained in depth in the original papers but a summary is given here.

To calculate B_{eff} simulated annealing¹ (154) is used to determine the connections between flux elements (each can be connected to two other elements), which simultaneously minimizes the distance between those elements and the flux imbalance in a magnetic region,

$$F = \sum_{i=1}^m \sum_{j=1}^l \left(\frac{|r_i - r_j|}{|r_i| + |r_j|} + \frac{\phi'_i + \phi'_j}{|\phi'_i| + |\phi'_j|} \right). \quad (4.2)$$

Then,

$$B_{eff} = \sum_{i=1}^m \sum_{j=1}^l \frac{\phi_{ij}}{L_{ij}^2}, \text{ for } \phi_{ij} \neq 0, \quad (4.3)$$

where the ratio of the net flux and distance between each connected element is summed over all elements.

Finally, Ising energy is determined in a similar way, but instead of using a minimization technique, the product of magnetic field values divided by the square of the distance between them is summed for all possible connections. Here we use a modified form of the equation given by Ahmed *et al.* (3). The version used in this work is calculated using,

$$\sum_{i,j} \left| \frac{B_i B_j}{D_{ij}} \right|, \quad (4.4)$$

¹Simulated annealing is a method of iteratively searching for a solution by minimising some function. The process is halted once the function returns a stable result.

4. DETECTING AND TRACKING SOLAR ACTIVE REGIONS

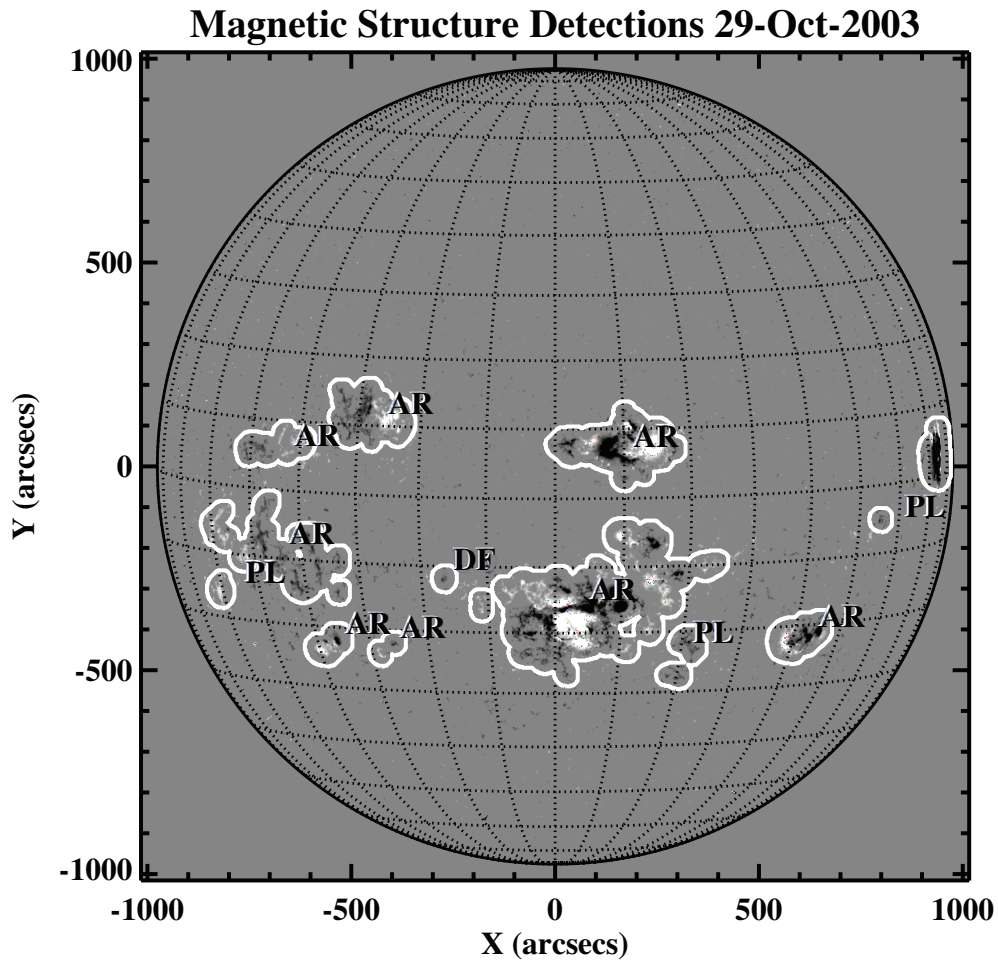


Figure 4.10: The set of SMART detections for 29 October 2003. Classifications for each detection are shown by the black labels. The detection types shown include AR (large multipolar), PL (large unipolar), and DF (small decaying unipolar).

where B_i (B_j) are pixel values of positive (negative) line-of-sight magnetic field and D_{ij} is the spatial distance between pixels i and j . The Ising energy increases as the negative and positive magnetic footprints within an active region become more entangled.

4.2.4 Classification

At this stage the SMART algorithm has characterized the properties of each automatically extracted feature. The classification process uses these properties to discriminate

between various feature types, which are saved in the algorithm output. Extracted features are initially grouped (as shown in Figure 4.8) into two categories: features with a flux imbalance (as defined in Table 4.1) greater than 90% are classified unipolar (U), while those having less than 90% are classified multipolar (M). The 90% threshold chosen is arbitrary and is not 100% to allow for small features of the opposite polarity to merge with the main feature and not change its classification to multipolar. After polarity balance, the total unsigned magnetic flux ($\Phi_{uns,t,i}$) is tested. Features with $\Phi_{uns,t,i}$ greater than 10^{21} Mx are classified as big (B), while features with $\Phi_{uns,t,i}$ less than 10^{21} Mx are classified as small (S). Finally, the sign of $\frac{d\Phi}{dt}|_{t,i}$ is tested to determine if features are increasing in flux (emerging, E) or decreasing in flux (decaying, D). This should indicate changes occurring over the dynamic time-scales of sunspot groups rather than those due to rotation on or off the solar disk, since the difference in flux is determined between consecutive images (nominally 96 minutes). The classification scheme results in eight possible feature classifications which are then also attributed to common magnetic feature designations: MBE and MBD are denoted evolving ARs; MSE and USE are denoted emerging flux concentration (EF); MSD, USD, and are denoted decaying flux concentrations (DF), and finally, UBE and UBD are denoted plage (PL). Plage can be described by extended unipolar regions of magnetic flux (see Section 1.7.2), and so is used as a designation here. These common designations are also saved in the algorithm output, allowing one to make a quick assessment of which regions on disk are interesting from a monitoring point of view. For example, EFs may become ARs and evolving ARs may produce activity during their evolution, while PL and DF are not likely to produce activity. An example set of classified detections is shown in Figure 4.10.

4. DETECTING AND TRACKING SOLAR ACTIVE REGIONS

4.3 Tracking

Having detected various solar features, the SMART algorithm associates features across different time intervals. Spatial and temporal information is used to track features between consecutive images (Section 4.3.1) and around the far-side of the disk between consecutive solar rotations (Sections 4.3.2). Features are then cataloged using the time of their first detection and their classification (Section 4.3.3).

4.3.1 Consecutive Images

The set of features in a magnetogram is compared with the previous five magnetogram sets to associate previously catalogued features with the current set. Feature positions ($HG_{pos,t,i}$) are differentially rotated, using the latitudinal dependence of the rotation rate derived in Howard *et al.* (102), to the same time t and features matched when their heliographic centroid separations are less than 5° . Features having one classification in previous sets may be associated with features having a different one in the current set. Thus, the SMART algorithm is capable of tracking possible ARs (MBE, MBD) back to their first emergence as an EF (MSE). Decaying features may also be associated with features previously denoted as possible ARs, allowing ARs to be followed through their final stages of evolution. Fragmentation often occurs in these late stages which SMART allows for since it does not preclude multiple features from being associated with a single previous feature. If one feature splits into two, each resulting fragment will be associated with the original feature if the resulting fragment positions are within the matching centroid-separation threshold of the original. A letter is appended to the catalog name of each additional associated feature so that individual fragments may be differentiated.

4.3.2 Far-side Passage

Features are tracked beyond the limb through multiple solar rotations to study their evolution from emergence to decay. We calculate the rotation period, $P_{rot,i}$, for each feature at time t , which depends on its heliographic latitude due to differential solar rotation. The feature position is compared to those in the five magnetogram sets centered on time $(t + t_{70}) - P_{rot,i}$ using the method in the previous section, where t_{70} is the time taken for the feature to rotate to 70° heliographic longitude from its position at t . In this approach the feature position is essentially rotated to a longitude of $+70^\circ$ then back one full solar rotation. In this way the feature is constrained to have been previously detected just before west limb passage, which increases the efficiency of the algorithm.

4.3.3 Cataloging

There are two identifications recorded for each detected feature in a magnetogram at time, t . The first, i is an index number that uniquely identifies the feature within a magnetogram and is obtained from IGM_t . The index number, i , also denotes the two-digit size order of the feature. The second identification is the static catalog name, YYYYMMDD.MG.NN, where YYYY is the four digit year, MM is the two digit month, and DD is the two digit day. The next two characters specify the feature type: MG denotes a photospheric magnetic feature and represents any SMART detections. This scheme can be expanded to incorporate coronal holes (CH), filaments (FI), and transient features such as flares (FL) and coronal mass ejections (CE) in EUV images. Finally, NN is i when the feature is given a static catalog name. This catalog name is determined once for each feature upon first detection, and is used for all measurements of the same feature as it is tracked through time.

4. DETECTING AND TRACKING SOLAR ACTIVE REGIONS

4.4 Results and Discussion

In this section we investigate the uncertainties involved in characterising the magnetic fields of sunspot groups using LOS photospheric magnetograms. The material presented in Section 4.4.2 is from (97) The finite resolution of the observations limits what can be said about the magnetic field magnitude, regardless of the method used to measure it (Section 4.4.1). Uncertainties due to the method used to detect and characterise sunspot groups are manifested in the stability of tracked detections (Section 4.4.2). These uncertainties are investigated further by simulating a feature on the solar surface and tracking its measured properties over time (Section 4.4.3).

Some calibration issues with the MDI data used by SMART are discussed in Wang *et al.* (215). It was found that the 2008 calibration of level 1.8 data has been partially corrected, in that it does not suffer from a disk center-to-limb variation like the 2007 calibration (205). However, MDI may largely underestimate the magnetic field as the ratio of MDI values to those retrieved from *Hinode*/Solar Optical Telescope data was found to be ~ 0.7 . This does not affect feature detections since the effect is consistent throughout the data set, but could contribute a considerable error of $\sim 30\%$ for any magnetic field or flux measurements. The data used in this work are level 1.8 data.

Strong magnetic field saturation in MDI data is discussed in Liu *et al.* (120). It is estimated that this phenomenon occurs in $\sim 5\%$ of sunspot groups, in which the magnetic field measurements in the umbral areas of very strong sunspots behave non-linearly. In extreme cases, the umbra may appear to have a smaller magnetic field than the surrounding penumbra. In reality, the field should continue to increase in the umbra, but in level 1.8 data showing NOAA 9002 at disk center, saturation is clearly observed at $\sim 3\,000$ G. Feature boundaries are not affected because saturation only occurs for very strong sunspot umbrae, although the derived magnetic properties of features which include strong sunspots will be underestimated.

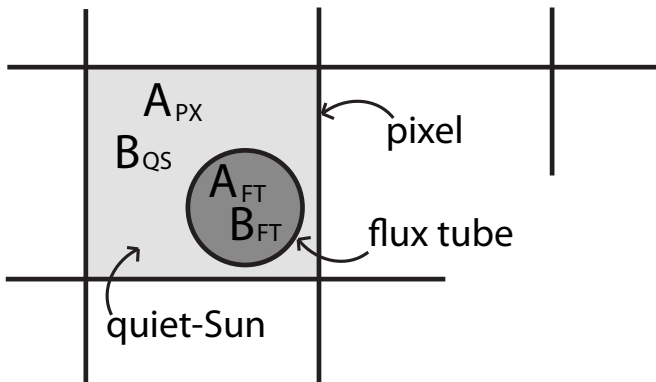


Figure 4.11: A schematic of an observation of a vertical flux-tube at the solar surface.

Another issue with using MDI magnetograms is the geometrical effect due to the use of LOS fields. As sunspots progress toward the limbs, the apparent magnetic field of the limb-ward penumbra can change polarity. Since penumbrae are close to horizontal, their field vector can dip below the plane perpendicular to the LOS, causing false PSL to emerge. This causes large errors in any property determination related to magnetic field gradient, such as PSL length.

4.4.1 Magnetic Filling Factor

When imaging the solar surface, the smallest feature that can be defined is limited both by the size of a single pixel and the size of the telescope aperture. This is due to the smearing effect of light diffraction within the telescope. There may be additional effects on the observed signal¹, resulting from other elements of the instrument design that are not well characterised in the literature. The optimum pixel size is the theoretical optical resolution² divided by 2.3, and is derived using the Nyquist theorem. For MDI, the pixel size is ~ 4 times that of the optimal pixel size (170), so the effect of diffraction should be negligible. HMI has a pixel size $\sim 30\%$ larger than the optimal size, so HMI

¹These effects are included in the instrument's point spread function (PSF), which indicates the spatial spread of an observed point source.

²The best achievable optical resolution of a telescope is $1.22\lambda/D$, where λ is wavelength and D is the diameter of the telescope aperture.

4. DETECTING AND TRACKING SOLAR ACTIVE REGIONS

should not be strongly affected by diffraction.

Consider a vertical magnetic flux-tube at disk center imaged by a magnetograph. It is likely that strong magnetic fields are bound into flux-tubes on the solar surface, so the magnetic field outside of them should be small in comparison. To simplify the problem we assume its magnetic field, B_{FT} , is constant over its cross-section. In reality the magnetic field must drop off at the edges of a flux tube since the field must be continuously differentiable. If the flux-tube cross-section perfectly fills the magnetograph resolution element, then the magnetic field measurement of the flux-tube has a filling factor of 1. In general the filling factor is given by,

$$f \equiv A_F/A_{px}, \quad (4.5)$$

where A_F is the cross-sectional area of a magnetic surface feature within a pixel and A_{px} is the area of a pixel. A schematic of this is shown in Figure 4.11.

The magnetic field measured, B_{OB} , is the average over a pixel. When $f < 1$, B_{OB} is between B_F and a presumably lower quiet-Sun field of the same polarity, B_{QS} . Thus,

$$B_{OB} = fB_{FT} + (1 - f)B_{QS}. \quad (4.6)$$

While the observed magnetic field is strongly dependent on f , flux is less so, depending on B_{QS} . Flux is given by,

$$\Phi_{FT} = A_{FT}B_{FT}, \quad (4.7)$$

$$\Phi_{OB} = A_{px}B_{OB}, \quad (4.8)$$

where Φ_{FT} is the flux of the flux-tube within a pixel and Φ_{OB} is the observed flux in a pixel. The measured flux will then be overestimated due to the quiet-Sun contribution.

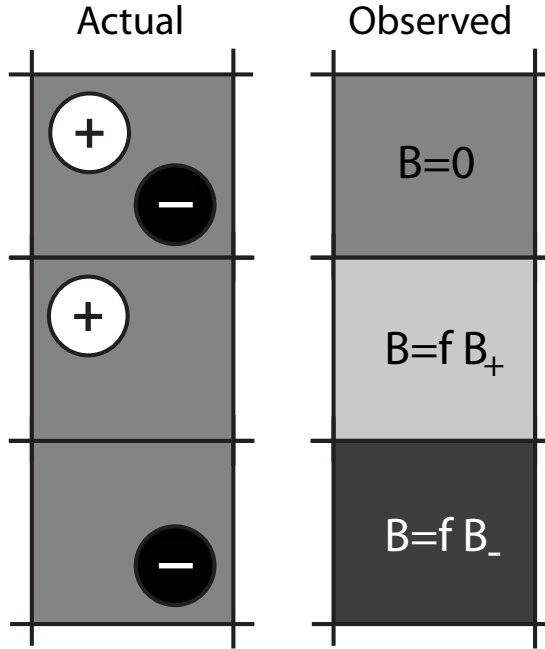


Figure 4.12: A schematic comparison between the actual configurations of flux-tubes in a pixel and what is observed. When two flux elements of equal area and field strength are present within a pixel, the observed field is 0.

However, if we assume that $f/(1 - f) \gg B_{QS}/B_{FT}$, then $\Phi_{FT} \approx \Phi_{OB}$ since,

$$\Phi_{OB} = A_{px}[fB_{FT} + \underbrace{(1 - f)B_{QS}}_{\text{negligible}}] \quad (4.9)$$

$$\approx A_{px}fB_{FT} \quad (4.10)$$

$$= A_{px} \left(\frac{A_{FT}}{A_{px}} \right) B_{FT} \quad (4.11)$$

$$\Phi_{OB} \approx A_{FT}B_{FT} = \Phi_{FT}. \quad (4.12)$$

Diffuse magnetic fields are likely to be grossly underestimated where flux tubes are spread out. So far, as new instruments achieve higher resolutions, they continue to resolve smaller magnetic features. The case is either that we have not yet observed the fundamental flux-tube, or that magnetic fields on the Sun are not bundled into flux-tubes but are self similar and scale-free and we will continue to observe ever smaller and

4. DETECTING AND TRACKING SOLAR ACTIVE REGIONS

features of similar complexity. On the other hand, since sunspot umbrae are composed of strong vertical fields densely packed in to contiguous structures, $f \approx 1$ in umbrae that extend over multiple pixels.

4.4.2 SMART Method Uncertainties

In the following sections we analyse the performance of sunspot group detection using SMART. These automatically detected and characterised data are compared to the manually detected NOAA sunspot group data (Section 4.4.2.1). Also, the uncertainties due to the MDI noise level are calculated (Section 4.4.2.2) and the tracking stability is determined Section 4.4.2.3. Tracking behaviour deviating from what is expected from NOAA is discussed (Section 4.4.2.4).

4.4.2.1 SMART-NOAA Comparison

Figure 4.13 summarizes a comparison of NOAA and SMART AR detections over the cycle 23, including numbers of detections and total feature area on disk. The top panel shows the total number of regions detected in each data set, arranged in monthly bins; the correlation coefficient between the (un-binned) NOAA and SMART daily detection data is 0.88. We determine how well the number of detected SMART and NOAA ARs match using the ratio of the number of observed NOAA to SMART AR detections on the solar disk each day: the ratio is between zero and one 6.4% of the time, equal to one 21.6% of the time, between one and two 60.3% of the time, and greater than two 11.7% of the time. We see a smaller number of SMART than NOAA AR detections in 72.0% of the time; the mean ratio of NOAA to SMART AR detections is 1.52. This is likely due to the joining of two or more nearby sunspot groups by SMART, while NOAA identifies each individual sunspot group, regardless of proximity¹. As such, SMART detections are representative of isolated magnetic systems, while NOAA detections represent a

¹NOAA may also detect very weak sunspots which may have a $\Phi_{uns,t,i}$ too small for designation as an AR by SMART.

4.4 Results and Discussion

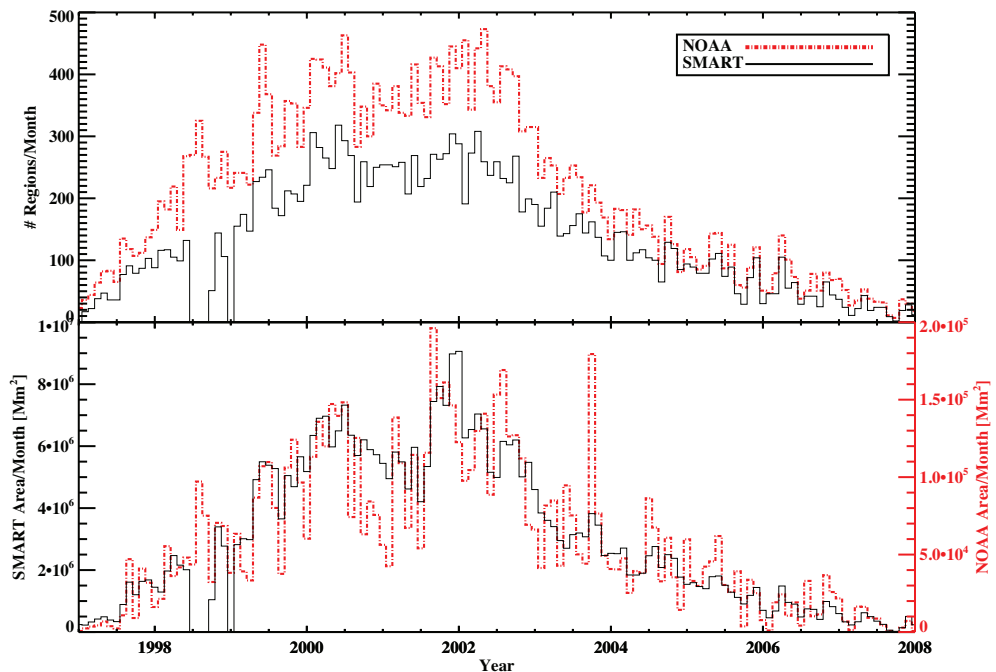


Figure 4.13: A comparison of NOAA and SMART AR detections over cycle 23. The data gap in 1998 is due to the loss of communications with the SOHO spacecraft for several months. The top panel shows the numbers of regions detected, while the bottom panel compares the summed area.

feature recognition approach. Although, NOAA records detections by eye, and only if they are visible in intensity data (i.e., if there is a magnetic flux concentration with no sunspot SMART may detect a region when NOAA does not). Clearly this is not as frequent as the grouping of multiple NOAA regions by SMART.

The bottom panel shows the total area of NOAA regions scaled to the total area of SMART regions. In fact, the NOAA area is lower by a factor of ~ 50 , since only the low-intensity area of sunspots is summed, while the area of extended magnetic features is recorded in SMART detections. The large discrepancy in area between NOAA and SMART around 2001 appears to indicate that the average size of spots within ARs decreased or that the magnetic area coverage increased, as compared with other times. But it is not clear why this would have occurred. Number and area are the only two feature properties which can be directly compared, as NOAA data do not contain any

4. DETECTING AND TRACKING SOLAR ACTIVE REGIONS

magnetic property measurements.

4.4.2.2 Data Uncertainties

The determination of the magnetic properties of a feature is affected by MDI magnetogram noise levels, calibration, strong field saturation, and LOS effects. The feature detection itself is generally not affected by these phenomena, however. The instrument noise threshold of MDI is nominally ± 20 G (165). This is smoothed by the gaussian convolution, and the segmentation threshold of ± 70 G is well above this. For magnetic property calculations, a gaussian convolution is not used, so noise contributes 20 G to the uncertainty of pixel values above the quiet-Sun threshold of 70 G. For SMART region 20031026.MG.11 observed at disk center on 25 November 2003, which is found to have an area of 3.8×10^4 Mm² and a total magnetic flux of 5.9×10^{22} Mx, the uncertainty is 7.9×10^{21} Mx, or 5.2%. This region is used as a test case because it is well studied, isolated, and is observed over multiple rotations. This allows multiple aspects of SMART to be tested and the results to potentially be compared to other work on this AR. The region is investigated in more detail in the following section.

4.4.2.3 Tracking NOAA 10488

An example of the SMART method of feature tracking and cataloging is shown in Figure 4.14. Region 20031026.MG.11 is tracked from 26 October 2003 to 26 December 2003. The AR rotates beyond the west limb and is detected again upon returning at the east limb twice. Although the AR is tracked to subsequent solar rotations its catalog name remains the same when it returns. NOAA first detects this AR on 28 October 2003 designating it as NOAA 10488. When the region returns it is designated a new region number, NOAA 10507 and is renamed upon the second return as NOAA 10525. SMART persistent naming through multiple rotations allows independent measurements of the same feature to be grouped into a single time plot.

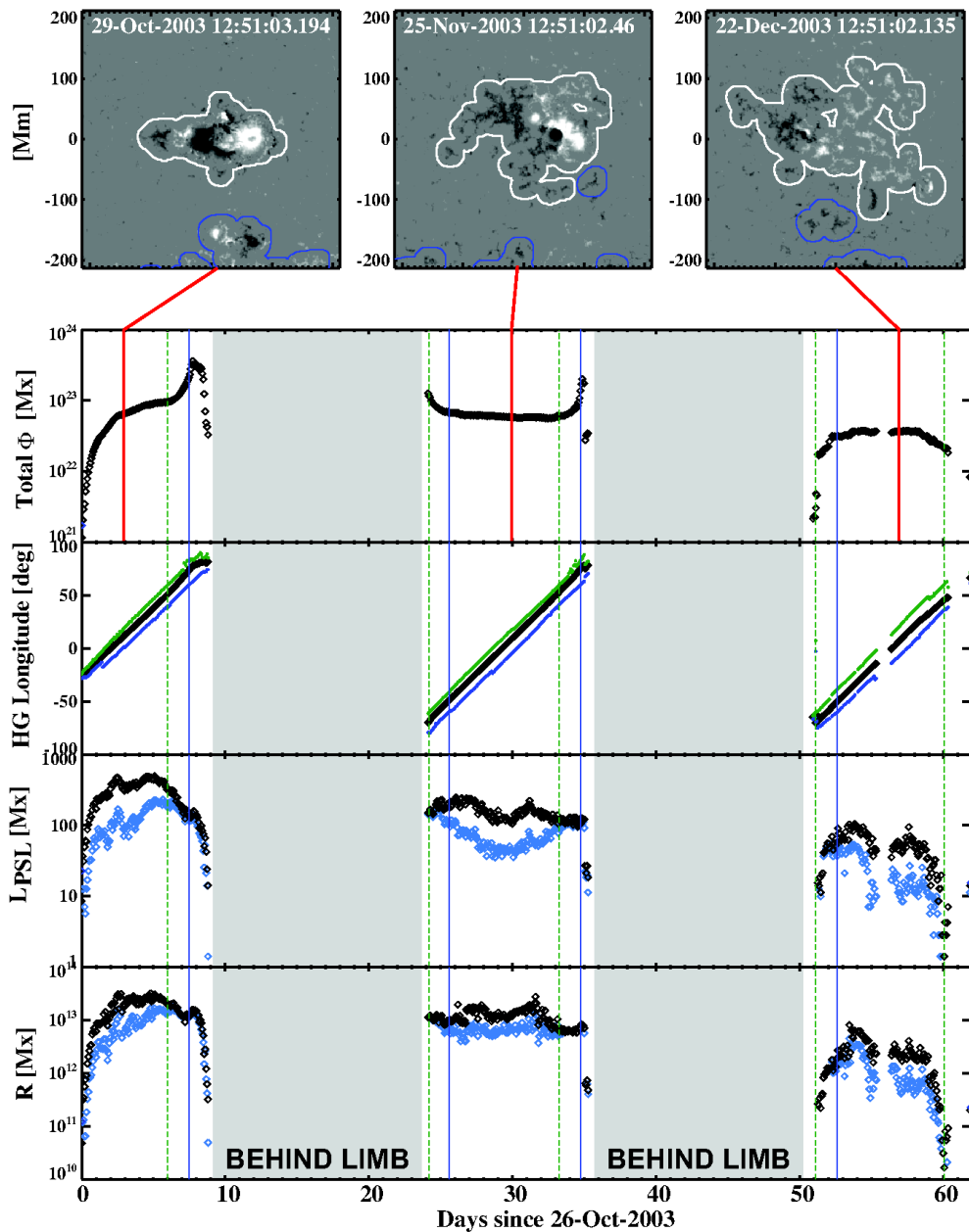


Figure 4.14: Tracking of 20031026.MG.11 (NOAA 10488) as it rotates around the Sun from 26 October to 26 December 2003. The top 3 panels show the AR near disk-centre during each disk passage. The time-series panels from top to bottom show properties of the AR: the total magnetic flux; the centroid heliographic longitude (black) and the eastern (blue) and western (green) edge longitudes; the PSL length (black) and strong-gradient PSL length (blue); R-value (black) and R^* (blue).

4. DETECTING AND TRACKING SOLAR ACTIVE REGIONS

The top panels in Figure 4.14 show MDI magnetograms of the region (clipped at $\pm 1\,000$ G) on three different dates, with the extracted AR outlined by a thick white contour (other detections on-disk are outlined in blue). A connecting red line shows where each falls on the timeline below. The remaining panels show, from top to bottom, time series of total unsigned flux, heliographic longitude, PSL length, and R-value extracted from 20031026.MG.11. Vertical dotted green (blue) lines denote crossings at ± 60 degrees of the leading (trailing) edge of the feature; in the second time plot, the green (blue) curve tracks this leading (trailing) edge in time. In the plot of PSL length, the black curve sums the length of all detected PSL segments, while the light-blue curve sums those having a gradient above 50 G Mm $^{-1}$. Finally, the plot of R-value shows R^* in black and R in blue. These measures indicate the amount of magnetic flux near any PSL (R^*) or near a strong-gradient PSL (R-value).

During the first disk passage of the AR, its first emergence occurs with rapid increase of magnetic flux and then levels off to a stable value. Very little change is observed during the following passage, and a slow decay is observed during the final passage. During periods where the AR is at the limb, the flux is much larger than at disk centre. This is a result of the cosine correction, which breaks down at the limb edge (see Section 4.4.3.1 for further discussion). The measures relating to the PSL all exhibit similar behavior. This first disk passage shows a spike after the initial emergence. The following passages have larger values near the limbs than at disk centre. This could be partially due to the geometrical line-of-sight effect that produces large errors in spatial gradients (see Section 4.4.3.2 for further discussion).

The stability of the algorithm is estimated using the plot of total flux between days 25.6 (20 November 14:24 UT) and 33.7 (28 November 16:48 UT). The location dependence of the AR's flux is well described by a quadratic function during this period; the AR is stable, but line-of-sight correction results in higher values at the beginning and end. A quadratic fit is subtracted to remove the long timescale variation, resulting

in an array of residuals. The residuals result from small magnetic features merging and splitting from the AR, due to supergranule motions. The manner in which this affects the property time series is a result of our region-growing technique. The two-sigma error of the residuals is determined to be 2.1×10^{21} Mx or 3.4% around the mean of total flux. This indicates the maximum short-term deviation with 95% certainty. The stability estimate is particular to this example, as cases such as those shown in Figure 4.15 could result in much larger short-timescale variation.

4.4.2.4 Tracking Behaviour Deviating from NOAA

There are several recurrent SMART feature tracking cases that diverge from the tracking behaviour of NOAA (Figure 4.15). NOAA ARs are first detected and given a NOAA number when a sunspot group is visible in white-light images. This designated number is persistent until the region rotates off the solar disk. The physical merging and splitting of regions is not taken into account. Each new sunspot group is given a number, regardless of whether it overlaps with a previous one.

The SMART tracking algorithm allows features to converge and to split apart. However, there may be side-effects, such as when a fragment separates from a larger feature and is given a new catalog name, due to the centroids of the two being greater than the tracking association threshold (top row of Figure 4.15). Also, an active region complex may be detected when there are multiple strong field ARs in close proximity (middle row). Finally, a bipolar region which is significantly disjointed and weak may not be properly grouped into a single region (bottom row). This is an example of where each polarity is detected as a separate region. As this work is designed to aid in flare forecasting, many examples of each of these cases may be studied to determine if they possess unexpected flaring properties. Also, their evolution maybe studied by tracking the features from first emergence. The frequency of occurrence for these special cases can be estimated using the data and analysis of Figure 4.13: when N_{NOAA} is greater

4. DETECTING AND TRACKING SOLAR ACTIVE REGIONS

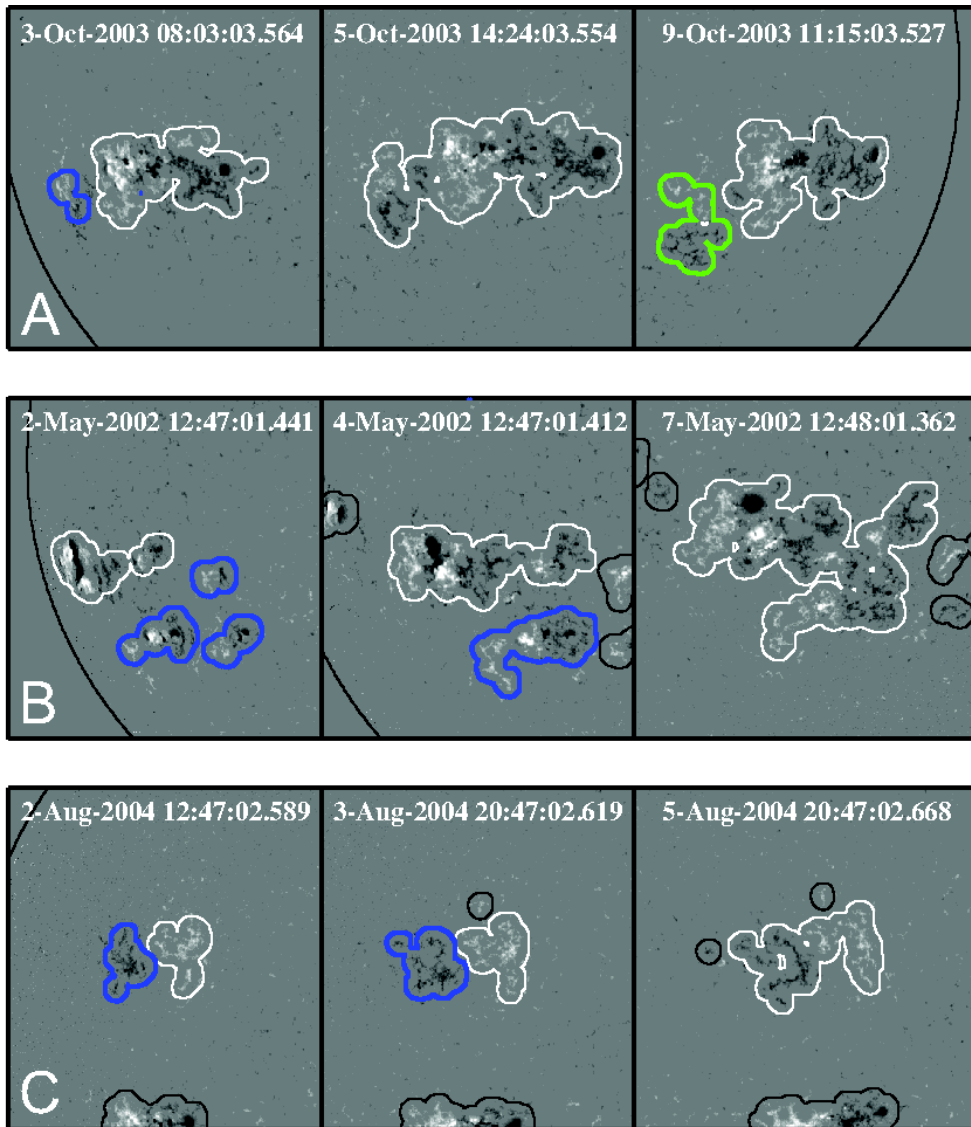


Figure 4.15: Feature detection and tracking cases which diverge from NOAA. A) Two bipolar regions join and subsequently fragment. B) Several small bipolar regions merge into an AR complex. C) A bipolar region is first detected as two unipolar features and then as a single bipolar region.

than N_{SMART} SMART is likely to group regions into AR complexes (or identifying NOAA ARs as EF or DF), and when N_{SMART} is greater than N_{NOAA} SMART may be detecting individual unipolar features when NOAA groups them into bipolar regions.

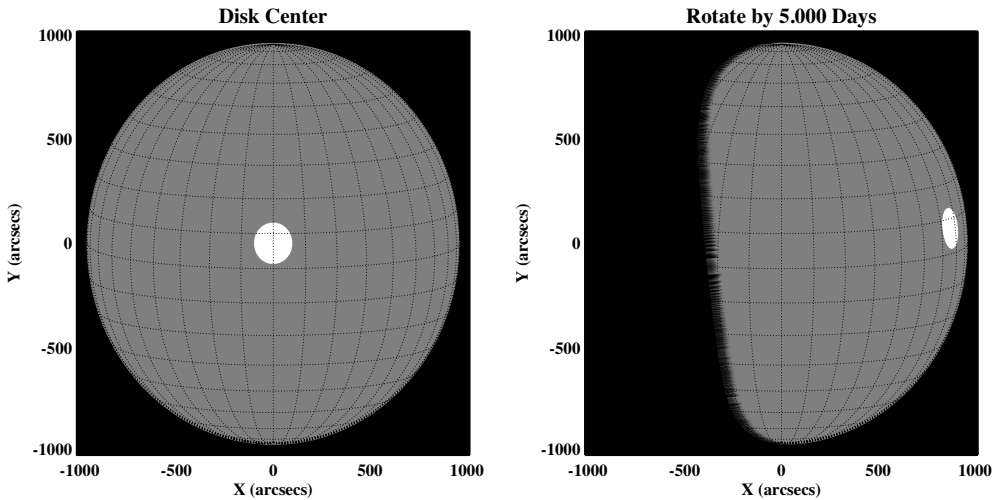


Figure 4.16: A simulation of a circular feature crossing the solar disk. The panels show the spot at disk center and past 60° longitude. This test represents the best-case scenario for the characterisation of a detection, since the feature begins at disk centre and has a simple morphology.

4.4.3 Simulating Feature Tracking

In the following subsections we run a series of simple simulations to test the reliability of methods used to determine the properties of sunspot groups. The longitude dependence of area for a circular spot (Section 4.4.3.1) is tested. The test is repeated for magnetic properties with a tilted magnetic bipolar feature (Section 4.4.3.2).

4.4.3.1 Area Detection of a Circular Feature

LOS effects occur when features are not observed at disk center. To estimate the effects of this the disk passage of a circular feature on the solar surface is simulated. The SSWIDL procedure DR0T_MAP is used to deproject and reproject the solar surface¹. This uses interpolation and assumes the (102) differential rotation profile. The simulated feature is shown in Figure 4.16. This simulation is performed using MDI's resolution, but the main results should be applicable to HMI and other instruments.

The area correction method used is described in Section 4.2.1. It is a pixel-by-pixel

¹http://hesperia.gsfc.nasa.gov/rhessidatacenter/complementary_data/maps/#s3.6

4. DETECTING AND TRACKING SOLAR ACTIVE REGIONS

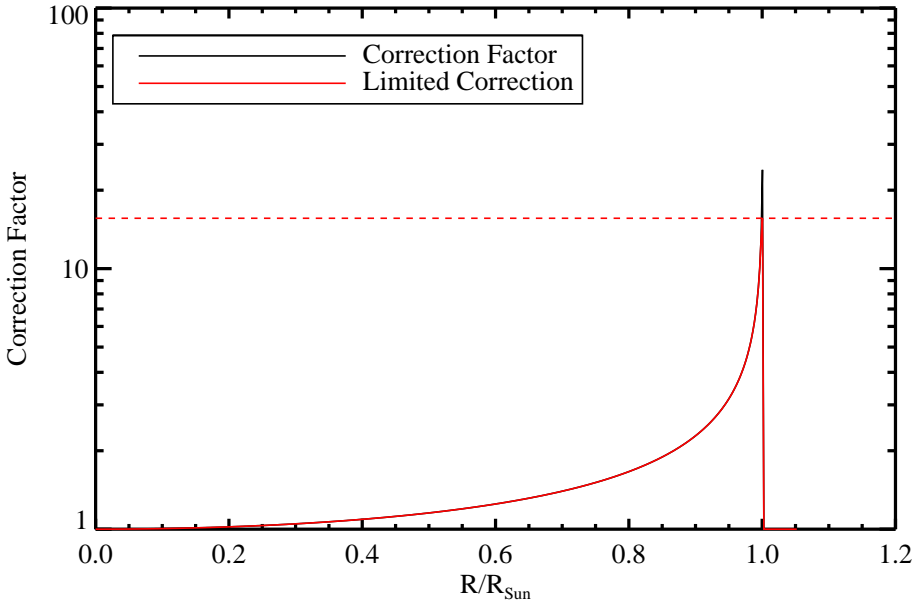


Figure 4.17: The area cosine-correction factor related to the apparent distance from disk center in solar radii. This is the factor used to determine the deprojected solar surface area covered by a given pixel. The correction factor is limited to ~ 15 , the factor for a pixel at the limb edge.

cosine correction factor, where the angle is measured between the normal vector to the solar surface at a given pixel and the LOS. Here we test limiting the correction factor to ~ 15 , that of a MDI pixel extending to the limb of the Sun (the maximum correction any pixel would have). A comparison between the limited and non-limited LOS correction profiles is shown in Figure 4.17. Limiting the correction factor reduces errors in determining the properties of extended magnetic features that reach the solar limb.

The comparison between the simulated apparent feature area, cosine-corrected area detected by SMART, and area detected by SMART limited to a correction factor of ~ 15 is shown in Figure 4.18. In this case, limiting the area correction is not important due to the simplicity of the tracked feature. The error in the detected area is shown to be less than 1% out to 60° longitude. This error depends on morphology and will be

4.4 Results and Discussion

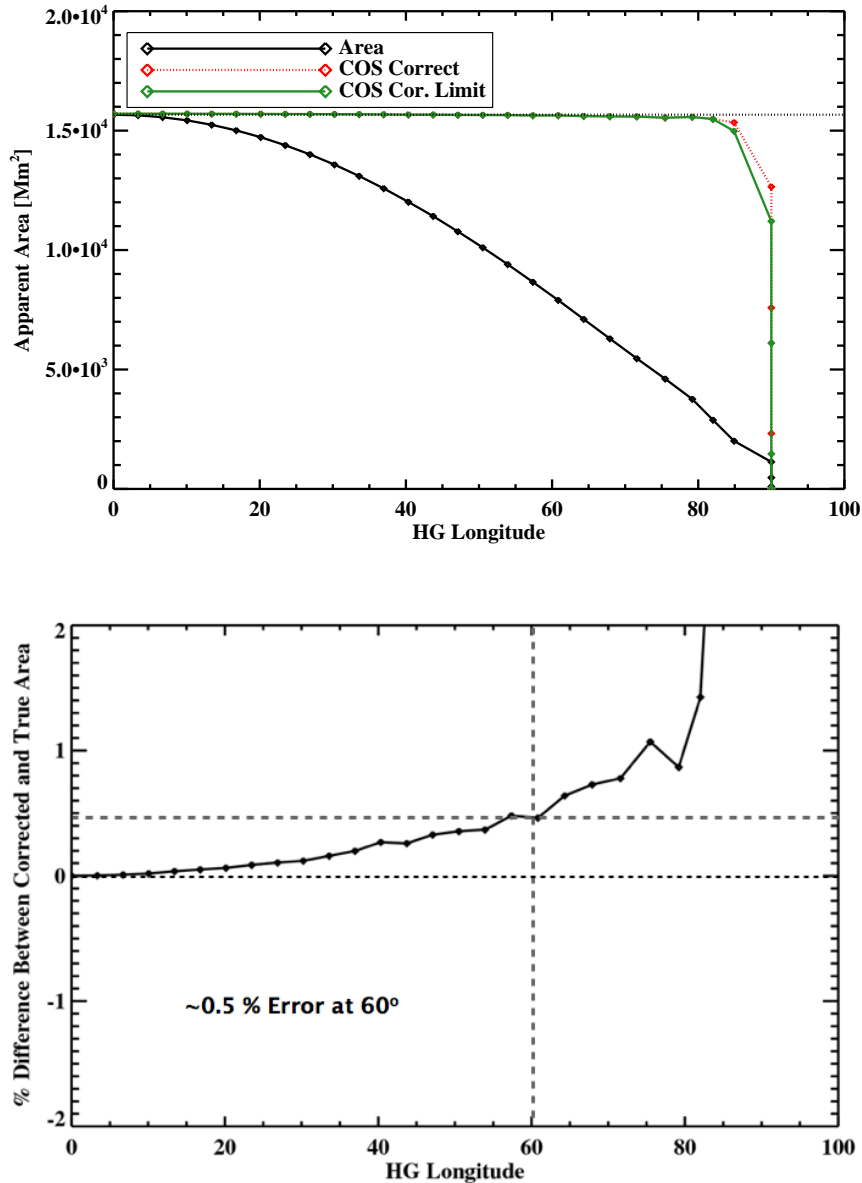


Figure 4.18: The reliability of circular surface feature area measurements with longitude. The top plot shows the apparent area of the circular feature decreasing as it progresses toward the limb. The black dashed line indicates the true area of the feature. The detected cosine-corrected area (red), and the detected area when the correction factor is limited to ~ 15 (green) are over plotted. The bottom plot shows the %-difference between the detected area (with the correction limited to ~ 15) and the true area. The black dashed line indicates the true area and the gray dashed lines indicate the data point at 60° for comparison.

4. DETECTING AND TRACKING SOLAR ACTIVE REGIONS

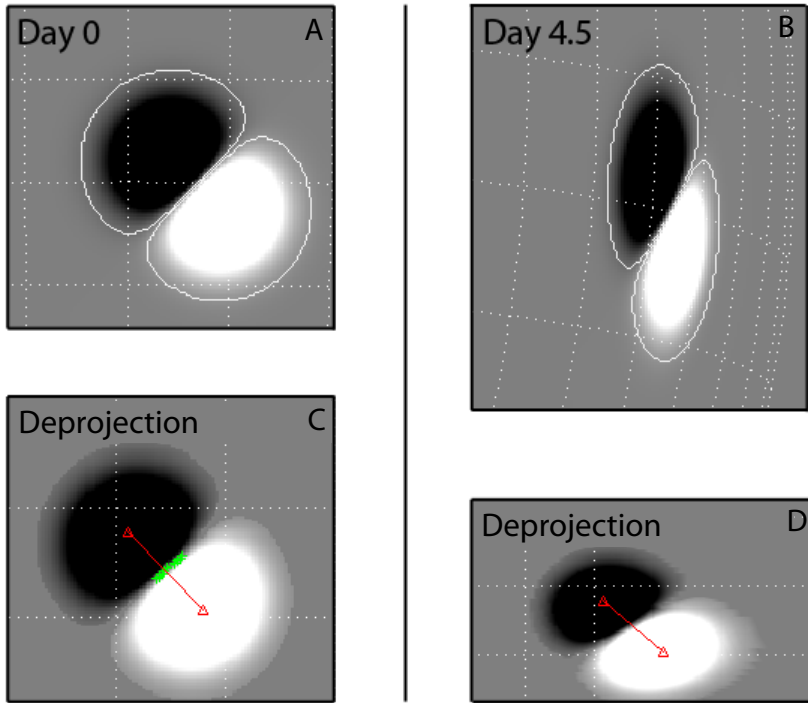


Figure 4.19: A simulation of a magnetic bipole feature crossing the solar disk. Bipole connecting lines are indicated by the red lines in the bottom panels.

more acute for complex feature boundaries.

4.4.3.2 Magnetic Properties of a Bipolar Feature

The superposition of a positive and negative 2D gaussian is used to simulate a bipolar magnetic feature crossing the solar disk. The full-width at half-max (FWHM) of the gaussians is ~ 30 Mm and the maximum magnetic field is 3 000 G. These values are meant mimic a typical sunspot group. This is a simplified representation of a compact magnetic bipole with a trailing high latitude negative sunspot and a leading positive sunspot, tilted toward the equator. The methods of projecting the feature onto the solar disk and simulating differential rotation are the same as that described

4.4 Results and Discussion

in Section 4.4.3.1. In addition to area, we determine the total flux, horizontal magnetic gradient and inclination angle of the PSL with respect to the BCL. Sections 4.2.2 and 4.2.3 describe the methods of determining these detected properties. Figure 4.19 shows the resulting bipole simulation with the apparent LOS projections in the top panels for disk center (A) and near the limb (B). The bottom panels (C and D) show the deprojections of the images into latitude-longitude space. Some distortion is observed at the west-ward edge of the deprojection in panel D, which is because latitude-longitude space becomes increasingly non-conformal¹ near the limb. The deprojected images are only used to determine the PSL and BCL orientation angles, so the distortion will not affect the area and flux measurements.

The area of the bipole is determined by creating a mask of the feature using a threshold of 70 G. This is the threshold used in Section 4.2.1 to detect magnetic features. The area is then corrected as described in Section 4.4.3.1. Likewise the total magnetic flux is summed within the masked region. Since the simulation does not include a cosine decrease of the field with longitude (the fields are all simulated to be normal to the solar surface), only a correction for the area is needed. The detected area and flux exhibit a \sim 6% error at 60° longitude. The main source of the error is the overestimation of area due to the shape of the feature PSL ends; the detection boundary has two dents, as shown by the white outline in panels A and B of Figure 4.19. These dents become less resolved and the detection boundary appears more smooth when the simulated feature is near the limb.

The measurement of gradient is performed as described in Section 4.2.2. The error in gradient increases rapidly as the bipole progresses toward the limb. This is not surprising as the apparent separation between the two polarities decreases, while the field strength is constant. The error at 30° is already significant at \sim 15%. Any statistical study of sunspot group properties using gradients will be strongly affected by the

¹Conformal projections mean that features keep their shape, while non-conformal projections result in stretching.

4. DETECTING AND TRACKING SOLAR ACTIVE REGIONS

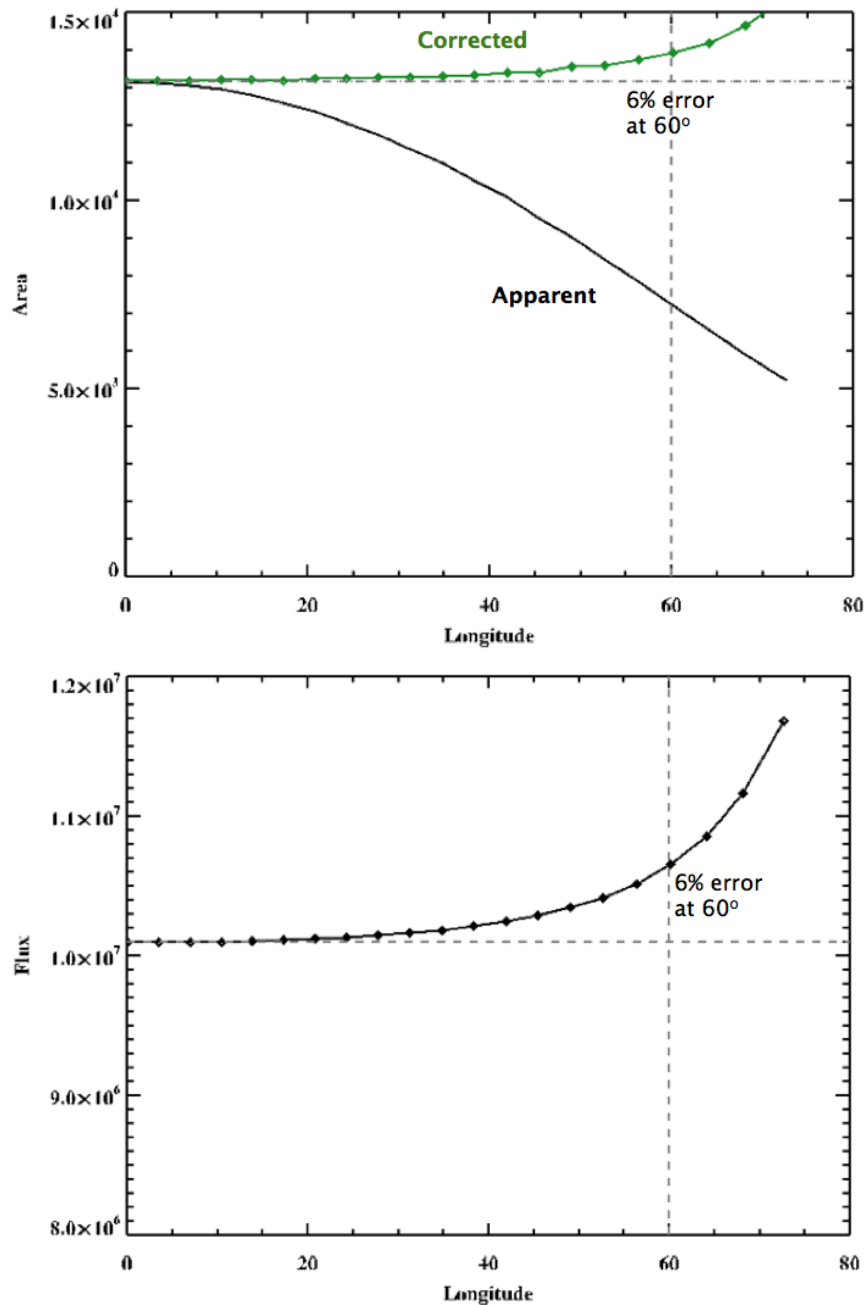


Figure 4.20: Plots of the apparent (black) and detected corrected area (green; *top*) and detected total flux (*bottom*). The horizontal dashed lines in each plot represent the true values of the properties.

4.4 Results and Discussion

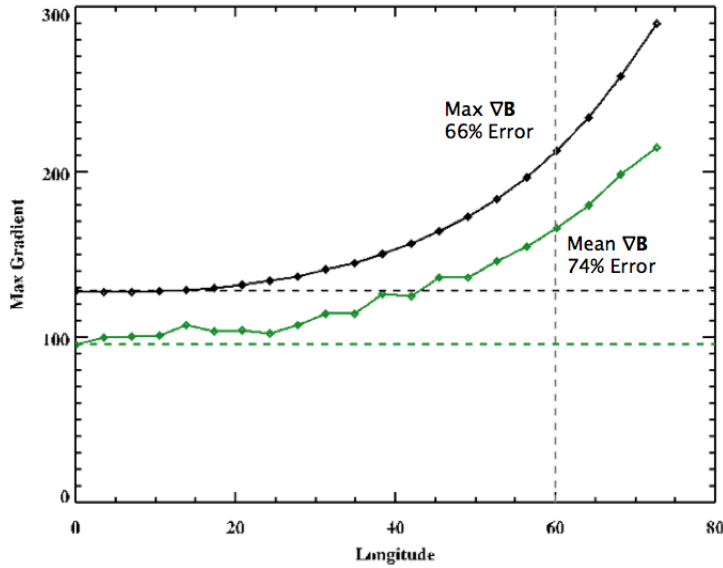


Figure 4.21: The longitude dependence of maximum (black) and mean (green) magnetic field gradient. The horizontal dashed lines indicate the true values of each property.

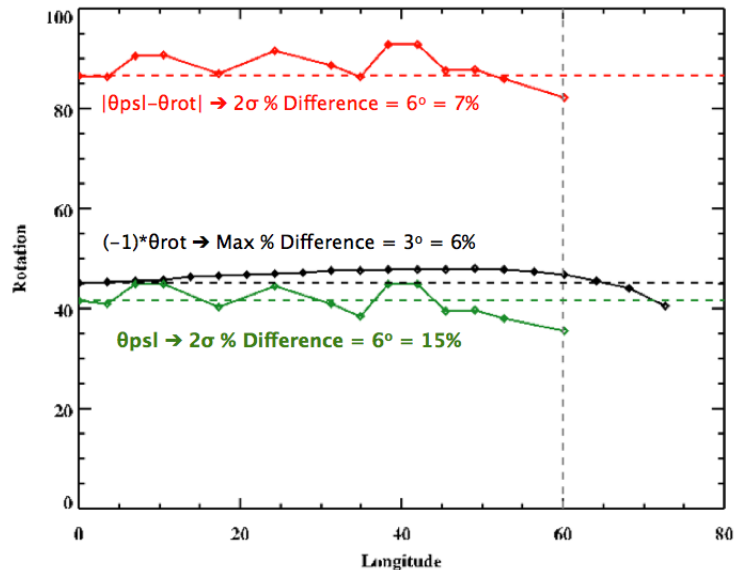


Figure 4.22: The longitude dependence of the BCL (black; multiplied by -1) and PSL (green) orientation. The difference in orientation between the BCL and PSL is plotted in red.

line-of-sight dependence of the observations.

The PSL is detected using the method described in Section 4.2.2. The error in

4. DETECTING AND TRACKING SOLAR ACTIVE REGIONS

the measurement of BCL inclination and PSL inclination are not strongly dependent on longitude. The errors in these inclinations range between 5% and 15%. The BCL orientation varies smoothly but the PSL orientation appears to vary randomly. The main source of the error in this simulation is likely due to the use of gaussians, which result in very small PSL detections. Detecting the orientation of a line defined by only a few pixels is highly sensitive to the deprojection interpolation.

This simulation assumes that the fields in the bipole are perfectly radial and that we have corrected the fields perfectly. The uncertainty introduced by inclined penumbral fields has not been accounted for. When determining the flux of a sunspot at disk center, we will be underestimating the fields since there will be only a very small LOS component of the penumbral field. Toward the limb, false PSLs may be introduced as the horizontal penumbral fields dip below the plane of sky and are measured as the opposite magnetic polarity to their true value at the solar surface. This causes a large error in any property determination using the horizontal field gradient.

4.5 Conclusions

In this chapter, the SMART method is described and characterised. It is run on a large magnetogram data set, is benchmarked against another detection method, and its performance is tested using simulated data sets.

- SMART is the first completely automated magnetic feature detection algorithm that detects, characterises, and tracks surface features over multiple solar rotations.
- The use of MDI LOS magnetograms leads to certain situations in which SMART results are unreliable, such as determining magnetic properties away from disk centre that involve gradients.
- The detection and tracking method is stable in time and its use results in a similar

representation of the sunspot cycle to that obtained from NOAA results.

The following sections provide more detail on these points.

4.5.1 The SolarMonitor Active Region Tracker

The SMART algorithm allows one to monitor ARs on the solar disk in near-realtime and perform extensive studies of AR magnetic properties. SMART is unique among automated AR extraction algorithms in that it allows the temporal analysis of magnetic properties from emergence and through multiple solar rotations. Previous algorithms include some of the functions performed by the SMART algorithm, such as feature and magnetic parameter extraction. However, new utilities are incorporated into SMART, such as day-to-day and multiple rotation feature tracking. Extensive AR properties such as area ($A_{tot,t,i}$) and total magnetic flux ($\Phi_{uns,t,i}$) are determined, as are intensive properties such as the maximum magnetic field ($B_{max,t,i}$) and statistical moments ($\mu, \sigma^2, \gamma, \kappa$). Some algorithms, including LaBonte *et al.* (110) only detect the largest regions, while others like Colak & Qahwaji (39) only detect ARs with sunspots in white-light images. All current algorithms track ARs using visually identified NOAA specifications. The SMART algorithm is independent from these specifications and needs no human intervention to detect and track ARs. Additionally, it utilizes an improved feature cataloging system which incorporates the date of first detection and the feature type¹.

4.5.2 Observational Uncertainties

The studies presented in this chapter show that the combination of MDI magnetograms and automated detection methods cannot be used to reliably determine the true magnetic field of the Sun. Several sources of error accumulate to result in data products

¹Incidentally, this cataloging system is very similar to the SOL number presented by Schrijver *et al.* in <http://spd.aas.org/SolarNews/archive/news.2009/15.aug> and can easily adapted to match its structure.

4. DETECTING AND TRACKING SOLAR ACTIVE REGIONS

that can only indicate the order-of-magnitude of the magnetic field. These sources of error are a result of the MDI instrument design, calibration, the physical structure of sunspots, and the automated methods used to detect them as discussed throughout this chapter.

The MDI instrument performs a sparse sampling of the Ni I spectral absorption line. This leads to strong magnetic fields being less trustworthy, as the Zeeman splitting becomes more complex. Since only LOS magnetic fields are measured, complicated magnetic field geometries, such as those in penumbrae, are poorly measured. The use of onboard MDI data processing has resulted in large errors within strong penumbrae. Weak fields measured in the quiet Sun suffer from the significant (nominally) 20 G noise of the instrument. However, plage fields are high enough above the noise level and low enough below the saturation level and should be, at the least, linear.

With these problems in mind, it is sensible to ask why MDI is used in this work. The instrument covers more than an entire solar cycle, allowing for long time-scale studies. The time coverage is extremely stable, with \sim 15 evenly spaced images available per day, save for the period at the end of 1998 when Solar and Heliospheric Observatory (SOHO) was out of contact. The instrument does not suffer from the seeing, weather, and night-time that ground-based instruments must deal with¹. So, MDI is very useful for statistical studies of sunspot group properties, as the regimes over which the properties are reliable are predictable.

4.5.3 Method Uncertainties

The automatic detection and characterisation algorithm, SMART, is shown to have very good stability in tracking features through time. This indicates that while the algorithm diverges from the detection and tracking behavior of NOAA, it is very useful for performing studies of the evolution of sunspot group properties.

¹There is a whole-earth observatory that produces magnetograms, but seeing conditions vary wildly at each observing location.

4.5 Conclusions

With regards to physical properties, we have shown that flux values are more useful than magnetic field values since flux is conserved, while the magnetic field is averaged over a pixel. Also, the properties determined for features with more complex morphologies are less reliable away from disk center than those with simple morphologies. The gradient values are especially problematic away from disk center. Despite this, near disk center they are extremely useful as flare indicators, as will be shown in Chapter 5.

Any future flare forecasting algorithm which makes use of magnetic properties output by SMART will need to take into account several sources of error. Random errors including magnetogram noise and algorithm stability for the example presented in Section 4.4.2 result in an error of $\pm 5\%$ and $\pm 3\%$ in $\Phi_{uns,t,i}$, respectively. This will not affect the forecasting potential of properties involving $\Phi_{uns,t,i}$ for a sufficiently large sample of regions. Calibration errors in MDI result in an underestimate of the true magnetic field on average by $\sim 30\%$. If the forecasting training set and test samples both exhibit this error, the prediction result will not be affected. However, for physical studies of energetics this must be taken into account. Finally, LOS effects which occur as regions approach the limb cause large measurement errors past 60 heliographic degrees from disk center, which limits the potential flare forecasting range of this algorithm.

4. DETECTING AND TRACKING SOLAR ACTIVE REGIONS

5

The Flare Productivity of Sunspot Groups

The flare productivity of detected magnetic features is investigated in this chapter. The magnetic properties that are most strongly associated with flaring are determined. SMART (Chapter 4) is used to detect and track features to determine the relationship between physical evolution and the onset of flaring. Case studies (performed by Higgins) are presented that were first published in Verbeeck & Higgins *et al.*, *Solar Physics* (2011) and Bloomfield, Carley, Gallagher & Higgins *et al.*, *Astronomy & Astrophysics* (2012). A large sample of feature detections is then associated with flares, allowing magnetic property thresholds for different levels of flare activity to be determined. Finally, the global flare productivity of the Sun is compared to combined property values of detected features on disk. Higgins performed the work included in this chapter (Section 5.2) that was first published in Section 4.3 of Verbeeck & Higgins *et al.*, *Solar Physics* (2011) and Section 3.1 of Bloomfield, Carley, Gallagher & Higgins *et al.*, *Astronomy & Astrophysics* (2012).

5. THE FLARE PRODUCTIVITY OF SUNSPOT GROUPS

5.1 Introduction

Many metrics, postulated to be related to flaring, have been developed to characterise sunspot group magnetic fields. These metrics are generally treated as proxies for physical quantities or qualitative descriptions of magnetic field configurations that cannot be directly measured. Proxies for non-potentiality include measurements of strong horizontal magnetic gradients (57; 70). Those extrapolating the 3D topology include measurements of free magnetic energy (158), twist (40), and multipolar moments (226). Proxies for complexity and polarity mixing include fractal indices (41; 42; 125), multi-scale power spectrum slope (96), and magnetic connectivity (73). The overall aim of these algorithms is to first extract a physically-motivated measure of the characteristics of a region of interest. Subsequently, this information is used to better understand the fundamental physics of active regions (ARs), and to relate the properties of AR magnetic fields to their flaring potential. A limitation of this is that if an AR has the potential to produce a flare, it means that a flare is possible, but not that one will definitely occur.

A particular time-dependent phenomenon that is reliably known to lead to flaring must be identified to know when an active region will actually produce a flare. So far, the best known flare indicator is the occurrence of other flares (70; 221). Flux emergence is also a good indicator (117; 181). Mason & Hoeksema (123) use superposed epoch analysis to show that various properties, such as a gradient-weighted PSL length, increase prior to flare occurrence and decrease afterward. Currently, sufficiently reliable flare indicators have not been identified and it remains impossible to predict when a flare will occur with any certainty (130).

In this chapter, the flare productivity of sunspot groups is investigated. The activity throughout the evolution of two sunspot groups is studied in detail (Section 5.2) to identify flare indicators in the time dependence of their magnetic property values. A

large sample of sunspot group detections is analysed to determine which properties are most indicative of the level of flaring to be expected and what minimum values of those properties are necessary for each flare magnitude to occur (Section 5.3). Finally, the solar cycle dependence of sunspot group properties is compared to the global flare productivity of the Sun (Section 5.4).

5.2 Case Studies

In this section, we analyse the time evolution and flare productivity of the sunspot groups that emerge as NOAA 10365 (210), a complex region, and NOAA 11226, which is related to the 7 June 2011 eruption (23). In both studies, we search for pre-flare signatures in the measured magnetic properties.

We investigate how activity in the corona results from changes in the photosphere in the study of NOAA 10365. Drawing a connection between photospheric and coronal sunspot group evolution is essential for flare prediction, since flares occur in the corona, within structures that are rooted in the photosphere. To perform this comparison, several automated detection and characterisation algorithms are used in addition to SolarMonitor Active Region Tracker (SMART). Automated feature detections using observations of magnetic fields, photospheric continuum intensity, and extreme ultraviolet (EUV) have not been previously compared. The corona is much more dynamic than the photosphere, so comparing the two atmospheric layers is difficult. The coronal evolution should indicate heating and flare activity, which is partially a result of the slower evolution of magnetic structures in the photosphere.

The Spatial Possibilistic Clustering Algorithm (SPoCA) detects features in coronal images (17) using a fuzzy-clustering algorithm in pixel-intensity space. Extreme ultraviolet Imaging Telescope (EIT) 171 and 195 Å EUV images are combined to produce a plot of pixel intensity in one image versus the other. This allows the pixels to be

5. THE FLARE PRODUCTIVITY OF SUNSPOT GROUPS

clustered in to “quiet”, “active”, and “coronal hole” classifications. Contiguous regions of each classification are grouped into detections.

Sunspot observations in the continuum around 6 768 Å (Michelson Doppler Imager (MDI) intensitygrams) are characterised using Sunspot Tracking And Recognition Algorithm (STARA) (216) and Automated Solar Activity Prediction (ASAP) (39). STARA uses morphological image processing to detect features of above a certain size scale and below a certain intensity. ASAP uses machine learning to detect regions in such a way as to match NOAA’s grouping of sunspots.

For the study of NOAA 11226, in addition to analysing the energy build-up phase in evolution, we also compare properties determined just before and just after a large flare that occurred. These short time-scale changes have been observed in the strength (199) and inclination (137) of magnetic fields for different sunspot groups. The work presented in this chapter is the first time that short time-scale changes have been investigated in both flux and magnetic connectivity.

Observations of NOAA 10365 and 11226 are compared with flares characterised by the Reuven Ramaty High Energy Solar Spectroscopic Imager (RHESSI) team and distributed in the RHESSI flare list¹. The flares, which have been associated with the individual sunspot groups by the RHESSI team, are represented as downward-pointing arrows in plots in the following sections, whose size is logarithmically proportional to their peak count rate.

5.2.1 NOAA 10365 (10386)

Active region NOAA 10365 rotates onto the visible solar disk on 19 May 2003 at heliographic latitude -5°. At this point 10365 is mature and decaying, having emerged and evolved on the far side of the Sun. On 24 May, a new bipolar structure rapidly emerges in the extended plage of the trailing (positive) polarity. National Oceanic

¹http://sprg.ssl.berkeley.edu/~jimm/hessi/hsi_flare_list.html

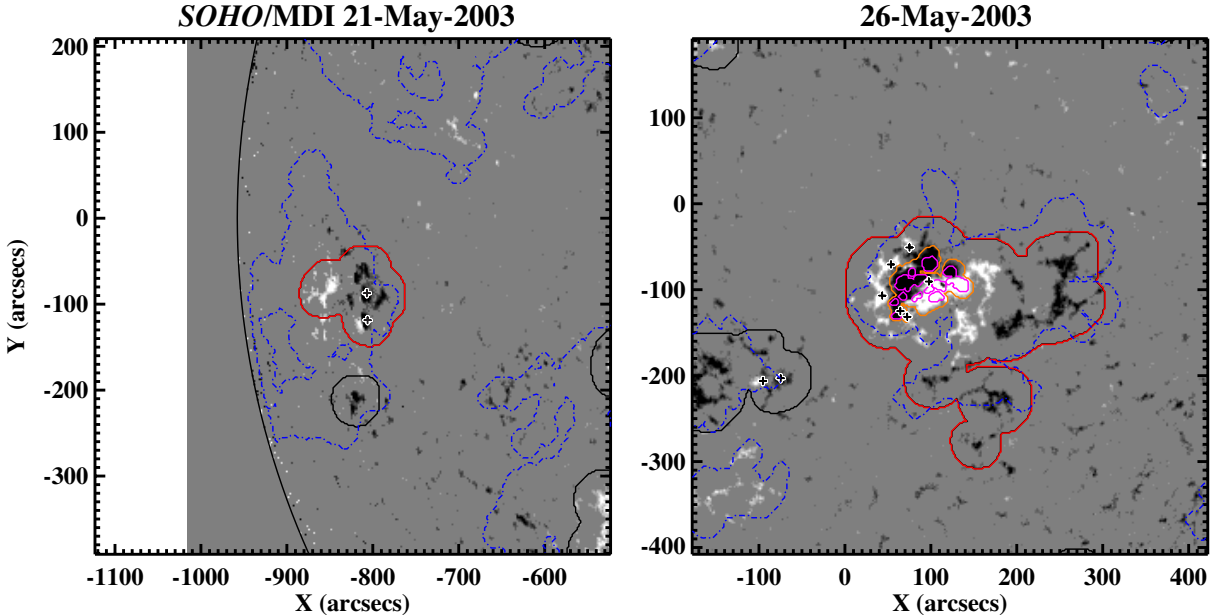


Figure 5.1: A comparison of detection contours for NOAA 10365. ASAP sunspots are represented by black crosses. The contours represent SMART in black (with the SMART detection of interest, NOAA 10365, outlined in red) for the magnetic features, SPoCA in dashed blue for coronal features, and STARA in orange for sunspot penumbrae and magenta for umbrae.

and Atmospheric Association (NOAA) switches the 10365 designation to this newly emerged bipole several days later. As the bipole evolves it develops a strong double polarity separation line (PSL) by merging with the decayed flux. It produces many C- and M-class flares and several X-class flares. The sunspot group progresses around the visible disk, eventually returning as NOAA 10386. The onset of decay occurs as C- and M-class flares are produced with decreasing frequency and the spot areas, magnetic flux, and field strengths decrease.

Figure 5.1 shows a comparison of the heliographic positions and sizes of two sets of SMART, ASAP, STARA and SPoCA detections of NOAA 10365. One can see that positions of the SMART, ASAP, STARA and SPoCA detections overlap. The SPoCA detection, however, includes coronal loops extending away from the footpoint boundary of NOAA 10365. Before 24 May, SPoCA merges NOAA 10367 with its detection of

5. THE FLARE PRODUCTIVITY OF SUNSPOT GROUPS

10365. NOAA 10367 can be seen in the right panel of Figure 5.1 as the black contour trailing behind the red one. From 24–27 May it only detects 10365, on 27 May at 1300 UT there is a single data point where these regions are merged by SPoCA, and from 29 May at 0100 UT onwards, SPoCA merges them for the remaining observation period. The longitudes of all detections within 24–27 May agree well. After 27 May the SPoCA longitude drifts, reflecting changes in the merged coronal structures. The magnetic centroid of 10365 at first trails behind the sunspot centroid but then precedes it, as evidenced by the top panel in Figure 5.2. This is because the new bipole, which develops many spots, emerges behind the existing weakly spotted bipole. The new emergence is clear in the plot of total sunspot area (middle panel), and is unclear in the magnetic and EUV area plots since the new bipole emerges partially within the boundary of the old one. The area determined by SMART is very sensitive to weak magnetic plage. This can be seen in the sudden jumps around May 25 and 28, which are due to nearby plage temporarily merging with the sunspot group. The jump in STARA area on 27 May can be attributed to a bad data file (note that there is no ASAP data point at that time).

From 25 May onwards, the total magnetic flux increases gradually to over four-fold the initial value during development and levels off around 29 May (see Figure 5.3). The maximum magnetic field increases abruptly on 25 May and also increases over time, albeit less smoothly than the magnetic flux.

The time series of SPoCA maximum intensity exhibits some peaks, which can be related to the following flares produced by NOAA 10365: the M 1.9 flare at 0534 UT on 26 May, the M 1.6 flare at 0506 UT on 27 May, the X 1.2 flare at 0051 UT on 29 May, and the M 9.3 flare at 0213 UT on 31 May. The last two flares are even visible in the total SPoCA intensity, which shows a mostly gradual increase over time. The flares not picked up by SPoCA likely occurred in between subsequent EIT images.

Signatures in the evolution of the magnetic configuration of NOAA 10365 precede

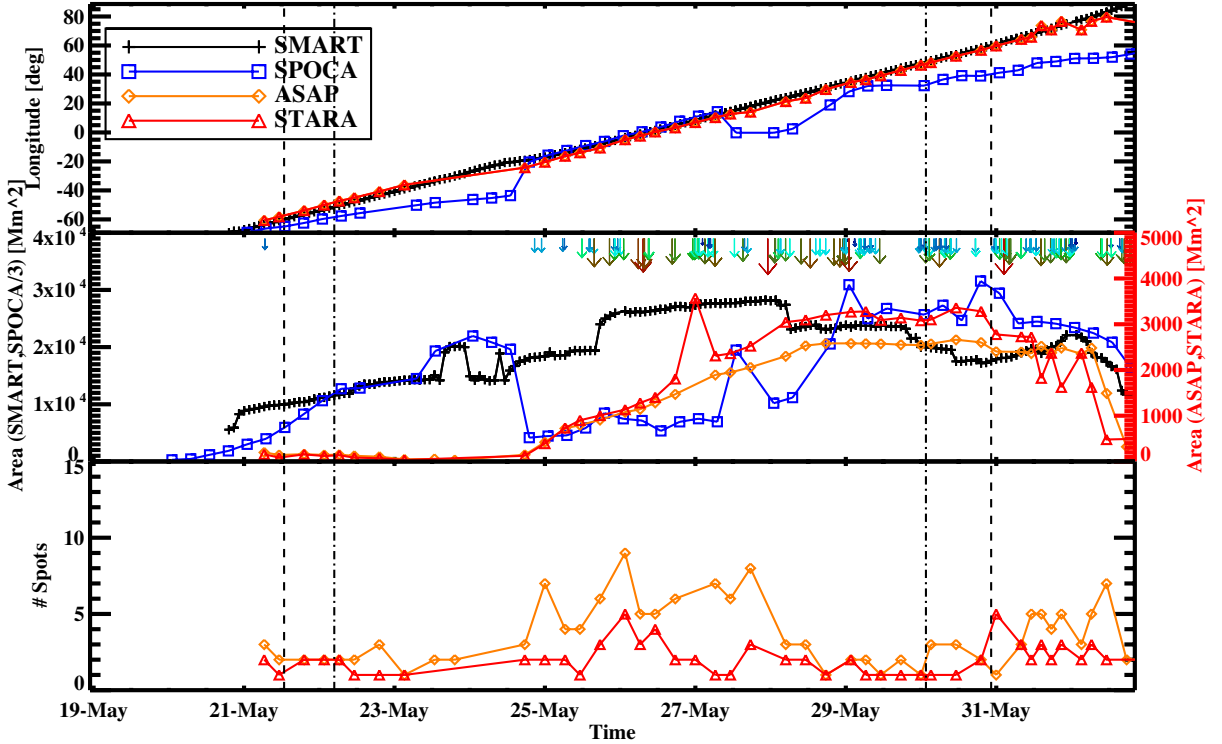


Figure 5.2: Time series of position, area, and sunspot information characterising the evolution of NOAA 10365. The legend indicates symbols and colors for each of the detection algorithms. The axes of the area plot are split between left (SPoCA and SMART) and right (ASAP and STARA). The SPoCA areas have been divided by three for display.

its intense coronal activity, indicated by the associated RHESSI flares in Figure 5.4. During 25 May 2003 the new emergence causes a jump in the main bipole separation line length. As the emergence continues and strong PSLs develop, this length decreases, while the total PSL length increases, as shown in the middle-top panel of Figure 5.4. Also, there are signs of gradual helicity injection as the angle between the main bipole connection line and the main PSL grows from near perpendicular (90°) to around 120° (top panel). The flux near PSL (R-value) grows during this time, as does the Ising energy (middle-bottom and bottom panels, respectively). The increase in R-value around 26 May is followed by a period of intense RHESSI flaring. The flaring continues as R-value increases and reaches a peak on 28 June. Examining the development of Ising energy, it appears that sharp increases in the property are followed by the most

5. THE FLARE PRODUCTIVITY OF SUNSPOT GROUPS

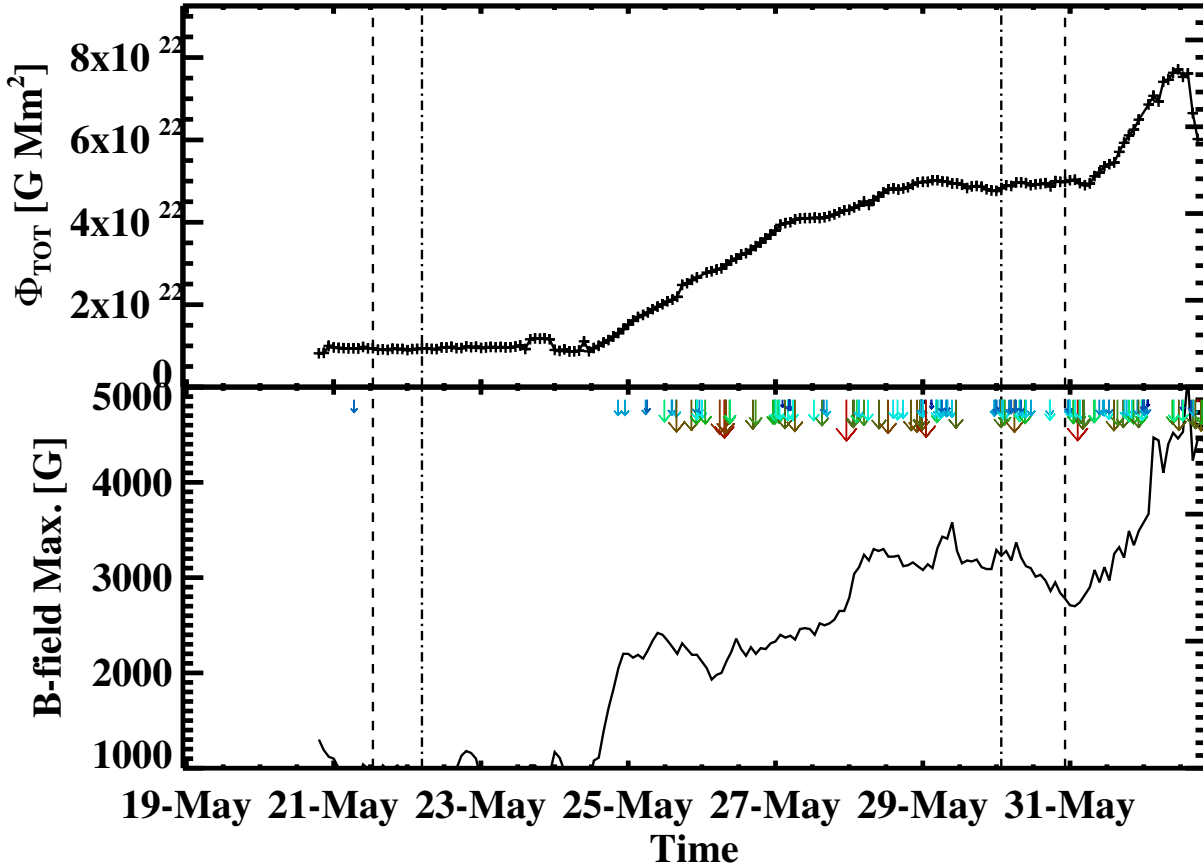


Figure 5.3: Time series of (top) total magnetic flux, total EUV intensity, (bottom) maximum magnetic field, and maximum EUV intensity for NOAA 10365. The axes of the plots are split between left (magnetic-field properties, black crosses) and right (coronal properties, blue squares). RHESSI flares associated with the AR are indicated by downward arrows.

intense flaring.

5.2.2 NOAA 11226

An M 2.5 flare, followed by a fast coronal mass ejection (CME), is released from NOAA 11226 on 7 June 2011. The region is beyond 50° longitude at the time of the flare, making it impossible to reliably measure any magnetic properties involving gradients. However, the interval over which the region evolves prior to the eruption (\sim 29 May – 7 June) is well observed by SDO/HMI. The magnetic flux and connectivity of the region

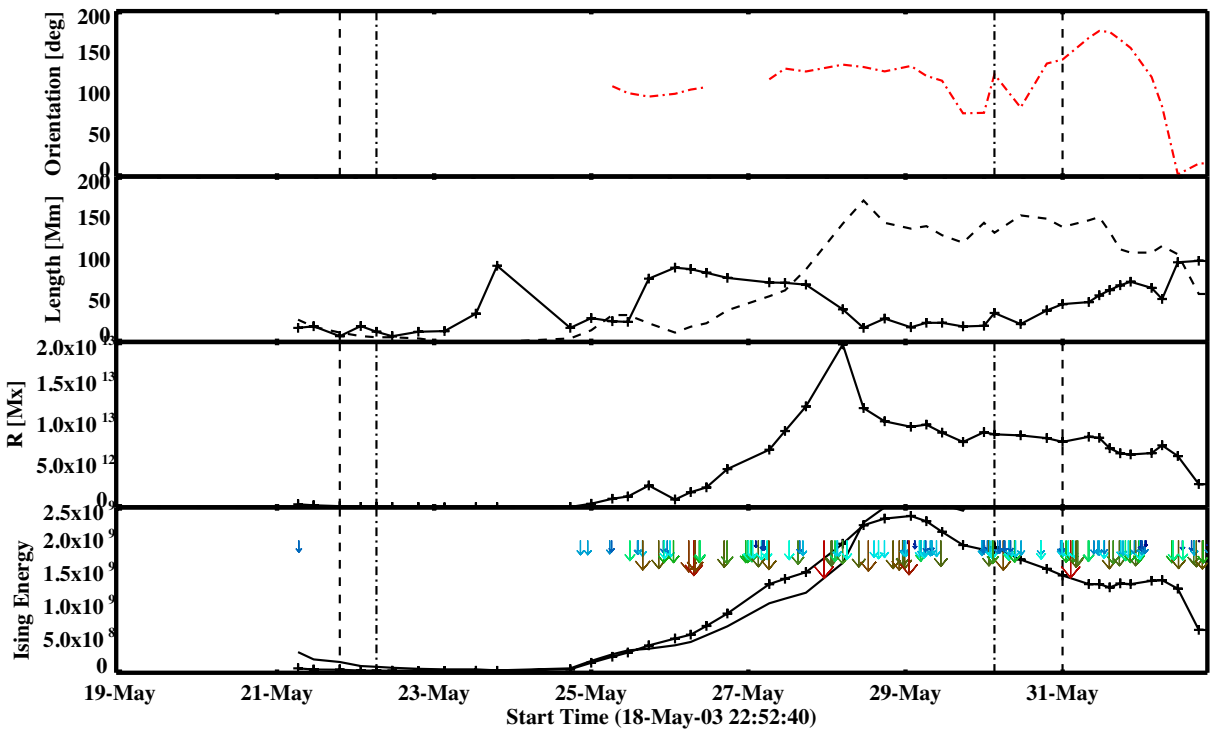


Figure 5.4: Time series showing proxies for the complexity and polarity mixing in NOAA 10365. (middle-top) bipole separation line length (crosses) and PSL length (dashed), (middle-bottom) R , and (bottom) Ising energy (crosses) and Ising energy per pixel (dashed; multiplied by 1 000 for display)

is also measured at the time of the eruption.

SMART is used to track and characterise the physical properties of NOAA 11226 throughout its disk passage¹. For the properties shown in Figure 5.5, the sunspot group bounding contours are dynamic, having been extracted for each magnetogram independently. However, in Figure 5.6 the detection contour detected by SMART nearest to the time of the 7 June flare is differentially rotated to each time prior to and following the flare, and is used in determining each of the properties shown in the plot. This helps to isolate changes in measured properties caused by the flare and to avoid having the feature detection method cause any changes in the properties.

In Figure 5.5 the magnetic evolution of the active region is tracked from $\sim -60^\circ$ to

¹See the supplementary movie: <http://dx.doi.org/10.6084/m9.figshare.96174>.

5. THE FLARE PRODUCTIVITY OF SUNSPOT GROUPS

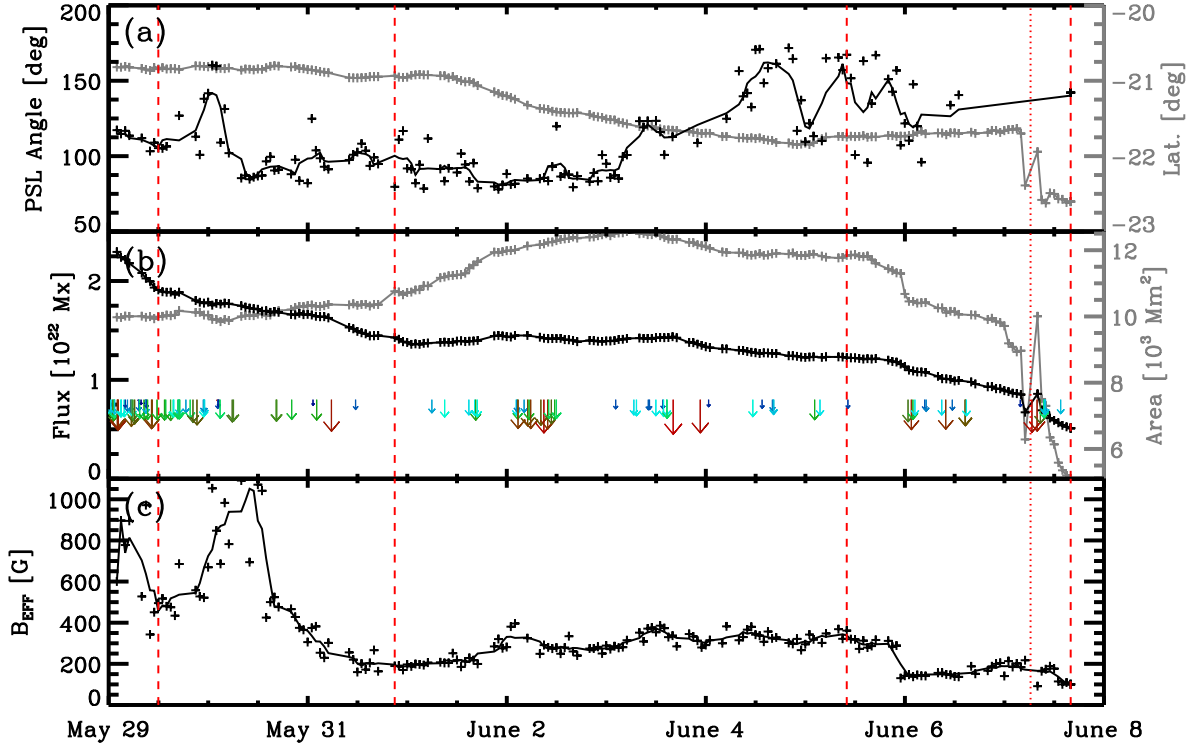


Figure 5.5: NOAA 11226 evolution using SMART algorithm detections. *a*: Polarity separation line orientation (black crosses), 5-point smoothing (solid black curve), and heliographic latitude (gray). *b*: Total magnetic flux (black) and area (gray). *c*: B_{eff} (black). Vertical dashed red lines indicate times that the active region crossed -60° , -30° , 30° , and 60° longitude. The vertical dotted red line indicates the GOES flare time. Flares from the GSFC RHESSI flare list are indicated by downward arrows with color and size being logarithmically proportional to total photon counts.

60° longitude. On 1 June 2011 the active region centroid begins to drift southward by $\sim 1^\circ$, as indicated by the latitude centroid (panel *a*; gray curve). This is cotemporal with a leveling off of the decay in total magnetic flux and with an increase in area (panel *b*; black and gray curves, respectively). At the same time, a rotation of the polarity separation line is observed (top panel; black curve). A movie¹ of the active region disk passage reveals the emergence of a negative flux concentration on the south west side of the region very close to the positive pole. This explains the polarity separation line

¹See supplementary movie: <http://dx.doi.org/10.6084/m9.figshare.96173>.

evolution on 3 June 2011 that is followed by a cluster of flares.

The angle of the polarity separation line with respect to the bipole connecting line is shown in panel *a*. An apparent rotation of over 30° occurs on 3 June 2011, resulting in two significant RHESSI flares (large red arrows); this rotation may indicate helicity injection (135). The aforementioned flux concentration is observed to progress northward along the main polarity separation line after its initial emergence. The curve indicating B_{eff} exhibits an increase on 2 June 2011 and 3 June 2011, the second of which is cotemporal with the polarity separation line rotation. This event is followed by clusters of events in the Goddard Space Flight Center (GSFC) RHESSI flare list¹ (downward arrows).

When NOAA 11226 first rotates onto the visible disk it is in a state of decay, as shown by the plot of total magnetic flux. However, the above analysis suggests that after several days on disk the active region becomes destabilized prior to the eruption. A compact negative polarity flux element emerges directly adjacent to the largest leading (positive) spot. The flux element moves northward injecting shear and helicity into the system. These observations suggest that the observed de-stabilisation is the cause of the eruptive phenomena on 7 June 2011 at \sim 06:00–07:00 UT.

In Figure 5.6 the thresholded area is shown (top panel; gray crosses) before and after the time of the M-class flare (7 June 2011 06:16 UT). The area decreases gradually over \sim 16 hr time range but an abrupt decrease of about 6% occurs near the flare time. The area of the differentially rotated static contour is shown for comparison (black crosses). The observed gradual decrease of \sim 5% over the entire time range can be attributed to the remapping algorithm as well as an imperfect line-of-sight correction.

The total magnetic flux (middle panel; black crosses) does not exhibit a clear change at the time of the flare. However, the difference between the positive (red diamonds) and negative (green triangles) magnetic flux increases by \sim 30%. The amount of positive

¹http://hesperia.gsfc.nasa.gov/hessidata/dbase/hessi_flare_list.txt

5. THE FLARE PRODUCTIVITY OF SUNSPOT GROUPS

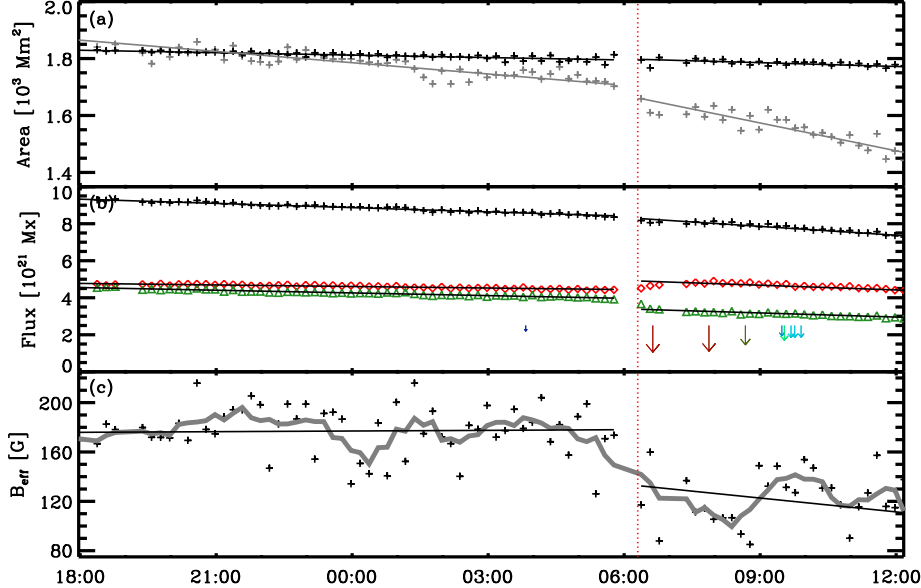


Figure 5.6: Evolution of the magnetic field in NOAA 11226. *a*: Area of differentially rotated static contour (black) and summed area of pixels above 90 G (gray). *b*: Total magnetic flux (black crosses), positive flux (red diamonds), negative flux (green triangles). *c*: B_{eff} (black crosses) and 5-point smoothed B_{eff} (gray curve). The horizontal red lines denote the mean B_{eff} for times before and after the flare, respectively. Flares are displayed as in Figure 5.5. A vertical red dotted line indicates the time of the flare of interest.

flux is greater than the negative flux during the entire time range, and increases by $\sim 5 \times 10^{20}$ Mx, while the negative flux decreases by $\sim 5 \times 10^{20}$ Mx. This may be due to changes of orientation with respect to the line-of-sight of fluxtubes within the active region. In this case, flux-tubes with positive (negative) footpoints must become more (less) parallel to the line-of-sight. Alternatively, positive (negative) flux must emerge (submerge) or condense (disperse) to increase (decrease) the amount of flux included in the 90 G contours. Upon reviewing a 12 min-cadence movie of the active region near the time of the flare, an isolated negative flux concentration in the northern portion of the active region can be seen to fall below the threshold, simultaneously with parts of the main negative flux concentration.

A measurement of magnetic inter-connectivity within the active region, B_{eff} (panel

5.3 Properties of Flaring Sunspot Groups

c ; black crosses), is shown to decrease by $\sim 30\%$. The measurements are smoothed by 5 data points (gray curve). Linear fits (black lines) are shown separately for points prior to and following the flare. The horizontal red lines indicate the mean value of B_{eff} for points before and after the flare start time (06:16 UT). The decrease of B_{eff} at the flare time is due to a combination of a decrease of the line-of-sight magnetic field magnitudes and the distance between magnetic flux elements of opposing polarities. After a large eruptive event the magnetic configuration of the host active region would be expected to exhibit decreased non-potentiality. In the corona, the fields have been seen to relax to a state of lower energy (40). In the photosphere the effect is small, but has been observed (137; 199).

Each of the properties begins to decay at a faster rate after the flare than before the flare, except for B_{eff} which is increasing slightly prior to the flare. This indicates that after the flare, the active region begins to diffuse and decay faster or that the magnetic fields become oriented further from the line-of-sight direction more quickly. The overall increase of B_{eff} prior to the flare is indicative of an increase in polarity mixing within the AR, which has been shown to be related to flaring (73).

5.3 Properties of Flaring Sunspot Groups

Currently, flares can not be reliably forecasted. This is partially because the mechanisms behind flaring can not be directly observed and are not well understood. Also, since the magnetic field can not be reliably measured in the corona, one must rely on photospheric fields and extrapolations to determine the magnetic structure in the corona. This lack of direct knowledge of what is really going on has resulted in the common use of proxies to indicate the build up of flare energy in a sunspot group (57; 173). So, determining the statistical relationship between sunspot group properties and flaring has become essential for any flare forecasting system.

5. THE FLARE PRODUCTIVITY OF SUNSPOT GROUPS

Table 5.1: The minimum total flux and R values for a sunspot group to have the potential to produce a flare of each GOES class.

Minimum Φ_{TOT}	Minimum R-Value
C $> 8.7 \times 10^{21} \text{ Mx}$	C $> 5.7 \times 10^{10} \text{ Mx}$
M $> 1.8 \times 10^{22} \text{ Mx}$	M $> 3.9 \times 10^{11} \text{ Mx}$
X $> 3.9 \times 10^{22} \text{ Mx}$	X $> 4.3 \times 10^{12} \text{ Mx}$

In this section, the properties of SMART sunspot group detections are associated with flares observed by Geostationary Operational Environmental Satellites (GOES), which measures the disk integrated X-ray flux in a 1 to 8 Å bandpass. Locations are obtained from the Latest Events Archive¹. The data coverage includes flares from 2002 through 2009 and the flare locations in the catalogue are determined by differencing sequential EUV images to detect coronal brightenings. The SMART detections cover the same time period and one observation per day is chosen from the 96 minute maximum cadence of MDI observations. We filter the associated sample to only include sunspot groups within 60° longitude of disk center to avoid large errors in property determinations due to line-of-sight (LOS) effects.

Each flare-sunspot group association is performed by overlaying each flare on the full-disk SMART detection mask attributed to the magnetogram closest in time to the catalogued flare start time. This association method uses flares as a base rather than the SMART detections. This avoids a bias in the sunspot group property distributions based on their lifetime, as those with longer lifetimes would result in more detections of the same feature. Instead, the bias is toward flare productivity, as a single feature that produces many flares will result in many detections of that feature being included.

In Figure 5.7, the distribution of areas for the complete sample of detections is shown in gray (both associated and not associated with flares). The distribution of detections associated with C-class flares is shown in blue and for the largest areas, the number of C-class detections is greater than the whole population of detections. This

¹http://www.lmsal.com/solarsoft/latest_events_archive.html

5.3 Properties of Flaring Sunspot Groups

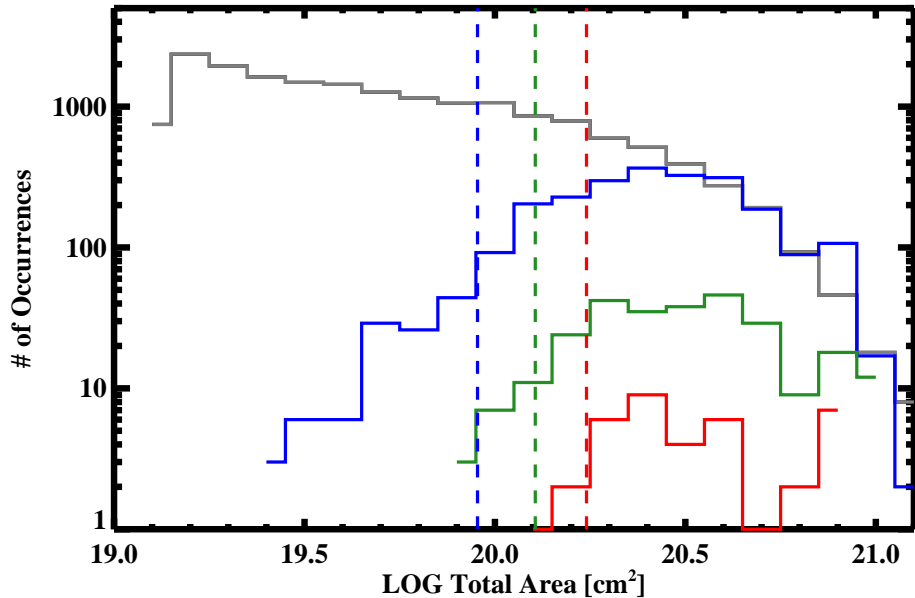


Figure 5.7: Distributions of sunspot group $\log(\text{area})$ for the entire population (gray) and those associated with C- (blue), M- (green), or X-class flares (red). 95% of each population lies above the vertical lines. Bumps in the distributions at the largest areas are visible resulting from the large AR complexes.

is due to the association method, since if multiple flares are produced from the same sunspot group close in time, the SMART detection best matched in time will be the same for each flare and will thus be counted multiple times. The area dependence of detections associated with flares shows that there is a most probable range of areas for producing flares ($\sim 2\text{-}4 \times 10^{20} \text{ cm}^2$). Beyond a certain size, large flares are not expected. This effect could indicate that the largest features detected by SMART (complexes of mature sunspot groups) are not as unstable as the more compact and isolated groups. Detections associated with M- and X-class flares are indicated by the green and red lines, and exhibit a similar area dependence to the C-class flares, but with a more limited extent. The most important information one can glean from the plots is the minimum property value needed to produce a flare. 95% of each population lies above the vertical dotted lines in Figure 5.7.

5. THE FLARE PRODUCTIVITY OF SUNSPOT GROUPS

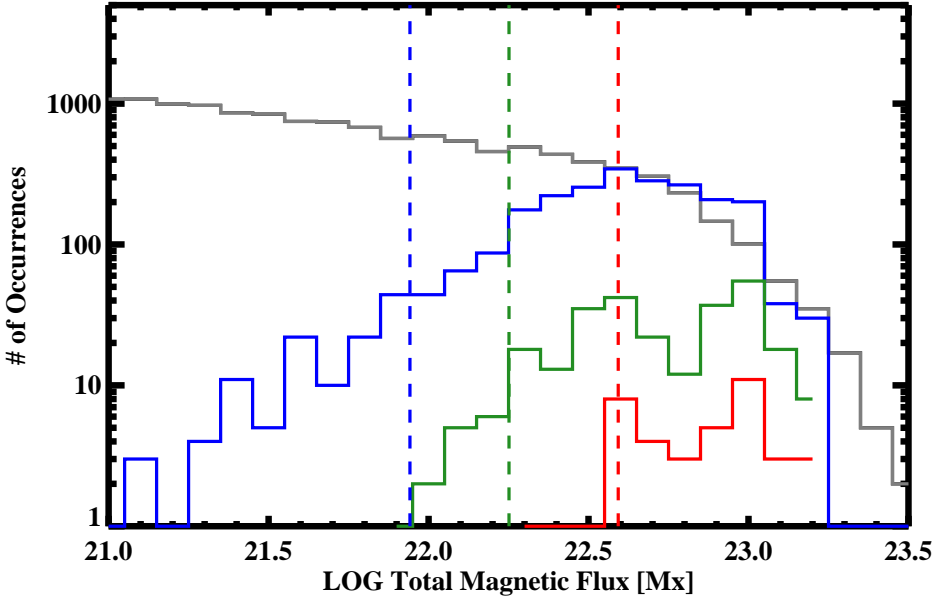


Figure 5.8: Distributions of sunspot group $\log(\text{total flux})$ with the same color coding as in Figure 5.7. 95% of each population lies above the vertical lines.

Figure 5.8 shows the distribution of total magnetic flux for each distribution. Compared to area, the drop off in the number of flares associated with detections of large flux is even more stark. As with area one can determine the minimum flux necessary for a sunspot to produce each class of flare, as listed in Table 5.1. In this case the three flare class minimum values for flaring have a larger relative separation than for area.

Distributions of sunspot group R-value are shown in Figure 5.9. The relative separation between the minimum flaring values is greater again for R-value than for flux. These values are listed in Table 5.1. The R-value and flux of the sample populations are plotted against each other in Figure 5.10. The property values that result in the largest flares lie at the apex of the 2D sample distribution. This is not surprising since the distributions indicate that the largest flares occur in the detections exhibiting the largest property values.

Figure 5.11 shows R-value against WL_{SG} . Again, those associated with the largest

5.4 Solar Cycle Dependence of Flaring Sunspot Groups

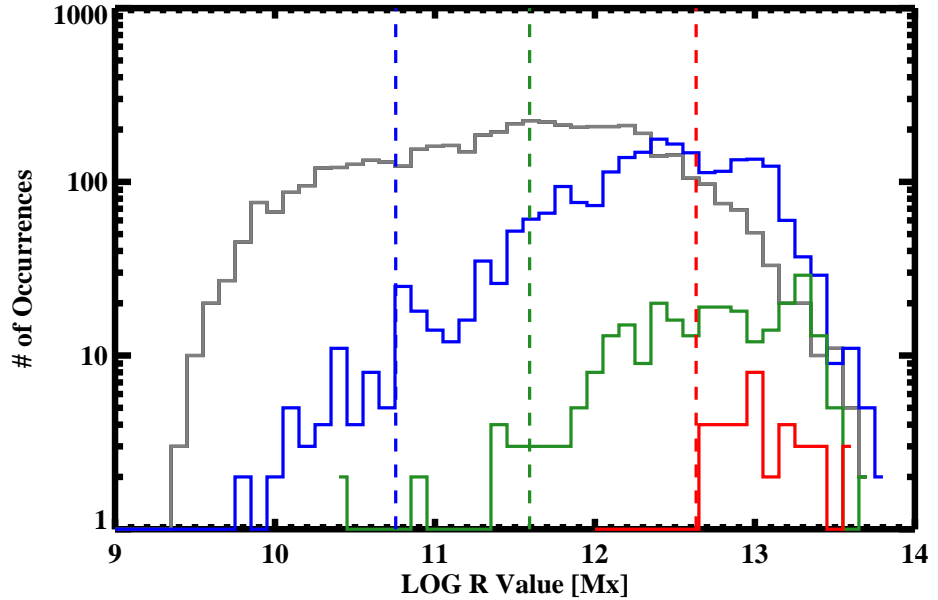


Figure 5.9: Distributions of sunspot group $\log(R\text{-value})$ with the same color coding as in Figure 5.7. 95% of each population lies above the vertical lines.

flares are clustered at the largest property values. In this case, another population of detections is also visible: detections that are not associated with flares, but have a larger WL_{SG} value than those that are associated with flares, for a given R-value. This is likely caused by LOS effects. WL_{SG} is directly related to the magnitude of gradients which are significantly over-estimated away from disk center, while R-value is directly related to flux and is much more reliable away from disk center. This indicates that using a combination of properties can more effectively discriminate between flaring and non-flaring sunspot group detections. This idea has been taken further using many properties with linear discriminant analysis (114; 115).

5.4 Solar Cycle Dependence of Flaring Sunspot Groups

In this section, the solar cycle dependence of sunspot group flare productivity is investigated. As in the previous section, SMART detections are associated with flares. As

5. THE FLARE PRODUCTIVITY OF SUNSPOT GROUPS

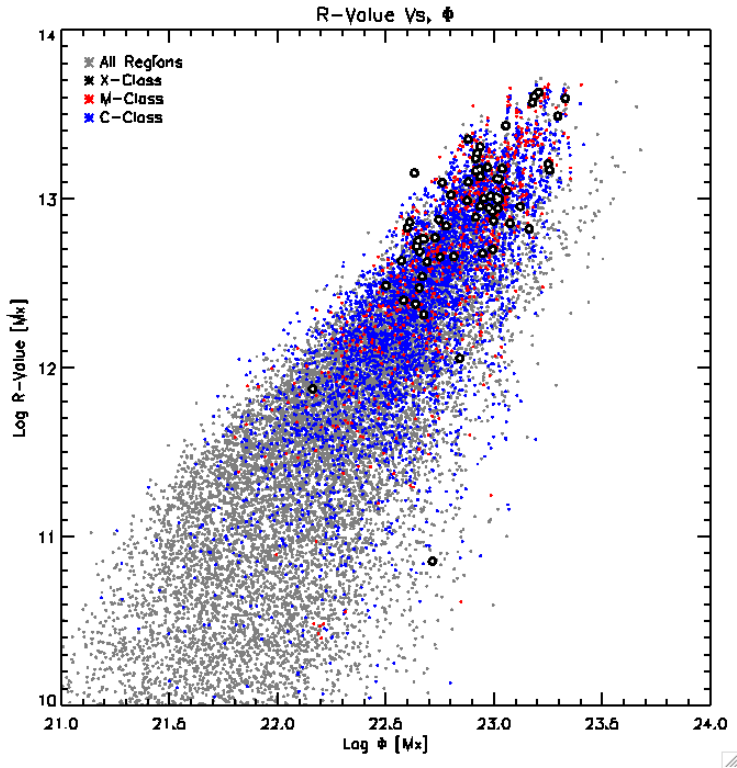


Figure 5.10: A plot of sunspot group log(R-value) versus log(total magnetic flux). The complete sample of detections is plotted (gray), with those producing C- (blue), M- (red) and X-class flares (black) over plotted.

before, one set of sunspot group detections is produced per day. Here, the National Geophysical Data Center (NGDC) flare list is used, as described in Chapter 3, since it covers all of solar cycle 23. This list is less complete than the Latest Events Archive (used in the previous section), especially for the smaller, more frequent flares. This is because ground-based H α observations are used to determine the flare locations (as opposed to EUV images). The observations are affected by atmospheric seeing, weather, and less consistent observations.

The following investigation is more concerned with the occurrence of larger flares at different times in the solar cycle. The aim is to determine if there is a quantitative difference in the properties of emerging sunspot groups over time, and how strongly flaring is determined by those properties. Flares are known to be a random stochastic

5.4 Solar Cycle Dependence of Flaring Sunspot Groups

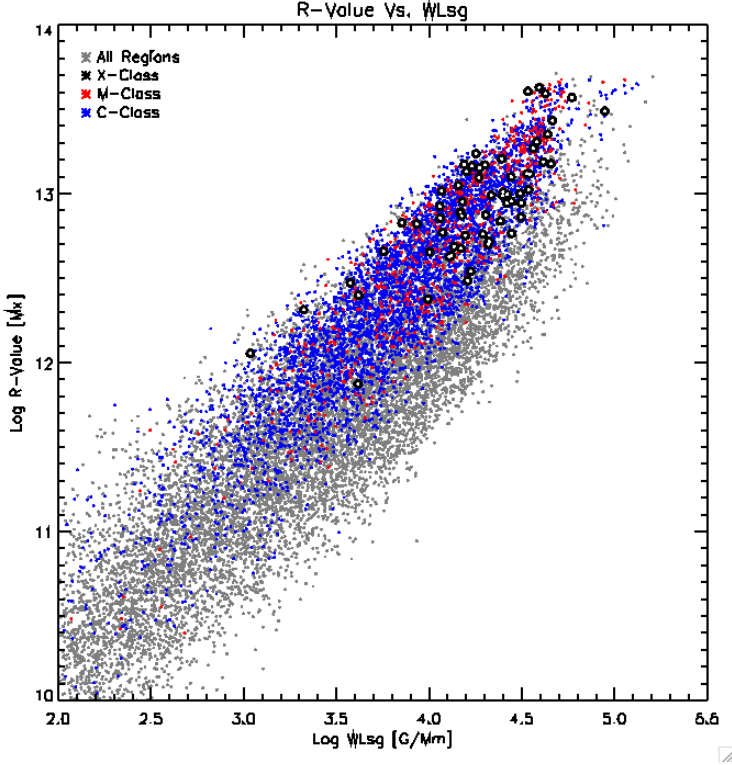


Figure 5.11: A plot of sunspot group log(R-value) versus log(WL_{SG}). The same color-scale is used as in Figure 5.10. The band of non-flaring detections at lower R-value than the flaring detections are likely due to WL_{SG} having unrealistically high values toward the limb, due its reliance on the magnetic gradient.

process (222), but some properties of the sunspot groups, such as area, are shown to be qualitatively predictable over a solar cycle (94).

In addition to investigating the number of large flares produced, we quantify the flaring index of the visible disk (6),

$$F = (1 \times \sum_n I_C + 10 \times \sum_n I_M + 100 \times \sum_n I_X) / \Delta t , \quad (5.1)$$

where I_C , I_M , and I_X are the numerical magnitude of each flare (i.e. 7 is the magnitude of a M7 class flare) occurring during Δt . This index is weighted toward the largest flares, and is treated as a proxy for the time integrated flare energy released.

Figure 5.12 shows a time-latitude map of SMART detection centroids for different

5. THE FLARE PRODUCTIVITY OF SUNSPOT GROUPS

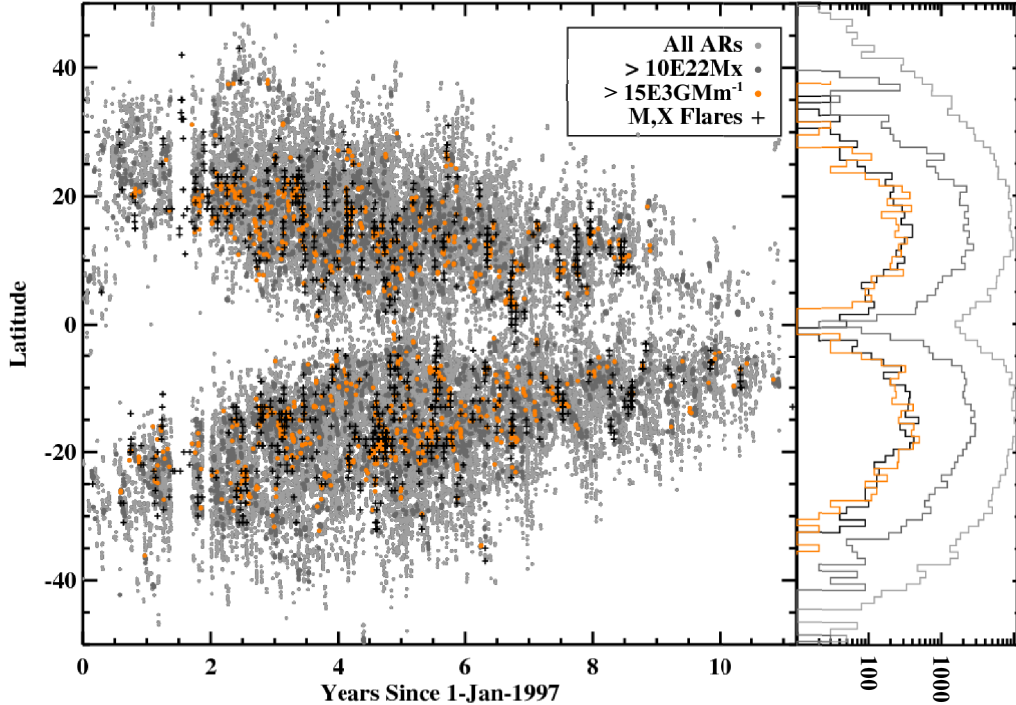


Figure 5.12: Top: Butterfly diagram of all AR detections (gray), overlaid with regions of greater than 10^{20} Mx flux (dark gray) and $> 15000 \text{ G Mm}^{-1}$ WLsg (orange), and M- and X-class flares (black). Right: Marginalized butterfly diagrams.

property thresholds and all M- and X-class flares produced over the solar cycle. The flare locations are generally co-spatial and co-temporal with the sunspot group detections of $WL_{SG} > 15 \times 10^3 \text{ G Mm}^{-1}$. A histogram of each population of daily detections is shown in the panel to the right. The populations of largest WL_{SG} and total flux $> 10^{22} \text{ Mx}$ are more confined in latitude than those of smaller flux. Although a coincidence, the number of M- and X-class flares is remarkably close to the number of daily detections above the WL_{SG} threshold.

The daily detections are then binned by 2 weeks and summed over latitude. Figure 5.13 shows the arbitrarily normalised¹ curves for R-value, WL_{SG} , flare index, the

¹Normalisation was chosen to highlight time dependent features in each curve. Each curve was divided by its maximum, and then multiplied by an arbitrary factor: 1.2 for R-value and WL_{SG} , 0.6 for flare index, and 0.5 for the number of M- and X-class flares.

5.4 Solar Cycle Dependence of Flaring Sunspot Groups

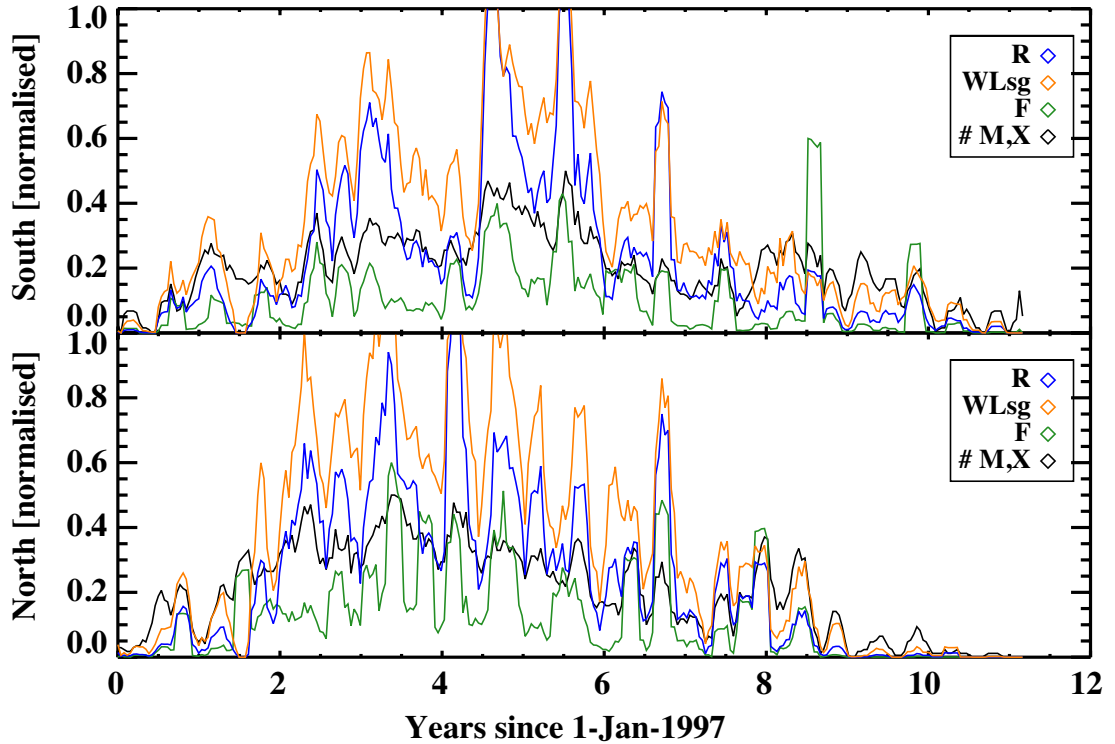


Figure 5.13: Top: Time-series of R-value (blue) and WL_{SG} (orange) in the south hemisphere. Flare index (green) and the number of M- and X-class flares (black) is over-plotted. Time-series are normalized by their maxima. Bottom: Corresponding time-series for the north hemisphere.

number of M- and X-class flares. Many features are present in each curve. Most of the time, when a peak in summed R-value and WL_{SG} is observed, a peak in flare index and the number of large flares is also seen. The variance in the curves is likely due to sunspot nests that are highly active for a period of time (in this case for apparently ~ 6 months) and then disappear again (153).

The time-series of each curve is then compared. Figure 5.14 shows the flare and property time-series plotted against each other and the correlation coefficient between each combination. For all three properties, there is better agreement with the number of M- and X-class flares than with flare index. Also, WL_{SG} exhibits the largest correlation with the number of flares of the three properties, although R-value exhibits a larger correlation with flare index than WL_{SG} . It makes sense that the number of large

5. THE FLARE PRODUCTIVITY OF SUNSPOT GROUPS

flares would be better correlated than flare index with sunspot group properties that are related to strong PSLs. As shown in Section 5.3, small flares are produced by detections of a wide range property values, but large flares are only associated with detections of the largest property values.

5.4 Solar Cycle Dependence of Flaring Sunspot Groups

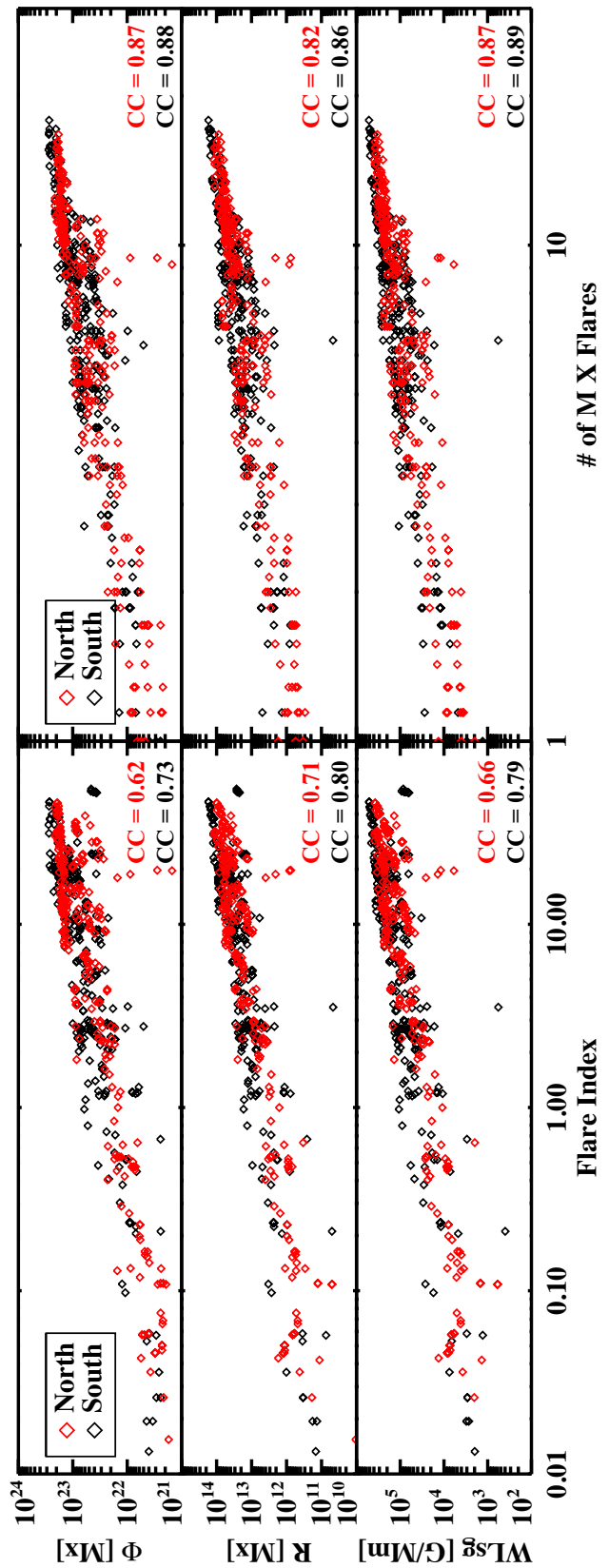


Figure 5.14: *Left:* Correlation between flare index and total flux, R-value, and WL_{SG} . *Right:* Correlation between the number of M- and X-class flares and total flux, R-value, and WL_{SG} . The outliers are likely due to incorrectly catalogued flares that are attributed to small inactive features.

5. THE FLARE PRODUCTIVITY OF SUNSPOT GROUPS

5.5 Conclusions

In this chapter, the relationship between the flare productivity and magnetic properties of sunspot groups has been explored.

- Individual sunspot groups are shown to undergo both long-term changes prior to flaring (Section 5.2.1 210) and short-term changes at the time of flaring (Section 5.2.2 23). This is the first time properties determined by different detection algorithms using both photospheric and coronal data have been compared over time. The coronal AR properties are difficult to interpret due to the high variability they exhibit, resulting from the unstable behaviour of the detection algorithm (SPoCA) and the corona itself. The coronal detections could be more useful if they were somehow tied to the magnetic detections to stabilise them.
- This is the first time B_{eff} has been compared just before and after a flare. A change in magnetic connectivity is observed before and after the flare.
- A large-scale statistical comparison of measured properties and associated flares has allowed the determination of thresholds in the property values for flares of different classes to occur (Section 5.3). This is the largest sample of magnetic detections ever used to study flaring and it is the first time the magnetic area, flux, R-value, and WL_{SG} of detections has been directly compared to study flaring.
- The comparison of global flare productivity and the disk integrated magnetic properties of SMART detections shows that properties involving strong PSLs are well correlated (correlation coefficients (CCs) of $\sim 70\text{--}90$) to flare activity (Section 5.4). This is the first time that these magnetic properties have been compared to each other and to flaring over the solar cycle.

The following sections provide more detail on some of these points.

5.5.1 Case Studies

Through the time-series analysis of two AR case studies (Section 5.2), the emergence of new magnetic flux, sunspots, and coronal loop structures within the boundaries of a decaying region (Section 5.2.1) has been observed. Increases in non-potentiality are observed, followed by the onset of flaring (Sections 5.2.1 and 5.2.2). Finally, differences in flux and B_{eff} are observed over short time-scales just before and after an M-class flare.

We find that the detection algorithms show good correspondence between centroid positions and areas, but significant divergence is seen in other properties. For example, the total number of detected sunspots fluctuates much more than other measured properties, especially near the limbs, as transient spots rapidly emerge and disappear. This is partly due to the visibility curve since the area of small spots is highly impacted by the observer's viewing angle (45; 216).

In terms of the usefulness of different properties, sunspot area is more indicative of the emergence and decay of an AR than coronal or magnetic area, which do not necessarily decrease during decay, as this is dependent on arbitrary detection thresholds. As a basis for long-term AR tracking, magnetic flux is more useful than the sunspot area, since sunspots are much more transient than their magnetic footprints, or maximum magnetic field value, since it is affected by the MDI saturation problem (120). Also, the maximum magnetic-field value is unstable since different positions in the active region will over-take each other in field magnitude as they develop, causing the location that the value is sampled from to vary wildly. Finally, the total EUV intensity determined by SPoCA has a smooth behaviour over time and is closely linked to area. The maximum EUV intensity peaks at the time the active region emits a large flare, and appears to be a useful indicator of eruptions in the corona.

The case study of complex, flaring NOAA 10365 (Section 5.2.1) shows that flaring can happen both in periods of flux emergence as well as non-potentiality enhance-

5. THE FLARE PRODUCTIVITY OF SUNSPOT GROUPS

ment (PSL rotation, increased R-value, and increased Ising energy) in an active region. Following the initial flaring during the emergence phase of evolution, further flaring occurs as the main PSL rotates with respect to the bipole connection line. This may be a sign of helicity injection and is coincident with increases of other properties related to polarity mixing. Helicity injection has been established as a method of increasing non-potentiality and may be caused by the emergence of subsurface twisted flux ropes, as seen in Dun *et al.* (50).

Flares detected by the RHESSI satellite are used to determine the activity of sunspot groups over time. Since it is Earth orbiting, it periodically enters regions in which it can not make reliable observations. These periods include eclipses, when the Sun is occulted by the Earth, and passes through the south Atlantic anomaly (SAA), a region near the east coast of South America which exhibits an irregular geomagnetic field. These drop-out periods are short lived on the timescale of a large flare (hours) so they should not cause a large flare to be missed, although some small flares could be missed. However, flaring is random and the frequency of small flares during a period of enhanced activity is large. Although some individual flares may be missed, it will be clear that enhanced activity is taking place, as the repeated occurrence of small flares will never be co-temporal with a sequence of eclipse periods.

5.5.2 Active Region Flaring Potential

The results of the large scale investigation into the relationship between sunspot group properties and flaring in Section 5.3 indicate the minimum property value for a flare of given GOES class to occur. This work cannot predict whether a sunspot group will produce a flare. However, it can be used to predict an “all-clear” – that no flare above a given magnitude will occur as long as no sunspot groups are observed to have properties above the threshold values. This is useful information for airline flight controllers and astronaut flight surgeons concerned with the human impact of dangerous radiation from

solar eruptive events.

5.5.3 Solar Cycle Dependence

In Section 5.4 we investigate the solar cycle dependence of global solar flare production. We also determine the relationship between global flare productivity and the properties of detected sunspot groups. It is found that large sunspot groups exhibiting strong PSLs are more confined in latitude than large sunspot groups without strong PSLs. PSL strength generally indicates complexity, as the mixing of polarities results in opposite-aligned fields in close proximity, and thus a larger PSL length is detected. Since more complex sunspot groups emerge at lower latitudes, the underlying toroidal magnetic field structures must also be more complex at lower latitudes. This could indicate either that the toroidal flux production mechanism is less organised at lower latitudes, or that the evolution of the magnetic structure encounters less regular flows.

The majority of large flares occur cospatially with sunspot groups exhibiting strong PSLs. The global value WL_{SG} is a better indicator of the potential for large flares to occur, while R-value is a better indicator of the global flare index. The relationship between global flare productivity and sunspot group properties could allow for long-term global flare forecasts.

These properties investigated in this chapter are known to be related to flaring, and show similar correlations when a large sample of property determinations is plotted against flare productivity. Other magnetic properties have not been compared in the same way on the same scale, so it is difficult to know if other magnetic properties, such as helicity injection would fare better. However, a flare prediction system utilising SMART properties¹ has been shown to be among the most accurate systems utilising other AR properties (4; 22). The methods used to perform the prediction also play a role.

¹The system uses machine learning to relate the previous flare productivity of detected ARs to a range of SMART properties.

5. THE FLARE PRODUCTIVITY OF SUNSPOT GROUPS

6

Sunspot Groups and the Global Magnetic Field of the Sun

*The research presented in this chapter will be published in Higgins et al., *Astronomy & Astrophysics* (2012a). The aim of this study is to determine how sunspot groups affect the global magnetic field of the Sun. A set of magnetic feature detections covering solar cycle 23, obtained using the methods described in Chapter 4, are studied and compared to the weak large-scale distribution of magnetic flux, and to the time dependence of global potential field source surface (PFSS) extrapolations. The distribution of magnetic feature properties are found to depend on the phase of the solar cycle. The average flux imbalance at high latitudes is found to be of opposite sign and of roughly equal magnitude to that in the active latitudes. Lastly, the dominant configuration of the global field is found to be strongly dependent on the distribution of flux imbalance over latitude.*

6. SUNSPOT GROUPS AND THE GLOBAL MAGNETIC FIELD OF THE SUN

6.1 Introduction

Current models of the solar dynamo, such as those relying on surface flux transport, can qualitatively reproduce the observed magnetic solar cycle. The Babcock-Leighton model relies on the bulk motion (decay and dispersal) of active region flux that manifests large-scale magnetic polarity imbalances. However, there are many aspects of the solar cycle that have not been quantitatively reproduced, such as the properties of active region emergence due to this process. Realistic models of the internal solar dynamo must accurately reproduce these phenomena to be considered successful.

Latitudinal observations of net flux over time show that while the active region belt progresses from high to low latitudes, unipolar flux is seen to be transported poleward, as observed in magnetic butterfly diagrams (85). Choudhary *et al.* (36) investigate large-scale flux imbalances finding that hemispheric flux imbalance is a function of the solar cycle and further more switches sign between cycles. Zharkov & Zharkova (230) study the excess flux of sunspot groups statistically for a portion of solar cycle 23, finding opposite imbalances in each hemisphere, that reverse at the cycle minimum. Zharkov *et al.* (229) state that a phase relation exists between active region flux imbalances and the background high-latitude magnetic field. These results support the Babcock-Leighton model.

Individual active region (AR) properties, such as flux imbalance, affect the solar magnetic topology locally, while on a global scale, hemispheric flux imbalance affects the structure of the solar magnetic field. For instance, a purely dipole configuration results from having a single opposing polarity in each hemisphere. Generally, the global field is multipolar and we can describe its topology extending into the solar atmosphere using the superposition of spherical harmonics, with a PFSS model. Mordvinov (134) determines a relationship between the IMF and global field harmonic modes—especially the $[l = 2, m = 0]$ (quadrupole) mode.

6.1 Introduction

Some studies focus on periodicities in the harmonic coefficients over multiple solar cycles finding separate frequencies in axisymmetric and non-axisymmetric modes (107; 196; 197). It has been determined that to accurately predict the magnetic field at Earth, the properties of low latitude magnetic features on the Sun must be taken into account (175; 183; 213). The distribution of open flux and the global field configuration determine the shape of the heliospheric field and thus can affect the space weather environment at Earth. Taking these findings into account, we seek to better understand the evolution of the global solar magnetic field in the context of a full 11-year activity cycle (half of a magnetic cycle) by characterizing spatio-temporal distributions of magnetic feature properties.

In this chapter, we compare the properties of low latitude ARs to the global configuration of the solar field. We establish a clear connection between strong-flux features emerging in the active region belt, the excess of high latitude weak positive (negative) unipolar flux, and the global magnetic field topology determined by multipolar spherical harmonic coefficients. The complete life cycle of surface magnetic flux—from active region to quiet Sun—has not before been studied quantitatively using both automated feature detection and global field measurements.

By statistically studying active region magnetic topology over a solar cycle we can both diagnose the subsurface dynamo which created them as well as determine how they affect the external global field configuration. Statistical studies of sunspot groups have been performed throughout the last 100 years. The area and magnetic flux of active regions have been analysed statistically in previous studies (202). Harvey & Zwaan (87) compare active region area distributions for the rise, decline, minimum, and maximum phases of the solar cycle. Utilizing automated feature detection to conduct the present study removes the subjectivity of visually identifying features in solar images (as has been done in the past). Work has been done using automated detection methods to study solar cycle dependence of AR emergence (97; 227).

6. SUNSPOT GROUPS AND THE GLOBAL MAGNETIC FIELD OF THE SUN

We aim to better understand how the statistical properties of active regions change over the solar cycle and to establish a quantitative connection between their properties and the global magnetic field configuration of the Sun. SolarMonitor Active Region Tracker (SMART) is run on line-of-sight magnetograms covering solar cycle 23, resulting in measurements of each active region on disk each day. Methods described in Secton 6.2 are used to construct butterfly maps from SMART detections and raw magnetograms and to determine the dominant spherical harmonic coefficients at different times in the solar cycle. The results and discussion is presented in Section 6.3 and the conclusion is presented in Section 6.4. The software used to perform the data analysis presented in this chapter is available through the distributed version control system, “github”¹.

6.2 Methods

The global solar magnetic field configuration is compared to the properties of sunspot groups in the active latitudes, determined using the methods in Chapter 4. In the following section the methods used in analysing the properties of features and the global field are discussed. The analysis is performed on maps of the detections binned in time and latitude (Section 6.2.1). Additionally, the spherical harmonics of the global magnetic field, as described in Section 6.2.2 are compared to the time-latitude maps.

In this chapter, AR detections are analysed using the properties summarised in Section 2.7. These include total flux (Φ_{tot}), net flux (Φ_{net}), and flux imbalance (Φ_{imb}). A Φ_{imb} of zero is a region of equal parts Φ_+ and Φ_- , while Φ_{imb} of unity is a region of completely unipolar flux. As in Section 4.2.4, we define unipolar regions as having a Φ_{imb} greater or equal to 0.9 and multipolar regions less than 0.9.

¹The repository is available for download here: <https://github.com/pohuigin/Global-Magnetic-Field-Study>. This software is written in IDL (<http://www.exelisvis.com/ProductsServices/IDL.aspx>) and is dependent on the SSW library (http://www.lmsal.com/solarsoft/ssw_whatitis.html) and another general library (https://github.com/pohuigin/gen_library).

6.2.1 Magnetic Butterfly Maps

To analyse long-timescale, spatio-temporal patterns in AR emergence, we construct butterfly maps and time series from the data. Individual AR properties are combined to describe the solar disk between -60° and $+60^\circ$ longitude at a given point in time. For the time series, we calculate the summed area, Φ_{tot} , and Φ_{net} for all ARs within the longitude limits. A separate Φ_{tot} map is created for regions above 10^{22} , 5×10^{22} , and 10^{23} Mx. The average Φ_{imb} of the detections is also determined. The data are then averaged in bins of 27 days, or about one solar rotation at active latitudes. This process smooths over all longitudes. For the butterfly maps, the method is repeated for bins of one degree latitude. Patterns in the time and latitude distribution of AR properties are studied using these maps.

While SMART is adept at characterizing the strong active region magnetic fields, it is not designed to detect diffuse features. The weak magnetic fields which compose the quiet-Sun are not readily apparent in individual magnetograms, partially due to the (nominally) 20 G Michelson Doppler Imager (MDI) noise level. To study the global configuration of these fields, a magnetic butterfly diagram (85) is created using the raw MDI images, with resolution of 1° in latitude and 1 day in time. Each slice of this map is created by averaging over all of the 96 minute magnetograms available on a given day. Only 5-minute averaged images are used, and each is differentially rotated to mid-day. After remapping the averaged magnetogram to a 180×180 longitude-latitude grid, pixels inside of -60° to $+60^\circ$ longitude are averaged across longitude. This results in a profile of $\langle B_{\text{signed}} \rangle$ in latitude for a given day. We repeat this process for the entire solar cycle, stacking the slices in time.

6. SUNSPOT GROUPS AND THE GLOBAL MAGNETIC FIELD OF THE SUN

6.2.2 Spherical Harmonic Decomposition

Assuming a current free ($\nabla \times \mathbf{B} = 0$), 3D magnetic field we can define a scalar potential field whereby,

$$\mathbf{B}(\mathbf{r}, \theta, \phi) = -\nabla\Psi, \quad (6.1)$$

where, r is in solar radii from Sun-center, θ is colatitude, ϕ is longitude, and Ψ is the potential field (Φ is normally used here, but we wish to differentiate this from magnetic flux). A solution to the above equation is:

$$\Psi(r, \theta, \phi) = \sum_{l,m} C_l^m(r) Y_l^m(\theta, \phi), \quad (6.2)$$

where $Y_l^m(\theta, \phi)$ are the spherical harmonics, and $C_l^m(r)$ are the harmonic coefficients. We can use $C_l^m(r)$ to determine the importance of various harmonic modes (ie. dipolar, quadrupolar etc.).

The SolarSoft¹ Potential Field Source Surface (PFSS) package² (175) is used to model the global structure of the potential magnetic field. The model requires a full solar rotation of line-of-sight (LOS) magnetograms as input to generate a complete global extrapolation. The source surface radius (R_s), or the point at which fields are forced vertical, is defined to be $2.5R_\odot$. The first few axi-symmetric ($m = 0$) spherical harmonic coefficients, as defined in Equation 6.2 are extracted from the model runs and combined into time series with around 27-day resolution (~ 1 solar rotation). These time series are compared to those of global AR property timeseries.

¹See: http://www.lmsal.com/solarsoft/ssw_whatitis.html

²See: http://cdaw.gsfc.nasa.gov/meetings/2009_gle/presentation/DeRosa-PFSSoverview.pdf

6.3 Results and Discussion

In the following section we characterize aspects of the magnetic active region cycle, including aspects of evolution in time, latitude, and the properties of emerging active regions. A connection is then established between the magnetic configuration in the photosphere and the large-scale field configuration away from the solar surface. First the properties of ARs over long time-scales are discussed in Section 6.3.1. In Section 6.3.2 a connection is drawn between high-latitude polarity imbalances, flux imbalances in ARs at lower latitudes, and the global configuration of the solar magnetic field.

6.3.1 The Magnetic Active Region Cycle

The solar cycle can be characterized by the properties of magnetic features present over time. Sunspots are composed of strong magnetic fields so it is natural to compare the amount of magnetic field on the Sun to the traditional sunspot cycle. The top panel of Figure 6.1 shows a comparison between the Solar Influences Data Center sunspot number (gray line) to the total magnetic flux Φ_{tot} , (black line), as measured from AR detections. Features in the Φ_{tot} curve on the scale of ~ 2 years are comparable to those of the sunspot number. A double peak is observed in both curves at ~ 3 and ~ 5 years after solar minimum. The first peak in the sunspot data is higher than the following peak, in contrast to Φ which exhibits a higher following peak. Also shown is the total flux in the northern hemisphere (Φ_N) and in the southern hemisphere (Φ_S). These two curves are markedly different: Φ_N appears to increase from solar minimum with a series of steadily increasing bursts of around 6 months in length up to solar maximum and dies off ~ 9 years after solar minimum, while Φ_S exhibits the double peaked structure characteristic of the sunspot number and continues producing AR flux for over a year after the north stops.

Double-peaked cycles are common (75), and the fact that only one hemisphere

6. SUNSPOT GROUPS AND THE GLOBAL MAGNETIC FIELD OF THE SUN

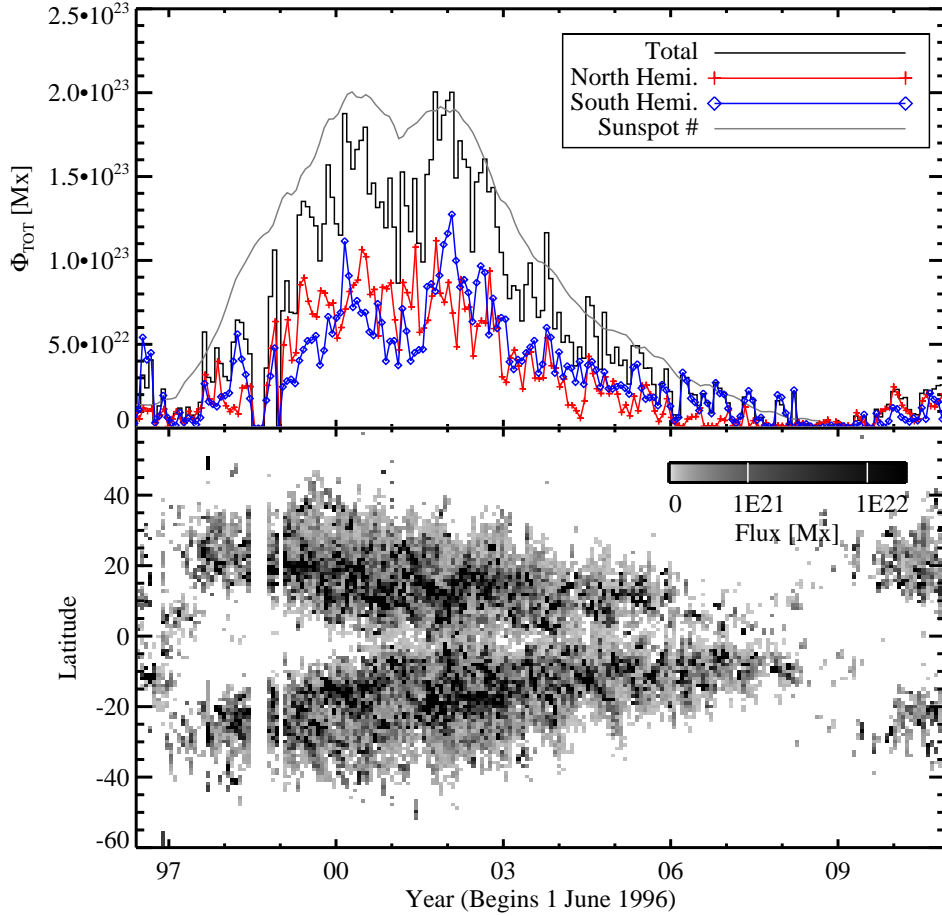


Figure 6.1: *Top:* Comparison of total magnetic feature Φ_{tot} (27 day bins) observed on disk (black line) with that in the northern (red crosses) and southern (blue diamonds) hemispheres. The SIDC sunspot number is over-plotted in gray. *Bottom:* Φ_{tot} binned in latitude (1°) and time (27 days).

exhibits the structure indicates that either the mechanism causing flux emergence is hemispherically asymmetric or the distribution of flux tubes at the base of the convection zone is hemispherically asymmetric. Wang & Sheeley (213) report that most cycles are variously multi-peaked, and that this is caused by an underlying stochastic process.

Using the Φ_{tot} butterfly diagram in the bottom panel of Figure 6.1, the dependence on latitude and time of magnetic feature emergence can be established. First, we

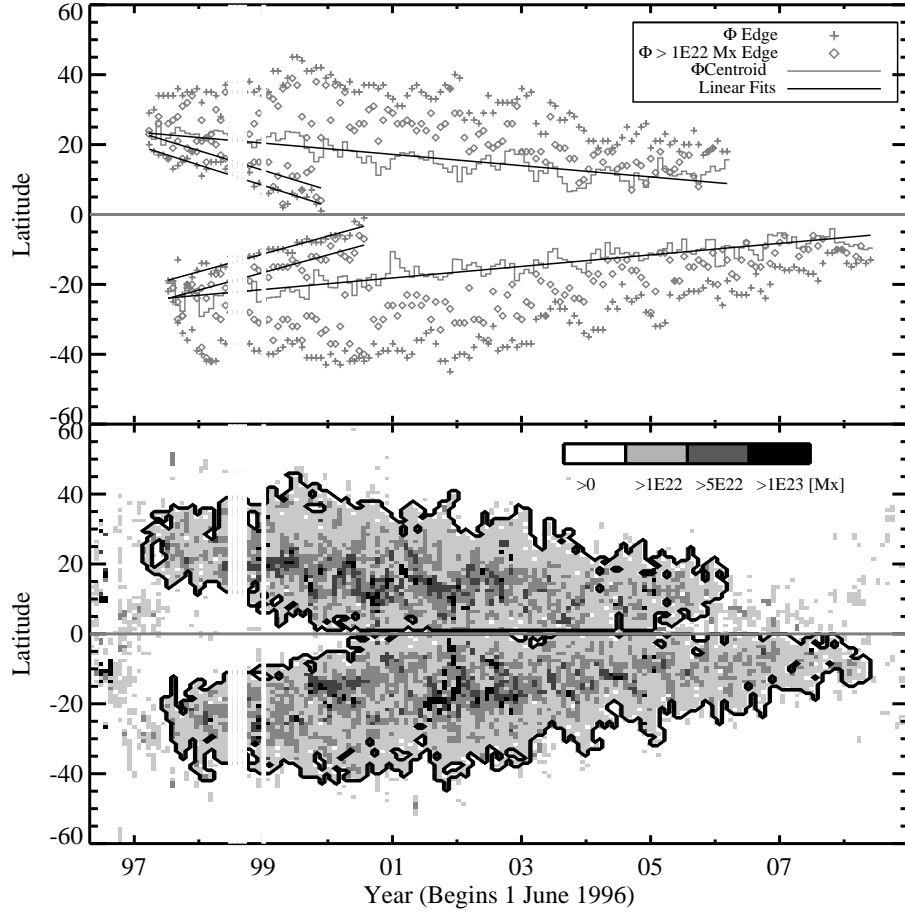


Figure 6.2: *Bottom:* Masks of detected centroids for features of greater than 0, 10^{22} , 5×10^{22} , and 10^{23} Mx in black, dark gray, light gray, and white, respectively. *Top:* Flux-weighted latitude centroid for the north and south hemispheres (gray lines), high and low latitude edges (crosses) of detection masks, edges of 10^{22} Mx mask (diamonds), and linear fits to centroids and edges (black lines).

characterize the equator-ward progression of AR emergence for the north and south hemispheres. The flux weighted centroid in latitude is determined at each time bin for each hemisphere (grey solid-lines in top panel of Figure 6.2). Further processing is required to extract information about the pole-ward and equator-ward edges of AR emergence from this map.

First, missing data is filled using bilinear interpolation in time so that there are

6. SUNSPOT GROUPS AND THE GLOBAL MAGNETIC FIELD OF THE SUN

Table 6.1: Linear fits to equatorward edges (>0 Mx contour) and latitude centroids of hemispheric flux in AR detections, with $t = 0$ defined as 1 January 1979 at 00:00 UT. Variables $\dot{\theta}$ and θ_0 have units of degrees year $^{-1}$ and degrees, respectively.

	Centroid		Equatorward	
	North	South	North	South
Slope $\dot{\theta}$	-1.61 ± 0.02	1.65 ± 0.01	-5.88 ± 0.10	5.08 ± 0.09
Intercept θ_0	52.62 ± 0.40	-54.48 ± 0.31	125.88 ± 2.04	-113.06 ± 1.73
Red. χ^2	27.37	4.44	22.40	11.51

no artificial gaps in the latitude-time map. We define the region containing cycle 23 as the largest contiguous contour in the AR detection flux map, using a threshold of 0 Mx (dotted line contour in bottom panel of Figure 6.2). Pixels outside this region are removed. The pole-ward and equator-ward edges are determined by taking the minimum and maximum pixels of this contour at each time bin. Lines are then fit to these edges. The line fits are of the form,

$$\theta = \dot{\theta}t + \theta_0 , \quad (6.3)$$

where θ is latitude, $\dot{\theta}$ is the slope or rate-of-change of θ , and θ_0 is the “Y-intercept” or the latitude at which the best-fit line crosses the Y-axis at $t = 0$, which is defined as 1 January 1979 at 00:00 UT. This process is repeated for maps including detections above 10^{22} , 5×10^{22} , and 10^{23} Mx. The top panel of Figure 6.2 shows the best-fit lines to the detected edges (symbols and black solid-lines), while the bottom panel shows contours in black at >0 Mx for the flux map.

Here it is seen that the equator-ward edges of AR emergence in each hemisphere progress toward the equator more rapidly than the flux-weighted latitude centroid. The north and south equator-ward edges progress at -5.88 and 5.08° year $^{-1}$, respectively, while the north and south centroids progress at -1.61 and 1.65° year $^{-1}$. These are the most accurate measurements of the equator-ward AR butterfly edge to date. Zhang *et al.* (227) measure the equatorward drift speed of the flux-weighted centroid of the

6.3 Results and Discussion

combined set of ARs detected in the northern and southern hemispheres, attaining a value of $1.83^\circ \text{ year}^{-1}$. Our centroid fits have reduced χ^2 values significantly larger than unity. This indicates that either a linear fit is not the function best suited to describe these observations, or the overall spread of centroid positions is too high to provide a reliable fit. The inner edges of AR emergence are physically more interesting than the centroid, as they have been shown to be co-spatial and co-temporal with observations of the surface shear torsional oscillation observations (103). The torsional oscillation precedes the onset of AR emergence by about 10° (78). Thus, if the torsional oscillation destabilises flux ropes at the tachocline, causing them to rise and emerge as ARs, then it must take ≥ 6 years for this to occur, assuming that the AR emergence front is moving equatorward at $\sim 1.6^\circ \text{ years}^{-1}$. Upon visual inspection of both the top and bottom panels of Figure 6.2, \sim year-scale oscillations in the latitude of the flux centroids maybe present, but a much longer time-scale study must be done to determine if they are significant.

We can see from the bottom panel of Figure 6.2, the ARs of largest flux are more confined in latitude. Regions below 10^{22} Mx emerge up to 40° in latitude, while those above 10^{22} Mx , $5 \times 10^{22} \text{ Mx}$, and 10^{23} Mx are confined to below 30° , 25° , and 20° respectively. Regions of larger area have shown to be more confined in latitude than those that are smaller (87; 132; 202).

Now we determine the amount of time over which flux is observed to emerge at each latitude (Figure 6.3) for solar cycle 23. This is done in two ways: the bins in which ARs are observed are counted for each latitude (thin black line); the time difference between the first and last observed AR at each latitude is measured (thick black line).

The relationship between latitude and the amount of time that ARs are observed to emerge may provide insight into the internal dynamo, including large-scale flows, at the base of the convection zone. It is thought that the omega effect results in a reservoir of toroidal flux tubes which become twisted and stretched due to shear at the

6. SUNSPOT GROUPS AND THE GLOBAL MAGNETIC FIELD OF THE SUN

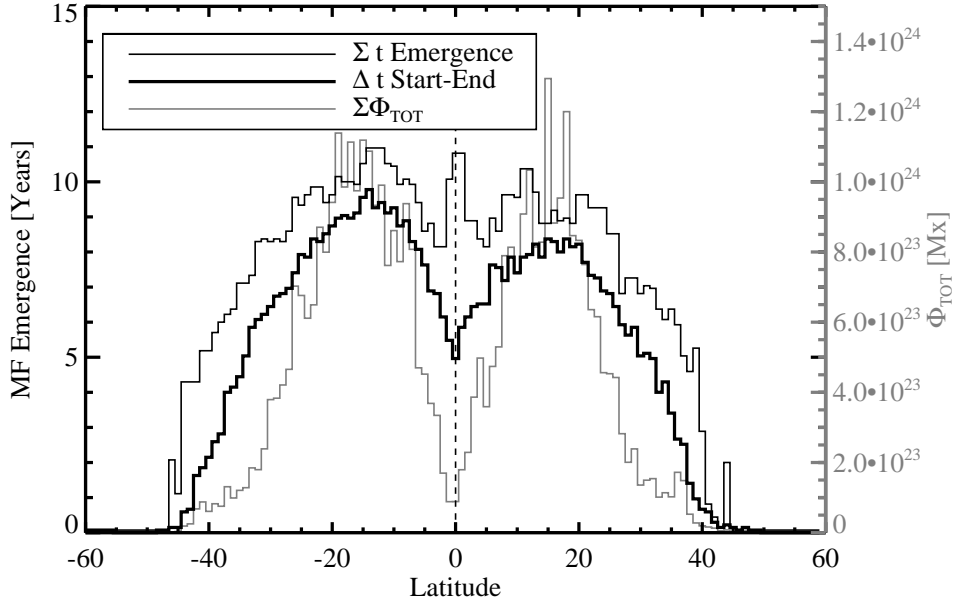


Figure 6.3: The amount of time that flux is observed to emerge at each latitude. This is measured both by counting the bins in which AR are observed for each latitude (thin black line) and measuring the time difference between the first and last observed AR at each latitude (thick black line). For comparison, Φ_{tot} at each latitude (averaged over a Carrington rotation) summed over time is shown (gray line).

tachocline. The observed torsional oscillation is thought to cause these flux tubes to become hydro-dynamically unstable, resulting in enhanced buoyancy that causes them to ascend through the convection zone, eventually emerging as ARs in the photosphere. So, the total flux that has emerged at each latitude may indicate the density of toroidal flux at the base of the convection zone (35). The poleward deflection of rising flux tubes due to the Coriolis effect would have to be taken into account to make a determination of the sub-surface flux distribution.

Through simulations, the Coriolis effect has been shown to deflect buoyant flux tubes toward higher latitudes as they rise. This is because as flux tubes rise they conserve angular momentum by exhibiting retrograde motion. This motion is then affected by the Coriolis effect and the flux tube is deflected poleward. The deflection is dependent on magnetic field, so flux-tube in which stronger fields are deflected less

6.3 Results and Discussion

as they resist the induced force more than those with weaker fields (59, and references therein). Our observations of the latitude distribution of AR flux support the simulation results; weaker features are observed at higher latitudes than stronger features. This holds if it is assumed that there is no dependence on latitude for the field strength of toroidal flux at the base of the convection zone.

As mentioned before, the equator-ward edge of AR emergence matches the latitude of the torsional oscillation shear (103). This is thought to initiate the emergence of ARs at each latitude as it progresses from pole to equator. The instability that is created at each latitude may persist for many rotations until the reservoir of flux at the base of the convection zone is depleted. This time scale may vary with latitude, depending on the amount of toroidal flux that has been generated at the bottom of the convection zone.

It is clear that the latitude distribution of ARs changes over the solar cycle, but the magnetic area (size) and Φ_{tot} are also observed to change. The top panel of Figure 6.4 shows the mean area and Φ_{tot} in yearly bins over the rise, maximum, and decay phases. Three low peaks are observed in each plot, two of which are coincident with the double peaks in total observed flux discussed earlier. A third peak is observed a year into the decay phase of the cycle, which is not as readily apparent in the previous plots. The average properties increase with the rise of the cycle, are roughly constant during the plateau, and decrease over the decay phase; this agrees with the findings of Tang *et al.* (202). Interpreting this plot alone, lower mean property values at solar minimum could either be due to an excess of small detections, or a lack of large detections relative to other times. Due to the large bins (1 year) and the number of detections ($\sim 10^4$), it is not likely that these peaks are merely statistical fluctuations.

In order to determine which is true, we plot the AR property distributions for each phase (middle and bottom panel of Figure 6.4). The area and Φ_{tot} distributions are roughly power-law from 2×10^3 and 2×10^{21} to $3 \times 10^4 \text{ Mm}^2$ and $3.5 \times 10^{22} \text{ Mx}$,

6. SUNSPOT GROUPS AND THE GLOBAL MAGNETIC FIELD OF THE SUN

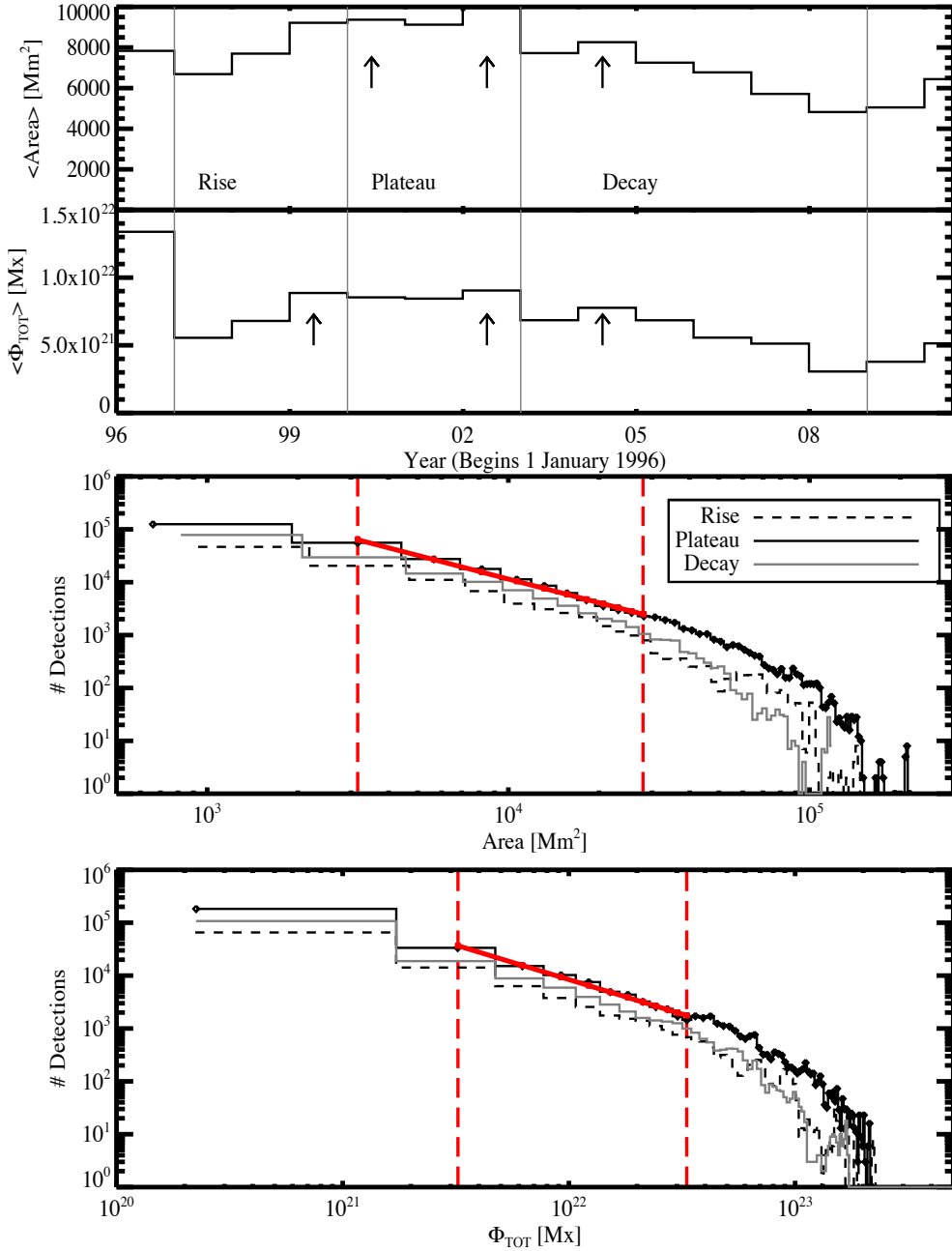


Figure 6.4: *Top:* Average magnetic feature area and Φ_{tot} in yearly bins (black line). Vertical lines denote beginning and end of solar cycle phases. Arrows indicate peaks in $\langle \text{area} \rangle$ and $\langle \Phi \rangle$. *Middle:* Distributions of detection areas for “rise” (dashed line), “plateau” (black line), and “decay” (gray line) phases defined in *top* panel. A power-law fit to the rise-phase distribution is indicated by the straight red line. The vertical red dashed lines denote the range of the fit. *Bottom* Same as *middle* panel for Φ_{tot} .

6.3 Results and Discussion

Table 6.2: Power-law fits to distributions of AR area and Φ_{tot} .

Cycle Phase	Area	Red. χ^2	Flux	Red. χ^2
Rise	-1.51 ± 0.29	81.69	-1.29 ± 0.28	4.99
Plateau	-1.49 ± 0.26	186.94	-1.30 ± 0.25	83.14
Decay	-1.50 ± 0.28	168.49	-1.27 ± 0.27	27.09

respectively. The distributions have similar power-law exponents over this range, as shown by the fits (Table 6.2). The first bin in each distribution is excluded from the fits due to the area threshold imposed by the detection method, which falls within this bin. This explains why the lowest bin falls below the power-law fits.

Recent statistical studies of the properties of active regions have found power-law distributions for area and flux. Parnell *et al.* (149) find a power-law with slope -1.85 for the distribution of AR flux between 2×10^{17} and 10^{23} Mx. The substantial differences in the distributions between various studies are likely due in part to feature detection method (46). Also, there are many more small features observed than large features, but feature lifetime tends to scale with size. So, many more observations of a given large feature will be included in the sample than of a given small feature. Thus, the effect of double counting the same physical feature due to the inclusion of multiple observations results in a less steep power-law slope (202). This explains why our fits (-1.5 for area and -1.3 for flux), that are based on many observations over a long period of time, are more shallow than the result of Parnell *et al.* (149), which is based on observations at single points in time.

The distributions diverge above the power-law fit range, with the plateau phase exhibiting an excess of detections with large flux as compared with the rise and decay phases ($>3 \times 10^{22}$ Mx). So, at solar maximum more large regions are observed than during other phases. Previous studies have found essentially the same result (87; 132; 202). This excess of large regions at the maximum of the activity cycle has also been observed in continuum sunspot observations over many cycles (89). It is possible that

6. SUNSPOT GROUPS AND THE GLOBAL MAGNETIC FIELD OF THE SUN

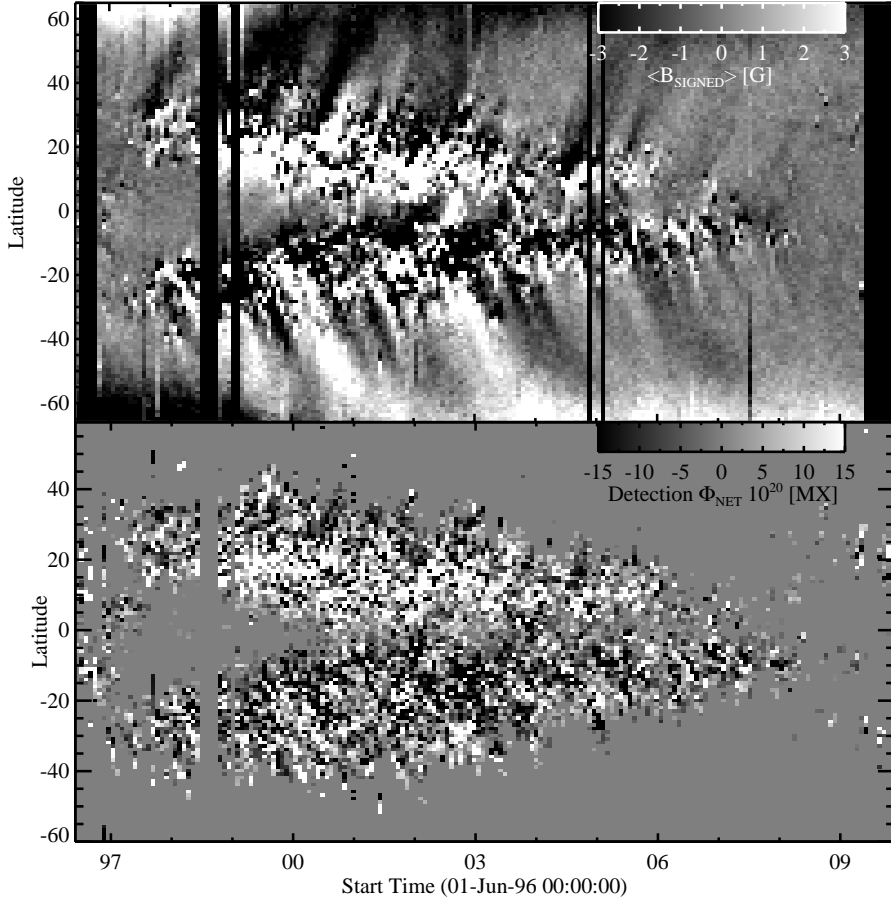


Figure 6.5: *Top:* Magnetic butterfly diagram (1° latitude and 27 day time binning) of mean signed magnetic field. *Bottom:* Total magnetic feature Φ_{net} with binning the same as the *top* panel.

the excess is due to the inclusion of very large AR complexes during the plateau phase, that last much longer than any single AR. Their extended lifetime results from the continued emergence of new flux within the complex that maintains its large size.

6.3.2 The Global Magnetic Field

The top panel of Figure 6.5 shows the mean magnetic field for each latitude over the solar cycle. This image allows us to draw several conclusions. In the northern hemi-

6.3 Results and Discussion

sphere, the polar field begins as positive and reverses to negative around January 2000. Large unipolar regions of negative flux can be seen to progress poleward, leading to the reversal. At about the same time an excess of positive flux is observed in the low-latitude active region belt. The same is observed in the southern hemisphere, but with reversed polarities. Similar large-scale unipolar regions are not observed to move toward the equator during 1997–2000 (when they would be visible). So, It is reasoned that the low latitude flux imbalance is primarily a result of one polarity of magnetic flux being preferentially dragged poleward due to the combination of meridional flow and Joy’s law, as is the accepted view (see 186, and references therein). This phenomena is described in Section 1.8.1.

The SMART detections of individual ARs are binned in time and latitude, resulting in the image shown in the bottom panel of Figure 6.5. The same polarity imbalances are observed in each hemisphere as in the top panel (albeit, less clearly); excess positive at low latitudes in the north and negative in the south. Since ARs are east-west oriented, it might be assumed that the observed polarity imbalances in the active region belt are created due to features being partially out of the 60° field of view. To rule out this possibility, Φ_{net} is determined for detected features with boundaries completely within $\pm 60^\circ$ longitude. Alternatively, if there was a net East-West tilt in fields from the normal to the surface of a flux balanced AR, one polarity would appear stronger in the western hemisphere while the other would appear stronger in the eastern hemisphere. This effect would be averaged out in our case, since the data are binned by 27 days.

A flux balanced magnetic feature can have completely closed magnetic fields. However, a feature which has an excess flux of one polarity must have field which is either quasi-open (connected to the solar wind) or connected to excess flux of the opposite polarity some distance away on the solar surface. In the case of the observed excess flux in Figure 6.5 the low latitude excess flux (which is summed over longitude) is likely connected trans-equatorially, and to the high latitude excess (36). The high latitude

6. SUNSPOT GROUPS AND THE GLOBAL MAGNETIC FIELD OF THE SUN

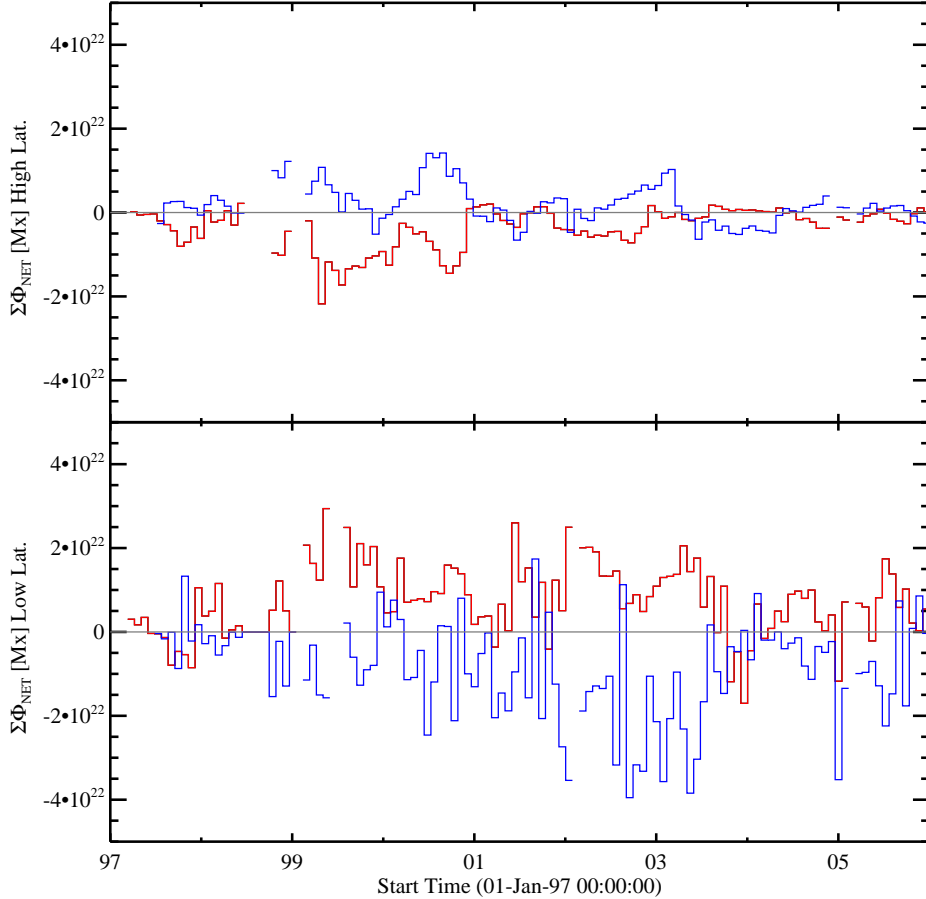


Figure 6.6: *Top:* Total Φ_{net} determined from $\langle B_{\text{signed}} \rangle$ in the magnetic butterfly diagram (poleward of detected features; $\Phi_{\langle B \rangle, HI}$) in northern (red) and southern (blue) hemispheres. *Bottom:* Summed Φ_{net} in the active longitudes detected in magnetic features (thick solid lines) and using the magnetic butterfly diagram (dashed lines; $\Phi_{\langle B \rangle, LOW}$). The subscript *HI* denotes the latitude range from the Φ -edge shown in the top panel of Figure 6.2 up to $\pm 54^\circ$, while *LOW* denotes the range from the Φ -edge down to the equator.

excess flux is likely connected to the poles.

To determine the total imbalanced flux in detected ARs at low latitudes, we sum their Φ_{net} in each hemisphere using the data shown in the bottom panel of Figure 6.5. Flux imbalances in the top panel of Figure 6.5 are quantified by defining two zones in each hemisphere using the poleward edges of the $\Phi_{\text{tot}} > 0$ detection mask shown in the

6.3 Results and Discussion

top panel of Figure 6.2: the high-latitude region is defined to be between the poleward edge of the detection mask and 54° (top panel of Figure 6.6); the low-latitude region is defined to be between the equatorward and poleward edges of the detection mask (bottom panel of Figure 6.6).

The upper bound for high-latitude flux (θ_{\max}) is determined by estimating the distance that flux from low-latitude magnetic features is carried poleward by the meridional flow during the time interval of the ~ 6 month activity bursts mentioned in discussion of Figure 6.1. This is calculated by,

$$\Delta\theta = v_{\text{flow}} \Delta t \times \frac{360^\circ}{2\pi R_\odot}, \quad (6.4)$$

where θ is heliographic latitude, Δt is chosen to be 6 months, v_{flow} is a characteristic meridional flow speed (chosen to be 15 m s^{-1} from measurements in Hathaway & Rightmire (90)), and R_\odot is the solar radius. Assuming most of the ARs emerge below 35° , we add $\Delta\theta$, and calculate a θ_{\max} of 54° . Using this value for θ_{\max} , high-latitude flux measurements should include the majority of the poleward moving flux from a given activity burst.

To calculate the total net flux at a given latitude we take the mean magnetic field measured in each latitude band (from the magnetic butterfly diagram in the bottom panel of Figure 6.5) and multiply by the area covered by a band encircling all longitudes. This yields the net flux in a given latitude range ($\Delta\theta = \theta_2 - \theta_1$) on the Sun at a given time,

$$\Phi_{\langle B \rangle} = \langle B \rangle 2\pi R_\odot^2 (\sin \theta_2 - \sim \theta_1), \quad (6.5)$$

where $\langle B \rangle$ is the averaged signed magnetic field. These flux measurements are compared to the summed AR Φ_{net} at low latitudes, as shown in Figure 6.6.

We find both the low- and high-latitude imbalances to be of opposite polarity in each hemisphere. Additionally, for each hemisphere, polarity imbalances are opposite for the

6. SUNSPOT GROUPS AND THE GLOBAL MAGNETIC FIELD OF THE SUN

high and low latitudes. By comparing Φ_{net} (determined from SMART detections) with $\Phi_{\langle B \rangle}$ for high latitudes (determined from the magnetic butterfly diagram), we can see that the flux imbalance in the active latitudes is of similar magnitude for the first half of the solar cycle, but opposite in polarity to that at high latitudes. This is the first time these measurements have been directly quantitatively compared.

Since significant (opposite) imbalances in flux are observed for each hemisphere, this implies that flux cancellation at the equator cannot be rapid enough to offset the missing flux carried to the poles by the meridional flow. It is likely that the excess flux at low latitudes (contained in the leading polarities of ARs) was not then carried to the equator because the leading poles of ARs decay more slowly than the trailing. The excess flux may be contained in the stronger magnetic fields of the leading poles, which, if anchored significantly below the photosphere could then resist the surface meridional flows, unlike the weaker trailing poles that were carried much more swiftly to the north and south poles. In a sense, the system is like panning for gold. The loose sand (representing weak magnetic fields) is washed away by the flow of the water, while the gold nuggets (representing strong magnetic fields) stay planted firmly in the pan.

The reason for the large difference in the magnitude of Φ_{net} and $\Phi_{\langle B \rangle}$ after 2001 may be due to the lower latitudes at which sunspot groups begin emerging. The meridional flow may not be strong enough at these latitudes to preferentially carry one polarity to high latitudes, resulting in the small values of $\Phi_{\langle B \rangle}$. Also, one polarity of flux may preferentially cancel at the equator, resulting in the large values seen in Φ_{net} at this time.

Magnetic field-line traces are overlaid on white-light coronagraph images to compare the magnetic structure in the lower corona to that further out. This is done using extrapolations from the global PFSS model¹ described in Schrijver & De Rosa (175)

¹The model runs rely on MDI LOS data and can be downloaded and visualised using the PFSS widget available through SolarSoft, as was done in this work. Documentation for the PFSS code is available here: <http://www.lmsal.com/~derosa/pfsspack/>

6.3 Results and Discussion

and Level 1 *SoHO*/Large Angle and Spectrometric Coronagraph Experiment (LASCO; 28) data, as shown in Figure 6.7. The coronagraph images are radially filtered by dividing out the average intensity in 5 pixel-width annuli. The coronagraph data and PFSS extrapolations are matched as close as possible in time.

These images show regions of enhanced density in the extended corona. The shape of these regions is determined by large-scale magnetic fields. We observe the majority of imaged helmet streamers to have roughly the same configuration as the dominant modeled closed-loop structures. The configuration of surface magnetic features is expected to match the global configuration of the atmosphere exterior to the Sun (175). Wang *et al.* (215) compare modeled coronal emission (determined using a PFSS algorithm) to LASCO data, remapped to time-latitude space, finding good agreement.

6. SUNSPOT GROUPS AND THE GLOBAL MAGNETIC FIELD OF THE SUN

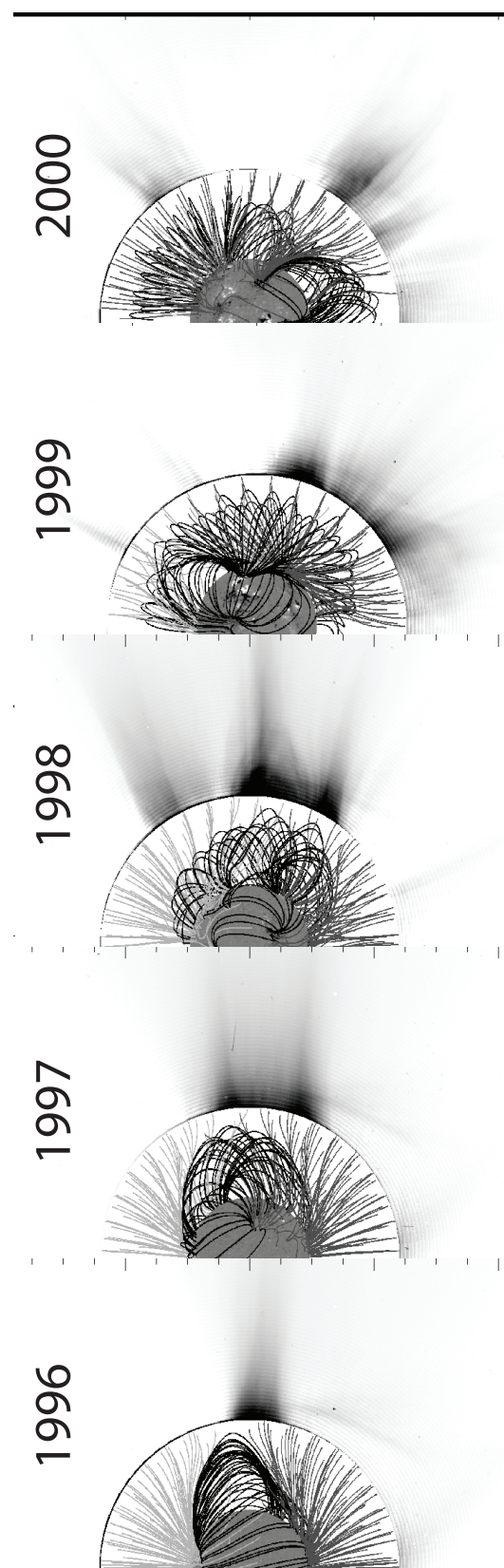


Figure 6.7: Comparison between global PFSS extrapolations and white-light coronagraph observations. Color denotes closed (black), positive open (light-gray) and negative open (dark-gray) field lines.

6.3 Results and Discussion

Differences occur because the structure of the corona is dynamic on the scale of hours, while photospheric features, once emerged tend exhibit dynamics on the scale of days. For instance, transient phenomena (coronal mass ejections and out-flows) may occur, which do not cause significant structural changes in the photosphere. Differences between the extrapolated magnetic structures and enhanced coronal density configuration may be caused by this as well as by the methods used to generate a 360° map of the solar surface, utilised by the PFSS model.

Rapid flux emergence could occur in the photosphere that is beyond the assimilation edge of the PFSS model. The model used in this work relies on photospheric field maps produced by assimilating new flux at the east edge of the solar disk as it rotates into view. Any flux beyond that edge is estimated from that which has rotated off the west edge of the disk \sim two weeks before. Regions which have emerged on the backside of the Sun and not yet rotated on disk will therefore not be included in a given extrapolation. Because reliable magnetic field observations of the far side of the Sun are not available and the dynamic timescale of the solar surface and atmosphere is much shorter than the rotation period, any PFSS results can not be a true snap shot of the Sun, and must smear out measurements in time and space. Finally, LOS effects in the magnetograms, as discussed in Chapter 4, such as false polarity separation lines (PSLs), can also affect the field extrapolation.

These magnetic field extrapolations are used to determine how the global magnetic field changes over the solar cycle. Spherical harmonics, as defined by Equation 6.2, are used here to describe the large-scale field topology. At different phases of the solar cycle the field can be described by different modes. When there are no magnetic features detected, such as during solar minimum, the global field configuration is that of a dipole ($\ell = 1, m = 0$), as shown in the first panel of Figure 6.8. After the first active regions of the cycle have emerged and begun to decay, the field gains a significant ($\ell = 5, m = 0$) moment (third panel). Finally, after the north and south poles have switched polarity,

6. SUNSPOT GROUPS AND THE GLOBAL MAGNETIC FIELD OF THE SUN

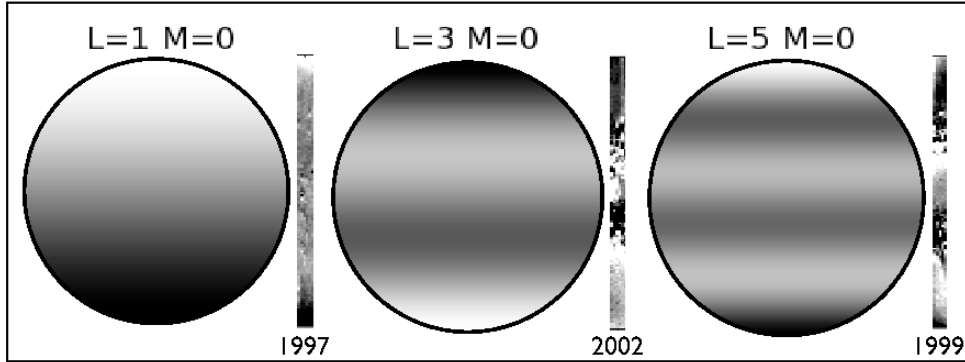


Figure 6.8: Examples of axially symmetric and hemispherically antisymmetric spherical harmonics. White represents positive and black represents negative regions of $\Psi(r, \theta, \phi)$ at radius R_\odot . Sections of the $\langle B_{\text{signed}} \rangle$ butterfly diagram are included adjacent to each mode for context.

the following polarity of an active region is the same as that of its nearest pole, and there is a significant ($\ell = 3, m = 0$) moment in the solar field (second panel).

Near the solar surface, these harmonic modes are not as useful for describing the magnetic field structure because of the presence of localised strong-field features (i.e., plage and sunspots). But, a few R_\odot from the surface low-order modes begin to dominate. This is because the magnetic field strength falls off faster with the higher-order modes.

The top panel of Figure 6.9 shows the polar field strengths averaged over two latitude bands. The southern hemisphere field appears to reverse before the northern one. Field reversal occurs smoothly over 2–3 years in the northern hemisphere while it happens in several \sim year timescale bursts in the south. This is similar to the progression of southern Φ_{tot} (Figure 6.1), which exhibits large peaks and troughs.

To determine how significant each of the harmonic modes are to the global field configuration, we can compare the harmonic coefficients of each mode (see Equation 6.2) over time, as calculated by the PFSS model. At solar minimum, when the field strengths are largest and the fewest magnetic features are present, the dipole ($\ell = 1, m = 0$)

6.3 Results and Discussion

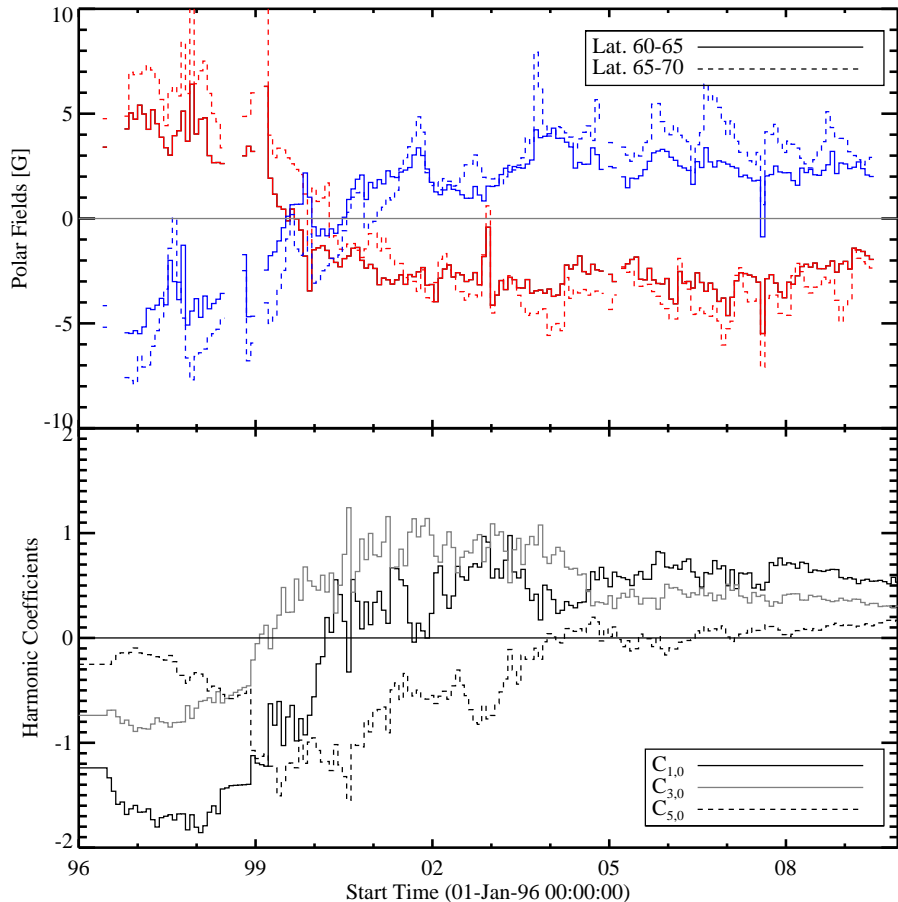


Figure 6.9: *Top:* Polar field strengths in the northern (Red) and southern (Blue) hemispheres, determined from the $\langle B \rangle$ map (top panel of Figure 6.5). Dashed lines indicate field values sampled from higher latitudes than the those indicated by the solid line. *Bottom:* Spherical harmonic coefficients for three different modes.

harmonic coefficient is largest (black line in bottom panel). There is also a significant ($\ell = 3, m = 0$) moment during this time, which is probably due to the presence of a single bipolar magnetic feature on disk. As more active regions emerge and decay, the ($\ell = 5, m = 0$) mode becomes dominant from around 1999 to 2001. From 2001 to mid 2004, the ($\ell = 3, m = 0$) mode is dominant since the poles have switched polarity. When few enough ARs are present, the dipolar mode becomes dominant again, from mid 2004 onward.

6. SUNSPOT GROUPS AND THE GLOBAL MAGNETIC FIELD OF THE SUN

6.4 Conclusions and Future Work

In this chapter, we use automated magnetic feature extraction to determine the properties of a large sample of magnetic features that emerge into the solar photosphere. The evolution of large-scale magnetic fields can be characterised by studying the dynamic properties of AR emergence. We support some previous work on the magnetic solar cycle, as well as provide some new insights and draw some new conclusions. A summary of our results is as follows:

- The double peak observed in the solar activity cycle only occurs in the southern hemisphere and activity in the northern hemisphere exhibits a much smoother rise and decline over the cycle. This indicates that the subsurface production of strong magnetic field structures due to the magnetic dynamo is asymmetric.
- The emergence of features of largest magnetic flux are most confined in latitude and this latitude moves equatorward over the solar cycle. This could indicate the magnetic flux distribution at the base of the tachocline at the start of the solar cycle. Alternatively, this could be related to the equatorward progression of the torsional oscillation, which may be responsible for the onset of AR emergence at a given latitude at the start of a solar cycle.
- There is an excess of magnetic features with large flux in the plateau phase of the solar cycle. This could result from the formation of sunspot nests or active longitudes, in which multiple magnetic features emerge at the same position on the solar surface¹, sometimes forming large AR complexes.
- The flux imbalance in the north (south) active latitudes is positive (negative) in polarity and of the same order of magnitude to that at north (south) high latitudes for cycle 23. This is the first time this comparison has been made. We

¹See the analysis of NOAA 10365 in Chapter 5.

6.4 Conclusions and Future Work

suggest that the observed flux imbalance results from one polarity of magnetic flux being preferentially carried to high latitudes by the meridional flow.

- The dominance of certain global magnetic field spherical harmonic moments over the solar cycle is a result of the large-scale distribution of imbalanced flux. Alternating latitudinal bands of imbalanced flux which vary over the solar cycle are shown to have a significant impact on the global magnetic field.

Many authors, including Temmer *et al.* (203), have shown that the emergence of sunspot groups is hemispherically asymmetric. This work presents one of the few comparisons of hemispheric flux imbalance. Meunier (132) compares the flux distribution of magnetic features in each hemisphere, finding different excesses of detected features in each hemisphere depending on the threshold used in their detection method, while our results show a clear dominance of each hemisphere at different times during the solar cycle.

The use of SMART for detecting ARs affects the measurement of flux imbalance. Weaker fields at the edges of trailing plage regions associated with ARs are less likely to be included in the SMART detection contours than the dense fields of sunspots. Thus, if a region emerges flux balanced, it will be left with an excess of dense leading-polarity flux as the trailing polarity decays. However, the same dominant-polarity pattern is observed in the butterfly diagram of flux imbalance (Figure 6.5) constructed using raw magnetograms (top panel) and the one constructed using SMART detections (bottom panel). Thus, it is likely that the observed polarity excesses are merely exaggerated, rather than incorrect.

This work has resulted in the characterisation of magnetic features and their emergence over the solar cycle. Although the choice of divisions for solar cycle phases differs, our results essentially agree with those of (132) in that there is an excess of large features around solar cycle maximum. This is important for constraining dynamo models.

6. SUNSPOT GROUPS AND THE GLOBAL MAGNETIC FIELD OF THE SUN

For instance, we have determined the latitudinal distribution of the flux and size of detected features over time and these results can be tied to a model of buoyant flux tube deflection due to the coriolis force to constrain their subsurface properties. A future detailed comparison of sunspot group detections to the residual meridional flow and differential rotation (torsional oscillation) could indicate the nature of their relationship. Currently, it is only clear that magnetic activity and the torsional oscillation is well correlated in time and latitude (91). The next step in studying the solar activity cycle is to tie observations of emergent solar features to both phenomenological and mean-field dynamo models of the solar convection zone.

Characterising the Transport of Diffuse Magnetic Flux

The material in this chapter will be published in Higgins et al., Solar Physics (2012b). This is an investigation of the large-scale plasma motions at the solar surface, using photospheric magnetic features as tracers for the surface flows. The aim of this work is to accurately characterise the flows that fuel the transport and decay of sunspot groups. A magnetic butterfly map is used to identify the poleward motion of unipolar magnetic flux. Simulations are run to separately determine the effects of supergranular motions, the meridional flow, and differential rotation on the poleward propagating flux. Finally, a data driven simulation is run and the results are compared with the observed motion of flux in the magnetic butterfly map to constrain the diffusion coefficient that characterises the effect of supergranular flows on the decay and dispersion of magnetic features.

7. MAGNETIC FLUX TRANSPORT

7.1 Introduction

Weak magnetic flux elements observed in the photosphere move across the solar surface under the influence of the differential solar rotation, meridional flow, and both granulation and supergranulation (rolling convection). Differential solar rotation and the meridional flow result in bulk motion, while supergranulation has a dispersive effect, resulting in the cellular distribution of flux seen in Figure 1.11). The random surface motions can be modeled as a diffusive process (186). The rate at which flux disperses is indicated by the diffusion coefficient (D 54).

D can be measured directly from observations of evolving magnetic flux. Alternatively, simulations of flux evolution can be run, assuming a value for D , and the results can be compared to observations. Previous work has measured a wide range of values that are, in general, too small to reproduce the observed solar cycle using flux transport simulations. This is thought to be due to the temporal and spatial scales of the observations used (178). In this chapter, we attempt to reconcile the difference between values of D used in most simulations ($\sim 600 \text{ km}^2 \text{s}^{-1}$) and those determined from observations ($\sim 100 - 300 \text{ km}^2 \text{s}^{-1}$). A data driven simulation of magnetic flux diffusion is directly compared to observations of several decaying active regions for over 1 year.

7.1.1 Modeling Supergranular Diffusion

The motion of weak magnetic elements can be described as a stochastic random walk process, similar to the Brownian motion of microscopic particles. (54) showed that statistically, the mean-squared distance a random walking particle has traveled from its starting location, $\langle r^2 \rangle$, is directly related to the time elapsed, t , and a constant describing the rate of diffusion, D (the diffusion coefficient). Considering diffusion across a surface this relation is,

$$\langle r^2 \rangle = 4Dt. \quad (7.1)$$

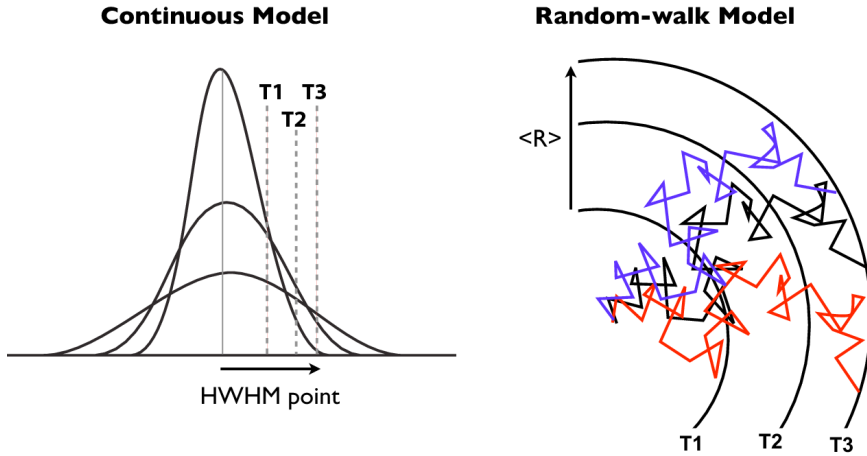


Figure 7.1: Schematics of the evolution of continuous and discrete random-walk diffusion. *Left:* the continuous model, assuming a Gaussian distribution of particles and showing the motion of the HWHM point. *Right:* the random-walk model, where the average displacement of particles moves outward over time.

A schematic of how $\langle r^2 \rangle$ might be measured from random walking particles is shown in the right image of Figure 7.1.

Assuming a continuous particle distribution, the ordinary two-dimensional diffusion equation is conventionally invoked to describe the dispersal of magnetic flux,

$$\frac{\partial \phi(r,t)}{\partial t} = D \nabla^2 \phi(r,t), \quad (7.2)$$

where D is the diffusion coefficient and the distribution of particles, ϕ , is a function of position and time. Generally, D is assumed to be constant over time and space. The left image of Figure 7.1 shows a schematic of a Gaussian distribution of particles diffusing over time. The increase in the half width at half maximum (HWHM) is shown by the dashed lines. By analytically solving Equation 7.2 for a Gaussian, the radial motion of a point on the Gaussian that is a constant fraction of its maximum (e.g., the $1/e$ -point or HWHM) can be determined as a function of time,

$$R_C = \sqrt{4|\ln(C)|Dt}, \quad (7.3)$$

7. MAGNETIC FLUX TRANSPORT

where C is the fraction of the Gaussian's maximum of the tracked point. To predict the motion of the HWHM, $C = 0.5$.

(112) pioneered the use of the continuous diffusion model to simulate surface magnetic flux dispersal. He took into account observational properties of supergranules such as lifetime and size to estimate D . An observational differential rotation profile was also included. Although the simulation lacked a meridional flow, the magnetic solar cycle was qualitatively reproduced.

The continuous 2D diffusion equation is applicable when modeling the dispersion of magnetic flux elements over long time scales and large spatial scales. The model results in a smooth dispersion of flux over time (at any scale), while the random-walk model must be run for many iterations using many particles to achieve a smooth distribution of flux. So, for the discrete random-walk and continuous models to be compared the observational scales must be much greater than the characteristic supergranule size and lifetime (185), as determined by (179), for instance. Measured diffusion rates have been shown to be larger when using larger observational scales (81).

In this work diffusion is simulated on a Cartesian planar surface, as opposed to a spherical surface (like the Sun). When considering the diffusion of a circular distribution of flux, the area becomes increasingly overestimated as the radius of the distribution increases. Once the distribution covered half of the solar surface, its area would be overestimated by $\sim 20\%$. This results in an overestimation of D that must be taken into account.

7.1.2 Observational Studies

A number of studies have used observations of a portion of the solar disk to determine the rate of magnetic flux dispersion, assuming the models explained in the previous section. (136) introduced a cross correlation technique to derive the diffusion coefficient, D , from a sequence of images of weak magnetic features using Ca II K images as a proxy

for magnetic flux, achieving D values of 200 and $400\text{ km}^2\text{s}^{-1}$ from two different data sets. Using the same technique, (211) derives D values of around $150\text{ km}^2\text{s}^{-1}$ from a sequence of vector magnetogram images. (111) determine D more directly by tracking the mean step size of magnetic flux elements near an active region over 5 days and applying Equation 7.1. The majority of observational studies of dispersing magnetic flux consider the time scales of a fraction of a solar rotation and only track magnetic features over a small portion of the solar disk (19; 80; 81). The observations may represent a local dynamic timescale for the particular feature being tracked, but not that of the large scale pattern of flux for which Equation 7.2 holds.

7.1.3 Simulation Studies

Contemporary models of magnetic flux circulation generally use the surface flux transport (SFT) equation (47; 187),

$$\frac{\partial B}{\partial t} = -\nabla \cdot (B\mathbf{v}) + D\nabla^2 B + S, \quad (7.4)$$

where, B is vertical magnetic field through the solar surface, \mathbf{v} is the horizontal flow velocity across the surface, and S is the magnetic source term, accounting for new flux emergence. This equation is based on work from (112) that neglected the meridional flow.

Most global flux transport simulations use some variation of Equation 7.4. The differences in application lie in the specific choice of D , \mathbf{v} , and S . The choices of each are often inspired by observations, but can vary significantly. (215) simulate SFT assuming a value for D of $500\text{ km}^2\text{s}^{-1}$, but assume a meridional flow amplitude that has a higher amplitude and peaks at a much lower latitude than the profile measured in (91), with uncertainties less than the discrepancy between the profiles. Many recent studies qualitatively reproduce the observed magnetic solar cycle using variations of

7. MAGNETIC FLUX TRANSPORT

magnetic sources, meridional flow, and D (49; 176; 214)

While previous observational work described in Section 7.1.2 focuses on small temporal and spatial scales, the investigations using global simulations allow a comparison with the observed magnetic solar cycle. An exception to this is the study of (214) that directly compares the simulation and observation of the evolution of a sunspot group over several rotations to determine D , as discussed further in Section 7.5.

Global flux-transport simulation studies generally assume the continuous model of diffusion (Equation 7.4), but other smaller-scale simulations have used the random-walk model (Equation 7.1) to simulate flux-element motion and investigate D . For example, (189) simulate the dispersion of magnetic flux by introducing a distribution of particles to a 2D flow field, based on observations of supergranules. The particles are tracked as they move under the influence from these flows. Their combined motion is used to solve Equation 7.1 for D , resulting in values between ~ 500 and $700 \text{ km}^2 \text{s}^{-1}$, depending on the assumed properties of the supergranular flow field. Another random-walk simulation is explored in (180), but does not deal with the diffusion coefficient. The simulation is utilised in further studies (171; 175; 176). (81) compare tracked flux elements to a simplified random walk simulation, similar to (189), assuming a step length and time step based on supergranule observations. The effect of the presence of an additional diffusion process on a larger scale is tested by simultaneously applying a longer time-scale random walk. The combination of diffusion processes is shown to combine, resulting in an over-all larger D . Additional scales of diffusion resulting from large-scale convective processes may explain the discrepancy between the large and small-scale investigations of D discussed in Section 7.1.4.

7.1.4 Constraining D

As shown in Figure 7.2, previous flux dispersal and magnetic solar cycle simulation studies assume D values of $\sim 500 - 600 \text{ km}^2 \text{s}^{-1}$, which are generally larger than values

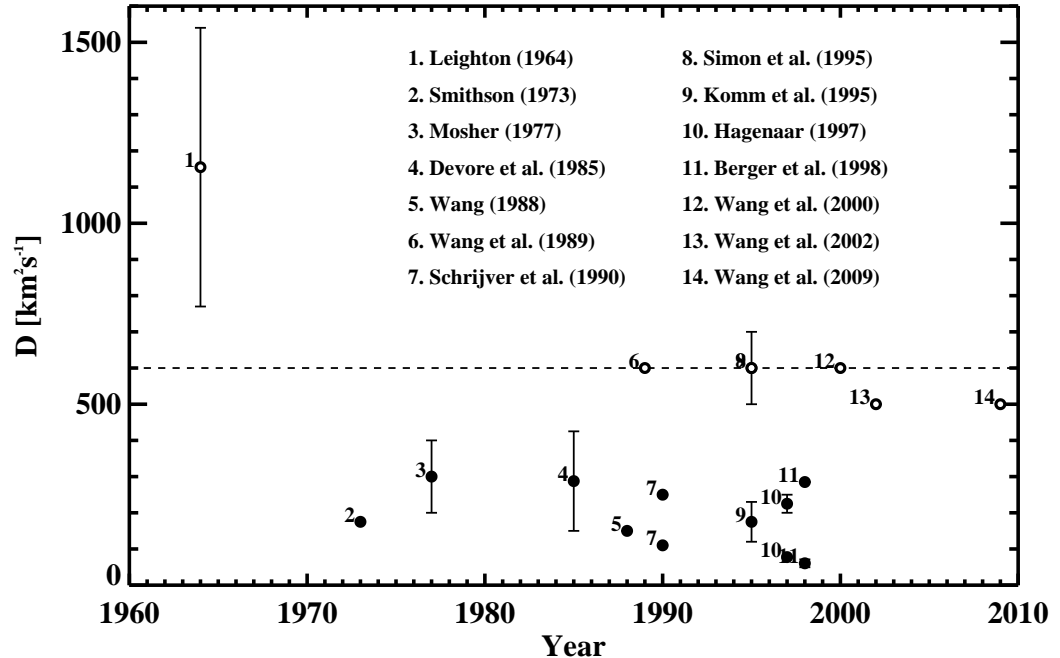


Figure 7.2: Previous results of studies treating the supergranular diffusion coefficient. Filled circles indicate observational results while empty circles indicate simulation results. The horizontal dashed line indicates the generally accepted value of $600 \text{ km}^2 \text{s}^{-1}$

determined more directly from observations ($\sim 100 - 300 \text{ km}^2 \text{s}^{-1}$). Simulations require larger values of D to match the observed properties of the solar cycle (polar field values and cycle length).

(178) show that the dispersion of magnetic elements decreases with magnetic flux density, B , by measuring their mean squared speed, $\langle v^2 \rangle$. Since D scales with $\langle v^2 \rangle$, assuming a dependency of $\langle v^2 \rangle$ on B . Studies tracking magnetic features are biased toward tracking larger, slow moving features, since these have longer lifetimes and are easier to follow. It is argued that D may be underestimated by up to a factor of three, as measured in the observational studies, and is likely to be around $600 \text{ km}^2 \text{s}^{-1}$.

Here we seek to get around the problems arising from tracking individual flux features. In this work we detect and analyse the progressing poleward boundary of two

7. MAGNETIC FLUX TRANSPORT

distinct large-scale decaying magnetic features for 10 solar rotations (\sim 1 year). The feature boundaries are observed in a magnetic butterfly diagram (85) using LOS magnetograms. (208) use wavelet methods and cross correlation to determine the speed of poleward drifting diffuse flux in a magnetic butterfly diagram with time binning of over a solar rotation, but they only attribute this to the meridional flow, not supergranular diffusion.

We then simulate the evolution of the observed features by taking into account differential rotation, the meridional flow, and supergranular diffusion. The diffusion coefficient, D , is varied in the simulations, allowing a fit to measurements of the poleward boundary of a diffusing magnetic feature. For a given simulation, D is assumed constant over time and space and not dependent on the magnetic field. This work forms the longest time-scale analysis so far of directly measured diffusing magnetic features.

Our investigation is outlined as follows: the magnetic field observations are summarised in Section 7.2; the method for generating the magnetic butterfly diagram is described in Section 7.3; the progressing poleward boundary tracking and simulation results are presented and compared in Section 7.4; finally, the limitations and implications of this work are presented in Section 7.5. The software used to perform the data analysis presented in this chapter is available through the distributed version control system, “github”¹.

7.2 Observations

Solar and Heliospheric Observatory (SOHO)/Michelson Doppler Imager (MDI; 165) data from 1996 to 2010 are used to construct a magnetic butterfly diagram covering solar cycle 23. Level 1.8 full-disk line-of-sight magnetograms are cosine corrected for

¹The repository is available for download here: <https://github.com/pohuigin/Supergranular-Diffusion-Study>. This software is written in IDL (<http://www.exelisvis.com/ProductsServices/IDL.aspx>) and is dependent on the SSW library (http://www.lmsal.com/solarsoft/ssw_whatitis.html) and another general library (https://github.com/pohuigin/gen_library).

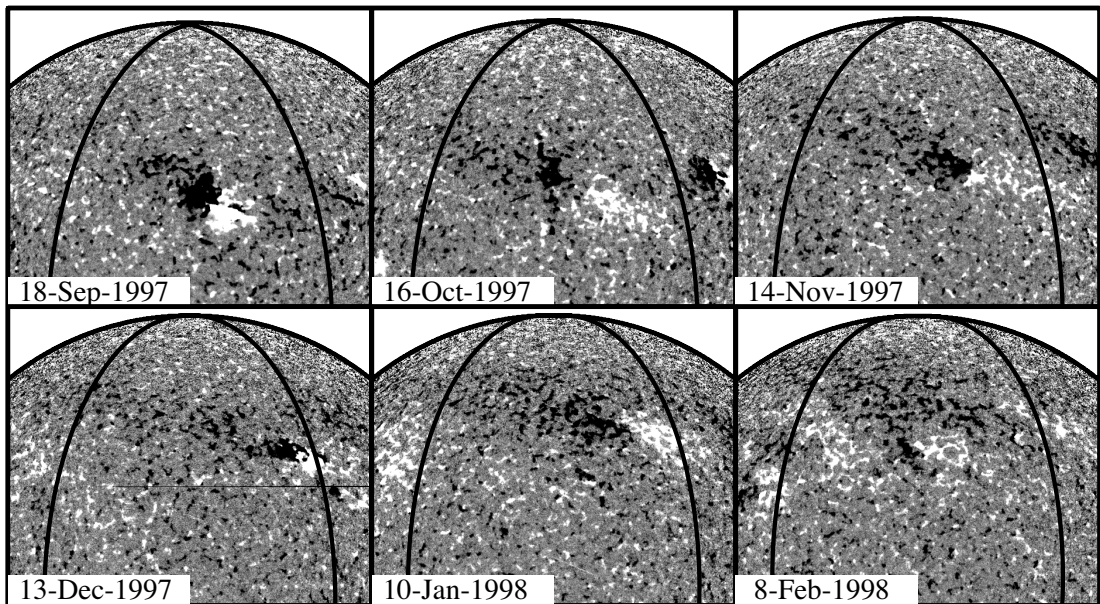


Figure 7.3: MDI magnetograms scaled to ± 20 G showing the diffusion of magnetic elements from NOAA 8068 over 6 solar rotations. The $\pm 30^\circ$ longitude limits are indicated by the black lines. New flux can be seen to emerge during the image sequence, but not poleward of the main feature, so the tracked poleward boundary of NOAA 8068 should not be affected.

the magnetic field fall off toward the limb, as explained in Chapter 4. This correction assumes all fields are normal to the surface. While this is far from true in sunspot penumbrae, it is a more accurate approximation for the diffuse fields we are interested in, as explained in Section 2.7. The method for constructing the butterfly map used to study the dispersal of magnetic flux is described in Section 7.3. A subset of this map (1996 to 1999) is analysed to detect the poleward boundary of diffusing magnetic flux originating from two decaying active regions, National Oceanic and Atmospheric Association (NOAA) 8068 and a complex composed of NOAA 8076, 8078, and 8079. Henceforth, the complex will be referred to as simply 8078.

We choose to study this time period due to the lack of contamination from emergence of other active regions. Several bipoles emerge, but not poleward of the initial feature. So, tracking the diffusing boundary should not be affected. Few features had

7. MAGNETIC FLUX TRANSPORT

emerged and decayed previously at mid and high latitudes, leaving a quiet zone for the two active regions of interest to diffuse into. Furthermore, the north magnetic pole is stable in terms of the amount of flux and exhibits a relatively constant boundary during the observations. This allows an assessment of how opposite polarity flux affects the polar field.

The images in Figure 7.3 show the diffusion of magnetic flux elements from the first region of interest analysed (NOAA 8068) over six solar rotations. Disk-center crossings of the poleward boundary of this flux are predicted using empirical meridional flow and differential rotation profiles, as described in Section 7.3.2. The images in the mosaic correspond to data used in the following investigation, specifically the times indicated by the black-on-white arrows shown in the top panel of Figure 7.8. The second diffusing feature analysed is NOAA 8078, with disk-centre crossings corresponding to the white-on-black arrows.

7.3 Methods

The data reduction and techniques used in the simulation and analysis of the poleward-propagating diffuse magnetic features is described here. In the following sections, the methods for constructing the magnetic butterfly map used for this work (Section 7.3.1) and for simulating the motion of a point particle on the Sun due to large-scale flows (Section 7.3.2) are described. The butterfly map described here differs from that described in Chapter 6, because the sensitivity needed to track dispersing magnetic flux is higher than that needed to simply determine the time-averaged global magnetic field configuration.

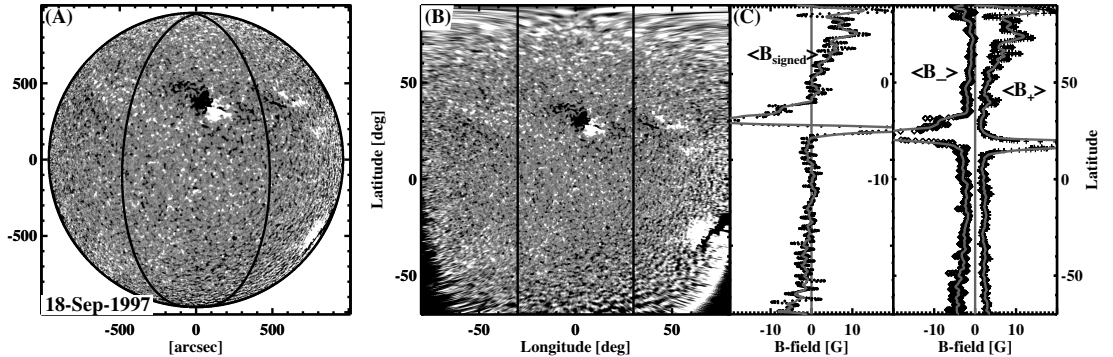


Figure 7.4: The processing steps used to generate a magnetic butterfly map. A full-disk MDI magnetogram scaled to ± 20 G with $\pm 30^\circ$ heliographic longitude indicated by the black lines (A), latitude-longitude remapping (B), and latitudinal magnetic field profiles (C). The profiles are determined by averaging over signed magnetic field in longitude (left panel) and separately for the positive (right panel; plus signs) and negative (right panel; diamonds) components. The gray lines show the profiles smoothed by 30 pixels ($\sim 3.5^\circ$).

7.3.1 Latitude-time Mapping

A series of processing steps are employed to produce a magnetic latitude-time (butterfly) map. Several of the intermittent data products are shown in Figure 7.4. Latitude profiles are constructed by performing spatial filtering, line-of-sight correction, and time averaging.

Magnetograms from MDI are prone to noise; near the limb, this dominates the signal. To alleviate this problem, we use a 3x3 median filter. Then, to account for the cosine dependence of the line-of-sight magnetic field from disk center to the limb, we employ the correction used and described in (97) and Chapter 4. This assumes that all magnetic fields at the solar surface are radial. The diffuse fields of decaying active regions analysed here are expected to be radial, so this should not significantly affect our results. To further increase the signal to noise ratio, we average the set of each day's 5-minute integrated magnetograms, after differentially rotating¹ them to the mid-point of each time bin (noon of each day), yielding a representative daily processed magnetogram.

¹the differential rotation remapping method used here is described in http://hesperia.gsfc.nasa.gov/rhessidatacenter/complementary_data/maps/#s3.6

7. MAGNETIC FLUX TRANSPORT

The full-disk observation is remapped to a latitude-longitude grid using the SSW World Coordinate System software (204). A resolution is chosen such that a pixel at disk centre in the original magnetogram will cover nearly the same area in the de-projected latitude-longitude map. The number of heliographic degrees per pixel is determined from,

$$\Delta\theta = \frac{360^\circ}{2\pi R'_\odot} \Delta\theta', \quad (7.5)$$

where R'_\odot is the radius of the Sun in helioprojective (plane-of-sky) coordinates, and $\Delta\theta'$ is the helioprojective angle of a pixel in the original magnetogram. Each latitude-longitude map is averaged over longitude from -30 to $+30^\circ$. This yields a 1D profile of average signed magnetic field, $\langle B_{\text{signed}} \rangle$ in latitude. Individual profiles from an example magnetogram are shown in panel *C* of Figure 7.4. These profiles are stacked to construct a map with latitude on the vertical axis and time on the horizontal axis.

The process described above is repeated, with negative pixels zeroed from the processed daily magnetograms, to construct a butterfly map with profiles of average positive magnetic field, $\langle B_+ \rangle$, in latitude over time. This is also done, with the positive pixels zeroed, to construct an average negative magnetic field $\langle B_- \rangle$ butterfly map.

7.3.2 Large-scale Flow Simulation

We predict the motion of a point on the Sun over time, affected by differential rotation and the meridional flow. This allows the prediction of disk-centre crossing times for the features of interest. Experimental profiles for the meridional flow and differential rotation velocities over latitude are extracted from the surface velocity profiles presented in (91). These profiles are determined by cross-correlating segments of MDI magnetograms in images subsequent in time. Corresponding segments are correlated in the East-West direction to determine the speed of solar rotation and correlated in the North-South direction to determine the speed of the meridional flow.

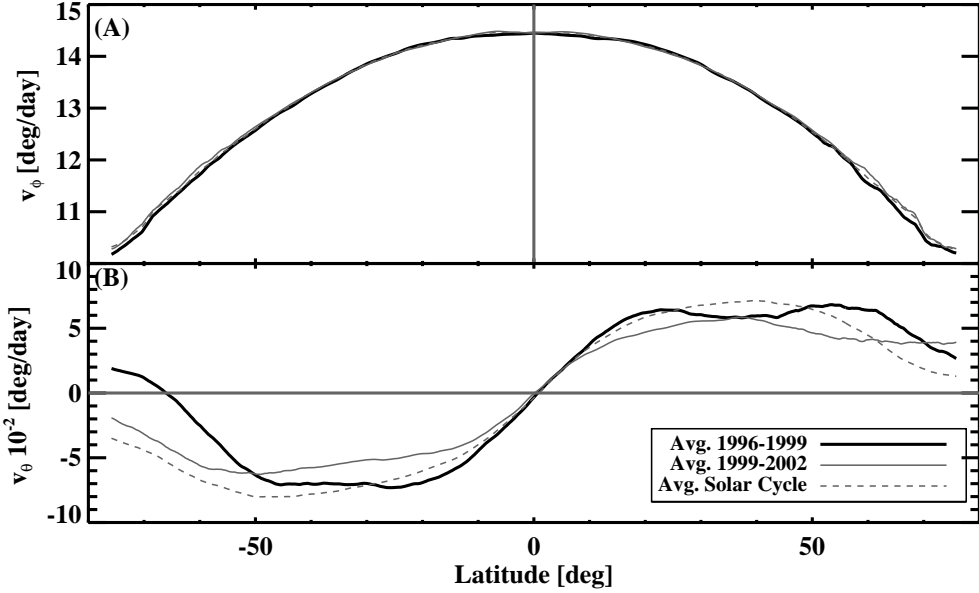


Figure 7.5: Assumed surface velocity profiles used in the diffusion simulations: (A) the solar rotation profile averaged over years 1996–1999 (black line); (B) the meridional flow profile averaged over the same period (black line). Profiles averaged over 1999–2002 (gray line) and 1996–2012 (dashed line) are shown.

As both flows are variable over long time-scales, we average the profiles over the interval of interest, 1996–1999, as shown in Figure 7.5. Averaged profiles for the periods 1999–2002 (gray lines) and 1996–2012 (dashed lines) are shown for comparison. The differential rotation profiles only deviate slightly at high latitudes, while the meridional flow profiles deviate significantly at all latitudes. The meridional flow and differential rotation profiles are then boxcar-smoothed by 100 and 10 points, respectively (Figure 7.5). The profiles obtained from (91) are calibrated in m s^{-1} and are presently converted to deg s^{-1} . Additionally, the differential rotation profile is originally given relative to the Carrington angular rotation speed. To convert the differential rotation speed into heliographic longitudinal deg s^{-1} we use,

$$v_\phi = v_s \left(\frac{360^\circ}{2\pi R_\odot \cos \theta} \right) + v_c , \quad (7.6)$$

7. MAGNETIC FLUX TRANSPORT

Table 7.1: The elements of the discrete Laplacian operator kernel. A 3×3 array, with the values shown in the table, is convolved with an image to produce the discrete version of ∇^2 .

0	1	0
1	-4	1
0	1	0

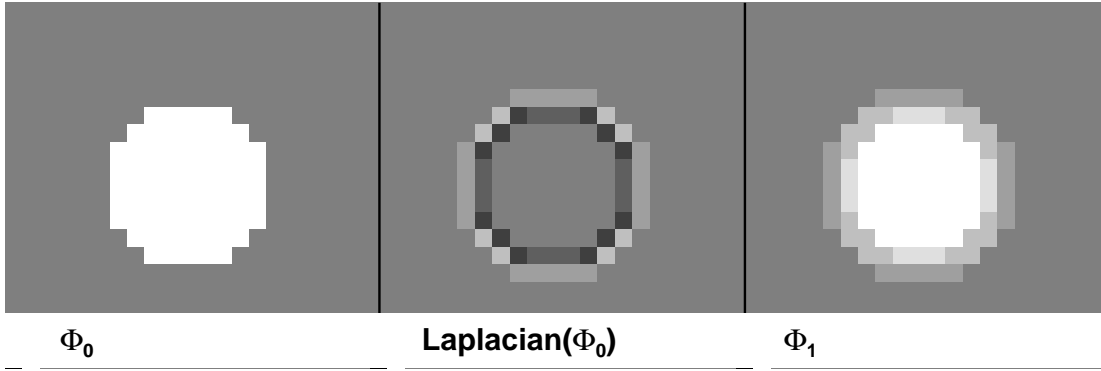


Figure 7.6: An example of applying the Laplacian operator to simulate diffusion. *Left:* An initial circular distribution of flux. *Middle:* The Laplacian of the initial distribution. *Right:* The diffused distribution.

where ϕ is longitude, v_s is the rotation speed in m s^{-1} , R_\odot is the radius of the Sun in meters, θ is latitude, and v_c is the Carrington speed, $14.184^\circ \text{day}^{-1}$. The meridional flow velocities are converted to degrees s^{-1} using,

$$v_\theta = v_s \left(\frac{360^\circ}{2\pi R_\odot} \right). \quad (7.7)$$

The evolution of a distribution of magnetic elements on large scales is simulated in latitude-longitude space. First the diffusion is simulated using the continuous diffusion equation (Equation 7.4). The algorithm convolves a discrete Laplacian operator (shown in Table 7.1) with the distribution (Φ_0) to calculate its change over a time step ($\Delta\Phi_0$) and adds it to the distribution to calculate the resulting distribution (Φ_1). This conserves total flux in the distribution while smearing it radially. An example of the process is shown in Figure 7.6.

Next, the meridional flow and differential rotation are simulated with sub-pixel

image shifting using cubic interpolation¹. The pixel shifts are determined for both, and then the differential rotation and then the meridional flow are simulated in turn. Because the time steps are only 12 minutes apart, the order of operations does not affect the resulting distribution. For differential rotation, each row of pixels is shifted separately, where the fractional pixel shift is determined by the speed of rotation at a given latitude in the profile shown in the top-left panel of Figure 7.5. The same method is used for the meridional flow, but a single flow speed is used to shift all of the columns in the image. The speed is measured at the location best matched to the tracked diffusing point in the butterfly diagram. This point is located where the latitude profile of magnetic field ($\langle B_{\text{sign}} \rangle$) values crosses zero (i.e., where the diffusing feature and static polar field average to zero over longitude; the north-most location in panel *C* of Figure 7.4) and is discussed in Section 7.4.1.

7.4 Results and Discussion

Figure 7.7 shows a magnetic butterfly diagram constructed using the method described in Section 7.3.1. It includes data between 1997 and 2011. The time range roughly corresponds to that of solar cycle 23, forming one half of a 22-year magnetic cycle. The vertical striping pattern is due to features rotating onto the solar disk over successive solar rotations. The undulating pattern of missing data at high latitudes is due to the yearly wobble of the Sun's inclination toward and away from the Earth (due to the $\sim 7^\circ$ inclination of the ecliptic plane to the Sun's equatorial plane).

In 1996 the magnetic field of the poles is strongly positive and (negative) in the north and (south). As active regions begin to emerge in the northern hemisphere, poleward propagating regions of net-negative magnetic field reach the pole after ~ 2 years. It is expected that these regions of diffuse flux have one or more active region sources. Positive weak flux also diffuses and progresses poleward, but much of it is likely to

¹The SSWIDL FSHIFT routine is used.

7. MAGNETIC FLUX TRANSPORT

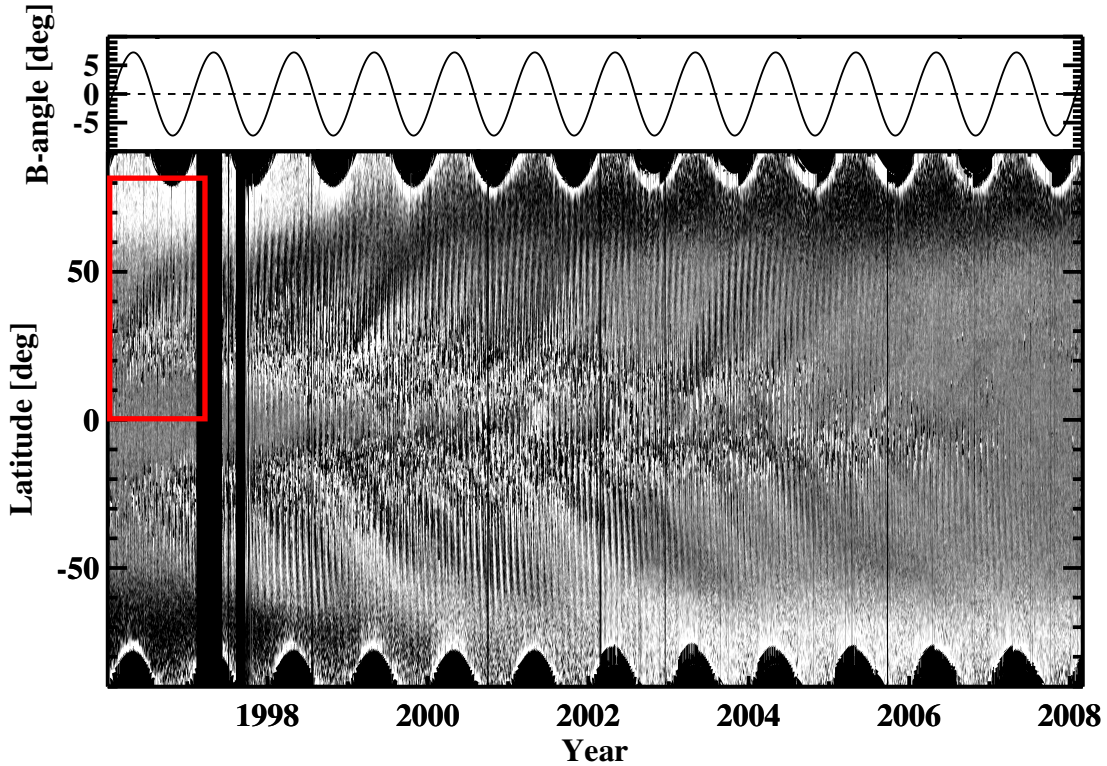


Figure 7.7: A magnetic butterfly diagram showing $\langle B_{\text{sign}} \rangle$. The red box indicates the region of interest for this study.

have canceled with the negative flux closer to the equator before arriving at the pole. Differential rotation shears diffusing ARs, as seen in Figure 7.3, decreasing the rate of flux cancellation over time. Similar diffuse poleward propagating magnetic regions are observed in the North and South hemispheres, and appear to be progressing at similar rates. In Section 7.4.1 we analyse the region of the butterfly diagram bounded by the red box to track the poleward migration of net-negative magnetic flux. In Section 7.4.2 we describe the results of several simulations used, including a data driven one to predict the tracking points detected in Section 7.4.1.

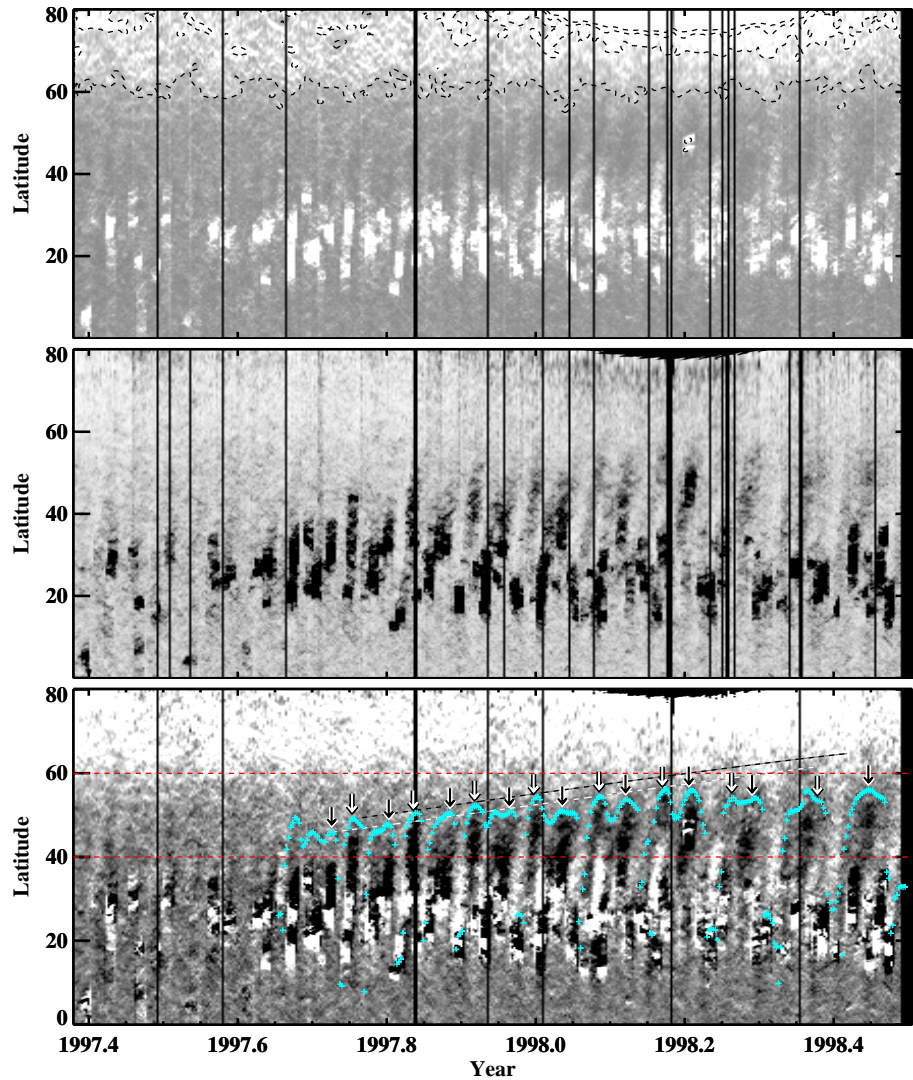


Figure 7.8: A zoom-in of Figure 7.7. *Top:* map of $\langle B_+ \rangle$ with contours indicating 5, 10, 15, and 20 G. *Middle:* map of $\langle B_- \rangle$. *Bottom:* map of $\langle B_{\text{sign}} \rangle$ with northward zero-crossing points (+) and arrows indicating disk crossings (key points) for NOAA 8068 (black on white) and NOAA 8078 (white on black). The white and black dashed lines indicate the integrated meridional flow from the first key point of each feature.

7.4.1 Diffusion Tracking

Dispersing features in the magnetic butterfly map (Figure 7.7) are tracked over subsequent solar rotations to measure the rate of their diffusion. Using latitude-magnetic field profiles, we determine the location of where the field transitions from positive at

7. MAGNETIC FLUX TRANSPORT

the pole to negative at the feature. This point is called a zero-point crossing. The time series of zero-crossing points indicated by the cyan crosses in Figure 7.8 is determined by performing three-point (3-day) boxcar smoothing in time and subsequently 35-point (7°) smoothing in latitude. The most northern zero-point crossings, between the positive pole and negative diffusing flux, are detected. The zero-point detections are bi-linearly interpolated between the preceding and following pixel positions in latitude. By visually comparing the original averaged magnetograms used to form each profile (such as those in Figure 7.3) to the time series of zero-point crossings, we see that peaks in the time series occur when regions of diffusing active region flux cross disk centre.

We select two distinct poleward propagating features to analyse and choose a starting point in latitude and time for each. Then we predict the latitudinal and longitudinal motion of each starting point in time, using the meridional flow and differential rotation profiles shown in Figure 7.5. This allows us to predict the disk-centre crossings of each feature forward and backward in time. This disk-centre crossing times are expected to match the peaks in the zero-crossing time series, as mentioned. The predicted motion of the starting points is indicated by the white and black dashed lines in the bottom panel of Figure 7.8. The closest match between predicted disk crossings and peaks in the zero-point crossing time series are chosen to be key points to compare with the diffusion simulation results later on (Section 7.4.2.3). The key points are indicated by the downward arrows in the bottom panel of Figure 7.8 for NOAA 8068 (black on white) and 8078 (white on black).

7.4.2 Simulations

In this work, we compare two types of flux diffusion simulation, random-walk (Section 7.4.2.1) and continuous (Section 7.4.2.2). This is done to test the equivalence of the methods for simulating diffusion. The magnetic particle motion obtained from the

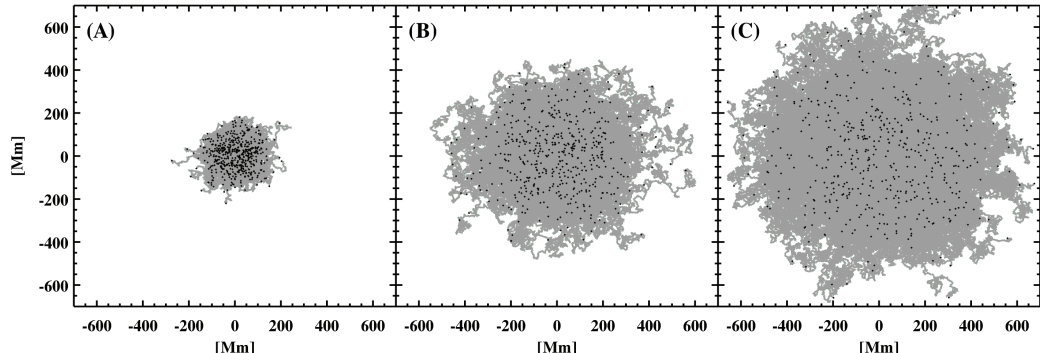


Figure 7.9: Snap-shots from a random walk simulation. The supergranular cells have parameters prescribed by the medium case, as summarised in Table 7.2.

random-walk simulation is analysed using Equations 7.1 and 7.3, to measure D . Then, a continuous diffusion simulation using a 2D Gaussian and prescribed D is run. The statistical particle motion is tracked and compared to the random-walk simulation.

Subsequently, a continuous simulation is run with an opposite polarity polar field and diffusing feature. Differential rotation and meridional surface flows are applied to test the effects of the large-scale flows on the diffusing boundary and zero-crossing point. Finally, a data-driven continuous simulation is run using magnetogram data as input to match the poleward motion of the zero-crossing point to that measured in the magnetic butterfly map, allowing an estimation of the effective D value on the Sun (Section 7.4.2.3).

7.4.2.1 Random-walk Simulation

The diffusion of magnetic flux elements is simulated in 2D by allowing a group of particles to step in random directions with time-steps (τ_c) and step lengths (L_c) chosen based on previous observational studies of the supergranular flow field. To simultaneously test Equation 7.1 and 7.3, we position 500 particles at position [0,0] in a 2D box (having a non-normalised δ -function spatial distribution). The box is effectively divided into a lattice of supergranular cells so that each particle is randomly positioned

7. MAGNETIC FLUX TRANSPORT

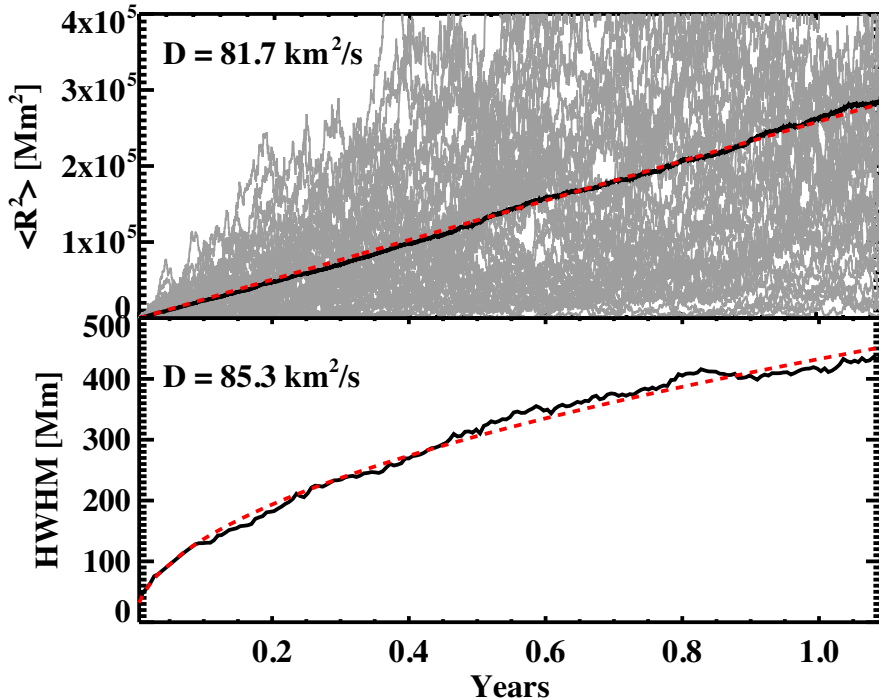


Figure 7.10: Tracking the diffusion of particles in a random walk simulation using two methods. *Top panel:* D is measured by fitting Equation 7.1. A selection of particle tracks $\langle R^2 \rangle$ is shown (gray) with the averaged track (black) and fit (red) over plotted. *Bottom panel:* D is measured by fitting Equation 7.3 (red) to the HWHM of the spatial distribution of particles (black).

within a cell. The probability of sitting at a given distance from a cell's center increases with radius (the area of concentric circular rings $\propto r_c \partial r_c$). Over a time-step, particles move radially to the cell boundaries with a speed equal to r_c/τ_c . The τ_c is held constant over a simulation run, but r_c is determined from a random distribution with a chosen mean and HWHM of 10 Mm. Runs cover 5 000 time-steps. Figure 7.9 shows the distribution of particles after a simulation time of 1 year, 6 years, and 12 years, assuming the minimum diffusion case¹. Each particle is random-walking on a different cellular pattern, but trajectories are considered collectively to statistically determine the diffusion coefficient from the cellular properties.

¹A supplementary movie of a representative random-walk simulation is available: <http://dx.doi.org/10.6084/m9.figshare.96148>.

7.4 Results and Discussion

Table 7.2: A summary of random-walk simulation runs. The mean supergranular cell diameter (r_c) and life-time (τ_c) for each run is given. The results of determining D by fitting time series of particle $\langle R^2 \rangle$ and spatial distribution HWHM are given in the last two columns.

Run	L_c [Mm]	τ_c [hr]	D [km^2s^{-1}]	
			Using $\langle R^2 \rangle$	Using HWHM
Minimum	30	48	81.7	85.3
Medium	36	36	129.4	133.7
Maximum	47.5	24	303.1	313.4
Simon <i>et al.</i> (1995)	30	30	84.4	87.4

Time-steps, τ_c , are chosen from statistical studies of supergranular life-time. This quantity is relatively poorly constrained, since the majority of studies have been performed on ground-based data, only allowing a total observation sequence on the order of the measured cell life-times. Previous values have been obtained in (224) (36 hr; correlation time-scale method), (212) (10, 20, and 48 hr; correlation time-scale method), and (99) (38.4 and 43.2 hr; helioseismology method). The spread of values between the studies is a result of differences in both analysis technique and observation type. The supergranular cell sizes, L_c (with cell radius $r_c = L_c/2$), determine the step lengths for the random walk. The generally accepted cell size is 32 Mm (113). However, recent studies using local correlation tracking (LCT) determine a distribution of cell sizes peaking at 36 Mm with half-maximum values at 20 and 63 Mm (92; 93) and 20 and 75 Mm (160).

For this simulation, we test 24 (maximum case), 36 (medium case), and 48 hr life times with mean cell diameters of 47.5, 36, 30 Mm, respectively. We also run a test using cell properties adopted in one of the random-walk simulations run by Simon *et al.* (189) which assumes cell size of 30 Mm, but no spread in cell sizes, and cell life-time of 30 hours.

The particle trajectories for each run (summarised in Table 7.2) are then analysed. The average mean-squared displacement, $\langle r^2 \rangle$, of particles from the origin over time

7. MAGNETIC FLUX TRANSPORT

allows a calculation of D using a linear fit to Equation 7.1. Additionally, the number of particles is summed over one dimension and we fit a Gaussian to the distribution. This allows the HWHM of the Gaussian fit to be tracked over time and fit using Equation 7.3, as shown in the middle panel of Figure 7.9. The two different fits for an example run are shown in Figure 7.4.2.1. The results of all of the simulation runs are summarised in Table 7.2. We find an agreement between the two methods of determining D of within 5%.

The cell parameters in the model runs are chosen to represent the range of possible D values. The minimum, medium and maximum D values are all significantly lower than $600 \text{ km}^2\text{s}^{-1}$. This should not be surprising since (189) investigate a similar model and find values of D close to ours when considering motion of particles to cell boundaries rather than to “sinks”. Magnetic elements are observed to collect in the intersection between multiple supergranules. (189) shows that when the motion of particles into sinks over τ_c is considered, D values of 350 to $500 \text{ km}^2\text{s}^{-1}$ are found.

7.4.2.2 Laplacian Continuous Simulation

The continuous diffusion model (Equation 7.2) is used to simulate the dispersion of magnetic flux elements. In addition to diffusion, meridional flow and differential rotation are also included in the simulation, as described in Section 7.3.2. A Gaussian is used to represent the negative portion of a decaying sunspot group. The peak magnetic field is -20 G and the HWHM is 5° .

A sigmoid curve is fit to the observed polar profile in Figure 7.7 and is used to represent the positive polar field,

$$B_{\text{sig}} = 5/(1 + \exp(15 - x/4)) + 0.01 , \quad (7.8)$$

where x is heliographic latitude. The simulation time-step is chosen to be only 12 minutes

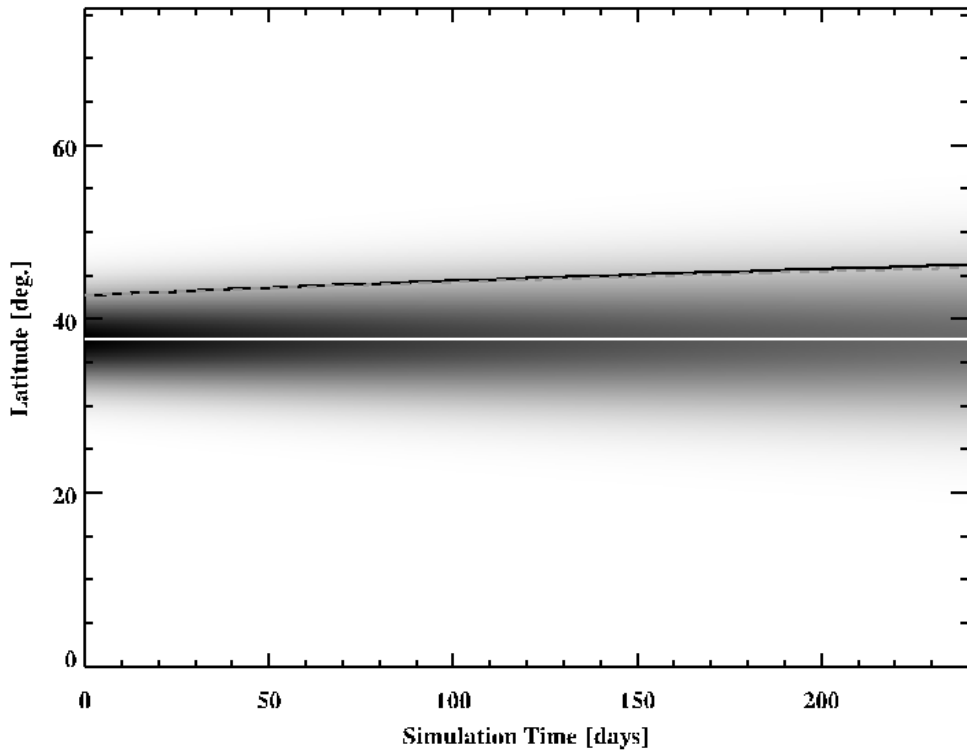


Figure 7.11: The results of a continuous (laplacian) diffusion simulation. The minimum diffusion case is assumed. Vertical slices represent the magnetic field profile of the diffusing Gaussian blob. The $1/e$ -point is tracked (black line) and compared to the prediction of the random-walk simulation for the same value of D (gray dashed line).

to maintain stability. The discrete Laplacian operator tends to cause run-away gradients to appear (rather than the expected smearing of strong gradients) if the time-step is chosen to be too large.

For the first run, we ignore the polar field and the $1/e$ -point of the diffusing Gaussian is tracked over time, for each run. A D of $83 \text{ km}^2 \text{ s}^{-1}$ (minimum diffusion case) is assumed. The results of this are compared with the random-walk results assuming the same parameters ($D \approx 83 \text{ km}^2 \text{ s}^{-1}$) and is shown in Figure 7.12. The random-walk (gray dashed line) and continuous (black line) agree well. This indicates that the Laplacian method of simulating diffusion (as described in Section 7.3.2) is roughly equivalent to

7. MAGNETIC FLUX TRANSPORT

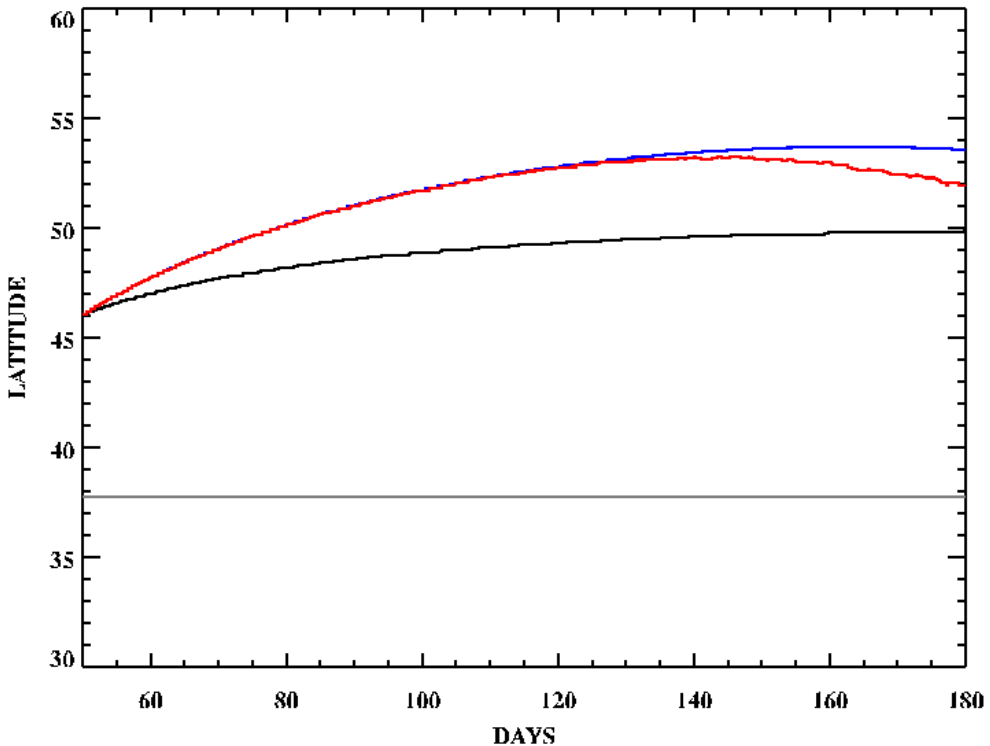


Figure 7.12: The results of a continuous (Laplacian) diffusion simulation including differential and meridional flows. A D of 600 km s^{-1} is assumed. The zero-crossing point is tracked with a simulation including only diffusion (black line), diffusion and the meridional flow (blue line), and a simulation including diffusion, differential rotation, and the meridional flow (red line). The starting point of the blob is shown by the gray line.

the random-walk method.

For the second run, a D of $600 \text{ km}^2 \text{s}^{-1}$ is input and the simulation covers an interval of 8 months. We track the zero-crossing point between the negative feature and the polar field. This is done by averaging the negative field between $\pm 30^\circ$ longitude. This is the same averaging window used to generate the magnetic butterfly diagram as described in Section 7.3.1.

The results of this simulation are shown in Figure 7.12. The black line represents the zero-crossing point including only diffusion, while the blue line includes both diffusion

and the meridional flow. It is clear that the meridional flow plays a large part in moving flux toward the pole. The red line shows the effects of including diffusion, the meridional flow, and differential rotation. The shearing effect of differential rotation helps to diffuse the fields laterally and thus decreases the concentration of flux in a given area. This causes the zero point to be lower in latitude, as the flux density is weaker.

7.4.2.3 Data-driven

Finally, an observation of a decaying active region and polar fields is input to the continuous diffusion simulation. The method described in Section 7.3.2 is used to simulate the evolution of the flux. The simulated zero-crossing point (green line) is compared to the measured zero-crossing point (blue dots; key points defined in Section 7.4.1) in Figure 7.13. A D of $100 \text{ km}^2 \text{ s}^{-1}$ (top panel) and $500 \text{ km}^2 \text{ s}^{-1}$ are tested. Setting $D = 100 \text{ km}^2 \text{ s}^{-1}$ appears to match the points early in time (day 0–100) much more closely than when setting $D = 500 \text{ km}^2 \text{ s}^{-1}$, but the opposite is true for the points later in time (day 100–200). From these tests it is difficult to determine which value is a better representation of what is observed. Considering that as time passes, the diffusing fields will become more difficult to detect, so it is probably more important to match the earlier tracked points in the data set. To arrive at a more definite result many more diffusion simulations need to be run for a series of different observations.

7.5 Conclusions

The tests performed in this work have not allowed us to arrive at a definitive value for the diffusion coefficient. A larger number of data sets must be simulated and compared in order to arrive at a conclusion. An important factor in our result is that the meridional flow is not well constrained and is in fact dynamic on a timescale of

7. MAGNETIC FLUX TRANSPORT

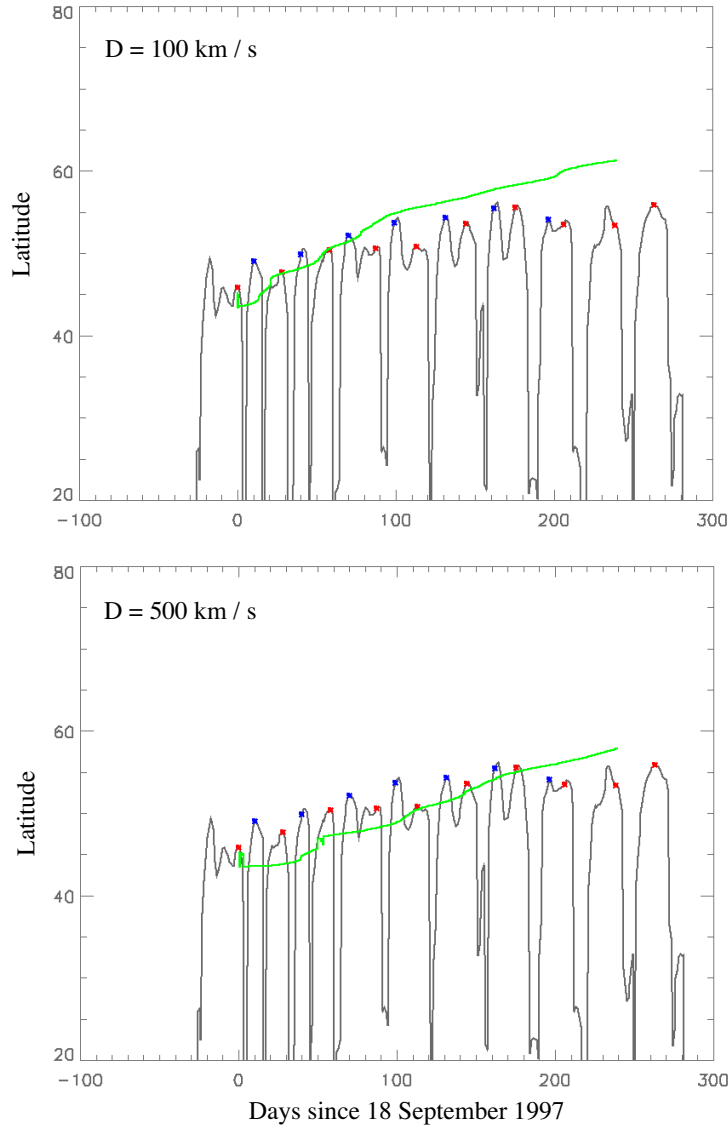


Figure 7.13: A data-driven simulation using the inputs specified in Section 7.3.2 and a D of 100 km s^{-1} (top panel). The diffusion zero-points of the feature of interest, tracked in the magnetic butterfly diagram, are shown in red. The simulated zero-point track is shown in green. The simulation is repeated for a D of 500 km s^{-1} . The black curve indicates the smoothed zero-crossing points.

years (Figure 7.5). This may make it impossible to compare a simulation using a static model of the meridional flow to observations.

That said, our results support the idea that the diffusion process is scale depen-

dent as discussed by (81). The data-driven simulation matches observations on small scales when assuming $D = 100 \text{ km}^2 \text{ s}^{-1}$ and matches observations on large scales when assuming $D = 500 \text{ km}^2 \text{ s}^{-1}$. A signature of convection that operates on a larger scale than supergranulation, such as giant cells, may play a part in the dispersal of magnetic flux across the solar surface.

7.5.1 Comparison to Previous Work

There is a lack of observational constraint on the supergranule diffusion coefficient, D . The same is true of other subsurface parameters, such as turbulent diffusivity, the subsurface meridional flow, and the magnitude of the α effect (48; 49). Thus, for more realistic and complicated simulations the system is under constrained. The value of D necessary to reproduce solar-like solutions using flux transport simulations cannot be definitively determined at present.

(214) track the decay of 4 active regions for several rotations by calculating the flux in $\pm 3 \text{ G}$ contours and find that simulating their decay assuming the widely used flux transport equation (Equation 7.4), the best fit to D is $600 \pm 200 \text{ km}^2 \text{ s}^{-1}$. This work compares continuous diffusion simulations to observations of dispersing magnetic flux fragments. An effect not taken into account by this model is the fragment clustering effect of converging supergranular flows (177). This causes dispersing flux to maintain larger magnetic field values than the continuous model gives. Thus, (214) likely measure a smaller value of D since flux is lost from the 3 G contours more quickly in the simulation than in the observations.

7. MAGNETIC FLUX TRANSPORT

8

Conclusions and Future Work

In this chapter, the results of each of the investigations presented in this thesis (Chapters 4, 5, 6, and 7) are summarised. The novel findings are highlighted and the prospects for future work on each topic are discussed.

8.1 Conclusions

The investigations presented in this thesis focus on examining the life-cycle of magnetic flux originating in sunspot groups, later dispersing to become part of the global field. The methods used to determine the properties of magnetic features are characterised (Section 4). Then, the evolution and properties of sunspot groups are compared to flare productivity (Section 5). Following this, the configuration of the global magnetic field of the Sun was compared to the properties of sunspot groups in the active latitudes over cycle 23 (Section 6). Finally, the mechanisms resulting in magnetic flux dispersal from decaying sunspot groups are characterised (Section 7). The main results of each study are summarised below.

8. CONCLUSIONS AND FUTURE WORK

1. *Detecting and Tracking Solar Active Regions:* In Chapter 4, the reliability of measurements using automated detection methods on line-of-sight (LOS) magnetic field observations is explored. It is clear that the measured magnetic field magnitudes are not representative of the true magnetic field strength. Also, it is not clear how much of an effect the nonlinearities in Michelson Doppler Imager (MDI) data affect our results. We have shown that flux is a more reliable indication of the magnetic field than magnetic field strength. The stability of SolarMonitor Active Region Tracker (SMART) detections over time is shown to be excellent relative to position and flux measurements. From our simple simulations, we see that area and flux measurements are not significantly affected by LOS effects out to 60° longitude. However, measurements involving magnetic gradients, such as polarity separation line (PSL) length and WL_{SG} , become dubious well before 60° longitude. Similar to much of the contemporary work in solar physics, the physical characteristics of the solar magnetic field determined here can only be compared with other work using the MDI instrument due to uncertainties involved in the instrument's design and calibration. **The need for a pair of space borne instruments with the sole purpose of providing regular spectropolarimetric observations of the vector magnetic field across the entire solar surface is absolutely clear.**
2. *The Flare Productivity of Sunspot Groups:* In Chapter 5, the evolution of individual sunspot groups is compared with the occurrence of flares. Specific behaviours of the magnetic field strength and configuration are identified that lead to flaring in the cases presented. A large sample of detections associated with flares are analysed to determine the values of measured physical properties that are necessary for flares of different magnitudes to be produced. While this work cannot be used to predict flares on its own, it could be combined with knowledge of the occurrence of behaviors observed in the case studies to determine when a flare is

expected to occur. For instance if the pre-flare behaviors are observed in a sunspot group that is below a given flaring threshold, no flare would be expected, but if the sunspot is above the threshold, a flare *would* be expected. The prospects for this kind of forecasting capability are described in Section 8.1. Additionally, the full-Sun flare productivity over cycle 23 is investigated. It is clear that on a global scale, the summed properties of individual sunspot group detections are highly indicative of the total flare production.

3. *Sunspot Groups and the Global Magnetic Field of the Sun:* In Chapter 6, the properties of sunspot groups are compared to the global magnetic field configuration. A statistical analysis of sunspot group detections indicates that in addition to the solar cycle dependence of the detection rate, the properties of sunspot groups also depend on the solar cycle. There is an excess of sunspot groups with large flux in the plateau phase of the cycle, while the distributions of sunspot group flux appear to be very similar for the rise and decay phases of cycle 23. Using magnetic butterfly diagrams, it is apparent that the large-scale flux imbalance measured from sunspot group detections matches that from the raw magnetograms. At high latitudes the flux imbalance is opposite to that at low latitudes and the magnitudes of the imbalances at high and low latitudes have similar magnitudes, during the first half of the solar cycle. This supports the idea that flux is transported from low to high latitudes, as per the Leighton-Babcock mechanism. Using potential field source surface (PFSS) extrapolations we find the configuration of the global magnetic field, indicated by the spherical harmonic coefficients, qualitatively matches the polarity banding pattern observed in the magnetic butterfly diagrams, that occurs due to the decay and transport of sunspot group magnetic fields. Thus, it is reasonable to say that the global magnetic field configuration of the Sun is determined in large part due to the life-cycle of sunspot groups.

8. CONCLUSIONS AND FUTURE WORK

4. *Characterising the Transport of Diffuse Magnetic Flux:* In Chapter 7, the mechanism by which decaying sunspot group magnetic fields are dispersed is characterised. We find that as a first-order approximation, the continuous ordinary gas diffusion model for surface magnetic field diffusion is acceptable to describe large scale magnetic field observations. However, previous work has shown repeatedly that determining the diffusion coefficient by tracking individual flux elements does not match that determined by global surface flux transport (SFT) simulations. For the first time, we have directly matched the results of tracking diffusion from large-scale observations with a data-driven SFT simulation. We attain a diffusion coefficient much closer to the global simulation studies than what has been found in the small scale studies. It is likely that the tracking methods used and the temporal and spatial coverage of the observations are responsible for the difference in diffusion coefficient for small-scale studies. Future studies should determine the diffusion coefficient using high resolution Helioseismic Magnetic Imager (HMI) data. Also, kinematic models of flux element dispersion should be investigated as an alternative to the continuous model.

The over-arching conclusion of this work is that the properties of localised magnetic features determine both the eruptive activity on the Sun, as well as the configuration of the global magnetic field. By studying the statistical properties of emergent magnetic features, the internal processes resulting in the magnetic solar cycle may eventually be characterised.

8.2 Future Work

I will continue to investigating each of the areas presented in this thesis. Each study presented here has answered one or more questions about the life-cycle of magnetic flux on the Sun. Often, more unanswered questions emerge, provoked by the results

of each study. In the following sections, the prospects for future work in each area of investigation are described, leading on from the results presented in this thesis.

8.3 Detecting and Tracking Solar Active Regions

Following on from the point-in-time statistical studies of sunspot groups presented in this thesis, we seek to characterize the time-dependent behavior of magnetic and coronal sunspot group properties using morphological tracking and time-series analysis. Patterns in the time dependence of sunspot group properties will be detected. Some of the properties to be investigated include rapid changes (increases and decreases) in magnetic flux, PSL development and rotation, helicity injection, coronal loop development, and previous flare history. The automated detection of sunspot group evolutionary behaviors has not been performed previously.

The time-series analysis of sunspot group evolution requires the tracking of sunspot groups throughout their entire life-cycle. The current tracking module used by SMART is a simple algorithm that allows multiple observations of the same sunspot group to be associated. It is novel since it allows groups to be tracked through multiple disk passages. This is important in allowing the complete evolutionary history to be characterized, as well as knowing when to expect the return of previous sunspot groups. However, the algorithm is limited in only matching detections adjacent in time by their centroids and is not robust when adjacent groups merge and split. More complex systems are available, such as Yet Another Feature Tracking Algorithm (YAFTA; 218), and take morphology into account to solve these issues. A new tracking algorithm able to robustly handle merging and splitting as well as multiple disk passage tracking will be developed for this project.

8. CONCLUSIONS AND FUTURE WORK

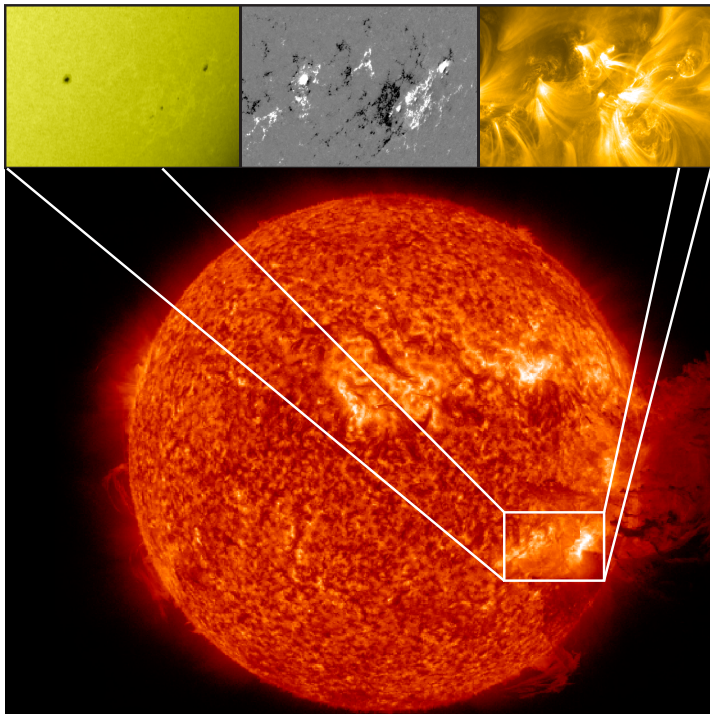


Figure 8.1: The 7 June 2011 eruption imaged by the AIA and HMI instruments onboard SDO.

8.4 The Flare Productivity of Sunspot Groups

Following this work, the multi-scale, multi-layer investigations of sunspot group lifecycles presented in this thesis will be continued. As discussed in Section 8.3, this will include tracking magnetic field detections, allowing for merging and splitting, which will allow more reliable analyses of their dynamics. This new catalog of detections will allow a large-scale statistical study of their *evolution* with respect to flaring, which has not been explored in any detail previously. Sunspot evolution will be determined, not only from photospheric observations, but also from coronal observations, where flares *actually* occur. The 7 June 2011 eruption will be used as one case study for these investigations (Figure 8.1). The eventual goal is to determine a set of reliable time dependent behaviors in the detection properties to combine with our knowledge

8.4 The Flare Productivity of Sunspot Groups

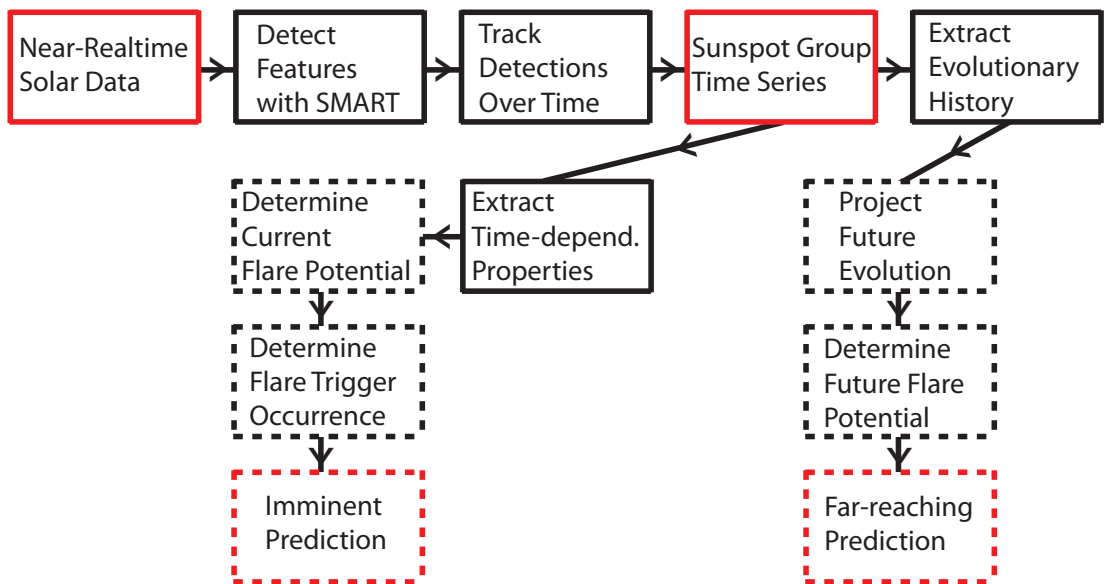


Figure 8.2: A block diagram of a flare prediction system incorporating the complete history of a tracked sunspot group.

of a sunspot group's potential to flare. This will be used to construct a more reliable flare prediction system than is currently available. Such a system would include short time-scale information (the last few observations of a feature) as well as the full history of the feature's evolution. A block diagram of such a system is shown in Figure 8.2.

The completion of this catalog will result in a large data-set of sunspot group detections and their associated coronal and magnetic characteristics. This data set will be analyzed to determine how the characteristics of a magnetic structure relate to the observed characteristics of structures in the corona above a sunspot group. This has previously been studied by generating a 3D extrapolation of surface magnetic field observations and determining how well it matches structures in the corona (40). In our case we will be comparing coronal and magnetic properties, such as proxies of complexity and twist, to determine the association between them as well as the occurrence of flares. Twist in directly-observed coronal structures has not been extensively studied and the comparison of coronal and footpoint evolution is in its infancy.

The distribution of some sunspot group properties observed at a point in time have

8. CONCLUSIONS AND FUTURE WORK

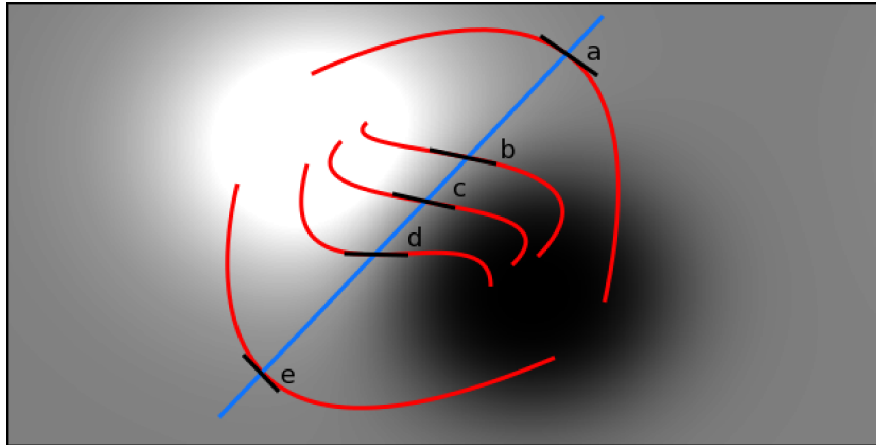


Figure 8.3: A schematic of detected loops overlaid on a magnetogram. The angle that the loops make with the polarity separation line is indicative of sheared magnetic fields.

been studied (227) as well as comparisons between photospheric and coronal properties (61). However, the connection between the evolution of a sunspot group in both the photosphere and corona is not well known (210). Using time dependent characterizations a large sample of tracked sunspot groups, we will determine the connection between photospheric and coronal evolution. The relationship between the characteristics of early development (or evolutionary properties) and the properties at some later time are also not known. In characterizing the emergence phase of sunspot groups we will determine if the nature of sunspot groups can be predicted at the time of emergence or if their long term evolution is chaotic, and thus inherently unpredictable in nature.

The Hale sunspot group magnetic classification system has proven to scale well with overall flare productivity (109) as well as the largest magnitude of flare produced. It is found that the delta classification (both magnetic polarities within a single sunspot penumbra) is responsible for the vast majority of X-class flares (163). In this work, delta-spots will be automatically identified by detecting sunspot contours in white-light images and overlaying them on magnetic field observations. Additionally, the flux within detected delta spots will be determined. Automated delta-spot detection has not previously been investigated for a large sample of sunspot groups.

8.5 Sunspot Groups and the Global Magnetic Field of the Sun

This work will utilize the coronal loop tracing method described in (8) that relies on a novel directional ridge finding algorithm to extract the skeletons of bright loop-like structures. First, EUV images are filtered using a method similar to un-sharp mask to accentuate high-gradient features. The algorithm iterates through each observed loop by beginning at the brightest point in the image, detecting the direction of curvature by sampling the flux along a line in every direction, and moving in both directions along the ridge to trace out the loop to its foot points. The detection is then removed from the image and the process is repeated. The collection of loop skeletons for the sunspot group is extracted and will be analyzed in our work. The collective directionality of a set of extracted loop-skeletons will be determined by detecting the polarity of loops by overlaying the loop foot-points on a smoothed magnetogram. In this way we can construct a map of the horizontal trace of coronal loop directionality. A schematic of how the loop detections will be characterised is shown in Figure 8.3.

Additionally, I am involved in work with a statistician aiming to identify statistical methods for forecasting flares using SMART detections as input. In an earlier collaboration with another group (4), machine learning was used to minimize incorrect forecasts. This resulted in a system that was able to produce the most accurate 24-hour forecasts to date. We now aim to use similar methods and incorporate dynamical information of sunspot group evolution.

8.5 Sunspot Groups and the Global Magnetic Field of the Sun

In this thesis the properties of magnetic features at the solar surface are investigated. One area we did not address in any detail is the nature of subsurface magnetic fields. Knowledge of their structure is important for determining how sunspot-group nests form. Statistically, magnetic flux tends to emerge repetitively in the same location

8. CONCLUSIONS AND FUTURE WORK

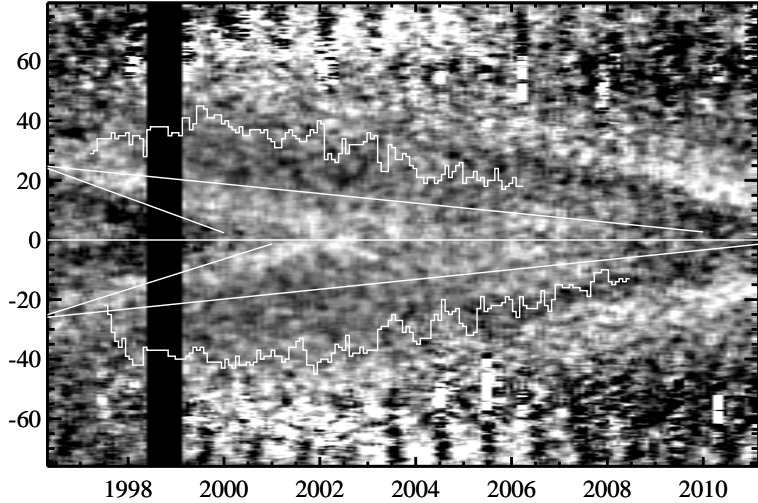


Figure 8.4: A butterfly map of residual differential rotation, overlaid with the bounds of the sunspot cycle.

(153). So far there is no accepted reason for why this occurs. The aim of this project is to characterise the surface and subsurface nature of sunspot nests and determine why they form. We aim to answer the questions: *What is the rate of flux emergence? What is the lag between emergence episodes? How much flux emerges all together? Do the nests drift with respect to the local solar rotation speed?* The drift speeds could indicate the anchoring depths of the nests and constituent sunspot groups. The improved feature tracking methods described in Section 8.3 will be useful for keeping track of the motion of sunspot groups over long periods of time and to know whether increases in flux are due to mergers or new emergence in within the same group.

Knowledge of the subsurface magnetic field structure may give some clues as to the relationship between sunspot group emergence and the torsional oscillation. Hathaway & Rightmire (91) present a plot of the residual differential rotation speed and a region of shear that progresses in latitude preceding the equator-ward progression of Sunspot emergence. It is thought that this dynamic shearing feature plays some role in destab-

8.5 Sunspot Groups and the Global Magnetic Field of the Sun

bilising subsurface magnetic flux ropes. Figure 8.4 shows a map of the residual rotation speed with the solar cycle bounds overlaid. It would be interesting to have an accurate measurement of the rotation speed of sunspot groups over the solar cycle, as well as that of small magnetic features, such as plage. There has not been a statistical study over time, comparing the rotation of these features to the background plasma rotation speed. The speed could also be compared to helioseismic measurements, possibly indicating the anchoring depths of the different features.

In addition to studies of subsurface magnetic structures, a substantial amount of work remains to be done in investigating the relationship between coronal holes and sunspot groups. Coronal holes are open magnetic field structures, that exhibit a decreased density in the corona. They appear to form in the decayed remains of sunspots, that emerge as closed magnetic field structures. We aim to answer the questions: *At what point of decay does coronal hole emergence become likely to happen? How decayed must a sunspot be, before it becomes an open magnetic field structure?* A comparison between coronal hole and sunspot detections and the predicted topology of the surface magnetic field using a PFSS model may help to answer these questions. I have begun using the method described in Henney & Harvey (95) to detect coronal holes in He I images¹, which are available from some ground-based observatories for multiple solar cycles.

Harvey & Recely (86) have shown that the magnetic flux at the poles can be estimated from polar coronal hole detections. We aim to compare the polar coronal hole boundaries with the averaged magnetic field spatial distribution to determine if there is any tilt in the global dipole field with respect to the Sun's equator. In Chapter 7 we showed that there is an apparent wobble in the 5 G contour of the $\langle B_+ \rangle$ butterfly

¹The software is being developed in a github repository available at: https://github.com/pohuigin/chole_detect. This software is written in IDL (<http://www.exelisvis.com/ProductsServices/IDL.aspx>) and is dependent on the SSW library (http://www.lmsal.com/solarsoft/ssw_whatitis.html) and another general library (https://github.com/pohuigin/gen_library).

8. CONCLUSIONS AND FUTURE WORK

map, alluding to an offset in the magnetic axis to the rotational axis of the Sun. The inclination of the axes would wobble back and forth, and hence the boundary of the polar field, from the perspective of the Earth. This has important implications, since it implies that the magnetic dynamo is not azimuthally symmetric and that we must abandon our classical view (144) of magnetic field generation. The size of the temporarily stable (at solar minimum) polar field configuration also has implications for magnetic surface diffusion.

8.6 Characterising the Transport of Diffuse Magnetic Flux

The shape and amount of flux of the static polar field configuration offers another method in which to estimate the diffusion coefficient, D , in addition to the method we have employed in Chapter 7. Assuming a meridional flow profile and an estimation of the amount of flux on the pole, there should be a characteristic size and profile of the polar field distribution. Diffusion acts to disperse the fields, but the meridional flow acts to collect them at the pole. At some point an equilibrium is reached. We can observe and measure this boundary, as shown in Chapter 7. Thus, we can run a cellular random-walk simulation to predict what the boundary shape and position should be. We have begun testing methods to perform this simulation¹ The simulation requires that we assume some statistical properties of supergranules. A 4th-year undergraduate student is currently working with us on simulations to theoretically predict their properties by combining the results of studies of the properties of the solar convection zone (14) and studies of the observed properties of supergranules using surface velocity measurements (92).

A further method of measuring D to be explored is to directly track magnetic flux elements in high-resolution, high time-cadence image sequences and determine their rate of motion from some starting point to the point when they merge or cancel with

¹See the supplementary movie available here: <http://dx.doi.org/10.6084/m9.figshare.96201>.

another flux element. By analyzing large numbers of these features, we can determine their squared average displacement, $\langle R^2 \rangle$, and apply the equation given in Chapter 7. This method leaves open the possibility of determining the magnetic flux dependency of D . It is known that not all magnetic features exhibit the same D (178).

A final exploration of the diffusion of magnetic elements across the solar surface involves analysing the birth and evolution of coronal holes. It is thought that coronal holes experience some form of diffusion that determines the rate of the expansion of their boundaries (62; 108). The evolution of coronal hole boundaries must be compared to the evolution of diffuse magnetic fields to determine their relationship and the mechanism by which they form. Very little work has been done on this topic.

8.7 Outreach Activities

There are several avenues I am pursuing to engage in public outreach, specifically those of astronomy education and promoting science policy. I have begun work on a website to relate astronomy topics in an interactive way to primary and secondary school students, as well as the general public. The project, <http://SolarSurfer.org>, will use a comic book style, story-oriented teaching methods, interactive physics widgets (phidgets), and videos to demonstrate and engage people in learning about the wonders of astronomy. This project differs from some similar projects (<http://UniverseAdventure.org> and <http://SunTrek.org>) in that it is oriented toward the Irish school curriculum and will offer corresponding classroom materials.

As an auxiliary project, Irish SkyMaps will allow users to generate a star map for their location, by inputting their IP address into Google's geolocation API. This printable map will include the constellations with the names in both Irish and English. An example star map is shown in Figure 8.5.

Finally, <http://LoveIrishScience.org>¹ is a politically motivated project meant

¹Inspired by the logo of <http://www.loveirishfood.ie/>

8. CONCLUSIONS AND FUTURE WORK

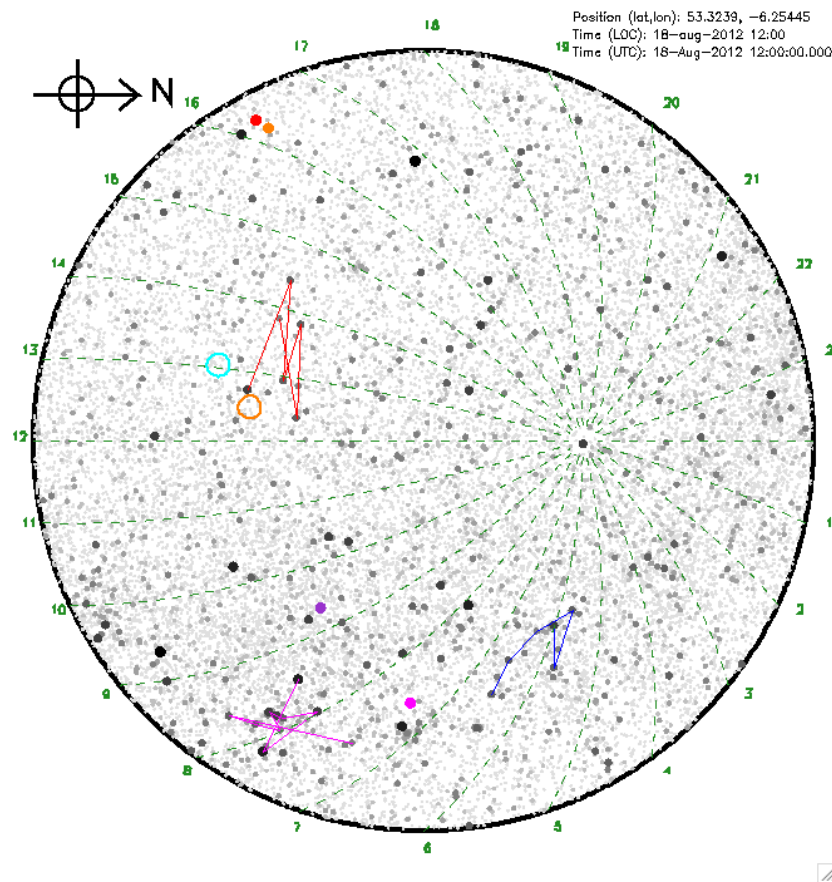


Figure 8.5: An example star map from the Irish SkyMaps project.

to engage with the public and government to bring attention to the science funding crisis in Ireland. Currently, there are no substantial funding sources from the government for basic science. Politicians seem to be in denial that this is the case, so this project aims to present the statistics about which areas of research are awarded grants and which are rejected by Irish government funding bodies (e.g., IRCSET and SFI). Also, the amount of funding given to different areas of research will be presented. If the government does not take a stand on this issue soon, basic science will be nonexistent in Ireland and my career in Ireland will be over before it begins.

References

- [1] ABBETT, W.P. & FISHER, G.H. (2003). A Coupled Model for the Emergence of Active Region Magnetic Flux into the Solar Corona. *Astrophysical Journal*, **582**, 475–485. 39
- [2] ABRAMENKO, V.I. (2005). Relationship between Magnetic Power Spectrum and Flare Productivity in Solar Active Regions. *Astrophys. J.*, **629**, 1141–1149. 50
- [3] AHMED, O., QAHWAJI, R., COLAK, T., DUDOKDEWIT, T. & IPSON, S. (2010). A new technique for the calculation and 3d visualisation of magnetic complexities on solar satellite images. *The Visual Computer*, **26**, 385–395, 10.1007/s00371-010-0418-1. 131
- [4] AHMED, O.W., QAHWAJI, R., COLAK, T., HIGGINS, P.A., GALLAGHER, P.T. & BLOOMFIELD, D.S. (2011). Solar Flare Prediction Using Advanced Feature Extraction, Machine Learning, and Feature Selection. *Solar Phys.*, **404**. 52, 185, 251
- [5] ALLEN, C.W. (1973). *Astrophysical quantities*. London: University of London, Athlone Press, —c1973, 3rd ed. 6
- [6] ANTALOVA, A. (1996). Daily Soft X-Ray Flare Index (1969=1972). *Contributions of the Astronomical Observatory Skalnate Pleso*, **26**, 98–120. 177
- [7] ASCHWANDEN, M.J. (2005). Physics of the Solar Corona. An Introduction with Problems and Solutions (2nd edition). *Pour la Science*. 3, 17, 25
- [8] ASCHWANDEN, M.J. (2010). A Code for Automated Tracing of Coronal Loops Approaching Visual Perception. *Solar Phys.*, **262**, 399–423. 251
- [9] ASCHWANDEN, M.J. (2011). *Self-Organized Criticality in Astrophysics*. 55, 56
- [10] ASCHWANDEN, M.J., NEWMARK, J.S., DELABOUDINIÈRE, J.P., NEUPERT, W.M., KLIMCHUK, J.A., GARY, G.A., PORTIER-FOZZANI, F. & ZUCKER, A. (1999). Three-dimensional Stereoscopic Analysis of Solar Active Region Loops. I. SOHO/EIT Observations at Temperatures of (1.0-1.5) $\times 10^6$ K. *Astrophys. J.*, **515**, 842–867. 38

REFERENCES

- [11] ATTIE, R., INNES, D.E. & POTTS, H.E. (2009). Evidence of photospheric vortex flows at supergranular junctions observed by FG/SOT (Hinode). *Astron. Astrophys.*, **493**, L13–L16. 40
- [12] BABCOCK, H.W. (1953). The Solar Magnetograph. *Astrophysical Journal*, **118**, 387–+. 105
- [13] BABCOCK, H.W. (1961). The Topology of the Sun's Magnetic Field and the 22-YEAR Cycle. *Astrophys. J.*, **133**, 572–+. 41, 43, 46
- [14] BAHCALL, J.N. & PINSONNEAULT, M.H. (1992). Standard solar models, with and without hem diffusion, and the solar neutrino problem. *Reviews of Modern Physics*, **64**, 885–926. 254
- [15] BAHCALL, J.N. & PINSONNEAULT, M.H. (2004). What Do We (Not) Know Theoretically about Solar Neutrino Fluxes? *Physical Review Letters*, **92**, 121301. 5, 6
- [16] BARNES, G. & LEKA, K.D. (2006). Photospheric Magnetic Field Properties of Flaring versus Flare-quiet Active Regions. III. Magnetic Charge Topology Models. *Astrophys. J.*, **646**, 1303–1318. 51
- [17] BARRA, V., DELOUILLE, V., KRETZSCHMAR, M. & HOCHÉDEZ, J.F. (2009). Fast and robust segmentation of solar EUV images: algorithm and results for solar cycle 23. *Astron. Astrophys.*, **505**, 361–371. 161
- [18] BENTLEY, R.D. & EGSO CONSORTIUM (2002). EGSO - the European Grid of Solar Observations. In A. Wilson, ed., *Solar Variability: From Core to Outer Frontiers*, vol. 506 of *ESA Special Publication*, 923–926. 116
- [19] BERGER, T.E., LÖFDAHL, M.G., SHINE, R.A. & TITLE, A.M. (1998). Measurements of Solar Magnetic Element Dispersal. *Astrophys. J.*, **506**, 439–449. 219
- [20] Higgins, P. A., BLOOMFIELD, D.S. & GALLAGHER, P.T. (2012). Active Regions and the Global Magnetic Field of the Sun. *Astronomy & Astrophysics*, in prep. 187
- [21] Higgins, P. A., BLOOMFIELD, D.S. & GALLAGHER, P.T. (2012). Quantifying Diffusion: Tracking Magnetic Flux Transport on the Sun. *Solar Physics*, in prep. 215
- [22] BLOOMFIELD, D.S., Higgins, P. A., MCATEER, R.T.J. & GALLAGHER, P.T. (2012). Toward Reliable Benchmarking of Solar Flare Forecasting Methods. *Astrophys. J. Lett.*, **747**, L41. 185

REFERENCES

- [23] BLOOMFIELD, D.S., GALLAGHER, P.T., CARLEY, E., HIGGINS, P.A., LONG, D.M., MALONEY, S.A., MURRAY, S.A., O'FLANNAGAIN, A., PÉREZ-SUÁREZ, D., RYAN, D. & ZUCCA, P. (2012). A Comprehensive Overview of the 2011 June 7 Solar Storm. *Astronomy & Astrophysics*, in prep. 159, 161, 182
- [24] BRANDENBURG, A. (2005). The Case for a Distributed Solar Dynamo Shaped by Near-Surface Shear. *Astrophys. J.*, **625**, 539–547. 32
- [25] BRICKHOUSE, N.S. & LABONTE, B.J. (1988). Mass and energy flow near sunspots. I - Observations of moat properties. *Solar Phys.*, **115**, 43–60. 36
- [26] BROWN, D.S., NIGHTINGALE, R.W., ALEXANDER, D., SCHRIJVER, C.J., METCALF, T.R., SHINE, R.A., TITLE, A.M. & WOLFSON, C.J. (2003). Observations of Rotating Sunspots from TRACE. *Solar Phys.*, **216**, 79–108. 89
- [27] BROWN, T.M. (1984). The Fourier tachometer 2: an instrument for measuring global solar velocity fields. In R. K. Ulrich, J. Harvey, E. J. Rhodes Jr., & J. Toomre, ed., *Solar Seismology from Space*, 157–163. 106
- [28] BRUECKNER, G.E., HOWARD, R.A., KOOMEN, M.J., KORENDYKE, C.M., MICHELS, D.J., MOSES, J.D., SOCKER, D.G., DERE, K.P., LAMY, P.L., LLEBARIA, A., BOUT, M.V., SCHWENN, R., SIMNETT, G.M., BEDFORD, D.K. & EYLES, C.J. (1995). The Large Angle Spectroscopic Coronagraph (LASCO). *Solar Phys.*, **162**, 357–402. 207
- [29] BRUN, A.S., MIESCH, M.S. & TOOMRE, J. (2004). Global-Scale Turbulent Convection and Magnetic Dynamo Action in the Solar Envelope. *Astrophys. J.*, **614**, 1073–1098. 16
- [30] CALIGARI, P., MORENO-INSERTIS, F. & SCHUSSLER, M. (1995). Emerging flux tubes in the solar convection zone. 1: Asymmetry, tilt, and emergence latitude. *Astrophys. J.*, **441**, 886–902. 33
- [31] CARRINGTON, R.C. (1854). Method of observing the Positions of Spots on the Sun. *Meetings of the Royal Astronomical Society*, **14**, 153–158. 116
- [32] CHAE, J. (2001). Observational Determination of the Rate of Magnetic Helicity Transport through the Solar Surface via the Horizontal Motion of Field Line Footpoints. *Astrophysical Journal*, **560**, L95–L98. 93
- [33] CHAE, J., MOON, Y. & PARK, Y. (2004). Determination of magnetic helicity content of solar active regions from SOHO/MDI magnetograms. *Solar Physics*, **223**, 39–55. 92, 93
- [34] CHAPMAN, S. & ZIRIN, H. (1957). Notes on the Solar Corona and the Terrestrial Ionosphere. *Smithsonian Contributions to Astrophysics*, **2**, 1. 29

REFERENCES

- [35] CHARBONNEAU, P. (2010). Dynamo models of the solar cycle. *Living Reviews in Solar Physics*, **7**. 74, 198
- [36] CHOUDHARY, D.P., VENKATAKRISHNAN, P. & GOSAIN, S. (2002). On Magnetic Flux Imbalance in Solar Active Regions. *Astrophys. J.*, **573**, 851–856. 44, 47, 188, 203
- [37] CHOUDHURI, A.R. & GILMAN, P.A. (1987). The influence of the Coriolis force on flux tubes rising through the solar convection zone. *Astrophys. J.*, **316**, 788–800. 35
- [38] COLAK, T. & QAHWAJI, R. (2008). Automated McIntosh-Based Classification of Sunspot Groups Using MDI Images. *Solar Physics*, **248**, 277–296. 117
- [39] COLAK, T. & QAHWAJI, R. (2009). Automated Solar Activity Prediction: A hybrid computer platform using machine learning and solar imaging for automated prediction of solar flares. *Space Weather*, **7**, 6001+. 52, 117, 155, 162
- [40] CONLON, P.A. & GALLAGHER, P.T. (2010). Constraining Three-Dimensional Magnetic Field Extrapolations Using the Twin Perspectives of STEREO. *Astrophys. J.*, **715**, 59–65. 160, 171, 249
- [41] CONLON, P.A., GALLAGHER, P.T., MCATEER, R.T.J., IRELAND, J., YOUNG, C.A., KESTENER, P., HEWETT, R.J. & MAGUIRE, K. (2008). Multifractal Properties of Evolving Active Regions. *Solar Physics*, **248**, 297–309. 50, 117, 160
- [42] CONLON, P.A., MCATEER, R.T.J., GALLAGHER, P.T. & FENNELL, L. (2010). Quantifying the Evolving Magnetic Structure of Active Regions. *Astrophys. J.*, **722**, 577–585. 48, 50, 117, 160
- [43] COUVIDAT, S., RAJAGURU, S.P., WACHTER, R., SANKARASUBRAMANIAN, K., SCHOU, J. & SCHERRER, P.H. (2012). Line-of-Sight Observables Algorithms for the Helioseismic and Magnetic Imager (HMI) Instrument Tested with Interferometric Bidimensional Spectrometer (IBIS) Observations. *Solar Phys.*, **13**. 110
- [44] COX, A., LIVINGSTON, W. & MATTHEWS, M. (1991). *Solar Interior and Atmosphere*. Space Science Series, University of Arizona Press. 64
- [45] DALLA, S., FLETCHER, L. & WALTON, N.A. (2008). Invisible sunspots and rate of solar magnetic flux emergence. *Astron. Astrophys.*, **479**, L1–L4. 183
- [46] DEFOREST, C.E., HAGENAAR, H.J., LAMB, D.A., PARRELL, C.E. & WELSCH, B.T. (2007). Solar Magnetic Tracking. I. Software Comparison and Recommended Practices. *Astrophys. J.*, **666**, 576–587. 201
- [47] DEVORE, C.R., BORIS, J.P. & SHEELEY, N.R., JR. (1984). The concentration of the large-scale solar magnetic field by a meridional surface flow. *Solar Phys.*, **92**, 1–14. 219

REFERENCES

- [48] DIKPATI, M., CORBARD, T., THOMPSON, M.J. & GILMAN, P.A. (2002). Flux Transport Solar Dynamos with Near-Surface Radial Shear. *Astrophys. J. Lett.*, **575**, L41–L45. 241
- [49] DIKPATI, M., DE TOMA, G., GILMAN, P.A., ARGE, C.N. & WHITE, O.R. (2004). Diagnostics of Polar Field Reversal in Solar Cycle 23 Using a Flux Transport Dynamo Model. *Astrophys. J.*, **601**, 1136–1151. 220, 241
- [50] DUN, J., KUROKAWA, H., ISHII, T.T., LIU, Y. & ZHANG, H. (2007). Evolution of Magnetic Nonpotentiality in NOAA AR 10486. *Astrophys. J.*, **657**, 577–591. 184
- [51] DUNN, R. (1981). *Solar instrumentation: what's next?: Sacramento Peak National Observatory Conference, Sunspot, N.M., 14-17 Oct, 1980, Proceedings.* NSO/SP summer workshop series, Sacramento Peak National Observatory. 105
- [52] DUVALL, T.L., D'SILVA, S., JEFFERIES, S.M., HARVEY, J.W. & SCHOU, J. (1996). Downflows under sunspots detected by helioseismic tomography. *Nature*, **379**, 235–237. 36
- [53] DUVALL, T.L., JR. & BIRCH, A.C. (2010). The Vertical Component of the Supergranular Motion. *Astrophys. J. Lett.*, **725**, L47–L51. 16
- [54] EINSTEIN, A. (1905). Über die von der molekularkinetischen Theorie der Wärme geforderte Bewegung von in ruhenden Flüssigkeiten suspendierten Teilchen. *Annalen der Physik*, **322**, 549–560. 216
- [55] EMSLIE, A.G., KUCHAREK, H., DENNIS, B.R., GOPALSWAMY, N., HOLMAN, G.D., SHARE, G.H., VOURLIDAS, A., FORBES, T.G., GALLAGHER, P.T., MASSON, G.M., METCALF, T.R., MEWALDT, R.A., MURPHY, R.J., SCHWARTZ, R.A. & ZURBUCHEN, T.H. (2004). Energy partition in two solar flare/CME events. *Journal of Geophysical Research (Space Physics)*, **109**, 10104. 53
- [56] EVERSHED, J. (1909). Radial movement in sun-spots. *Mon. Not. Roy. Astron. Soc.*, **69**, 454. 36
- [57] FALCONER, D.A., MOORE, R.L. & GARY, G.A. (2008). Magnetogram Measures of Total Nonpotentiality for Prediction of Solar Coronal Mass Ejections from Active Regions of Any Degree of Magnetic Complexity. *Astrophysical Journal*, **689**, 1433–1442. 117, 128, 129, 160, 171
- [58] FALCONER, D.A., MOORE, R.L., GARY, G.A. & ADAMS, M. (2009). The "Main Sequence" of Explosive Solar Active Regions: Discovery and Interpretation. *Astrophys. J. Lett.*, **700**, L166–L169. 50, 131
- [59] FAN, Y. (2009). Magnetic Fields in the Solar Convection Zone. *Living Reviews in Solar Physics*, **6**, 4. 34, 42, 199

REFERENCES

- [60] FAN, Y., FISHER, G.H. & DELUCA, E.E. (1993). The origin of morphological asymmetries in bipolar active regions. *Astrophys. J.*, **405**, 390–401. 37
- [61] FISHER, G.H., LONGCOPE, D.W., METCALF, T.R. & PEVTSOV, A.A. (1998). Coronal Heating in Active Regions as a Function of Global Magnetic Variables. *Astrophys. J.*, **508**, 885–898. 250
- [62] FISK, L.A. (2005). The Open Magnetic Flux of the Sun. I. Transport by Reconstructions with Coronal Loops. *Astrophys. J.*, **626**, 563–573. 255
- [63] FITZPATRICK, R. (2008). *The Physics of Plasmas*. Lulu, 2nd edn. 84
- [64] FLETCHER, L., DENNIS, B.R., HUDSON, H.S., KRUCKER, S., PHILLIPS, K., VERONIG, A., BATTAGLIA, M., BONE, L., CASPI, A., CHEN, Q., GALLAGHER, P., GRIGIS, P.T., JI, H., LIU, W., MILLIGAN, R.O. & TEMMER, M. (2011). An Observational Overview of Solar Flares. *Space Sci. Rev.*, **159**, 19–106. 53, 54
- [65] FORBES, T.G., LINKER, J.A., CHEN, J., CID, C., KÓTA, J., LEE, M.A., MANN, G., MIKIĆ, Z., POTGIETER, M.S., SCHMIDT, J.M., SISCOE, G.L., VAINIO, R., ANTIOCHOS, S.K. & RILEY, P. (2006). CME Theory and Models. *Space Sci. Rev.*, **123**, 251–302. 87
- [66] FOX, P.A., SOFIA, S. & CHAN, K.L. (1991). Convective flows around sunspot-like objects. *Solar Phys.*, **135**, 15–42. 36
- [67] GABRIEL, A.H. (1976). A magnetic model of the solar transition region. *Royal Society of London Philosophical Transactions Series A*, **281**, 339–352. 25, 26
- [68] GALLAGHER, P.T. (2000). *Optical and EUV Observations of the Solar Atmosphere*. Ph.D. thesis, The Queen's University of Belfast and the Rutherford Appleton Laboratory. 19
- [69] GALLAGHER, P.T., PHILLIPS, K.J.H., HARRA-MURNION, L.K. & KEENAN, F.P. (1998). Properties of the quiet Sun EUV network. *Astron. Astrophys.*, **335**, 733–745. 26, 29
- [70] GALLAGHER, P.T., MOON, Y. & WANG, H. (2002). Active-Region Monitoring and Flare Forecasting I. Data Processing and First Results. *Solar Physics*, **209**, 171–183. 51, 116, 117, 160
- [71] GARY, G.A. (2001). Plasma Beta above a Solar Active Region: Rethinking the Paradigm. *Solar Physics*, **203**, 71–86. 17, 27, 28
- [72] GEORGOULIS, M.K. (2012). Are Solar Active Regions with Major Flares More Fractal, Multifractal, or Turbulent Than Others? *Solar Phys.*, **276**, 161–181. 50
- [73] GEORGOULIS, M.K. & RUST, D.M. (2007). Quantitative Forecasting of Major Solar Flares. *Astrophysical Journal*, **661**, L109–L112. 117, 131, 160, 171

REFERENCES

- [74] GIZON, L., BIRCH, A.C. & SPRUIT, H.C. (2010). Local Helioseismology: Three-Dimensional Imaging of the Solar Interior. *Ann. Rev. Astron. Astrophys.*, **48**, 289–338. 23
- [75] GNEVYSHEV, M.N. (1977). Essential features of the 11-year solar cycle. *Solar Phys.*, **51**, 175–183. 193
- [76] GOOSSENS, M., ed. (2003). *An introduction to plasma astrophysics and magnetohydrodynamics*, vol. 294 of *Astrophysics and Space Science Library*. 17
- [77] GOPALSWAMY, N., YASHIRO, S., MÄKELÄ, P., MICHALEK, G., SHIBASAKI, K. & HATHAWAY, D.H. (2012). Behavior of Solar Cycles 23 and 24 Revealed by Microwave Observations. *Astrophys. J. Lett.*, **750**, L42. 63
- [78] HABER, D.A., HINDMAN, B.W., TOOMRE, J., BOGART, R.S., LARSEN, R.M. & HILL, F. (2002). Evolving Submerged Meridional Circulation Cells within the Upper Convection Zone Revealed by Ring-Diagram Analysis. *Astrophys. J.*, **570**, 855–864. 17, 43, 197
- [79] HAGENAAR, H.J. (2001). Ephemeral Regions on a Sequence of Full-Disk Michelson Doppler Imager Magnetograms. *Astrophysical Journal*, **555**, 448–461. 24, 121
- [80] HAGENAAR, H.J., SCHRIJVER, C.J. & TITLE, A.M. (1997). The Distribution of Cell Sizes of the Solar Chromospheric Network. *Astrophys. J.*, **481**, 988. 219
- [81] HAGENAAR, H.J., SCHRIJVER, C.J., TITLE, A.M. & SHINE, R.A. (1999). Dispersal of Magnetic Flux in the Quiet Solar Photosphere. *Astrophys. J.*, **511**, 932–944. 218, 219, 220, 241
- [82] HALE, G.E. (1908). On the Probable Existence of a Magnetic Field in Sun-Spots. *Astrophys. J.*, **28**, 315. 104
- [83] HALE, G.E., ELLERMAN, F., NICHOLSON, S.B. & JOY, A.H. (1919). The Magnetic Polarity of Sun-Spots. *Astrophys. J.*, **49**, 153+. 41, 42, 50
- [84] HANSER, F.A. & SELLERS, F.B. (1996). Design and calibration of the GOES-8 solar x-ray sensor: the XRS. In E. R. Washwell, ed., *Society of Photo-Optical Instrumentation Engineers (SPIE) Conference Series*, vol. 2812 of *Society of Photo-Optical Instrumentation Engineers (SPIE) Conference Series*, 344–352. 113
- [85] HARVEY, K.L. (1992). The Cyclic Behavior of Solar Activity. In K. L. Harvey, ed., *The Solar Cycle*, vol. 27 of *Astronomical Society of the Pacific Conference Series*, 335. 43, 46, 47, 188, 191, 222
- [86] HARVEY, K.L. & RECELY, F. (2002). Polar Coronal Holes During Cycles 22 and 23. *Solar Phys.*, **211**, 31–52. 46, 253

REFERENCES

- [87] HARVEY, K.L. & ZWAAN, C. (1993). Properties and emergence of bipolar active regions. *Solar Phys.*, **148**, 85–118. 35, 189, 197, 201
- [88] HASSLER, D.M., DAMMASCH, I.E., LEMAIRE, P., BREKKE, P., CURDT, W., MASON, H.E., VIAL, J.C. & WILHELM, K. (1999). Solar Wind Outflow and the Chromospheric Magnetic Network. *Science*, **283**, 810. 29
- [89] HATHAWAY, D.H. (2010). The Solar Cycle. *Living Reviews in Solar Physics*, **7**, 1–+. 42, 45, 201
- [90] HATHAWAY, D.H. & RIGHTMIRE, L. (2010). Variations in the Sun’s Meridional Flow over a Solar Cycle. *Science*, **327**, 1350–. 43, 205
- [91] HATHAWAY, D.H. & RIGHTMIRE, L. (2011). Variations in the Axisymmetric Transport of Magnetic Elements on the Sun: 1996-2010. *Astrophys. J.*, **729**, 80. 15, 214, 219, 226, 227, 252
- [92] HATHAWAY, D.H., BECK, J.G., BOGART, R.S., BACHMANN, K.T., KHATRI, G., PETITTO, J.M., HAN, S. & RAYMOND, J. (2000). The Photospheric Convection Spectrum. *Solar Phys.*, **193**, 299–312. 235, 254
- [93] HATHAWAY, D.H., BECK, J.G., HAN, S. & RAYMOND, J. (2002). Radial Flows in Supergranules. *Solar Phys.*, **205**, 25–38. 16, 235
- [94] HATHAWAY, D.H., WILLIAMS, P.E. & CUNTZ, M. (2009). The Advection of Supergranules by Large-Scale Flows. In M. Dikpati, T. Arentoft, I. González Hernández, C. Lindsey, & F. Hill, ed., *Solar-Stellar Dynamos as Revealed by Helio- and Asteroseismology: GONG 2008/SOHO 21*, vol. 416 of *Astronomical Society of the Pacific Conference Series*, 495. 177
- [95] HENNEY, C.J. & HARVEY, J.W. (2005). Automated Coronal Hole Detection using He 1083 nm Spectroheliograms and Photospheric Magnetograms. In K. Sankarasubramanian, M. Penn & A. Pevtsov, eds., *Large-scale Structures and their Role in Solar Activity*, vol. 346 of *Astronomical Society of the Pacific Conference Series*, 261. 253
- [96] HEWETT, R.J., GALLAGHER, P.T., MCATEER, R.T.J., YOUNG, C.A., IRELAND, J., CONLON, P.A. & MAGUIRE, K. (2008). Multiscale Analysis of Active Region Evolution. *Solar Physics*, **248**, 311–322. 40, 50, 65, 117, 160
- [97] HIGGINS, P.A., GALLAGHER, P.T., MCATEER, R.T.J. & BLOOMFIELD, D.S. (2011). Solar magnetic feature detection and tracking for space weather monitoring. *Advances in Space Research*, **47**, 2105–2117. 51, 52, 115, 136, 189, 225
- [98] HINDMAN, B.W., HABER, D.A. & TOOMRE, J. (2009). Subsurface Circulations within Active Regions. *Astrophys. J.*, **698**, 1749–1760. 36, 37

REFERENCES

- [99] HIRZBERGER, J., GIZON, L., SOLANKI, S.K. & DUVALL, T.L. (2008). Structure and Evolution of Supergranulation from Local Helioseismology. *Solar Phys.*, **251**, 417–437. 235
- [100] HOWARD, R. & HARVEY, J. (1970). Spectroscopic Determinations of Solar Rotation. *Solar Phys.*, **12**, 23–51. 16
- [101] HOWARD, R.F. (1991). Axial tilt angles of sunspot groups. *Solar Phys.*, **136**, 251–262. 42
- [102] HOWARD, R.F., HARVEY, J.W. & FORGACH, S. (1990). Solar surface velocity fields determined from small magnetic features. *Solar Physics*, **130**, 295–311. 123, 134, 147
- [103] HOWE, R., HILL, F., KOMM, R., CHRISTENSEN-DALSGAARD, J., LARSON, T.P., SCHOU, J., THOMPSON, M.J. & ULRICH, R. (2011). The torsional oscillation and the new solar cycle. *Journal of Physics Conference Series*, **271**, 012074. 197, 199
- [104] INNES, D.E., INHESTER, B., AXFORD, W.I. & WILHELM, K. (1997). Bi-directional plasma jets produced by magnetic reconnection on the Sun. *Nature*, **386**, 811–813. 27
- [105] IRELAND, J., YOUNG, C.A., MCATEER, R.T.J., WHELAN, C., HEWETT, R.J. & GALLAGHER, P.T. (2008). Multiresolution Analysis of Active Region Magnetic Structure and its Correlation with the Mount Wilson Classification and Flaring Activity. *Solar Phys.*, **252**, 121–137. 50
- [106] KELLER, C.U., SCHÜSSLER, M., VÖGLER, A. & ZAKHAROV, V. (2004). On the Origin of Solar Faculae. *Astrophys. J. Lett.*, **607**, L59–L62. 38
- [107] KNAACK, R. & STENFLO, J.O. (2005). Spherical harmonic decomposition of solar magnetic fields. *Astron. Astrophys.*, **438**, 349–363. 47, 189
- [108] KRISTA, L.D., GALLAGHER, P.T. & BLOOMFIELD, D.S. (2011). Short-term Evolution of Coronal Hole Boundaries. *Astrophys. J. Lett.*, **731**, L26. 255
- [109] KÜNZEL, H. (1960). Die Flare-Häufigkeit in Fleckengruppen unterschiedlicher Klasse und magnetischer Struktur. *Astronomische Nachrichten*, **285**, 271–+. 49, 50, 117, 250
- [110] LABONTE, B.J., GEORGULIS, M.K. & RUST, D.M. (2007). Survey of Magnetic Helicity Injection in Regions Producing X-Class Flares. *Astrophysical Journal*, **671**, 955–963. 117, 130, 155
- [111] LAWRENCE, J.K., RUZMAIKIN, A.A. & CADAVID, A.C. (1993). Multifractal Measure of the Solar Magnetic Field. *Astrophys. J.*, **417**, 805. 219

REFERENCES

- [112] LEIGHTON, R.B. (1964). Transport of Magnetic Fields on the Sun. *Astrophys. J.*, **140**, 1547–+. 41, 43, 46, 75, 218, 219
- [113] LEIGHTON, R.B., NOYES, R.W. & SIMON, G.W. (1962). Velocity Fields in the Solar Atmosphere. I. Preliminary Report. *Astrophys. J.*, **135**, 474. 235
- [114] LEKA, K.D. & BARNES, G. (2003). Photospheric Magnetic Field Properties of Flaring versus Flare-quiet Active Regions. I. Data, General Approach, and Sample Results. *Astrophys. J.*, **595**, 1277–1295. 51, 175
- [115] LEKA, K.D. & BARNES, G. (2003). Photospheric Magnetic Field Properties of Flaring versus Flare-quiet Active Regions. II. Discriminant Analysis. *Astrophys. J.*, **595**, 1296–1306. 51, 175
- [116] LEKA, K.D. & BARNES, G. (2007). Photospheric Magnetic Field Properties of Flaring versus Flare-quiet Active Regions. IV. A Statistically Significant Sample. *Astrophys. J.*, **656**, 1173–1186. 51
- [117] LI, H., SAKURAI, T., ICHIMOTO, K. & UENO, S. (2000). Magnetic Field Evolution Leading to Solar Flares I. Cases with Low Magnetic Shear and Flux Emergence. *Pub. Astron. Soc. Japan*, **52**, 465–481. 160
- [118] LIN, R.P., DENNIS, B.R., HURFORD, G.J., SMITH, D.M., ZEHNDER, A., HARVEY, P.R., CURTIS, D.W., PANKOW, D., TURIN, P., BESTER, M., CSILLAGHY, A., LEWIS, M., MADDEN, N., VAN BEEK, H.F., APPLEBY, M., RAUDORF, T., McTIERNAN, J., RAMATY, R., SCHMAHL, E., SCHWARTZ, R., KRUCKER, S., ABIAD, R., QUINN, T., BERG, P., HASHII, M., STERLING, R., JACKSON, R., PRATT, R., CAMPBELL, R.D., MALONE, D., LANDIS, D., BARRINGTON-LEIGH, C.P., SLASSI-SENNOU, S., CORK, C., CLARK, D., AMATO, D., ORWIG, L., BOYLE, R., BANKS, I.S., SHIREY, K., TOLBERT, A.K., ZARRO, D., SNOW, F., THOMSEN, K., HENNECK, R., MCCHEDLISHVILI, A., MING, P., FIVIAN, M., JORDAN, J., WANNER, R., CRUBB, J., PREBLE, J., MATRANGA, M., BENZ, A., HUDSON, H., CANFIELD, R.C., HOLMAN, G.D., CRANNELL, C., KOSUGI, T., EMSLIE, A.G., VILMER, N., BROWN, J.C., JOHNS-KRULL, C., ASCHWANDEN, M., METCALF, T. & CONWAY, A. (2002). The Reuven Ramaty High-Energy Solar Spectroscopic Imager (RHESSI). *Solar Phys.*, **210**, 3–32. 113
- [119] LIU, Y., ZHAO, X. & HOEKSEMA, J.T. (2004). Correction of Offset in MDI/SOHO Magnetograms. *Solar Phys.*, **219**, 39–53. 122
- [120] LIU, Y., NORTON, A.A. & SCHERRER, P.H. (2007). A Note on Saturation Seen in the MDI/SOHO Magnetograms. *Solar Physics*, **241**, 185–193. 136, 183
- [121] LONG, D.M., GALLAGHER, P.T., MCATEER, R.T.J. & BLOOMFIELD, D.S. (2008). The Kinematics of a Globally Propagating Disturbance in the Solar Corona. *Astrophys. J. Lett.*, **680**, L81–L84. 27

REFERENCES

- [122] LU, E.T., HAMILTON, R.J., MCTIERNAN, J.M. & BROMUND, K.R. (1993). Solar flares and avalanches in driven dissipative systems. *Astrophys. J.*, **412**, 841–852. 56
- [123] MASON, J.P. & HOEKSEMA, J.T. (2010). Testing Automated Solar Flare Forecasting with 13 Years of Michelson Doppler Imager Magnetograms. *Astrophys. J.*, **723**, 634–640. 52, 160
- [124] MAUNDER, E.W. (1904). Note on the distribution of sun-spots in heliographic latitude, 1874–1902. *Mon. Not. Roy. Astron. Soc.*, **64**, 747–761. 41
- [125] MCATEER, R.T.J., GALLAGHER, P.T. & IRELAND, J. (2005). Statistics of Active Region Complexity: A Large-Scale Fractal Dimension Survey. *Astrophysical Journal*, **631**, 628–635. 50, 117, 160
- [126] MCATEER, R.T.J., GALLAGHER, P.T., IRELAND, J. & YOUNG, C.A. (2005a). Automated Boundary-extraction And Region-growing Techniques Applied To Solar Magnetograms. *Solar Physics*, **228**, 55–66. 116
- [127] MCATEER, R.T.J., GALLAGHER, P.T. & CONLON, P.A. (2010). Turbulence, complexity, and solar flares. *Advances in Space Research*, **45**, 1067–1074. 118
- [128] MCINTOSH, P.S. (1990). The classification of sunspot groups. *Solar Physics*, **125**, 251–267. 48, 49, 117
- [129] MENGOTTI, E., HEYDERMAN, L.J., RODRIGUEZ, A.F., NOLTING, F., HUGLI, R.V. & BRAUN, H.B. (2010). Real-space observation of emergent magnetic monopoles and associated Dirac strings in artificial kagome spin ice. *Nature Physics*. 88
- [130] MESSEROTTI, M., ZUCCARELLO, F., GUGLIELMINO, S.L., BOTHMER, V., LILENSTEN, J., NOCI, G., STORINI, M. & LUNDSTEDT, H. (2009). Solar Weather Event Modelling and Prediction. *Space Sci. Rev.*, **147**, 121–185. 51, 160
- [131] METCALFE, T.S., BASU, S., HENRY, T.J., SODERBLOM, D.R., JUDGE, P.G., KNÖLKER, M., MATHUR, S. & REMPEL, M. (2010). Discovery of a 1.6 Year Magnetic Activity Cycle in the Exoplanet Host Star ι Horologii. *Astrophys. J. Lett.*, **723**, L213–L217. 2
- [132] MEUNIER, N. (2003). Statistical properties of magnetic structures: Their dependence on scale and solar activity. *Astron. Astrophys.*, **405**, 1107–1120. 197, 201, 213
- [133] MIESCH, M.S. (2005). Large-scale dynamics of the convection zone and tachocline. *Living Reviews in Solar Physics*, **2**. 16

REFERENCES

- [134] MORDVINOV, A.V. (2007). Magnetic Flux Imbalance of the Solar and Heliospheric Magnetic Fields. *Solar Phys.*, **246**, 445–456. 47, 188
- [135] MORITA, S. & MCINTOSH, S.W. (2005). Genesis of AR NOAA10314. In K. Sankarasubramanian, M. Penn, & A. Pevtsov, ed., *Large-scale Structures and their Role in Solar Activity*, vol. 346 of *Astronomical Society of the Pacific Conference Series*, 317–+. 93, 130, 169
- [136] MOSHER, J.M. (1977). *The magnetic history of solar active regions*. Ph.D. thesis, California Inst. of Tech., Pasadena. 17, 40, 43, 218
- [137] MURRAY, S.A., BLOOMFIELD, D.S. & GALLAGHER, P.T. (2012). The Evolution of Sunspot Magnetic Fields Associated with a Solar Flare. *Solar Phys.*, **277**, 45–57. 88, 162, 171
- [138] NANDY, D. & CHOUDHURI, A.R. (2001). Toward a Mean Field Formulation of the Babcock-Leighton Type Solar Dynamo. I. α -Coefficient versus Durney's Double-Ring Approach. *Astrophys. J.*, **551**, 576–585. 42, 76
- [139] NEUPERT, W.M. (1968). Comparison of Solar X-Ray Line Emission with Microwave Emission during Flares. *Astrophys. J. Lett.*, **153**, L59. 55
- [140] NEWTON, H.W. & NUNN, M.L. (1951). The Sun's rotation derived from sunspots 1934–1944 and additional results. *Mon. Not. Roy. Astron. Soc.*, **111**, 413. 16
- [141] NORTON, A.A., GRAHAM, J.P., ULRICH, R.K., SCHOU, J., TOMCZYK, S., , Y., LITES, B.W., LÓPEZ ARISTE, A., BUSH, R.I., SOCAS-NAVARRO, H. & SCHERRER, P.H. (2006). Spectral Line Selection for HMI: A Comparison of Fe I 6173 Å and Ni I 6768 Å. *Solar Phys.*, **239**, 69–91. 110, 111
- [142] OFMAN, L. (2010). Wave Modeling of the Solar Wind. *Living Reviews in Solar Physics*, **7**, 4. 32
- [143] ON THE SOCIETAL, C. & ECONOMIC IMPACTS OF SEVERE SPACE WEATHER EVENTS: A WORKSHOP, N.R.C. (2008). *Severe Space Weather Events—Understanding Societal and Economic Impacts: A Workshop Report*. The National Academies Press. 51
- [144] PARKER, E.N. (1955). Hydromagnetic Dynamo Models. *Astrophys. J.*, **122**, 293. 2, 46, 74, 254
- [145] PARKER, E.N. (1955). The Formation of Sunspots from the Solar Toroidal Field. *Astrophys. J.*, **121**, 491. 33, 34
- [146] PARKER, E.N. (1957). Sweet's Mechanism for Merging Magnetic Fields in Conducting Fluids. *J. Geophys. Res.*, **62**, 509–520. 84

REFERENCES

- [147] PARKER, E.N. (1957). The Solar Hydromagnetic Dynamo. *Proceedings of the National Academy of Science*, **43**, 8–14. 33, 72
- [148] PARKER, E.N. (1958). Suprathermal Particle Generation in the Solar Corona. *Astrophys. J.*, **128**, 677. 29
- [149] PARRELL, C.E., DEFOREST, C.E., HAGENAAR, H.J., JOHNSTON, B.A., LAMB, D.A. & WELSCH, B.T. (2009). A Power-Law Distribution of Solar Magnetic Fields Over More Than Five Decades in Flux. *Astrophys. J.*, **698**, 75–82. 35, 65, 201
- [150] PÉREZ-SUÁREZ, D., MACLEAN, R.C., DOYLE, J.G. & MADJARSKA, M.S. (2008). The structure and dynamics of a bright point as seen with Hinode, SoHO and TRACE. *Astron. Astrophys.*, **492**, 575–583. 26
- [151] PESNELL, W.D., THOMPSON, B.J. & CHAMBERLIN, P.C. (2012). The Solar Dynamics Observatory (SDO). *Solar Phys.*, **275**, 3–15. 26
- [152] PETSCHEK, H.E. (1964). Magnetic Field Annihilation. *NASA Special Publication*, **50**, 425. 86
- [153] POJOGA, S. & CUDNIK, B. (2002). The Clustering Properties of Active Regions During the First Part of Solar Cycle 23. *Solar Phys.*, **208**, 17–32. 179, 252
- [154] PRESS, W.H., TEUKOLSKY, S.A., VETTERLING, W.T. & FLANNERY, B.P. (1992). *Numerical recipes in C. The art of scientific computing*. 131
- [155] QAHWAJI, R. & COLAK, T. (2005). Automatic Detection and Verification of Solar Features. *International Journal of Imaging Systems Technology*, **15**, 199–210. 117
- [156] QIU, J., GARY, D.E. & FLEISHMAN, G.D. (2009). Evaluating Mean Magnetic Field in Flare Loops. *Solar Phys.*, **255**, 107–118. 53
- [157] REALE, F. (2010). Coronal loops: Observations and modeling of confined plasma. *Living Reviews in Solar Physics*, **7**. 77, 78
- [158] RÉGNIER, S. & PRIEST, E.R. (2007). Free Magnetic Energy in Solar Active Regions above the Minimum-Energy Relaxed State. *Astrophysical Journal, Letters*, **669**, L53–L56. 160
- [159] RIEUTORD, M. & RINCON, F. (2010). The Sun’s Supergranulation. *Living Reviews in Solar Physics*, **7**, 2. 23
- [160] RIEUTORD, M., MEUNIER, N., ROUDIER, T., RONDI, S., BEIGBEDER, F. & PARÈS, L. (2008). Solar supergranulation revealed by granule tracking. *Astron. Astrophys.*, **479**, L17–L20. 23, 235
- [161] ROBERTS, B. (2000). *Solar Photospheric Magnetic Flux Tubes: Theory*. 77

REFERENCES

- [162] SAGAN, C. (1980). *Cosmos*. London: Macdonald Futura Publishers, and New York: Random House and Wings Books, —c1980. 1
- [163] SAMMIS, I., TANG, F. & ZIRIN, H. (2000). The Dependence of Large Flare Occurrence on the Magnetic Structure of Sunspots. *Astrophysical Journal*, **540**, 583–587. 50, 250
- [164] SCHATZMAN, E. (1949). The heating of the solar corona and chromosphere. *Annales d'Astrophysique*, **12**, 203. 25
- [165] SCHERRER, P.H., BOGART, R.S., BUSH, R.I., HOEKSEMA, J.T., KOSOVICHEV, A.G., SCHOU, J., ROSENBERG, W., SPRINGER, L., TARBELL, T.D., TITLE, A., WOLFSON, C.J., ZAYER, I. & MDI ENGINEERING TEAM (1995). The Solar Oscillations Investigation - Michelson Doppler Imager. *Solar Physics*, **162**, 129–188. 106, 107, 142, 222
- [166] SCHERRER, P.H., SCHOU, J., BUSH, R.I., KOSOVICHEV, A.G., BOGART, R.S., HOEKSEMA, J.T., Y., DUVALL, T.L., ZHAO, J., TITLE, A.M., SCHRIJVER, C.J., TARBELL, T.D. & TOMCZYK, S. (2012). The Helioseismic and Magnetic Imager (HMI) Investigation for the Solar Dynamics Observatory (SDO). *Solar Phys.*, **275**, 207–227. 109
- [167] SCHLICHENMAIER, R. & SOLANKI, S.K. (2003). On the heat transport in a sunspot penumbra. *Astron. Astrophys.*, **411**, 257–262. 36
- [168] SCHOU, J. (2004). SOHO MDI CCD performance. In F. Favata, S. Aigrain & A. Wilson, eds., *Stellar Structure and Habitable Planet Finding*, vol. 538 of *ESA Special Publication*, 411–415. 122
- [169] SCHOU, J., ANTIA, H.M., BASU, S., BOGART, R.S., BUSH, R.I., CHITRE, S.M., CHRISTENSEN-DALSGAARD, J., DI MAURO, M.P., DZIEMBOWSKI, W.A., EFF-DARWICH, A., GOUGH, D.O., HABER, D.A., HOEKSEMA, J.T., HOWE, R., KORZENNIK, S.G., KOSOVICHEV, A.G., LARSEN, R.M., PIJPERS, F.P., SCHERRER, P.H., SEKII, T., TARBELL, T.D., TITLE, A.M., THOMPSON, M.J. & TOOMRE, J. (1998). Helioseismic Studies of Differential Rotation in the Solar Envelope by the Solar Oscillations Investigation Using the Michelson Doppler Imager. *Astrophys. J.*, **505**, 390–417. 15, 16
- [170] SCHOU, J., SCHERRER, P.H., BUSH, R.I., WACHTER, R., COVIDAT, S., RABELLO-SOARES, M.C., BOGART, R.S., HOEKSEMA, J.T., Y., DUVALL, T.L., AKIN, D.J., ALLARD, B.A., MILES, J.W., RAIRDEN, R., SHINE, R.A., TARBELL, T.D., TITLE, A.M., WOLFSON, C.J., ELMORE, D.F., NORTON, A.A. & TOMCZYK, S. (2012). Design and Ground Calibration of the Helioseismic and Magnetic Imager (HMI) Instrument on the Solar Dynamics Observatory (SDO). *Solar Phys.*, **275**, 229–259. 109, 110, 111, 137

REFERENCES

- [171] SCHRIJVER, C.J. (2001). Simulations of the Photospheric Magnetic Activity and Outer Atmospheric Radiative Losses of Cool Stars Based on Characteristics of the Solar Magnetic Field. *Astrophysical Journal*, **547**, 475–490. 68, 220
- [172] SCHRIJVER, C.J. (2001). The Coronae of the Sun and Solar-type Stars (CD-ROM Directory: contribs/schrijv). In R. J. Garcia Lopez, R. Rebolo, & M. R. Zapatero Osorio, ed., *11th Cambridge Workshop on Cool Stars, Stellar Systems and the Sun*, vol. 223 of *Astronomical Society of the Pacific Conference Series*, 131. 18, 19
- [173] SCHRIJVER, C.J. (2007). A Characteristic Magnetic Field Pattern Associated with All Major Solar Flares and Its Use in Flare Forecasting. *Astrophysical Journal*, **655**, L117–L120. 48, 50, 54, 128, 129, 171
- [174] SCHRIJVER, C.J. (2009). Driving major solar flares and eruptions: A review. *Advances in Space Research*, **43**, 739–755. 131
- [175] SCHRIJVER, C.J. & DE ROSA, M.L. (2003). Photospheric and heliospheric magnetic fields. *Solar Phys.*, **212**, 165–200. 43, 46, 47, 189, 192, 206, 207, 220
- [176] SCHRIJVER, C.J. & LIU, Y. (2008). The Global Solar Magnetic Field Through a Full Sunspot Cycle: Observations and Model Results. *Solar Phys.*, **252**, 19–31. 43, 220
- [177] SCHRIJVER, C.J., ZWAAN, C., BALKE, A.C., TARBELL, T.D. & LAWRENCE, J.K. (1992). Patterns in the photospheric magnetic field and percolation theory. *Astron. Astrophys.*, **253**, L1–L4. 241
- [178] SCHRIJVER, C.J., SHINE, R.A., HAGENAAR, H.J., HURLBURT, N.E., TITLE, A.M., STROUS, L.H., JEFFERIES, S.M., JONES, A.R., HARVEY, J.W. & DUVALL, T.L., JR. (1996). Dynamics of the Chromospheric Network: Mobility, Dispersal, and Diffusion Coefficients. *Astrophys. J.*, **468**, 921–+. 40, 43, 216, 221, 255
- [179] SCHRIJVER, C.J., HAGENAAR, H.J. & TITLE, A.M. (1997). On the Patterns of the Solar Granulation and Supergranulation. *Astrophys. J.*, **475**, 328. 14, 218
- [180] SCHRIJVER, C.J., TITLE, A.M., VAN BALLEGOOIJEN, A.A., HAGENAAR, H.J. & SHINE, R.A. (1997). Sustaining the Quiet Photospheric Network: The Balance of Flux Emergence, Fragmentation, Merging, and Cancellation. *Astrophysical Journal*, **487**, 424–+. 22, 24, 40, 220
- [181] SCHRIJVER, C.J., DE ROSA, M.L., TITLE, A.M. & METCALF, T.R. (2005). The Nonpotentiality of Active-Region Coronae and the Dynamics of the Photospheric Magnetic Field. *Astrophys. J.*, **628**, 501–513. 48, 160

REFERENCES

- [182] SCHRIJVER, C.J., DEROSA, M.L., METCALF, T., BARNES, G., LITES, B., TARBELL, T., MCTIERNAN, J., VALORI, G., WIEGELMANN, T., WHEATLAND, M.S., AMARI, T., AULANIER, G., DÉMOULIN, P., FUHRMANN, M., KUSANO, K., RÉGNIER, S. & THALMANN, J.K. (2008). Nonlinear Force-free Field Modeling of a Solar Active Region around the Time of a Major Flare and Coronal Mass Ejection. *Astrophysical Journal*, **675**, 1637–1644. 50
- [183] SCHÜSSLER, M. & BAUMANN, I. (2006). Modeling the Sun's open magnetic flux. *Astron. Astrophys.*, **459**, 945–953. 47, 189
- [184] SCHWABE, M. (1844). Sonnenbeobachtungen im Jahre 1843. Von Herrn Hofrat Schwabe in Dessau. *Astronomische Nachrichten*, **21**, 233–+. 42
- [185] SHEELEY, N.R., JR. (1992). The Flux-Transport Model and Its Implications. In K. L. Harvey, ed., *The Solar Cycle*, vol. 27 of *Astronomical Society of the Pacific Conference Series*, 1. 218
- [186] SHEELEY, N.R., JR. (2005). Surface Evolution of the Sun's Magnetic Field: A Historical Review of the Flux-Transport Mechanism. *Living Reviews in Solar Physics*, **2**, 5. 17, 203, 216
- [187] SHEELEY, N.R., JR., DEVORE, C.R. & BORIS, J.P. (1985). Simulations of the mean solar magnetic field during sunspot cycle 21. *Solar Phys.*, **98**, 219–239. 219
- [188] SIMON, G.W. & LEIGHTON, R.B. (1964). Velocity Fields in the Solar Atmosphere. III. Large-Scale Motions, the Chromospheric Network, and Magnetic Fields. *Astrophys. J.*, **140**, 1120. 77
- [189] SIMON, G.W., TITLE, A.M. & WEISS, N.O. (1995). Kinematic models of supergranular diffusion on the Sun. *Astrophys. J.*, **442**, 886–897. 220, 235, 236
- [190] SOLANKI, S.K. (1986). Velocities in solar magnetic fluxtubes. *Astron. Astrophys.*, **168**, 311–329. 77
- [191] SOLANKI, S.K. (2003). Sunspots: An overview. *Astron. Astrophys. Rev.*, **11**, 153–286. 24
- [192] SOLANKI, S.K., MONTAVON, C.A.P. & LIVINGSTON, W. (1994). Infrared lines as probes of solar magnetic features. 7: On the nature of the Evershed effect in sunspots. *Astron. Astrophys.*, **283**, 221–231. 36
- [193] SPIEGEL, E.A. & WEISS, N.O. (1980). Magnetic activity and variations in solar luminosity. *Nature*, **287**, 616. 32
- [194] SPRUIT, H.C. (1976). Pressure equilibrium and energy balance of small photospheric fluxtubes. *Solar Phys.*, **50**, 269–295. 24, 38

REFERENCES

- [195] SPRUIT, H.C., TITLE, A.M. & VAN BALLEGOOIJEN, A.A. (1987). Is there a weak mixed polarity background field? Theoretical arguments. *Solar Phys.*, **110**, 115–128. 40, 41
- [196] STENFLO, J.O. & GUEDEL, M. (1988). Evolution of solar magnetic fields - Modal structure. *Astron. Astrophys.*, **191**, 137–148. 47, 189
- [197] STENFLO, J.O. & VOGEL, M. (1986). Global resonances in the evolution of solar magnetic fields. *Nature*, **319**, 285–290. 47, 189
- [198] STOKES, G.G. (1851). On the Composition and Resolution of Streams of Polarized Light from different Sources. *Transactions of the Cambridge Philosophical Society*, **9**, 399. 102
- [199] SUDOL, J.J. & HARVEY, J.W. (2005). Longitudinal Magnetic Field Changes Accompanying Solar Flares. *Astrophys. J.*, **635**, 647–658. 162, 171
- [200] SWEET, P.A. (1958). The Neutral Point Theory of Solar Flares. In B. Lehnert, ed., *Electromagnetic Phenomena in Cosmical Physics*, vol. 6 of *IAU Symposium*, 123. 84
- [201] TANAKA, K. (1986). High-energy observations of solar flares. *Astrophys. Spac. Sci.*, **118**, 101–113. 83
- [202] TANG, F., HOWARD, R. & ADKINS, J.M. (1984). A statistical study of active regions 1967-1981. *Solar Phys.*, **91**, 75–86. 189, 197, 199, 201
- [203] TEMMER, M., RYBÁK, J., BENDÍK, P., VERONIG, A., VOGLER, F., OTRUBA, W., PÖTZI, W. & HANSLMEIER, A. (2006). Hemispheric sunspot numbers $\{R_n\}$ and $\{R_s\}$ from 1945-2004: catalogue and N-S asymmetry analysis for solar cycles 18-23. *Astron. Astrophys.*, **447**, 735–743. 213
- [204] THOMPSON, W.T. (2006). Coordinate systems for solar image data. *Astron. Astrophys.*, **449**, 791–803. 226
- [205] TRAN, T., BERTELLO, L., ULRICH, R.K. & EVANS, S. (2005). Magnetic Fields from SOHO MDI Converted to the Mount Wilson 150 Foot Solar Tower Scale. *Astrophys. J. Suppl. Series*, **156**, 295–310. 136
- [206] ULRICH, R.K. & BOYDEN, J.E. (2005). The Solar Surface Toroidal Magnetic Field. *Astrophys. J. Lett.*, **620**, L123–L127. 17, 43, 46
- [207] ULRICH, R.K., EVANS, S., BOYDEN, J.E. & WEBSTER, L. (2002). Mount Wilson Synoptic Magnetic Fields: Improved Instrumentation, Calibration, and Analysis Applied to the 2000 July 14 Flare and to the Evolution of the Dipole Field. *Astrophys. J. Suppl. Series*, **139**, 259–279. 43

REFERENCES

- [208] ŠVANDA, M., KOSOVICHEV, A.G. & ZHAO, J. (2007). Speed of Meridional Flows and Magnetic Flux Transport on the Sun. *Astrophys. J. Lett.*, **670**, L69–L72. 222
- [209] VAIANA, G.S., KRIEGER, A.S. & TIMOTHY, A.F. (1973). Identification and Analysis of Structures in the Corona from X-Ray Photography. *Solar Phys.*, **32**, 81–116. 26
- [210] VERBEECK, C., HIGGINS, P.A., COLAK, T., WATSON, F.T., DELOUILLE, V., MAMPAEY, B. & QAHWAJI, R. (2011). A Multi-wavelength Analysis of Active Regions and Sunspots by Comparison of Automatic Detection Algorithms. *Solar Phys.*, **369**. 93, 115, 159, 161, 182, 250
- [211] WANG, H. (1988). Structure of magnetic fields on the quiet sun. *Solar Phys.*, **116**, 1–16. 14, 219
- [212] WANG, H. & ZIRIN, H. (1989). Study of supergranules. *Solar Phys.*, **120**, 1–17. 235
- [213] WANG, Y.M. & SHEELEY, N.R., JR. (2003). On the Fluctuating Component of the Sun’s Large-Scale Magnetic Field. *Astrophys. J.*, **590**, 1111–1120. 47, 189, 194
- [214] WANG, Y.M., NASH, A.G. & SHEELEY, N.R., JR. (1989). Magnetic flux transport on the sun. *Science*, **245**, 712–718. 43, 46, 220, 241
- [215] WANG, Y.M., ROBBRECHT, E. & SHEELEY, N.R. (2009). On the Weakening of the Polar Magnetic Fields during Solar Cycle 23. *Astrophys. J.*, **707**, 1372–1386. 136, 207, 219
- [216] WATSON, F., FLETCHER, L., DALLA, S. & MARSHALL, S. (2009). Modelling the Longitudinal Asymmetry in Sunspot Emergence: The Role of the Wilson Depression. *Solar Phys.*, **260**, 5–19. 162, 183
- [217] WEISS, N.O. (2006). The Puzzling Structure of a Sunspot. In J. Leibacher, R.F. Stein & H. Uitenbroek, eds., *Solar MHD Theory and Observations: A High Spatial Resolution Perspective*, vol. 354 of *Astronomical Society of the Pacific Conference Series*, 213. 36
- [218] WELSCH, B.T. & LONGCOPE, D.W. (2003). Magnetic Helicity Injection by Horizontal Flows in the Quiet Sun. I. Mutual-Helicity Flux. *Astrophys. J.*, **588**, 620–629. 247
- [219] WHEATLAND, M.S. (2000). The Origin of the Solar Flare Waiting-Time Distribution. *Astrophys. J. Lett.*, **536**, L109–L112. 56
- [220] WHEATLAND, M.S. (2001). Rates of Flaring in Individual Active Regions. *Solar Physics*, **203**, 87–106. 56

REFERENCES

- [221] WHEATLAND, M.S. (2005). A statistical solar flare forecast method. *Space Weather*, **3**, 7003. 52, 56, 160
- [222] WHEATLAND, M.S. & LITVINENKO, Y.E. (2002). Understanding Solar Flare Waiting-Time Distributions. *Solar Phys.*, **211**, 255–274. 177
- [223] WILCOX, J.M. & HOWARD, R. (1970). Differential Rotation of the Photospheric Magnetic Field. *Solar Phys.*, **13**, 251–260. 16
- [224] WORDEN, S.P. & SIMON, G.W. (1976). A study of supergranulation using a diode array magnetograph. *Solar Phys.*, **46**, 73–91. 235
- [225] YAMADA, M., KULSRUD, R. & JI, H. (2010). Magnetic reconnection. *Reviews of Modern Physics*, **82**, 603–664. 87
- [226] ZHANG, J., WANG, Y. & ROBINETTE, S. (2009). Toward Creating A Comprehensive Digital Active Region Catalog. In *AAS/Solar Physics Division Meeting*, vol. 40 of *AAS/Solar Physics Division Meeting*, 09.21–+. 160
- [227] ZHANG, J., WANG, Y. & , Y. (2010). Statistical Properties of Solar Active Regions Obtained from an Automatic Detection System and the Computational Biases. *Astrophys. J.*, **723**, 1006–1018. 189, 196, 250
- [228] ZHAO, J. & KOSOVICHEV, A.G. (2004). Torsional Oscillation, Meridional Flows, and Vorticity Inferred in the Upper Convection Zone of the Sun by Time-Distance Helioseismology. *Astrophys. J.*, **603**, 776–784. 43
- [229] ZHARKOV, S., GAVRYUSEVA, E. & ZHARKOVA, V. (2008). The Observed Long-and Short-Term Phase Relation between the Toroidal and Poloidal Magnetic Fields in Cycle 23. *Solar Phys.*, **248**, 339–358. 47, 188
- [230] ZHARKOV, S.I. & ZHARKOVA, V.V. (2006). Statistical analysis of the sunspot area and magnetic flux variations in 1996–2005 extracted from the Solar Feature Catalogue. *Advances in Space Research*, **38**, 868–875. 35, 47, 188
- [231] ZHARKOVA, V.V. & SCHETININ, V. (2005). Filament Recognition In Solar Images With The Neural Network Technique. *Solar Physics*, **228**, 137–148. 116
- [232] ZHARKOVA, V.V., ABOUDARHAM, J., ZHARKOV, S., IPSON, S.S., BENKHALIL, A.K. & FULLER, N. (2005). Solar Feature Catalogues In Egso. *Solar Physics*, **228**, 361–375. 116

REFERENCES

Glossary

WL_{SG} a sum of the horizontal gradient along a detected PSL. 50, 128, 174, 175, 178, 179, 182, 185, 244

active region magnetic structures often associated with flaring sunspot groups that usually have loop structures reaching into the corona. 35, 77, 78, 82

AR active region. 38, 116–118, 121, 123, 125, 133, 134, 140, 142, 144–146, 155, 160, 171, 183, 188, 189, 191–193, 195–199, 201, 203–206, 211–213

ASAP Automated Solar Activity Prediction. 162–164

BCL bipole connecting line. 130, 151, 154

CC correlation coefficient. 182

CCD charge-coupled device. 108

cgs the unit system using centimeters, grams, and seconds for length, mass, and time. 61

CME coronal mass ejection. 53, 166

EIT Extreme ultraviolet Imaging Telescope. 161, 164

EUV extreme ultraviolet. 19, 29, 38, 54, 77, 161, 164, 172, 176, 183

FITS Flexible Image Transport System. 120

flux rope a twisted collection of flux tubes. 33–35, 40

flux-tube an elongated structure with a magnetic field along the longer axis, strongest at the center and dying off rapidly at the edges. 26, 33, 38, 40, 46, 76–78, 138, 139, 198

FWHM full-width at half-max. 150

GOES Geostationary Operational Environmental Satellites. 172, 184

Glossary

GSFC Goddard Space Flight Center. 169

HMI Helioseismic Magnetic Imager. 95, 246

HWHM half width at half maximum. 217, 218, 236

HXR hard X-ray. 54, 55

LCP left-hand-circularly-polarised. 105, 112

LCT local correlation tracking. 93, 235

LOS line-of-sight. 23, 36, 81, 87, 95, 101, 102, 106, 107, 110, 112, 116, 120, 121, 123, 126, 136, 137, 147, 148, 151, 154, 156, 157, 172, 175, 192, 209, 244

LTE local thermodynamic equilibrium. 3, 10

MDI Michelson Doppler Imager. 95, 120, 123, 136, 137, 140, 144, 148, 155, 156, 162, 172, 183, 191, 244

MHD magnetohydrodynamics. 65, 68, 90

NGDC National Geophysical Data Center. 113, 176

NOAA National Oceanic and Atmospheric Association. 113, 116–118, 136, 140–142, 146, 155, 156, 163, 183, 223, 232

penumbra the boundary of a sunspot where the magnetic fields are highly inclined to the solar surface and exhibit a filamentary structure. 48, 49, 136, 137, 156

PFSS potential field source surface. 82, 187, 188, 206, 207, 209, 210, 245

PP proton-proton. 8, 9

PSL polarity separation line. 52, 93, 127, 128, 130, 137, 144, 151, 153, 154, 163, 165, 180, 182, 184, 185, 209, 244

quiet-Sun regions on the solar surface characterised by weak magnetic fields and a lack of eruptive activity. 107, 122, 123, 138, 142

R-value the total magnetic flux near a detected PSL. 128, 144, 165, 174, 175, 178, 179, 182, 185

RCP right-hand-circularly-polarised. 105, 112

RHESSI Reuven Ramaty High Energy Solar Spectroscopic Imager. 162, 165, 169, 184

SEP solar energetic particle. 121

SFT surface flux transport. 219, 246

SMART SolarMonitor Active Region Tracker. 118, 119, 125, 126, 130, 132, 134, 136, 140–142, 145, 146, 154–157, 161, 163, 164, 167, 172, 173, 175, 177, 182, 190, 191, 206, 213, 244, 247, 251

SOHO Solar and Heliospheric Observatory. 106, 156, 222

SPoCA Spatial Possibilistic Clustering Algorithm. 161, 163, 164, 183

SSWIDL a repository of routines written in IDL generally pertaining to the analysis of solar data. 147

STARA Sunspot Tracking And Recognition Algorithm. 162–164

SXR soft X-ray. 54–56

umbra the dark center of a sunspot where the magnetic fields are nearly vertical at the solar surface. 136, 140

Glossary

Reference Tables

8. REFERENCE TABLES

Table 8.1: A list of physical constants.

Constant	Variable	cgs	SI
Permeability of Free-space	μ_0	1	$4\pi \times 10^{-7} \text{ m kg s}^{-2} \text{ A}^{-2}$
Permittivity of Free-space	ε_0	1	$8.85 \times 10^{-12} \text{ C}^2 \text{ N}^{-1} \text{ m}^{-2}$
Boltzmann's Constant	k_b	$1.38 \times 10^{-16} \text{ cm}^2 \text{ g s}^{-2} \text{ K}^{-1}$	$1.38 \times 10^{-23} \text{ m}^2 \text{ kg s}^{-2} \text{ K}^{-1}$
Gravitational Constant	G	$6.67 \times 10^{-8} \text{ cm}^3 \text{ g}^{-1} \text{ s}^{-2}$	$6.67 \times 10^{-11} \text{ m}^3 \text{ kg}^{-1} \text{ s}^{-2}$
Mass of Atomic Hydrogen	m_H	$1.67 \times 10^{-24} \text{ g}$	$1.67 \times 10^{-27} \text{ kg}$
Stephan-Boltzmann Constant	σ_{sb}	$5.67 \times 10^{-3} \text{ erg cm}^{-2} \text{ s}^{-1} \text{ K}^{-4}$	$5.67 \times 10^{-8} \text{ W m}^{-2} \text{ K}^{-4}$
Plank's Constant	h	$6.63 \times 10^{-27} \text{ cm}^2 \text{ g s}^{-1}$	$6.63 \times 10^{-34} \text{ m}^2 \text{ kg s}^{-1}$
$h/2\pi$	\hbar	$1.05 \times 10^{-27} \text{ cm}^2 \text{ g s}^{-1}$	$1.05 \times 10^{-34} \text{ m}^2 \text{ kg s}^{-1}$
Speed of Light	c	$3.00 \times 10^{10} \text{ cm s}^{-1}$	$3.00 \times 10^8 \text{ m s}^{-1}$
Mass of Electron	m_e	$9.11 \times 10^{-28} \text{ g}$	$9.11 \times 10^{-31} \text{ kg}$
Charge of Electron	e	$4.80 \times 10^{-10} \text{ esu}$	$1.60 \times 10^{-19} \text{ C}$
Coulomb's Constant	k_c	1	$8.00 \times 10^9 \text{ N m}^2 \text{ C}^2$

Table 8.2: A list of unit conversions.

Measurement	cgs	SI	other
Distance	1 cm	10^{-2} m	10^8 Å
Magnetic Field	1 G	10^{-4} T	—
Energy	1 erg	10^{-7} J	6.24×10^{11} eV
Magnetic Flux	1 Mx	10^{-8} Wb	10^{-16} G Mm
Force	1 dyn	1×10^{-5} N	—
Pressure	1 Ba	10^5 Pa	—